

The Influence of Member Orientation on Hollow section Joint Strength

Thesis submitted to the University of Nottingham for the Degree of Doctor of Philosophy

by

Robert Kelly
Master Mariner. B.Eng. (Hons)

Department of Civil Engineering
University of Nottingham
Date 24th November 1998

Abstract

The influence of the member orientation on the strength of joints formed with square hollow sections is examined. The bird beak joint system is a relatively new truss arrangement for square hollow sections, where the chord and the brace have each been rotated by 45° about their own centreline axes. Based on previous experimental testing it has been suggested that this joint system leads to a stronger joint arrangement.

Finite element analysis has been used to study the strength and behaviour of such bird beak joints and to compare them to similar joints in CHS and the traditional RHS configuration to test this claim. A comprehensive study has been undertaken for bird beak X-joints and T-joints and comparisons are made with similar traditional joints in RHS and CHS as the parameters of the width ratio β , the chord slenderness ratio 2γ and the chord length ratio α are varied. Displaced shape and contoured stress plots are included to aid understanding of the failure mechanisms.

The finite element work on K-joints allows comparisons of the strength and stiffness of bird beak K-joints with those formed in the traditional RHS configuration as the boundary conditions (at the ends of the members), the brace angle and loading conditions are varied.

A limited amount of experimental work has been carried out in the laboratories at Nottingham University, with some assistance from the author, involving the physical testing of bird beak joints so that the finite element models can be validated. This work is reported and examined critically.

The conclusions focus on the claims that the bird beak joints are stronger and how they differ from the traditional form of joints. Equations are presented to extend the design information available for a practical parameter range.

Acknowledgements

During the course of the research reported in this thesis the author has received many helpful suggestions from staff and colleagues of the department of Civil Engineering and other members of the staff at the University of Nottingham. In particular the author wishes to record his gratitude to the following:

Dr. G. Davies and Dr. J.S. Owen for acting as the supervisors to this work and for their support and encouragement, when the task of writing this thesis seemed impossible.

Miss A. Fundament, Miss M. Grunberg Mr A. Steller and Mr M. Bettison for carrying out the physical tests of the bird beak joints which have been used for the validation of the finite element models in this work.

To the staff at Cripps Computing Centre at the University of Nottingham for their assistance, but particularly Dr A. Jack, Dr J. Whitehorn and Dr T. Lomax for their expertise and assistance in solving the computing problems that have arisen during the course of this work.

Prof. Clayton and the department of Mechanical Engineering for allowing the author to use the ABAQUS Finite Element suite of programs and their computing equipment in the CAE laboratory, without which there would be no graphics in this work.

The author is very grateful and would like to express his sincere thanks to Delft University for supplying a copy of van der Vegte's thesis which has proved very informative.

To EPSRC who provided the funding for this work to be carried out

Finally, but in no means least my mother, Mrs A. Carter for reading through and correcting the finished manuscript.

Spelling Checkers

I have a spelling chequer
It came with my PC
It plainly marks four my revue
Miss takes I cannot sea
I've run this thesis threw it
I'm shore that your pleased too no
It's letter perfect in it's weigh
My chequer tolled me sew

Unknown

Table of Contents

1. Introduction and aims of the research	
1.1 Introduction	1
1.2 Structural hollow sections	1
1.2.1 History of development	2
1.2.2 Production	3
1.3 Design codes	4
1.3.1 Current design practice	4
1.3.2 Physical testing of the joints	5
1.3.3 Finite element research	5
1.4 Member orientation	6
1.4.1 Bird beak joints	6
1.4.2 Terminology used	7
1.5 The aim of the research	7
1.5.1 The topics covered in the thesis	8
2. Literature review	
2.1 Design codes	10
2.1.1 American Petroleum Institute, API RP2A and API RP2A-LRFD (API 1993)	12
2.1.2 American Welding Society Structural Welding Code	14
2.1.3 International Institute of Welding Design recommendations for hollow section joints. IIW (1989)	16
2.1.4 CIDECT design guides	16
2.1.5 Eurocodes	17
2.1.5.1 Eurocode 3 Annex K (1994)	18
2.2 A brief history of the development of finite element analysis (FEA)	18
2.3 The use of a square hollow sections in a diamond configuration	20
2.3.1 The bird beak joints	22
2.4 van der Vegte's work	30
2.4.1 X-joints in CHS	30
2.4.2 The effects of chord length on CHS X joints	31
2.4.3 T-joints in CHS	32
2.4.4 Interaction diagrams in CHS	33
2.4.5 Interaction diagrams in RHS	34
2.5 Peter Crockett's research work	35
2.5.1 Welds and Corner radii	35
2.5.1.1 Welds	36
2.5.1.2 Corner radii	39
2.5.2 Overlapped K joints in RHS with $\beta = 0.6$	40
2.5.2.1 The effects of boundary conditions	40
2.5.2.2 The effect of the hidden weld	41
2.6 The definition of the ultimate joint capacity	41
3. Finite element modelling and general details	
3.1 Introduction	44
3.2 Finite element programs and the hardware used	44
3.3 The finite element method	45
3.3.1 The finite element theory	46
3.3.1.1 An example of the construction of the stiffness matrix	46
3.3.1.2 The alternative energy formulation	49
3.3.1.3 Shape functions	50

3.3.1.4	Continuity at the boundaries of the element	53
3.3.1.5	Numerical integration	53
3.4	Analysis options	55
3.4.1	Method of loading	55
3.4.2	The modified RIKS algorithm	55
3.4.3	Non-linear material behaviour	56
3.4.4	The material properties used in this thesis	57
3.4.5	Geometric non-linearity	58
3.4.6	Boundary conditions	58
3.5	Element types	58
3.5.1	Shell elements	58
3.5.2	Solid elements	61
3.5.3	Comparison between shell elements	61
3.5.4	The shell elements used in this research	63
3.6	Modelling welds	63
3.7	Problems caused by the 3D geometry	64
3.7.1	Calculating the angle between the welded faces	64
4.	The effect of member orientation on the X joint	
4.1	Introduction	65
4.2	Definition of terms used in this Chapter	65
4.2.1	The joint capacity $F_{u,1}$	65
4.2.2	Load deformation curves	66
4.2.3	Descriptions of chord failure	66
4.2.4	The Chord length, L_0	66
4.2.5	Chord width ratio β	66
4.3	The model details for the X joints studied	67
4.3.1	The finite element meshes	68
4.3.2	Mesh connectivity and weld considerations	69
4.3.2.1	The diamond bird beak X joints	69
4.3.2.2	Square bird beak X joint	71
4.3.2.3	Traditional RHS X joints	71
4.3.2.4	CHS X joints	72
4.3.3	The type of weld assumed in the finite element models	72
4.3.4	The material properties used in the analysis	73
4.3.5	Method of loading	73
4.3.6	Convergency tests	73
4.3.6.1	Diamond bird beak X joint	73
4.3.6.2	Square bird beak X joint	75
4.3.6.3	CHS X joint	77
4.3.6.4	Traditional RHS X joint	78
4.3.7	Validation of the bird beak models	79
4.4	The numerical results for the diamond bird beak X joints	84
4.4.1	The effect of chord length L_0 and boundary conditions on the strength of diamond bird beak joints	85
4.4.2	The effect of changing the chord width ratio β and the chord wall slenderness ratio on the strength of diamond bird beak joints	85
4.4.3	The effect of brace thickness t_1 on the strength of diamond bird beak joints	87
4.5	Discussion of the results for the diamond bird beak X joint	87
4.5.1	The presence of yield lines at the corners of the chord	87
4.5.2	The effect of changing the chord width ratio β and the chord wall slenderness ratio on the strength of diamond bird beak joints	88

4.5.2.1	The variation of the joint capacity with the chord width ratio β and chord wallslenderness b_0/t_0	90
4.5.3	The effect of changing the brace thickness t_1 on the strength of diamond bird beak joints	90
4.5.4	The effect of chord length L_0 and boundary conditions on the strength of diamond bird beak joints	93
4.5.4.1	Displaced shape diagrams and contoured stress plots	96
4.5.4.2	Moment along the hinge at the corner of the chord	101
4.5.4.3	Load/lozenging curves	103
4.5.4.4	Load/indentation curves	104
4.5.4.5	Determining the joint capacity when the chord length is varied for the diamond bird beak X joint	106
4.5.4.6	Comparisons with the work of Ono, Iwata and Ishida	107
4.6	The numerical results for the square bird beak X joints	108
4.6.1	The effect of chord length L_0 and boundary conditions on the strength of square bird beak X joints	108
4.7	Discussion of the results for the square bird beak X joint	109
4.7.1	The effect of chord length L_0 and boundary conditions on the strength of square bird beak X joints	109
4.7.1.1	Displaced shape diagrams and contoured stress plots	110
4.7.1.2	Load/indentation curves	112
4.7.2	Determining the joint capacity when the chord length is varied for the square bird beak X joint	114
4.8	Traditional RHS X joints	114
4.8.1	The numerical results for the traditional RHS X joints	115
4.8.2	Discussion of the traditional RHS X joints	115
4.9	The numerical results for the CHS X joints	118
4.10	The discussion of the results for the CHS X joints	119
4.10.1	Load/indentation curves	120
4.10.2	Displaced shape diagrams and contoured stress plots for the CHS X joints	121
4.10.3	Determining the joint capacity when the chord length is varied for the CHS X joints	122
4.11	Comparisons between the joint types	124
4.11.1	The variation of joint capacity with chord length	124
4.11.2	Load/indentation curves	125
4.11.3	Failure mechanisms	126
4.12	Summary	126
5.	The analysis of the bird beak X joint	
5.1	Introduction	129
5.2	The plastic mechanisms operating in the bird beak X joints	129
5.2.1	Yield lines at the corners of the chord section	130
5.2.2	Membrane action in the chord walls	131
5.3	Short chord length joints	132
5.4	Medium chord length joints	135
5.5	Long chord length joints	139
5.5.1	Yield line and in-plane yielding mechanisms	139
5.5.2	Semi-rigid mechanisms	141
5.5.2.1	The twisting of the chord walls	142
5.5.2.2	The bending of the chord walls	144
5.6	Discussion	147
5.7	Summary	148
5.8	Conclusion	149

6. The effect of member orientation on the T joint	
6.1 Introduction	150
6.2 The model details of the T joints studied	152
6.3 The method of loading	153
6.4 The material properties	154
6.5 The method of supporting the chord	154
6.6 The type of weld assumed	155
6.7 The method of measuring the indentation	155
6.8 The moment capacity of the chord	156
6.9 Validation of the model	158
6.9.1 Convergency tests	158
6.9.2 Validation of the finite element models	159
6.9.2.1 Introduction	160
6.9.2.2 The general arrangement of the joint	161
6.9.2.3 The material properties	163
6.9.2.4 The physical properties	164
6.9.2.5 Comparison of the results	164
6.9.2.6 Conclusions	169
6.10 Diamond bird beak T joint <u>with</u> the effects of chord bending	169
6.10.1 The results of the finite element analyses for the diamond bird beak T joint with the effects of chord bending	171
6.10.2 The variation of joint capacity with chord length with the effects of chord bending.	171
6.10.2.1 Introduction	171
6.10.2.2 The influence of the chord length on joint capacity $F_{u,1}$	172
6.10.2.3 The influence of the chord length on the moment acting in the chord	173
6.10.2.4 Von Mises contoured stress plots and displaced shape diagrams	175
6.10.2.5 Load indentation curves	178
6.10.3 Calculation of joint strength for the diamond bird beak T joints	179
6.10.4 A comparison of the results to current design methods	181
6.11 Diamond bird beak joints <u>without</u> the effects of chord bending	182
6.11.1 Removing the effects of chord bending	182
6.11.1.1 Removing the effects of chord bending from CHS T joints	183
6.11.1.2 Removing the effect of chord bending from diamond bird beak T Joints	189
6.11.1.3 Displaced shape diagrams and von Mises contoured stress plots	192
6.11.1.4 Load/indentation curves for the diamond bird beak T joints without the effects of chord bending	194
6.11.1.5 Conclusions	194
6.11.2 The results of the finite element analyses without the effects of chord bending for the diamond bird beak T joints, for various β and b_0/t_0 values	195
6.11.3 Discussion of the finite element analyses without the effects of chord bending for the diamond bird beak T joints, for various β and b_0/t_0 values	195
6.12 The interaction curve method	198
6.12.1 Introduction	198
6.12.2 The theoretical determination of the reduced plastic moment capacity due to coincident shear	199
6.12.3 Interaction curves for the diamond bird beak T joints	201
6.13 Comparisons between the predicted joint capacity and the observed joint capacity	204
6.13.1 The traditional design method	205
6.13.2 Predicted design capacity from the interaction diagrams	205
6.13.3 Conclusions	206
6.14 RHS T joints	206
6.14.1 The results of the finite element analyses for the RHS T joints with the effects	

	of chord bending	207
6.14.2	Discussion of the results of the finite element analyses for the variation in joint capacity with chord length RHS T joints with the effects of chord bending	207
6.14.2.1	Displaced shape and von Mises contoured stress plots	210
6.14.2.2	Load indentation curves	213
6.14.2.3	Comparisons between the traditional RHS T joints and the diamond bird beak T joints	215
6.14.3	The method of loading used to remove the effects of chord bending	217
6.14.3.1	The results of the finite element analyses for the RHS T joints without the effects of chord bending	217
6.14.4	Discussion of the results of the finite element analyses for the RHS T joints without the effects of chord bending	218
6.14.4.1	Displaced shape diagrams and von Mises contoured stress plots for the RHS T joints without the effects of chord bending	219
6.14.4.2	Load indentation curves	221
6.14.5	Calculation of the reduced moment capacity of the traditional RHS chord	222
6.14.6	Interaction diagrams for the traditional RHS T joints	226
6.14.7	A comparison between finite element values and the different design techniques	230
6.15	Comparison of the Interaction diagrams	231
6.16	Summary	234
6.17	Conclusions	235
7.	The effect of member orientation on the K joint	
7.1	Introduction	237
7.2	The requirement for an angle function.	237
7.3	Finite element model details for the traditional RHS K joints	241
7.3.1	The advantages of using a very high yield stress value	243
7.4	The different boundary and the loading conditions.	244
7.4.1	Defining the joint capacity for the K joints	245
7.5	The results of the analyses for the traditional RHS K joints	245
7.6	Discussion of the results for the traditional RHS K-joints	246
7.6.1	The direction of the shear reactions at the brace members	248
7.6.2	Traditional RHS overlapped K Joints where $\theta = 30^\circ$	250
7.6.3	Traditional RHS overlapped K Joints where $\theta = 60^\circ$	253
7.7	The effect of disconnecting the hidden weld	259
7.8	Conclusions about the failure of the traditional RHS K joints	261
7.9	Bird beak K-joints	261
7.10	Model details of the bird beak K joint	263
7.11	Initial investigation on the bird beak K joints	264
7.11.1	Discussion of the initial investigation for $\theta = 30^\circ$	265
7.11.2	Discussion of the initial investigation for $\theta = 60^\circ$	265
7.11.3	Conclusions from the initial investigations.	266
7.12	The results of the analyses of the bird beak K joints	266
7.13	Discussion of the results for the bird beak K joints	267
7.13.1	The direction of the reactions on the brace members	268
7.13.2	Bird beak K joints where $\theta = 30^\circ$	269
7.13.3	A comparison of the bird beak to the traditional RHS K joints	272
7.13.4	Bird beak K joints where $\theta = 45^\circ$	272
7.13.5	Bird beak K joints where $\theta = 60^\circ$	275
7.13.6	A comparison of the bird beak to the traditional RHS K joints for $\theta = 60^\circ$	278
7.13.7	Conclusions about the failure of the bird beak joint	278
7.13.8	Design information	279

7.14	The principal differences between the traditional RHS K joints and the bird beak K joints	280
7.15	Conclusions on traditional and bird beak K joints	281

8. Bird beak K joints with purlin loads

8.1	Introduction	282
8.1.1	The axial load in the chord members	282
8.2	Method of loading used	283
8.3	Initial investigations	284
8.3.1	The method of supporting the purlin load	284
8.3.1.1	The T joint	285
8.3.1.2	The purlin plate	285
8.3.1.3	The T bar	285
8.3.2	Applying a compressive purlin load	286
8.3.3	The results of the initial investigation	286
8.3.4	Conclusions of the initial investigation when loading the chord with a purlin load	288
8.3.5	Determining the failure capacity of purlin loaded K joints	289
8.4	The results of the analyses of the purlin loaded K joints	290
8.4.1	Design information	295
8.5	A special case where only one purlin load is applies to a truss	296
8.5.1	Introduction	296
8.5.2	Method of loading a diamond bird beak K joint where there is an axial chord load and the cross loading of the chord is significant	297
8.5.3	The results of the analyses for diamond bird beak K joints where there is an axial chord load and the cross loading of the chord is significant	298
8.5.4	The discussion of the results for diamond bird beak K joints where there is an axial chord load and the cross loading of the chord is significant	299
8.5.5	Conclusions	301
8.6	Summary	301

9. Conclusions and Recommendations for Further Work

9.1	Introduction	303
9.2	Diamond and square bird beak X joints	303
9.2.1	Theoretical analysis of the X joints	304
9.3	Diamond bird beak T joints	305
9.3.1	T joints loaded with the effects of chord bending	305
9.3.2	T joints loaded without the effects of chord bending	306
9.3.3	Interaction diagrams	306
9.4	Traditional RHS overlapped K Joints	307
9.5	Diamond bird beak K joints	308
9.6	General advantages and disadvantages of bird beak joints	309
9.7	Future investigation	309

Table of Figures

Chapter 1 Introduction and aims of the research

Figure 1.1	Three different diamond bird beak joint configurations	6
Figure 1.2	The descriptive terminology used	7

Chapter 2 Literature review

Figure 2.1	RHS Triangular truss arrangement	21
Figure 2.2	The double T and K joints tested by Bauer & Redwood (1988)	21
Figure 2.3	The difference between the square and diamond configurations	21
Figure 2.4	Deformation of the chord observed by Bauer and Redwood (1988)	22
Figure 2.5	The arrangement shown by Ono et al (1991) for testing the bird beak T joint	23
Figure 2.6	Schematic diagram of the test rig used by Ono et al (1991) for the testing of bird beak K joints	25
Figure 2.7	Ishida et al's model for the collapse of the diamond bird beak T joint.	27
Figure 2.8	Traditional RHS X joint loaded with axial forces on the brace members and bending moments on the chord	35
Figure 2.9	Four different forms of weld modelled with 4 node shells elements	36
Figure 2.10	Four different forms of weld modelled with 8 node shells elements	37
Figure 2.11	3 Methods of modelling the corner of the weld	39

Chapter 3 Finite element modelling and general details

Figure 3.1	A 2-dimensional discrete pin ended element	47
Figure 3.2	Two forms of triangular elements	51
Figure 3.3	Compatibility requirements at inter element boundaries	53
Figure 3.4	A square 8-node element showing two different arrangements of integration points	54
Figure 3.5	The different shell elements available in ABAQUS	60
Figure 3.6	Solid elements available in ABAQUS to model the weld material	61
Figure 3.7	Example of the detail when a butt weld is assumed	63
Figure 3.8	Example of the detail when a fillet weld is assumed	63

Chapter 4 The effect of member orientation X joint

Figure 4.1	The definition of datum lengths for "indentation" and "lozenging"	66
Figure 4.2	The different forms of X joint studied in this Chapter	67
Figure 4.3	Examples of the finite element meshes for the X joints considered	68
Figure 4.4	The connection between brace and chord elements	69
Figure 4.5	Examples of the different types of weld	71
Figure 4.6	Recommened positioning of fillet and butt weld on the square bird beak joint	71
Figure 4.7	The three diamond bird beak meshes used in the convergence study	74
Figure 4.8	The results of the convergency study for the diamond bird beak X joint	75
Figure 4.9	The three square bird beak meshes used in the convergency study	76
Figure 4.10	The results of the convergency study for the square bird beak X joints	77
Figure 4.11	The two CHS meshes used in the convergency study	77
Figure 4.12	The results of the convergency study for the CHS X joints	78
Figure 4.13	The results of the convergency study for the traditional RHS X joints	78

Figure 4.14	The three traditional RHS meshes used in the convergency study	79
Figure 4.15	The engineering material properties of the joints tested	80
Figure 4.16	Validation curves for the diamond bird beak X joint $L_0=520\text{mm}$	81
Figure 4.17	Validation curves for the diamond bird beak X joint $L_0=1000\text{mm}$	81
Figure 4.18	Validation curves for the square bird beak X joint $L_0=520\text{mm}$	82
Figure 4.19	Validation curves for the square bird beak X joint $L_0=1000$	82
Figure 4.20	The effect of length and boundary conditions on the joint capacity for the diamond bird beak X joint	83
Figure 4.21	Transverse stress in B45V7 at maximum load (138.8 kN) showing the presence of yield lines	88
Figure 4.22	The variation of the joint capacity with chord width ratio β and chord wall thickness, normalised by the plastic moment capacity per unit length of the chord wall m_p	89
Figure 4.23	The fit of the predicted joint capacities against the normalised results	90
Figure 4.24	The cause of the shear action in the brace	93
Figure 4.25	The deformation apparent in the failure of the chord with no restraint at the ends	94
Figure 4.26	The deformed shape and von Mises contoured stress plot (outside surface, maximum load) of a X joint B45V12 where $\alpha = 8$ and there is no restraint at the end of the chord	96
Figure 4.27	The deformed shape and von Mises contoured stress plot (outside surface, maximum load) of a diamond bird X joint B45V10 where $\alpha = 5.33$ and the ends of the chord are held encastré	97
Figure 4.28	Three cross section of the chord shown in Figure 4.29c	97
Figure 4.29	The deformed shape and von Mises contour stress plot of the outside layer of a diamond bird beak X joint B45V7, where $\alpha = 18.7$ and there is no restraint at the end of the chord	98
Figure 4.30	Deformed shape and von Mises contour stress plot of a long diamond bird beak X joint B45V15 where $\alpha = 40$ and at maximum load of 158.6kN. There is no restraint at the end of the chord	99
Figure 4.31	Deformed profile of the top and middle corners of the chord for the joint B45V1	100
Figure 4.32	Cross section deformation of the chord in joint B45V1 at last recorded load (151.5 kN)	101
Figure 4.33	The stress distribution through the shell element	102
Figure 4.34	The magnitude of the moment along the middle corner of the chord of the joint B45V15 at maximum load 158.5kN	103
Figure 4.35	A comparison between the load/indentation curve and load/lozengeing curve for the joint B45V15	103
Figure 4.36	The relationship between the indentation and the lozengeing at the centre line of the joint B45V15	104
Figure 4.37	Load indentation curves for the diamond bird beak X joints of different chord lengths and no restraint on the chord ends	105
Figure 4.38	Load/Indentation curves for the Diamond bird beak X joint, chord ends held encastré	105
Figure 4.39	A comparison between long diamond bird beak X joints of the same length with different chord end boundary conditions	106
Figure 4.40	The predicted joint capacity against chord length for the diamond bird beak X joint	107
Figure 4.41	The effect of length and boundary conditions at the end of the chord on the joint capacity for the square bird beak joint	109
Figure 4.42	The displaced shape and von Mises contoured stress plots for the square bird beak joint for the outside surface at maximum load and no restraint at the	

	end of the chord	111
Figure 4.43	A contrast in the von Mises contoured stress plots between the diamond and square bird beak X joints for the middle layer at maximum load and no restraint at the end of the chord	112
Figure 4.44	Load indentation curves for square bird beak cross joint with no restraint on the ends of the chord	113
Figure 4.45	Load indentation curves for square bird beak X joint with the ends of the chord held encasté	113
Figure 4.46	The estimated joint capacity against chord length for the square bird beak X joint	114
Figure 4.47	Load/indentation curve for the traditional RHS X joint	116
Figure 4.48	The yield line failure mechanism in RHS X joints	116
Figure 4.49	The deformed shape diagrams and the von Mises contoured stress plots for the traditional RHS X joints at the joint capacity and for the outside surface	117
Figure 4.50	The variation of joint capacity with chord length for the CHS X joint	119
Figure 4.51	Load indentation curves for the CHS X joints	120
Figure 4.52	The displaced shape diagrams and the von Mises contoured stress plots for the CHS X joints at maximum load and the outside surface, no restraint at the end of the chord	121
Figure 4.53	The von Mises contoured stress plots for the CHS X joints at maximum load at the middle layer, no restraint at the end of the chord	122
Figure 4.54	The predicted joint capacity against chord length for CHS X joint	123
Figure 4.55	A comparison of joint capacity with chord length and boundary conditions at the end of the chord for all the joints studied	124
Figure 4.56	A comparison of some the load/indentation curves of the various joints studied	125

Chapter 5 The analysis of the bird beak X joint

Figure 5.1	The magnitude of the moment along the middle corner AB of the chord of the joint B45V15 at maximum load 158.5kN	130
Figure 5.2	A yield line model of the collapse mechanism	131
Figure 5.3	The effect of the restraint of the brace member on the deformation of the chord wall	131
Figure 5.4	The assumed deformation and the yield line mechanism for short chord length joints	133
Figure 5.5	A comparison between the finite element joint capacity and the analytical capacity for short chord length diamond bird beak X joints	134
Figure 5.6	A comparison between the finite element joint capacity and the analytical capacity for short square bird beak X joints	134
Figure 5.7	The deformed shape of the top corner of the chord for joint B45V1 for successive load levels	136
Figure 5.8	The deformed shape of the top corner of the chord for joint B45V1 for successive load levels, zoomed in on the point of zero deformation	136
Figure 5.9	The assumed relationship between the moment and the angle of rotation of the yield line along the length of the chord	137
Figure 5.10	A comparison between the finite element joint capacity and the analytical capacity for medium chord length diamond bird beak X joints	139
Figure 5.11	Togo's ring model for CHS X joints	141
Figure 5.12	Togo's ring model applied to the diamond bird beak X joint	141
Figure 5.13	Modified ring model for the diamond bird beak X joint	141
Figure 5.14	Comparisons of plastic and semi-rigid load/deflection curves	142

Figure 5.15	Cross section profiles along the length of the model without a brace present	142
Figure 5.16	A simplified view of the cross section profiles along the length of the model	144
Figure 5.17	The first assumed shape of the chord face under the bending action	145
Figure 5.18	The second assumed shape of the chord face under the bending action	146

Chapter 6 The effect of member orientation on the T joint

Figure 6.1	An example of the interaction diagrams consider in this Chapter	151
Figure 6.2	The traditional RHS and diamond bird beak T joints studied	152
Figure 6.3	Examples of the finite element mesh for the traditional RHS and diamond bird beak T joint	153
Figure 6.4	The two methods of loading the diamond bird beak T joint	154
Figure 6.5	The method of supporting the end of the chord	155
Figure 6.6	The datum point for the measuring the indentation of the diamond bird beak T joint	156
Figure 6.7	The orientation of the chord in the traditional RHS and bird beak joints	157
Figure 6.8	Calculation of the plastic moment of the chord for a diamond bird beak joint by calculus	157
Figure 6.9	The load/indentation curves for the convergency tests	159
Figure 6.10	The support arrangements at the ends of the chord	162
Figure 6.11	The plate at the end of the chord	162
Figure 6.12	Engineering stress/strain relationship of the test joints and used in the finite element analyses to validate the diamond bird beak T joint models	163
Figure 6.13	Load/deflection and load/lozenging curves for the diamond bird beak T joints used to validate the finite element models	166
Figure 6.14	The effect of chord length on the joint capacity when $\beta = 0.6$ for various chord thicknesses	173
Figure 6.15	The variation of the moment at the joint with chord wall thickness when $\beta=0.6$	174
Figure 6.16	The variation in the normalised moment in the chord with the chord length when $\beta=0.6$ and the failure is assumed to occur in the chord free of the influence of the brace member (M_p using Eqn 6.7)	175
Figure 6.17	Displaced shape diagrams and von Mises contoured stress plots for the diamond bird beak joint with the effects of chord bending at maximum load on the outside surface	177
Figure 6.18	Load indentation curves for the diamond bird beak T joint with the effect of chord bending	178
Figure 6.19	Moment/deflection curves for the diamond bird beak T joint with the effect of chord bending	179
Figure 6.20	A comparison between the observed finite element and the predicted joint capacities	181
Figure 6.21	The method used to remove the effects of chord bending	182
Figure 6.22	Removing the effects of chord bending from a diamond bird beak T joint	183
Figure 6.23	Three different methods of applying the moment to the chord	184
Figure 6.24	The method of applying moment in the model series CHS3	184
Figure 6.25	The comparison between the different methods of eliminating the chord bending effects for the CHS T joints	186
Figure 6.26	Examples of the von Mises contoured stress plots for the different methods of applying the moment to remove the effects of chord bending, shown for the outside surface at the maximum load	187
Figure 6.27	Load indentation curves for the model series CHS3, CHS T joint loaded without the effects of chord bending	188
Figure 6.28	Von Mises contoured stress plots for different chord lengths for model	

	series CHS3 for the outside surface at maximum load	189
Figure 6.29	The method of applying moment to the diamond bird beak joint	190
Figure 6.30	The axial forces applied to the chord in the finite element model to cause a moment in the chord	190
Figure 6.31	The variation of joint capacity with chord length without the effects of chord bending	191
Figure 6.32	Displaced shape diagrams and von Mises contoured stress plots for the diamond bird beak T joints without the effects of chord bending for identical joints with differing chord lengths for the outside surface at maximum load	192
Figure 6.33	Load indentation curves of the diamond bird beak T joints without the effects of chord bending for different chord lengths	194
Figure 6.34	The variation in local joint capacity $F_{u,1,loc}$ with the chord wall thickness t_0 for diamond bird beak T joints without the effects of chord bending	196
Figure 6.35	The variation in local joint capacity $F_{u,1,loc}$ with the chord width ratio β for diamond bird beak T joints without the effects of chord bending	197
Figure 6.36	The loading of the diamond bird beak T joint with the effects of chord bending	199
Figure 6.37	Interaction curve for the diamond bird beak T joint	203
Figure 6.38	Interaction diagram for the diamond bird beak T joint showing the fit of the design prediction	204
Figure 6.39	A comparison of the different design methods to the finite element joint capacities for diamond bird beak T joints with varying chord lengths	205
Figure 6.40	The method of measuring the indentation of the traditional RHS T joint	207
Figure 6.41	The variation of joint capacity with chord length for the traditional RHS T joint with the effects of chord bending	209
Figure 6.42	The variation of the normalised moment with chord length and chord wall thickness for traditional RHST joints with the effects of chord bending	209
Figure 6.43	Displaced shape diagrams and von Mises contoured stress plots of the outside level for the traditional RHS T joints at the joint capacity $F_{u,1}$. Joints loaded with the effects of chord bending	211
Figure 6.44	Example of the load/indentation curves for the traditional RHS T joints with varying chord length	213
Figure 6.45	The three different forms of curves seen in Figure 6.44	214
Figure 6.46	Example of the load/indentation curves for the traditional RHS T joints with varying chord slenderness	215
Figure 6.47	Comparison between identical bird beak and traditional RHS T joints, assuming butt welds	216
Figure 6.48	The methods of removing the effects of chord bending	217
Figure 6.49	Local joint capacities normalised by the plastic moment capacity of the chord wall, $\alpha = 36$	219
Figure 6.50	Displaced shape diagrams and von Mises contoured stress plots of the outside level for the traditional RHS T joints at the joint capacity $F_{u,1,loc}$. Joints loaded without the effects of chord bending	220
Figure 6.51	Displaced shape diagram of joint RHST1 zoomed in on the deformation in the vicinity of the brace. (displacements magnified by 3)	221
Figure 6.52	Load indentation curve for similar traditional RHS T joints with varying chord length without the effects of chord bending	221
Figure 6.53	Examples of load/indentation curves for RHS T joints without the effects of chord bending for different values of slenderness	222
Figure 6.54	The loading of the traditional RHS T joint with the effects of chord bending	225
Figure 6.55	Interaction diagram for the traditional RHS T joint ($0.2 \leq \beta \leq 0.6$)	228
Figure 6.56	Modified interaction diagram for the traditional RHS T joint ($0.2 \leq \beta \leq 0.6$)	228

Figure 6.57	Interaction diagram produce by Yu (1995) for RHS T joints	229
Figure 6.58	A comparison of the different design methods to the finite element joint capacities for diamond bird beak T joints with varying chord lengths	231
Figure 6.59	233	
Figure 6.60	233	
Figure 6.61	233	

Chapter 7 The effect of member orientation on the K joint

Figure 7.1	Overall shear failure of the chord	238
Figure 7.2	Punching shear failure of the chord face	238
Figure 7.3	Flexural failure of the chord face	238
Figure 7.4	Representation of the terms used in Eqns 7.4 - 7.6	240
Figure 7.5	The Engineering Material Properties	241
Figure 7.6	The arrangement of the elements representing the weld detail	242
Figure 7.7	Partially overlapped K joint	243
Figure 7.8	Finite element idealisation of the four traditional RHS K joints	243
Figure 7.9	The effect of the yield stress on the buckling behaviour of a simple strut	244
Figure 7.10	The four combinations of load and boundary conditions considered	245
Figure 7.11	A summary of the results for the traditional RHS K joints	247
Figure 7.12	The calculation points of the moment/load interaction diagrams	248
Figure 7.13	The theoretical reactions and the actual reactions experienced	249
Figure 7.14	The action of the braces on the top face of the chord	249
Figure 7.15	Illustration of the reactions/sense of the moments discussed	250
Figure 7.16	Chord and Brace moment/load interaction diagrams $\theta=30^\circ$	252
Figure 7.17	von Mises contoured stress plots and displaced shapes at the maximum load for the outside surface $\theta = 30^\circ$	253
Figure 7.18	Chord and Brace moment/load interaction diagrams $\theta = 60^\circ$	255
Figure 7.19	von Mises contoured stress plots and displaced shapes at maximum load for the outside surface $\theta = 60^\circ$	256
Figure 7.20	Chord and brace interaction diagrams $\theta = 40^\circ$	257
Figure 7.21	Chord and brace interaction diagrams $\theta = 50^\circ$	258
Figure 7.22	The arrangement of nodes at the hidden weld	259
Figure 7.23	The effect of not welding the hidden joint upon joint capacity	260
Figure 7.24	The projected shape of the braces on the chord of a bird beak K joint	262
Figure 7.25	Finite element idealisation of the 3 bird beak K joints, $\beta = 0.6$	263
Figure 7.26	A comparison between different models of bird beak K joint	265
Figure 7.27	A summary of the results for the bird beak K joints	267
Figure 7.28	An example of the reactions for the bird beak K joint	269
Figure 7.29	Moment load interaction diagrams for the bird beak joint $\theta = 30^\circ$	270
Figure 7.30	Bird beak K joints von Mises and displaced shape diagrams at maximum load for the outside surface, for $\theta = 30^\circ$	271
Figure 7.31	Moment load interaction diagrams for the bird beak joint $\theta = 45^\circ$	273
Figure 7.32	Bird beak K joints von Mises and displaced shape diagrams at maximum load for the outside surface, for $\theta = 45^\circ$	274
Figure 7.33	Moment load interaction diagrams for the bird beak K joint, $\theta = 60^\circ$	276
Figure 7.34	von Mises contoured stress plot and displaced shapes at the maximum load for the outside surface, $\theta = 60^\circ$	277

Chapter 8 Bird beak K joints with purlin loads

Figure 8.1	An example of a truss loaded with many purlin loads	282
------------	---	-----

Figure 8.2	The eight combinations of load and boundary conditions considered ($\theta_1 = \theta_2 = 45^\circ$)	283
Figure 8.3	Three different forms of supporting the purlin load	284
Figure 8.4	The restraint offered by the member carrying the purlin load	286
Figure 8.5	Examples of the load/deflection curves for purlin loaded K joints (Load case 1)	289
Figure 8.6	The results of the analyses for the purlin loaded K joints	291
Figure 8.7	Moment/load interaction diagrams for the purlin bird beak joint $\theta = 45^\circ$ $x=0.2$ Tension	292
Figure 8.8	Moment load interaction diagrams for the bird beak joint $\theta = 45^\circ$ no purlin plate	292
Figure 8.9	Moment/load interaction diagrams for the purlin bird beak joint $\theta = 45^\circ$ $x=0.2$ Compression	293
Figure 8.10	Examples of the contoured stress plots when a purlin load is applied to the chord	294
Figure 8.11	Example of a truss arrangement where the purlin load may be very high	296
Figure 8.12	Four different methods of loading diamond bird beak K joint with a substantial cross loading of the chord and an axial chord load	297
Figure 8.13	The variation in joint capacity of the K joints where there is an axial chord load and the cross loading of the chord is significant	299

List of Tables

Chapter 1 Introduction and aims of the research

Table 1.1	The grades of steel available for hot finished structural sections and their basic properties. (British Steel 1994a)	3
-----------	--	---

Chapter 4 The effect of member orientation in X joints

Table 4.1	Details of the joints tested by Grunberg (1994) and Fundament (1995)	80
Table 4.2	The stress/strain relationship of the test joints	80
Table 4.3	The variation of joint capacity with chord length and boundary conditions for the diamond bird beak X joint	84
Table 4.4	The finite element results of the parameter study, chord length $\alpha = 40$	86
Table 4.5	The normalised joint capacities of the parameter study	86
Table 4.6	The finite element results of the parameter study for the change in brace thickness with the chord length L_0 constant ($\alpha = 40$)	87
Table 4.7	A comparison between the chord punching shear capacity and the brace capacity to the joint capacity	92
Table 4.8	The results of the finite element investigation on the effects of chord length and boundary conditions on the square bird beak X joint.	108
Table 4.9	The variation of joint capacity with chord length and boundary condition for the traditional RHS X joint	115
Table 4.10	The variation of joint capacity with chord length and boundary condition for the CHS X joint	118

Chapter 6 The effect of member orientation in T joints

Table 6.1	The results of the convergency test	159
Table 6.2	The nominal dimensions of the diamond bird beak T joints tested by Steller (1996)	159
Table 6.3	The outside corner radii of the hot rolled and cold formed sections used in the validation of the X and T joints respectively	160
Table 6.4	Engineering stress/strain relationship of the test joints and used in the finite element analyses to validate the diamond bird beak T joint models	163
Table 6.5	Physical properties of the test joints and used in the finite element analyses to validate the diamond bird beak T joint models	164
Table 6.6	A comparison of the initial stiffness and maximum joint capacity for the validation of the diamond bird beak T joint models	167
Table 6.7	The deflection at maximum joint capacity	168
Table 6.8	The finite element analysis results of bird beak T joints with the effects of chord bending, width ratio $\beta = 0.6$	170
Table 6.9	The finite element analysis results of diamond bird beak T joints with the effects of chord bending for all other chord width ratios	172
Table 6.10	A comparison between Ishida et al design equation for diamond bird beak T joints and similar finite element results where $\alpha = 6$	180
Table 6.11	The material properties used in the CHS T joints	185
Table 6.12	The results of the finite element analyses for the CHS T joints without the effects of chord bending.	186
Table 6.13	The variation of local joint capacity $F_{u,1,loc}$ with chord length α for diamond bird beak T joints without the effects of chord bending	191
Table 6.14	The local joint capacities $F_{u,1,loc}$ for diamond bird beak T joints without the effects of chord bending	196
Table 6.15	The values used to produce the interaction diagrams for the diamond bird	

	beak T joints	202
Table 6.16	The variation of the joint capacity $F_{u,1}$ with chord length α for traditional RHS T joints with the effects of chord bending	208
Table 6.17	The local joint capacity $F_{u,1,loc}$ for traditional RHS T joints without the effects of chord bending	218
Table 6.18	The values used to produce the interaction diagram for the traditional RHS T joints	227

Chapter 7 The effect of member orientation in K joints

Table 7.1	The Engineering Material Properties	241
Table 7.2	The eccentricities of the various models	242
Table 7.3	A summary of the results for the traditional RHS K joints (overlap = 56%)	247
Table 7.4	A summary of the failure mechanisms at $\theta = 30^\circ$	251
Table 7.5	A summary of the failure mechanisms at $\theta = 60^\circ$	254
Table 7.6	The results of the analyses when the hidden weld is released	260
Table 7.7	Parameters varied in the initial investigations	264
Table 7.8	A summary of the results for the bird beak K joints	266

Chapter 8 Bird beak K joints with purlin loads

Table 8.1	Purlin loaded in tension by 0.1559P (Load case 1)	287
Table 8.2	Purlin loaded in tension by 0.3118P (Load case 1)	287
Table 8.3	Purlin loaded in compression by 0.4 P (Load case 1)	288
Table 8.4	The results of the analyses for the purlin loaded K joints	290
Table 8.5	The joint capacities of the K joints where there is an axial chord load and the cross loading of the chord is significant	298

List of symbols

a	Throat thickness of the weld
A	Area of the section, general
A_1	Area of the brace
A_0	Area of the chord
A_v	The area of the section resisting shear
\underline{b}	Vector normal to the face of the brace
b_{eff}	Effective width of the through brace
$b_{e,ov}$	Effective width of the overlapping brace
b_i	Width of the through brace
b_j	Width of the discontinuous brace
b_0	Width of the RHS chord
b_l	Width of the RHS brace
\underline{c}	Vector normal to the face of the brace
$C_{1.....5}$	Constants or functions
d_0	Diameter of the CHS chord member
d_1	Diameter of the CHS brace member
e	Eccentricity
E	Young's Modulus
$f(n)$	Stress level function of the chord
f_y	Yield stress
$f_{y,0}$	Yield stress of the chord
$f_{y,1}$	Yield stress of the brace
F	Force, general
F_k	Characteristic applied force or action
$F_{m_{ij}}$	Horizontal axial force in chord causing a moment
F_p	Force applied to the purlin
F_u	Horizontal axial reaction of chord or the load applied to the braces in K joints
F_k	Characteristic applied force or action
$F_{m_{ij}}$	Horizontal axial force in chord causing a moment
$F_{u,1}$	The force applied to the brace at the joint capacity
$F_{p,v,0}$ is	Force applied the brace when the moment capacity $M_{p,v,0}$ of the chord achieved
$F_{u,1,asymptotic}$	The force applied to the brace at the joint capacity, constant with changing chord length
$F_{u,1,fy}$ yield	The force applied to the brace at the joint capacity, with a different stress
$F_{u,1,length}$ varies	The force applied to the brace at the joint capacity, when capacity with length
$F_{u,1,loc}$	The force applied to the brace at the joint when the effects of chord bending have been removed
$F_{u,1,\alpha=11.5}$	The force applied to the brace at the joint capacity, when the chord length of ratio $\alpha=11.5$
F_{sq}	Squash load, general
$F_{0,sq}$	Squash load of the chord
$F_{1,sq}$	Squash load of the brace

g	Gap between the brace members
G	Torsional rigidity Modulus
h_i	Height of through brace (when not square)
h_j	Height of discontinuous brace (when not square)
h_0	Height of chord (when not square)
H_j	Distance of horizontal axial force $F_{m_{ij}}$ from centre line of the chord
I	Second moment of area
J	Torsional constant
k	Reduction in the moment due to position along the chord
L	Leg length of the weld/Length of yield line/Length of semi-rigid mechanism
L_0	Length of the chord
m_p	Moment capacity of the section wall (per unit length)
M	Moment, general
M_D	Factored bending moment in the brace member
M_e	Elastic moment capacity (of a section)
M_p	Plastic moment capacity (of a section)
$M_{e,v,0}$	The elastic moment capacity of the chord, reduced for the shear
$M_{p,v,0}$	The plastic moment capacity of the chord, reduced for the shear
M_u	Moment acting in the member, (total of primary and secondary moments)
$M_{u,1}$	The moment applied to the brace at the joint capacity
$M_{u,0}$	The moment acting in the chord at the joint capacity
$N_{i,R}$	Internal axial resistance of the joint
N_s	Serviceability Load
N_u	Ultimate load
p	Length of the foot print of the brace on the chord, projected if necessary
P	Load applied to the brace
P_1	Load supported by the yield line
P_2	Load support by the shear in the chord
P_D	Factored axial load in the brace member
P_{uj}	Ultimate joint axial capacity
q	Length of the overlap between the brace members
Q_f	Chord stress factor
Q_u	Load and geometry parameter
Q_β	Chord width ratio parameter
R_B	Reaction of brace (at right angle to centre line)
$R_{C,h}$	Reaction of the chord, horizontal
$R_{C,v}$	Reaction of the chord, vertical
t	Thickness general
t_0	Chord wall thickness
t_1	Brace wall thickness
T	Applied Torque
V	Shear
V_p	Shear capacity of the section
Z_0	Elastic Modulus of the chord
x	Reduction factor in the load applied to a member
α	Chord length ratio ($=2L_0/b_0$)

α^*	Coefficient of effective area of the chord
β	Chord width ratio ($=b_1/b_0$)
β_c	Chord width ratio of the compression brace
δ	Displacement of the brace
$\epsilon_{el,yield}$	Strain at yield
ϵ_{eng}	Engineering strain (or nominal strain)
ϵ_{in}^{pl}	Log plastic strain
2γ	Chord wall slenderness ($=b_0/t_0$ or d_0/t_0)
ϕ_j	Resistance factor for tubular joints
γ_F	Partial safety factor to account for the variability of the load
γ_m	Partial safety factor to account for the variability of the material
γ_{Mj}	Partial safety factor for the resistance of the joint
l	Slenderness of the compression member
λ_{ov}	Overlap ratio in K joints
θ	Angle between the brace and chord members
σ_c	Critical Euler stress
σ_{eng}	Engineering Stress
σ_n	Normal stress
σ_{true}	True Stress (or Cauchy Stress)
$\sigma_{1.....5}$	Stress at different level in the shell element
τ	Shear stress
Φ	Angle through which the chord face is twisted

1.

Introduction and Aims of the Research

1.1 Introduction

The use of Structural Hollow Sections (SHS) has increased enormously world-wide due to their structural advantages and ready availability. Research has also been an important factor in their popularity as this has led to a greater understanding of joint strength and the behaviour of structural sections essential so that designers can use them with confidence. This work hopefully contributes to the field of knowledge and understanding of a new form joint proposed by Ono et al (1991)

1.2 Structural hollow sections

Nature makes many uses of hollow sections, canes, reeds and bones being just a few examples. Architects are attracted to the clean aesthetic lines of SHS that allow them to produce the elegant structures that we see all around us daily. Is this just a preference, or do hollow sections have significant advantages over other structural members?

SHS have distinct properties that make their use as structural members very desirable and this has led to their increased use in recent years as the cost of manufacture has fallen in real terms. SHS have a very high strength to weight ratio when subjected to compressive axial loads. The larger radius of gyration about the “minor” axis provides a superior column performance and resistance to buckling. The void inside the hollow section can also be filled with concrete which not only allows an increase in strength of the column, but also the fire resistance. There is also a reasonably good resistance to bending in both directions provided by the high I values of the section, as most of the material is located away from the neutral axis. The closed cross section profile gives SHS a very high resistance to torsional forces when compared to sections with an open cross section profile.

As the external surface area of a SHS is only about two thirds of that of an open section the maintenance costs of cleaning and painting are reduced. Providing the ends

of the section are closed then the risk of ponding of water is reduced which lowers the corrosion possibilities when used in an exposed location. Circular Hollow Sections (CHS) are used extensively in offshore platforms and other structures that have wind and/or wave loading, as their shape has a relatively low drag coefficient. The hollow section can also be used to supply services or transport fluids around the structure.

There are disadvantages in using SHS, for example the higher cost of manufacturing the section, which is up to 25% more expensive and the higher cost of producing the joints during the fabrication stage. This is particularly so for CHS where the ends of the member have to be profiled so the members fit together for welding. However, this is offset by the fact that smaller lighter sections can be used and this reduction in weight can lead to significant savings in material purchase, transportation and erection costs. Each module of the structure produced by the fabrication yard is less flimsy and not so prone to damage during the transport and erection stage, although the relatively thin walls of the section are very susceptible to collision and corrosion damage. As there is no internal access to the section it is almost impossible to use bolts in the construction unless the sections to be joined are flanged. For the fixture of fittings to hollow sections British Steel has developed a system called "flow drill" that enables bolts to be used, although it is relatively expensive in labour.

1.2.1 History of development

Early uses of fabricated structural hollow sections can be seen in the Britannia Bridge across the Menai straits (rectangular section) designed by Stephenson and Fairbairn and completed in 1850, the Royal Albert bridge at Saltash across the river Tamar (elliptical section) designed by I. K. Brunel and completed in 1851, the Firth of Forth Bridge (circular section) in Scotland designed by Baker and Fowler and completed in 1890. (The Forth bridge was also the first major structure built using mild steel.) In these early examples, the structural hollow sections were made by riveting rolled plates together to form a hollow section.

The first tubes were produced by an Englishman called Whitehouse in the nineteenth century from steel plate by rounding it and then fire welding the seam. SHS grew in importance after the development of the continuous welding process by Frenz-Moon in 1930 and the further development of the welding processes that occurred in the Second World War. However, the design procedures dated back to the riveting days

when gusset plates were used in the construction of joints. It was only in the early fifties that Jamm (1951) began to determine the strength of welded tubular joints.

1.2.2 Production

SHS are manufactured in this country by British Steel at their plant in Corby, Northants. Rolls of steel strip are fed into the rollers and joined together so that the manufacturing process is a continuous operation. The strip is rolled into circular shape and the free edges joined together by induction welding.

RHS is formed from CHS by rolling the circular tube into a rectangular shape. After being cut to size the sections may then be heat treated to remove the residual stresses and restore the loss in ductility caused by the rolling process to form Hot-finished sections. Hot finished RHS sections can be visually identified by the small radii at the corners of the section, made possible by the heat treatment removing the very high residual stresses that would otherwise be present from the cold working.

Cold formed sections where no heat treatment has been applied are increasing in popularity as they are cheaper to produce and although the steel is not as ductile as hot finished sections it has a similar ultimate strength. The hot finished and cold formed CHS have identical geometric properties but, due to the larger radii at the corners in the cold formed RHS they have slightly lower geometric properties than the hot finished sections.

All technical information on the hot finished and cold formed sections can be found in the relevant British Steel publications (1994a & 1994b).

All steel delivered by British Steel comes with the appropriate dual certification, according to British Standard/European Standard required. These certificates give the dimensions of the sections, chemical composition, material properties and the manufacturing process.

	Grade 43C S275J0H	Grade 50C S355J2H
Yield Value, f_y ($t < 16\text{m}$)	275 N/mm ²	355 N/mm ²
Ultimate Tensile Strength	410/560 N/mm ²	490/630 N/mm ²

Table 1.1 The grades of steel available for hot finished structural sections and their basic properties. (British Steel 1994a)

1.3 Design codes

Current design recommendations which will be reviewed in greater detail in Chapter 2, have been compiled on the basis of a series of physical tests or more recently using Finite Element Analysis (FEA) to determine the resistance of joints. These results are compiled together in a simplified form to enable the designer to assess the design strength of any joint.

1.3.1 Current design practice

In order to understand some of the failings of modern design methods a brief outline of the design procedure is considered here. Wardenier et al (1991) & Packer et al (1992) recommend that the following stages should be considered for a safe economical design:

- determine the geometry of the structure keeping the number of joints to a minimum
- determine the loads at the connections and on the members
- determine the axial load in the members assuming a pinned structure and all centrelines are nodding
- determine chord member size by considering the axial loading
- determine the brace member size based on the axial loading
- standardise chord and brace members to minimise the number of different sections in the structure
- check the joint geometry to satisfy the validity limits given in the code.
- check the joint resistance, modifying the members if required
- check the effect of the primary moments on the chord. For chords in compression the moments caused by the joint eccentricities are to be considered as well. Then check that the factored resistance of all the chord members is still adequate under the influence of both axial loads and the primary bending moments
- check the deflections
- design the welds

One of the failings of current design practice is that the reduction of the joint resistance due to the interaction of axial load and bending moments in the chord is not always considered. In this thesis a new method is considered that allows for the reduction of the joint resistance due to the presence of bending moments in the chord.

There is very little design information on bird beak joints, although Packer et al (1992) briefly reports the findings of Ono, Iwata and Ishida (1991), no reference is made to them in Eurocode 3 Annex K (1994).

1.3.2 Physical testing of the joints

All the data for the formation of the original codes came from the physical testing of the joints in the laboratory, which is a long, expensive and tedious process. In any physical test joint there is an amount of uncertainty. Is the thickness of the material consistent? What are the exact material properties? Is there an unknown flaw in the test specimen that will increase/decrease the observed strength of the joint? Are the boundary conditions known exactly? These are just some of the unknown variables which could be present in a experimental test and although steel is a very consistent material there will always be a scatter in the results.

The physical joints used to validate the computer models in this thesis were tested in the Civil Engineering laboratory at the University of Nottingham.

1.3.3 Finite element research

Recent progress in computing technology has enabled large advances to be made in finite element analysis. Large numbers of joints can now be tested economically on a workstation and provided that the standard models are verified against a few physically tested joints the results can be very reliable. Increasingly the results of finite element analysis are being used to provide the databank on the basis of which the design codes are being prepared.

Some of the advantages of finite element modelling are that the values of the parameters entered into the input program are known precisely so that the errors due to measurements etc. are eliminated from the assessment procedure. In addition to this different load and boundary conditions can be easily imposed on the computer model, which would be difficult or impossible in a laboratory.

There is however an important proviso, viz. "Is the computer modelling the joint that the user thinks that the computer is modelling?" Also it should always be borne in mind that just because the solution is given to four significant figures, there are inaccuracies inherent in the numerical idealisation so that the solution is not correct to this level of accuracy.

All the Finite Element Analysis in this work has been done using the ABAQUS suite of programs (Versions 5.2 to 5.5). ABAQUS Post was used to process the results and produce the graphics presented in this thesis. A mesh generation package FEMGEN (FEMVIEW 1989) was used when required for complex intersection models. The computational analysis was carried out on a DEC Alpha cluster of work stations at Nottingham University.

1.4 Member orientation

This thesis considers the effect that member orientation has on the strength of the joint, principally by comparing the bird beak joint with the more traditional forms of joint in RHS and CHS. However, in the work on K-joints the effect of changing the angle between the chord and the brace members is also considered both for the traditional RHS and the bird beak joints.

1.4.1 Bird beak joints

The bird beak joint system is a relatively new truss system in which the chord and the brace have each been rotated by 45° about their own centreline axes. Examples of the joints considered in this thesis are shown in Figure 1.1.

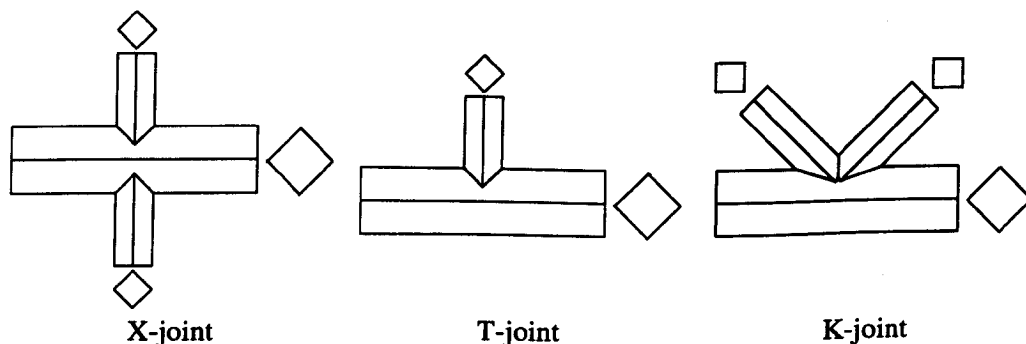


Figure 1.1 Three different diamond bird beak joint configurations

One of the advantages of a traditional RHS joint is that the profiling of the joint is a lot simpler than for CHS. However, with the increasing use of automated cutting equipment in the fabrication workshop more complex joints can be produced economically. The geometry of the bird beak joint, whilst more complex than the traditional RHS joint, is simpler than for a CHS joint and it should be possible to profile both ends of a member, which cannot be done for CHS without very sophisticated cutting equipment. The profiling required for bird beak joints made from cold formed

sections is a lot more complex than for hot finished sections due to the large corner radii. There has been no attempt to model the corner radii of RHS in this thesis, with one exception, so the models are more representative of hot finished rather than cold formed sections.

1.4.2 Terminology used

The term bird beak joint is used throughout this thesis. However, it is referred to by other names in other literature. Ono et al (1991) refer to a Y truss system, whilst Packer et al (1992) refer to either a bird mouth joint or a bill-shaped joint.

Figure 1.2 shows the descriptive terminology used in this thesis when discussing the bird beak joints.

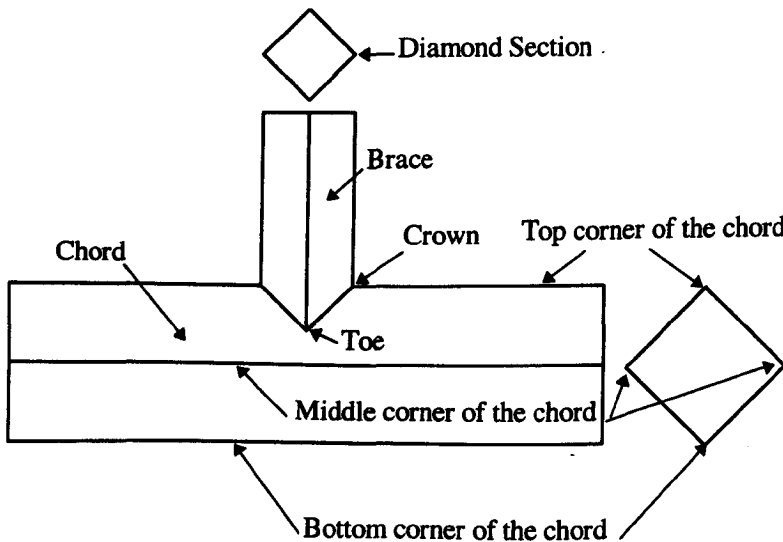


Figure 1.2 The descriptive terminology used

1.5 The aim of the research

Up to the present no other work has been carried out on bird beak joints other than the original work in Japan by Ono, Iwata and Ishida (1991, 1993 & 1994) which is reviewed in more detail in Chapter 2. The principal aim of this investigation is to increase the understanding of the behaviour of bird beak joints and particularly to critically examine the claims made by Ono et al, about the increase in strength over other joint configurations and to see if they are justified.

Finite element analysis methods will be used to compare the strength, stiffness and failure mechanisms of bird beak joints with the more traditional forms of joints in RHS and CHS. There is very little design information on the strength of the bird beak joints published in the design recommendations for RHS joints by CIDECT (Packer et al 1992). There is also a caution that the equations presented should only be used for the same parameter ranges as the tests conducted. The results of this thesis will provide additional design equations and enlarge the parameter range. Furthermore there will be guidance on the behaviour of bird beak joints and how the failure mechanisms differ from that of the traditional RHS joints.

1.5.1 The topics covered in the thesis

There is very little literature to review on bird beak joints, Chapter 2 examines the published work by Ono, Ishida and Iwata on bird beak joints and other instances where square RHS sections have been used in the diamond configuration. During the course of this research some of the ideas and results presented in published work are explored and developed, principally by van der Vegte (1995) and Crockett (1994). A short summary of the relevant sections is given to provide the reader, who may not have read these works, a review of the work that has been carried out previously.

Chapter 3 examines some of the basic theory of the finite element method and reviews some of the analysis options used in the thesis, explaining what they are and why they are used.

The work reported in this thesis was carried out in approximately the same order in which it is reported. Bird beak X joints where $\theta = 90^0$ were studied first and are reported in Chapter 4 to examine the joint behaviour in the absence of chord bending moments. Two forms of bird beak joint are examined, the diamond bird beak, shown Figure 1.1 and a hybrid joint referred to as the square bird beak joint (where the braces have not been rotated through 45^0). In order to compare the diamond and square bird beak joints with similar joints, a limited number of X joints in the traditional RHS and CHS configuration are examined and the results used in the comparison with the bird beak joints.

Chapter 5 examines the possibilities of developing a yield line model to predict the joint capacity based on observations of the FE results in Chapter 4. The formulation of a pure yield line model proved impossible due to the many different complex

mechanisms operating at failure. These mechanisms are examined and an attempt is made to assess the contribution of each to the joint capacity.

Van der Vegte (1994a, 1994b and 1995) proposed a new method of calculating the strength of CHS T joints where the force acting on the brace and the moment acting in the chord are considered when determining the joint capacity. This method requires that the joint capacity is known when the chord bending moment under the brace is zero. Consequently Chapter 6 examines T joints, first with and then without the effects of chord bending for the diamond bird beak joint. Again a series of traditional RHS T joints are examined in the same way and the results compared with those for the bird beak joints.

Crockett (1994) posed the question of whether an angle function was required in the design formula for traditional RHS overlapped K joints. A series of analyses for overlapped traditional K joints, in addition to those reported by Crockett (1994), were examined and these results are reported in Chapter 7. Similar overlapped bird beak K joints were then analysed and the results compared to those obtained for the overlapped traditional RHS K joints.

There has been no work to date on the effects of a purlin load on the joint capacity of diamond bird beak K joints. The effects of cross loading the chord, seen in the X and T joints studied previously, could possibly reduce the joint capacity significantly. Chapter 8 examines different methods of how the purlin load may be applied to the joint and the effect that this has on the joint capacity.

2.

Literature Review

2.1 Design codes

The consequences of a badly designed structure can be catastrophic and designers need to know that their structures will be safe and fulfil the design requirements. It is therefore clearly to the designer's advantage to use standardised methods and assumptions that have proven acceptable in the past and can be used in the design of future structures. Examples of this procedure can be seen in some of the earlier civil engineering works (the construction of churches and cathedrals) where a proven structure was copied and adapted to fit the new situation. The need to define what is safe and acceptable has led to the development of design codes. The earliest example of a "design code" was published by Hammurabi the king of Babylon in 2200 BC and although it does not specify how the structure should be built, the king laid down fearsome penalties should the structure collapse, which could lead to the builder being put to death.

In Britain there have been government regulations of some sort since the Middle ages and their development has been based on disasters such as the Great Fire of London 1666 and the collapse of the Ronan Point flats 1968. The first standardisation of good design practice began in 1901 with the setting up of the Engineering Standards Committee (a forerunner of the British Standards Institute). Today there are a wide variety of different regulations, made under various government acts which in general do not specify specific detail, but refer to codes of practice published by the British Standards Institution. These British Standards now incorporate the regulations issued by the European Union in its attempt to standardise the various codes used throughout Europe.

Before examining the individual design codes in greater detail, it is worth considering the historical development of design codes for tubular joints and structural members. The earlier design codes were based on a permissible stress approach, for example BS449, which limited the allowable stress in a structure. This approach limited

the working stress - based on an elastic analysis - to the material yield stress divided by a safety factor and did not allow for the plastic redistribution which occurs in ductile material such as mild steel. This method gave little indication of the real safety factor against collapse.

In tubular joints where an elastic analysis of the joint is impossible to perform without finite element analysis due to the complex stress patterns involved, the working stress design codes have had to take a strongly empirical approach to the design of tubular connections.

A more recent philosophy is the development of the "limit state" design codes, for example BS5950, which make the designer more aware of the real level of safety against a particular failure or limit state. A limit state is the point where the structure no longer satisfies the design requirements and can be considered as unfit for further use. Limit states are divided into two groups, the ultimate limit state based on structural collapse and the serviceability limit state when the structure is no longer fit for ordinary use without remedial work being carried out. Ultimate limit states include the strength of the structure, stability against overturning, fatigue and brittle fractures, whilst the serviceability limit state considers excessive deflections, vibration, repairable fatigue damage and corrosion. The reliability of the structure is controlled by the non-occurrence of each particular limit state and is determined by a series of partial safety factors. Some partial safety factors are associated with the applied forces (loads) or actions and others with the resistance or capacity of the element being considered. The former have to take into account the likelihood of a particular loading condition occurring within the design life of the structure, together with its distribution, whilst the latter consider the variability of the material properties (including strength) and the geometric tolerances associated with manufacturing and fabrication procedures. However, additional effects may also be included such as the difficulty of inspection and repair, the consequences of a failure and other socio-economic design criteria. All these factors are included on a rational probabilistic basis to achieve an overall safety margin that considers individually all the hazards and risks that have been identified.

The principle of safe design is then embodied in the inequality

$$\text{Limit state action} < \text{Corresponding limit state resistance}$$

i.e. a general equation for the ultimate limit state design for the strength of an axially loaded joint is

$$F_k < \frac{N_{i,R}}{\gamma_{Mj} \gamma_m \gamma_F} \quad \text{Eqn 2.1}$$

Where

F_k is the characteristic applied force or action

$N_{i,R}$ is the internal axial resistance of the joint

γ_F partial safety factor to account for the variability of the load

γ_m partial safety factor to account for the variability of the material

γ_{Mj} partial safety factor for the resistance of the joint

Additional partial safety factors may be included by the designer to increase the level of safety in the design of the joint at the designer's discretion.

The most recent development in the standardisation of the design codes is the introduction of the Eurocode, which attempts to standardise good building design throughout Europe. Whilst BS449 and BS5950 are still valid in the UK, they will be eventually replaced by Eurocode 3 (1992).

As BS449 and BS5950 have been written for the design of open section steel structures, recommendations for the design of hollow section steel joints have always been covered by separate guidelines. It was not until the introduction of the Eurocode 3 that the design recommendations for the design of steel hollow section joints were included into the main code, in Eurocode 3 Annex K (1994). Some of the more important codes concerning the design of SHS joints are now examined in greater detail.

2.1.1 American Petroleum Institute, API RP2A and API RP2A-LRFD (API 1993)

The clauses for the design of tubular joints in API RP2A are based on a lower-bound interpretation of test data and a number of extrapolations which allow the design rules to be applied to joints where the geometry and load cases considered are outside the range covered by the test data. Although the API RP2A code is based on the ultimate strength test data for tubular joints the code is not formulated as a limit state design code and requires that the design load is not greater than the allowable joint capacity. This joint capacity is calculated by reducing the observed maximum strength from the test data to allow for changes in the loading conditions, configuration and geometry of the joint. The design load is calculated from the applied load magnified by a safety factor against static collapse appropriate to the load case (operating or storm loading).

The latest edition (20th) of this code RP2A has also been published as the first edition of RP2A-LRFD (LRFD = Load and Resistance Factored Design) as an alternative where a limit state approach is used. The main provisions of this code remain generally the same as API RP2A where the working strength approach is used, but where the safety factors against failure are considered as a series of partial safety factors as used in any other limit state code. This code is in the process of being adopted as the international standard ISO/DIS 13819.

When considering the nominal load approach for a simple joint the API design code considers the following subsections in section E3.

Joint classification. Defines the appropriate joint for calculating the allowable load.

Allowable joint capacity. The API code requires that the nominal brace loads should not exceed the allowable joint capacity of

$$P_D < \phi_j P_{uj} \quad \text{Eqn 2.2}$$

$$M_D < \phi_j M_{uj} \quad \text{Eqn 2.3}$$

where

P_D is the factored axial load in the brace member ($P_D=1.7P$)

M_D is the factored bending moment in the brace member ($M_D=1.7M$)

P_{uj} is the ultimate joint axial capacity = $\frac{f_y t_0^2}{\sin \theta} Q_u Q_f$

M_{uj} is the ultimate joint bending moment capacity = $\frac{f_y t_0^2}{\sin \theta} (0.8d_1) Q_u Q_f$

ϕ_j resistance factor for tubular joints (given in a table)

f_y is the (specified) yield strength

t_0 is the (nominal) chord wall thickness

d_1 is the diameter of the brace member

When Eqns 2.2 & 2.3 are applied for the operating conditions the safety factor is 1.7. When environmental loads are considered, the load is permitted to increase by 33% so that the safety factor is reduced to 1.28.

The value of the load and geometry parameter (Q_u). This includes many different factors that affect the strength of the joint of which the principal one is Q_β , the effect of the chord width ratio β .

The value of the chord stress factor (Q_f). This provides for a reduction in joint strength when there are high stresses in the chord.

Brace-load interaction requirement. This provides for the interaction between axial load and the moments present in the brace acting together to be less than the capacity of the joint.

Joint detailing. This provision details the requirements that have to be met for any extra material added to the joint configuration before it may be considered as a part of the joint.

When the load is transferred through the chord i.e. X joints, then the chord should be designed to resist these forces. This may be an approximate ring analysis where an effective length of three chord diameters through the joint is considered. The provision of this clause is for checking the stresses in the hoop direction of the chord wall caused by the bending of the chord wall under the action of the applied loads.

2.1.2 American Welding Society Structural Welding Code

The AWS design code concerning tubular joints is more extensive than the API code in that RHS is considered. However, the basic approach is very similar to the API code with the main differences confined to detail and presentation. The “punching shear” is the only approach considered with no guidance for the nominal load approach being given.

Considering only the sections that differ significantly with the API code for the static strength of welded hollow section joints, four different areas have been identified (UEG 1986).

Geometric definitions. The AWS definition of a T joint includes Y joints where $\theta \geq 80^\circ$. Acting and allowable “punching shear stress”. The formulation of permissible “punching shear” stress is similar to that described in the API however, the AWS introduces an ovalising parameter α_0 , to match more closely the test data. This technique has the advantage that there is an allowance made of the effects of multi-planar joints, although it should be used carefully until more multi-planar joint test data becomes available.

The in-plane and out-of-plane bending stresses are combined to a single effective bending stress. (Whereas in the API the two components are kept separate.) The

combined bending moment and axial stresses are then checked to ensure that the interaction between them is below the joint capacity.

Brace load interaction requirements. The interaction between the brace loads discussed above is taken to be

$$\left(\frac{\text{Acting}}{\text{Allowable}} \right)_{\text{axial}}^{1.75} + \left(\frac{\text{Acting}}{\text{Allowable}} \right)_{\text{bending}} \leq 1.0 \quad \text{Eqn 2.4}$$

Load transfer through the chord. The compression in any brace of a DT/X joint is limited to

$$P = \frac{f_y t_0^2}{\sin \theta} (1.9 + 7.2\beta) Q_\beta Q_f \quad \text{Eqn 2.5}$$

In the 1992 edition of the AWS code a section is included in the tubular connection design on the ultimate strength format using a load reduction factor design (Marshall 1992). This was derived from and is intended to be equivalent to the earlier punching shear format.

For the design of RHS connections the design formulae are based on the yield line theory and although other failure modes have been considered as the chord width ratio varies, material shear, web crippling and side wall buckling they all have been adapted to the punching shear format used in the rest of the code.

$$V_p = \frac{f_{y,0}}{0.6\gamma} Q_\beta Q_f \quad \text{Eqn 2.6}$$

where

$$Q_\beta = 1/(4\beta(1-\beta)) \text{ for } \beta \geq 0.5 \quad \text{and} \quad Q_\beta = 1 \text{ for } \beta \leq 0.5$$

For small values of the chord width ratio β the AWS gives a more conservative value for the joint capacity than the IIW/CIDECT design codes for the same joint; however, as the chord width ratio β increases this tendency is reversed. This discrepancy may be attributed to an acceptance of a larger deformation at failure and an allowance of reserve strength factor of 1.5.

The 1992 edition of the AWS code has substantially revised the area of the code concerning RHS as a general overhaul of the code to include both Allowable stress designs (ASD) and Load reduction factored design (LRFD) in the AWS code (Marshall

1992). The LRFD section is very similar to the IIW and CIDECT design codes in that it is based on the thickness squared ultimate strength format.

2.1.3 International Institute of Welding Design recommendations for hollow section joints. IIW (1989)

Prior to the publication of the first IIW recommendations in 1981, there were considerable differences in the design recommendations for tubular joints around the world. Through the work of the IIW-Subcommittee XV-E a consensus was obtained and published as the IIW design recommendations 1981 and updated in 1989. Many of these updated regulations were adopted into the CIDECT design recommendations and then into Eurocode 3 Annex K with little or no change. (CIDECT = Comité International pour le Développement et l' Etude de la Construction Tubulaire)

Much of the work on which the IIW recommendations are based was initiated by CIDECT and financed by the European Coal and Steel Community (ECSC), CIDECT and their associated governments. The recommendations cover the design and calculation of predominately statically loaded, planar, unstiffened lattice girder joints, which may be fabricated from circular, square, rectangular hollow sections or any combination of these on to open section chords. It is laid out in an original manner with the recommendations on one page and the explanatory notes on the opposite page. This allows the authors to give further information on a clause, explain more clearly or reference other documents on which the clause was based.

Some of the design formulae have been adapted from the monographs published by CIDECT (1986) and made simpler for the designer to use. The design information is presented in tabular form giving the nature of the joint as a diagram, with the design formula and the range of parameters applicable to the design information given in adjacent columns. (This format has been copied in the CIDECT and Eurocode 3 Annex K design codes.)

2.1.4 CIDECT design guides

CIDECT was formed 1962 and is funded by the manufacturers of hollow sections from all around the world. The aim of CIDECT is to combine all the research, application of technical data, development of simple design and calculation methods on a world-wide basis and to disseminate the information by various publications. Since its formation 35 years ago CIDECT has initiated, sponsored and co-ordinated 160 projects

researching all aspects of tubular design (Dutta 1996). Originally this information was published as series of monographs covering various design aspects for structural hollow sections. It has subsequently published 5 design guides, such as the “Design guide for circular hollow sections (CHS) joints under predominately static loading” (Wardenier et al 1991) and the “Design guide for rectangular hollow sections (RHS) joints under predominantly static loading” (Packer et al 1992).

The CIDECT Monograph No. 6 “The strength and behaviour of statically loaded welded connections in structural hollow sections” (CIDECT 1986) summarises all the research up to the late 70’s giving details of modes of failure, strength formula and the range of parameters for which it is valid. Although this information can be of use to the designer it is not principally a design code and the information is not laid out in a user friendly manner.

The design guides published by CIDECT are much more comprehensive than the design recommendations published by the IIW (1989) and are intended to lead the designer through all aspects of tubular design in simple stages, instead of concentrating solely on the strength of the connections. There are also areas covered in the CIDECT design guides, which are not given in the IIW design guide, (but have been considered by the IIW sub-commission XV-E). These include for example multi-planar joints, joints loaded with moments, bolted connections, flattened and cropped end bracing joints and the effect of filling the hollow sections with concrete.

The origins of these design codes in the CIDECT monographs can be seen in that there are numerous references to the research on which the design guidance is based in the text. However, there is far less detail of the research and generally the design codes are much easier to understand than the monographs. The design information and the manner in which it is presented is taken from the IIW design recommendations (IIW 1989) with many of the diagrams and joint capacity formulae copied directly.

2.1.5 Eurocodes

The structural Eurocodes were initiated by the Commission of European Communities to provide a common structural design standard that is accepted in all the EU countries with the purpose of eliminating barriers to trade. Issued by the European Standards Organisation CEN, the standards are actually published by the relevant national standards office, which in the UK is the British Standards Institution. The

Eurocode for the design of steel structures is Eurocode 3 (1992), of which Annex K is concerned with the design of hollow section joints.

The level of different symbols and subscripts used in the Eurocodes is far more complex and comprehensive than that used previously in design codes, for example CIDECT design guides or BS5950. The aim of this is to explain what the designer is doing in the calculation without the need for text, so making the code and subsequent designs multinational, i.e. language is not a barrier to understanding the design method.

2.1.5.1 Eurocode 3 Annex K (1994)

All the information in the Annex K of the Eurocode 3 is the same or very nearly the same as the CIDECT design guides and is presented in the same manner. (It is claimed that most of the design codes and recommendations regarding the use of steel hollow sections have a common basis in the research carried out for CIDECT (Dutta 1996)). However, Annex K only contains the information on the strength of hollow section joints and omits a lot of the more general information on the design of steel structures (trusses etc.) which the designer may find useful. There are no references to any of the research on which the design formulae are based and several smaller topics of less general interest are omitted. (Interestingly the work on bird beak joints and the joint strength equations published in Ono et al (1991), is mentioned in the CIDECT design guide (Packer et al 1992) but is not included in Annex K.) This is a reflection of the manner in which they are funded and the purpose they are intended to fulfil. (The CIDECT guide is funded by the steel producers and is published so that designers can easily and confidently design steel structures using hollow sections, providing where possible imaginative solutions to gain maximum strength advantage of the hollow sections. On the other hand Annex K is published through the British Standards Institution and only provides the basic standardised design information that is needed.)

2.2 A brief history of the development of finite element analysis (FEA)

Although the label “Finite element method” first appeared in a paper by Clough (1960) on plane elasticity problems, the idea of finite elements dates back much further. It was recorded that ancient mathematicians calculated the value of π to an accuracy of

forty significant digits by representing a circle as a polygon with a finite large number of sides.

The Finite Element Method (FEM) has three origins depending on whether you ask a mathematician, physicist or an engineer. However, concentrating on the engineering aspects of finite element analysis, Hrenikoff, McHenry and Newmark (see Clough 1960) all published papers in the 1940's on numerical analysis of engineering problems using a lattice structure. In 1954 Argyris published a series of papers covering linear structural analysis using energy theorems which are well suited to automatic digital computations. The actual solution of plane stress problems using triangular elements with properties determined by the elasticity theory was given by Turner et al (1956), a method that is now known as the direct stiffness method. After further treatment of the plane elasticity problem by Clough (1960) engineers began to see the potential of the finite element method. Zienkiewicz and Chueng (1965) gave finite element analysis a much broader interpretation when they reported that this method could be used in a large number of areas that could be mathematically modelled by basic equations.

Turner et al (1960) were responsible for the incremental step procedure, which developed the way for non-linear analysis. Non-linearity occurs in the analysis when response to an action is non-linear. Take for example Hooke's Law

$$\sigma = E \epsilon \qquad \text{Eqn 2.7}$$

where

σ is the stress

ϵ is the strain

E is a constant, called Young's Modulus

In the elastic range Eqn 2.7 is valid and the response to an increase in stress is a proportional increase in the strain i.e. linear relationship. However, in the plastic range when the yield stress of the material is reached, then Eqn 2.7 is no longer valid as there will be relatively large and variable increases in strain for small increases in stress and the response may be considered non-linear. The incremental step procedure allows the final solution to be divided into a series of analyses where the response over a small range may be considered as linear.

Non-linearity may occur in three different ways in finite element analysis:

- material non-linearity is used to describe the change in the behaviour of material after the yield stress has been exceeded
- geometric non-linearity is used in problems where there are large deformations that change the shape of the model and so affect basic equilibrium and the future behaviour of the model
- boundary non-linearity where the boundary conditions change during the course of the analysis

Since then there have been many advances in the algorithms used so that the solution to each increment may be achieved more efficiently. For a long time non-linearity remained the domain of those who could afford the computers to run these complex programs. In the 70's perhaps only 1% of the finite element analyses modelled non-linearity, rising to 5-10% in the early 80's (NAFEMS 1986). However, with rapid developments in computers in recent years the software designers have released finite element packages which can model non-linearity and can be run on a personal computer (PC), opening the way for all potential users of FEM to use non-linear methods. ABAQUS for instance, released a program in 1995 which will run on a high powered PC.

Offshore tubular joints were analysed in the early days using elastic behaviour for the assessment of the fatigue life of such joints - which is very important in offshore structures that are subjected to very high cyclic loads. Such analyses could also be used to provide lower bound estimates of strength. As computer storage and speed increased, it was possible to refine element meshes to obtain stress concentration factor (SCF) estimates for ever more complicated joints for specific designs or to provide general guidelines through parametric studies.

2.3 The use of a square hollow sections in a diamond configuration

The use of a square hollow section in a diamond shaped configuration has been suggested before as part of a triangular truss arrangement, shown in Figure 2.1. Bauer (1988) reports on the testing of sixteen double T joints (DT) and seven double K joints (DK) shown in Figure 2.2. The ultimate strength observed for these joints is then compared to that calculated by a yield line model with very favourable results in that the joint capacity was predicted with reasonable accuracy.

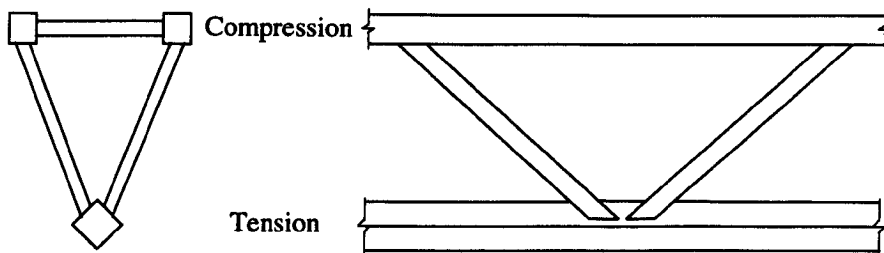


Figure 2.1 RHS Triangular truss arrangement

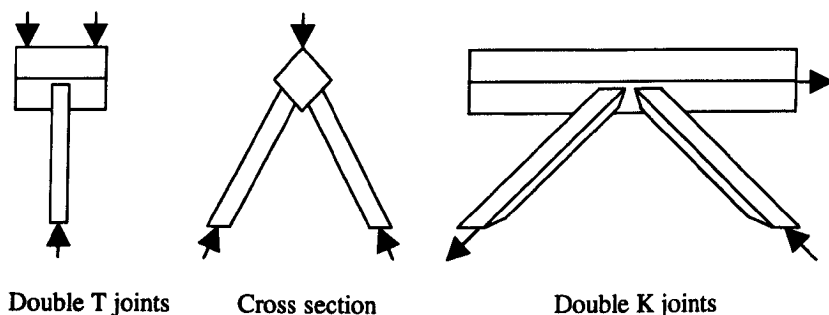


Figure 2.2 The double T and K joints tested by Bauer & Redwood (1988)

In the triangular truss arrangement the two compression chords are in the traditional RHS configuration (i.e. square), whilst the tension chord is in the diamond configuration, shown in Figure 2.1. The higher capacity of a tension member has enabled only one (tension) chord member to be used, resulting in the triangular nature of the truss. Orienting the tensile chord in the diamond configuration enables larger bracing members to be used when compared to the case where two bracing members meet on the single face of the chord in the square configuration, shown in Figure 2.3.

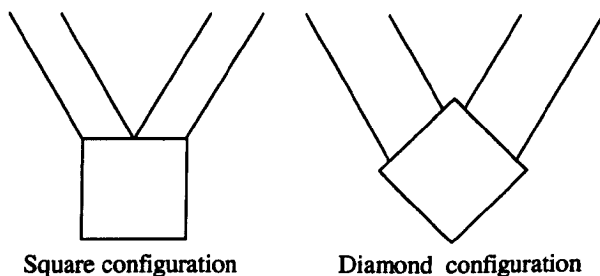


Figure 2.3 The difference between the square and diamond configurations

The advantages of using the diamond orientation of the tensile chord are:

- cheaper fabrication, in that less steel is used

- a lighter and more efficient structure
- larger brace members can be used, enabling stronger joints to be formed

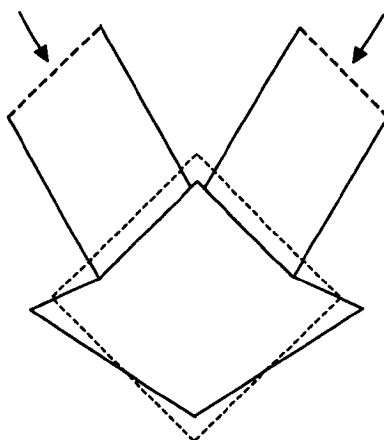


Figure 2.4 Deformation of the chord observed by Bauer and Redwood (1988)

The use of the square RHS in a diamond configuration in this truss arrangement is different to that proposed in the bird beak joint, in that the joint is formed on the faces of the chord member instead of on the corners, although there are similarities. The cross sectional deformation of the chord member given by Bauer & Redwood (1988) and shown in Figure 2.4, is very similar to the type of deformation seen in all the chords of the bird beak joints. The chord can be seen to increase in width and decrease in depth, referred to as lozengeing in this work. The decrease in the moment capacity of the deformed (tension) chord is not mentioned in Bauer and Redwood (1988), although this will not significantly affect the capacity of the truss arrangement.

2.3.1 The bird beak joints

T Ono, M Iwata and K Ishida (1991) first proposed the bird beak joint configuration (although they refer to it as the Y-shaped joint) to improve the efficiency of joints in trusses using square hollow sections. They considered the advantages of the new configuration are:

- as the sides of the chord form an angle of 45° with the brace axis, the joint has a high stiffness and smoothly carries the axial force of the brace into the chord
- the brace serves as a stiffener plate for the chord and restrains any local deformation of the chord in the immediate vicinity of the joint
- the weld length of the joint is longer than that of a conventional joint

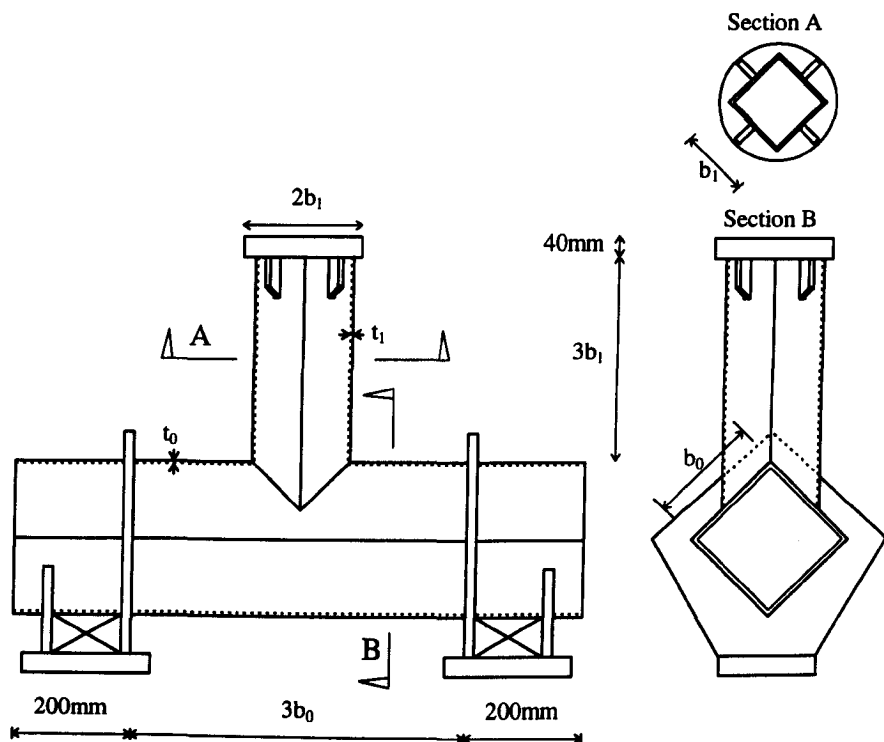


Figure 2.5 The arrangement shown by Ono et al (1991) for testing the bird beak T joint

Ono et al (1991) describe the experimental testing of twenty five T joints where the parameters of chord wall slenderness b_0/t_0 and the chord width ratio β are varied. In all cases the angle of intersection between the centre lines of the brace and the chord was 90° and the chord length ratio was maintained at $\alpha = 2L_0/b_0 = 6$. The general arrangement of the joint as tested is shown in Figure 2.5. Regrettably no further detail is provided of the support arrangement, as this would have been useful in assessing the accuracy of these experimental results in the light of some of the analytical work carried out in this thesis. However, it is thought that this arrangement would provide a condition similar to holding the ends of the chord encasté.

The ultimate strength of the joint was judged to be governed by a local failure of the chord in the vicinity of the brace member in all cases. A considerable strain concentration was noted in the brace member at the crown of the joint where the brace member sits on the corner of the chord, indicating that the major load path between the brace and the chord members is at the intersection of the corners of the sections.

In four of the joints tested, the chord is pre-loaded with a compressive axial force of either 30 or 60% of the squash load of the chord. When a squash load of 30% was applied to the chord no significant difference was found in the strength or the

stiffness of the joint. However, when a squash load of 60% was applied to the chord there was a small decrease in the stiffness and the joint capacity decreased to 70% of that expected for the joint.

Ono et al (1991) concluded that the ultimate strength of the diamond bird beak T joint could be given by

$$F_{u,1} = t_0^2 f_y \left(\frac{1}{0.211 - 0.147\beta} + \frac{1}{1.794 - 0.942\beta} \frac{b_0}{t_0} \right) \quad \text{Eqn 2.8}$$

based on the experimental tests they carried out and this equation is given in the CIDECT design for RHS sections under a static loading (Packer et al 1992) for the strength of bird beak T joints.

The bird beak joint capacities given by this equation are compared to similar T joints in RHS and CHS (where the cross sectional area and second moment of area were kept constant) and found to be very much stronger than these joints.

In addition to the T joints tested, the results of sixteen gap K joints are reported. The angle of the brace members was 45° in all the K joints tested, where the parameters of chord wall slenderness b_0/t_0 , chord width ratio β (of both the tension and compression brace members), the eccentricity and the gap between the brace members was varied.

Although it is stated that no moment is applied to the joint during the loading procedure, the method of testing the K joints described in Ono et al (1991) and shown schematically in Figure 2.6, will load the joint with a moment as soon as any displacement of the compression brace occurs. This is actually a common problem where K joints are loaded by only one actuator applying a compressive load to the brace member, the tensile load being applied by restraining the end of the tensile brace from moving and anchoring only one end of the chord. The length of the members is not given so it has not been possible to calculate the magnitude of the moment caused by the method of loading. No attempt is made by Ono et al to try to establish the secondary moments operating in the joint as it is loaded or the effect that these secondary moments would have on the collapse load or mechanism.

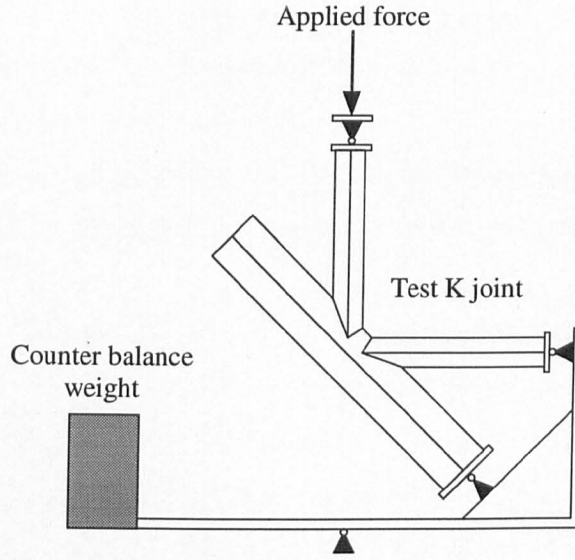


Figure 2.6 Schematic diagram of the test rig used by Ono et al (1991) for the testing of bird beak K joints

The deformation of the K joint as it is loaded is mainly confined to the chord face in the gap between the brace members with little deformation observed in the rest of the cross section. It was concluded that the force was transmitted between the brace members by the chord face between the brace members and this was used to determine a model on which the ultimate strength could be determined. An effective area of the cross section of the chord is determined and the joint is assumed to fail when the combination of normal stress and shear transmitted by the compression brace causes yielding across this effective area. The ultimate joint strength for a gap bird beak K joint is determined by

$$F_{u,1} = \frac{t_0^2 f_{y,0}}{\sqrt{1 + \sin^2 \theta_1}} 4\alpha^* \left(\frac{b_0}{t_0} \right) \quad \text{Eqn 2.9}$$

where

α^* is the coefficient of the effective area of the chord and can be determined from the relevant diagram. This formula is given in the CIDECT design guide for RHS (Packer et al 1992) with the relevant diagrams to determine α^* .

No reference is made to the tension brace in this formula and whilst failure is likely to occur in the compression brace when the members are the same size, the joint capacity could be influenced by the presence of a smaller tension brace. The effect of

this was not investigated in the sixteen joints tested in the experimental program, where the tension and compression braces were the same size in thirteen of the joints and the tension brace was larger in the remaining three.

When similar RHS, CHS and bird beak K joints were compared, in a comparison similar to that made for the bird beak T joints, the bird beak K joints were found to be much stronger.

The failure of the bird beak T joints subject to in-plane and out-of-plane bending is reported in Ono (1993 and 1994 respectively), based on a further series of experimental tests. These forms of loading are not covered in this thesis and will only be discussed briefly. Failure was attributed to 2 different modes of collapse, failure of the brace by bending (mode B) and cracking of the chord on the tension side of the brace and at the same time failure of the chord wall on the compression side of the brace (mode C).

For in-plane bending the moment capacity of the joint when the failure was in the brace (i.e. mode B) is given as

$$M_{u,1} = 1.41 b_1^2 t_1 f_{y,1} \quad \text{Eqn 2.10}$$

This is not the true moment capacity of the brace, but for all practical purposes this equation will suffice.

For in-plane bending the moment capacity of the joint when the failure was in the chord (i.e. mode C) is given as

$$M_{u,1} = 0.816 b_0 b_1 t_0 f_{y,0} \frac{\sqrt{0.5(3-1.41\beta)^2 + 3}}{2(1.794-0.942\beta)} \quad \text{Eqn 2.11}$$

and that the moment capacity of any joint subjected to in-plane bending is the smallest moment capacity predicted by Eqns 2.10 and 2.11. A comparison is made between the moment capacities of similar RHS and CHS to the bird beak T joints. The bird beak T joints were found to have a higher moment capacity in nearly every case.

For out-of-plane bending in all the bird beak T joints with the exception of one, failure was caused by cracking of the chord on the tension side of the brace and local deformation of the chord on the compression side of the brace (mode C). The mean ultimate joint capacity is given as

$$M_{u,1} = b_1 t_0 f_y \left(1.414 - \left[\left(0.0189 \frac{b_0}{t_0} - 0.802 \right) \beta - 0.0102 \frac{b_0}{t_0} + 1.421 \right]^2 \right) \quad \text{Eqn 2.12}$$

For the one joint when the brace failed, the bending moment in the brace was 96% of the bending moment capacity and Eqn 2.10 can be used to estimate the joint capacity.

In a comparison with traditional RHS and CHS T joints, the bird beak T joint was found to be stronger when loaded with out-of-plane moment on the brace in all cases where $\beta < 1.0$. In the case where $\beta = 1.0$, the bird beak joint is weaker than similar T joints with RHS and CHS sections.

The fatigue properties of the bird beak T joints and further details on the models used to determine the ultimate strength of T and K bird beak joints are reported in Ishida (1993). In the model for the bird beak T joint, failure is assumed to occur as the result of yield lines forming in the vicinity of area 1, shown in Figure 2.7 and the combination of the normal stress σ_n and shear stress τ in area 2 reaching the yield stress f_y , based on the deformation and the strains observed in the experimental tests.

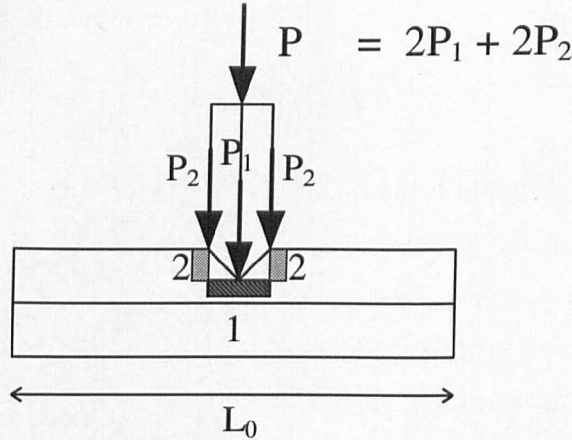


Figure 2.7 Ishida et al's model for the collapse of the diamond bird beak T joint.

The reasoning for the validation of this model appears to be incomplete. Five equations are given, with little explanation.

$$\tau = \frac{P/2 - P_1}{A_{\text{eff}}} \left(= \frac{P_2}{A_{\text{eff}}} \right) \quad \text{Eqn 2.13}$$

$$\sigma_n = \frac{\sqrt{2} PL_0}{4A_{\text{eff}} b_0} \quad \text{Eqn 2.14}$$

$$f_y^2 = \sigma_n^2 + 3\tau^2 \quad \text{Eqn 2.15}$$

$$P_1 = f_1(\beta) t_0^2 f_y \quad \text{Eqn 2.16}$$

$$A_v = f_2(\beta) 4b_0 t_0 \quad \text{Eqn 2.17}$$

where

P is the load applied to the brace

P₁ is that part of the load supported by the yield line in area 1

P₂ is that part of the load supported by the shear in area 2

A_v is the effective cross sectional area of the chord affected by the shear

Quoting directly from Ishida et al (1993) "Using equations 2.13, 2.14, 2.15, 2.16 and 2.17 [the] ultimate strength P is obtained by the following equation" (Note authors numbering but otherwise the same equations.)

$$\frac{P}{t_0^2 f_y} = f_a(\beta) + f_b(\beta) \frac{b_0}{t_0} \quad \text{Eqn 2.18}$$

How this can be achieved is not explained. The functions of β in Eqns 2.16 and 2.17 are not the same functions used in Eqn 2.18. In fact the values of $f_a(\beta)$ and $f_b(\beta)$ are determined by the variation of the slope and the intercept (with the chord width ratio β) of the plotted joint capacities $P/t_0^2 f_y$ (y axis) against the chord wall slenderness b_0/t_0 (x axis), assuming that the plotted joint capacities form a straight line and Eqn 2.18 only represents the equation of this straight line

$$y = c + mx \quad \text{Eqn 2.19}$$

The solution of this equation is shown in Eqn 2.8.

In view of this Eqn 2.8 should not be considered as being based on a model but merely an empirical equation based on the results obtained from the experimental tests.

When considering a model for the K joint Ishida et al (1993) admit that it is a similar model to that used in the analysis of the bird beak T joint. The ultimate strength formula that is derived from this model is

$$\frac{P_k}{t_0^2 f_y} = \frac{3C_2 \sin \theta}{((1+C_1)\cos\theta - \beta_c)^2 + 3\sin^2 \theta} + \frac{4C_1}{\sqrt{((1+C_1)\cos\theta - \beta_c)^2 + 3\sin^2 \theta}} \frac{b_0}{t_0}$$

Eqn 2.20

where

$$C_1 = \frac{\sqrt{0.5(3 - \sqrt{2}\beta_c)^2 + 3}}{8(1.794 - 0.942\beta_c)} \quad \text{and} \quad C_2 = \frac{0.5(3 - \sqrt{2}\beta_c)^2 + 3}{3(0.211 - 0.147\beta_c)}$$

β_c = chord width ratio of the compression brace

However, when the influence of the gap between the brace members is considered, the ultimate strength formula is given as

$$\frac{P_k}{t_0^2 f_y} = f \cdot f_\theta \cdot f_g \quad \text{Eqn 2.21}$$

where

$$f = \frac{1.33}{1.23 - \beta_c} + 10.8 + \left(\frac{0.374}{2.11 - \beta_c} + 0.266 \right) \frac{b_0}{t_0}$$

$$f_\theta = \left(\frac{1 + 0.561 \cos \theta - 0.354 \cos^2 \theta}{\sin \theta} - 1 \right) (0.95\beta_c + 0.05) + 1$$

and

$$f_g = 0.853 + \frac{0.201}{1 + e^{\left(0.5 \left[\frac{g}{t_0} \right] - 1 \right)}} \quad \text{where } g \text{ is the gap between the braces}$$

Eqns 2.20 and 2.21 are very different from Eqn 2.9 published in Ono (1991) and in the CIDECT RHS design guide (Packer et al 1992) for the strength of bird beak K joints. (Both equations are based on the same experimental results.)

An approach similar to that described for the T joint model is used for the validation of the K joint model; however, even less information is given. However, as Eqn 2.20 has the same format as Eqns 2.8, 2.18 and 2.19 it is concluded that a similar process has been performed on the results and that Eqn 2.20 should be counted as an empirical equation, at least until more details of how the model is validated are published. A letter has been written to Messrs T. Ono, K. Ishida and M. Iwata

requesting further information on this and a variety of topics but no replies have been received.

2.4 van der Vegte's work

Gerhardus Jacob van der Vegte was a research student at Delft University, in the Netherlands, completing his thesis in Jan 1995 (van der Vegte 1995). Whilst all his work has been on uni-planar and multi-planar CHS joints, there have been areas of similarities with this work, notably the effect of chord length on the resistance of the joint and development of interaction diagrams for the design of T joints.

Van der Vegte used the finite element program MARC to analyse all the joints he studied, with the necessary experimental work to validate the finite element results. Butt welds were modelled in all the CHS joints studied, with the exception of those where the chord width ratio $\beta=1$, with shell elements being used to model the small amount of reinforcement present in a butt weld.

2.4.1 X-joints in CHS

Van der Vegte notes, with some truth, that in the last thirty years many CHS X joints have been tested and that there are many different semi-empirical approaches which have led to different design formulae. In order to investigate the effects of the chord width ratio β and the chord wall slenderness d_0/t_0 , twenty two CHS X joints with an axial load applied to the brace (where $\theta=90^\circ$) were analysed by finite element analysis. A ring model, based on Togo's ring model for CHS, was developed and using regression analysis the results of the finite element analysis were fitted to the model with suitable regression constants.

Using this method van der Vegte gives the mean ultimate strength of a CHS X joint as being

$$\frac{F_{l,u}}{f_{y,0}t_0^2} = \frac{8.7 \left(\frac{d_0}{t_0} \right)^{0.5\beta - 0.5\beta^2}}{(1 - 0.9\beta) + \sqrt{(1 - 0.9\beta)^2 + (2 - (0.9\beta)^2) \left(\frac{t_0}{d_0} \right)^2}} \quad \text{Eqn 2.22}$$

which is a good deal more complex than the present design formula given in the CIDECT CHS design guide (Wardenier et al 1991) for the same joint

$$\frac{F_{l,u}}{f_{y,0} t_0^2} = \frac{5.2}{1-0.81\beta} \quad \text{Eqn 2.23}$$

Eqn 2.22 is not tested beyond comparing it with the results observed by his own finite element analyses.

The majority of the load/deflection curves published for these CHS X joints all demonstrated a maximum joint capacity, a point which is taken up further when CHS X cross joints are analysed for comparative purposes in this thesis.

2.4.2 The effects of chord length on CHS X joints

In order to investigate the effects of chord length on the strength of CHS X joints with an axial load applied to the brace, sixteen joints were analysed by finite element methods. (Chord width ratio $\beta = 0.25, 0.48, 0.73$ and 1.0 and chord length ratio $\alpha = 3, 6, 11$ and 18 .) Had van der Vegte analysed a wider variety of chord lengths and boundary conditions at the end of the chord he would have developed a greater understanding of the variation of the joint capacity with chord length.

The CHS X joint capacity was found to increase with chord length significantly when compared to the shorter chord lengths joints and this variation is given by:

$$F_{u,1(\alpha)} = \frac{12.5}{11.5(1+\alpha)} F_{u,1(\alpha=11.5)} \quad \text{Eqn 2.24}$$

where

α is the chord length ratio ($=2L_0/d_0$)

$F_{u,1(\alpha)}$ is the joint capacity at a specific value for α

$F_{u,1(\alpha=11.5)}$ is the joint capacity of a similar joint where $\alpha = 11.5$ and is given by

$$F_{u,1(\alpha=11.5)} = \frac{f_{y,0} t_0^2 8.7 (d_0/2t_0)^{0.5\beta-0.5\beta^2}}{(1-0.9\beta) + \sqrt{(1-0.9\beta)^2 + \frac{2-(0.9\beta)^2}{d_0/2t_0}}} \quad \text{Eqn 2.25}$$

No limiting value of the chord length ratio was identified beyond which the joint capacity did not increase in value, although van der Vegte does note that after $\alpha = 11.5$ the increase in the joint capacity is small.

2.4.3 T-joints in CHS

In his introduction to uni-planar T joints van der Vegte (1994a & 1995) notes that different forms of failure can be observed in the T joint as the chord length is varied. The failure may be due to the plastification of the chord face for short chord length joints and an overall chord bending failure for long chord length joints, or a combination of the two. This variation in joint capacity with chord length is different to that noted in the previous section, as there is no chord bending in the X joints.

In order to establish what the effects of chord bending were seventeen CHS T joints were analysed by van der Vegte with an axial load applied to the brace without the effect of chord bending to establish the local joint strength $F_{u,1,loc}$. The effects of chord bending are eliminated by applying a moment to the ends of the chord such that the chord bending moment under the brace is zero. During the course of the investigation the parameters of chord width ratio β and the chord wall slenderness d_0/t_0 were varied and in one joint the chord length was changed to establish that the local joint capacity $F_{u,1,loc}$ was independent of the chord length.

Again using the ring model (based on Togo's ring model) an equation for the ultimate strength of CHS T joints was developed. Using regression analysis the results of the finite element analyses were fitted to the model with suitable regression constants so that the local joint capacity of CHS T joints where the effects of chord bending have been eliminated is

$$\frac{F_{u,1,loc}}{f_{y,0}t_0^2} = \frac{2.3\left(\frac{d_0}{t_0}\right)^{0.66\beta-0.3\beta^2} + (1+C_1)}{\left(1-\frac{0.8\psi_2}{\pi}\right)\sin(0.8\psi_2)(1+C_1) - \left(1-\frac{\arcsin 0.8\beta}{\pi}\right)0.8\beta(1+\cos 0.8\psi_2) + \frac{0.7t_0^2}{d_0^2}}$$

Eqn 2.26

where

$$C_1 = \sqrt{1-(0.8\beta)^2} \quad \text{and} \quad \psi_2 = 1.2 + 0.8\beta^2 \text{ rad}$$

In order to provide a comparison to the previous results twenty nine CHS T joints (van der Vegte 1995) were analysed with the effects of chord bending, where the parameters of the chord length ratio α , the chord width ratio β and the chord wall

slenderness d_0/t_0 were varied to find the effect of chord length on the joint capacity of the CHS T joints.

2.4.4 Interaction diagrams in CHS

Van der Vegte (1995) notes that the factor which governs the joint capacity of a T joint most is not included in the design calculation for the joint strength directly, namely that of chord length. The idea of using an interaction approach was first proposed by van der Vegte (1994b) where the relationship between the force on the brace and the moment acting in the chord are plotted to form an interaction curve. The magnitude of the moment acting in the chord is dictated by the force acting on the brace and the length of the chord, so that the length of the chord is now considered in the design process.

In order to normalise the interaction curve so that it can be used in all circumstances the values of the force and the moment are normalised against their respective capacities. The capacity of a joint to withstand the force applied to the brace is determined by analysing a similar joint (to that being designed) without the effects of chord bending, to obtain the local joint capacity $F_{u,1,loc}$ discussed in the previous section. The moment acting in the chord is normalised by the moment capacity of the chord reduced to allow for the effects of the shear acting in the chord, due to the action of the force on the brace. The moment capacity of the chord calculated in this manner reflects the true moment capacity in the presence of a force acting on the brace.

The interpretation of the results varies between van der Vegte (1994b) and (1995). In the earlier paper van der Vegte (1994b), the interaction curve produced for the CHS T joints was defined as

$$0.67 \left(1.0 + \frac{d_0}{100t_0} \right) \left(\frac{M_{u,0}}{M_{p,v,0}} \right) + \left(\frac{F_{u,1}}{F_{u,1,loc}} \right)^{3.7} = 1 \quad \text{Eqn 2. 27}$$

where as in the latter, van der Vegte (1995), the interaction curve produced for the CHS T joints is defined as

$$0.32 \left(\frac{M_{u,0}}{M_{p,v,0}} \right) + \left(\frac{F_{u,1}}{F_{u,1,loc}} \right) = 1 \quad \text{Eqn 2.28}$$

where by definition $\frac{M_{u,0}}{M_{p,v,0}} \leq 1$

Eqn 2.27 produces a series of curves, varying with chord wall slenderness and some of the values of the normalised moment exceed 1, whilst Eqn 2.28 produces two straight lines which are used to define the interaction between applied force and the moment acting in the chord. No reason is given for this. However, it is noted that Eqn 2.27 provides an accurate representation of the points plotted but is impossible to solve directly. (To solve for $F_{u,1}$, substitute $M_{u,0} = 0.25F_{u,1}L_0$). Eqn 2.28 provides a less accurate representation of the points plotted but provides a safe lower bound solution and can be simply solved by the designer.

2.4.5 Interaction diagrams in RHS

Yu (1995) uses the same approach as van der Vegte (1994b) to establish the strength of RHS T joints with varying chord lengths. Using finite element analysis Yu analysed thirty four RHS T joints with the effects of chord bending, varying the parameters of chord length L_0 , chord width ratio β and chord wall slenderness b_0/t_0 . The local joint strength for similar RHS T joints was determined by analysing ten RHS T joints without the effects of chord bending, varying the parameters of the chord width ratio β and chord wall slenderness b_0/t_0 . (In addition to these results there are three T joints analysed with only half the moment applied to ends of the chord, “to provide extra data points for the regression analysis”. No further reference is made to these joints and it is not known how these results were incorporated into the interaction diagram.)

The interaction diagram produced by Yu is very similar to that produced by van der Vegte (1994b) in that the results are represented by a series of curves. The major difference being that the curves produced by Yu are banded according to the chord width ratio β and accordingly the definition of the interaction curve for RHS T joints given by Yu is

$$\left(\frac{F_{u,1}}{F_{u,1,loc}} \right)^3 + \left(\frac{M_{u,0}}{M_{p,v,0}} \right)^{\frac{1}{1-\beta^2}} = 1 \quad \text{Eqn 2.29}$$

Eqn 2.29 suffers from the same problem as Eqn 2.27 in that it cannot be solved easily.

Recent work published by Yu (1996) has considered using interaction diagrams for traditional RHS X joints loaded by axial forces on the brace members and by

moments on the chord in the manner shown in Figure 2.8. This approach represents the design of a joint in a structure where the strength of the joint may be influenced by the bending moment acting on the chord from the rest of the structure. The adaptation of the interaction diagram applied in this way is a natural progression of the initial concept and will probably influence all future methods of design.

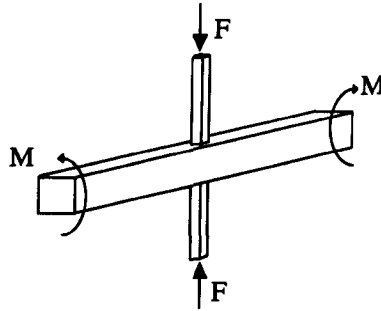


Figure 2.8 Traditional RHS X joint loaded with axial forces on the brace members and bending moments on the chord

The interaction diagram for the traditional RHS X joint loaded in this manner is very similar to the one produced for the traditional RHS T joints described previously. The points plotted by Yu on the interaction diagram clearly vary with the chord width β and the interaction curve can be defined in the same manner. Yu has combined the results for the T and X joints and concludes that both joints can be represented by an interaction curve defined by

$$\left(\frac{F_{u,l}}{F_{u,l,loc}} \right)^3 + \left(\frac{M_{u,0}}{M_{p,v,0}} \right)^{\frac{1}{1-0.85\beta^{1.6}}} = 1 \quad \text{Eqn 2.30}$$

2.5 Peter Crockett's research work

Peter Crockett was a research student at Nottingham University, who completed his Ph.D. thesis in July 1994 (Crockett 1994). Some of the work on K joints herein is a direct continuation of his work, whilst other parts make use of some of his findings.

2.5.1 Welds and Corner radii

Crockett compared the results between experimental tests and finite element modelling of the same joints with corner radii and different forms of weld to replicate the test results as closely as possible. The experimental test results used were 3D T-DT joints in RHS (T in-plane, DT out of plane) tested at the University of Nottingham as

part of a larger project for the European Coal and Steel Community (ECSC), Davies et al (1993).

2.5.1.1 Welds

The importance of modelling welds in RHS joints is widely recognised as the extra weld material increases the effective width ratio β , leading to an increased joint resistance. Crockett considered four different forms of modelling the weld using 4 node shell elements, shown in Figure 2.9, for comparison on a T joint which had been previously physically tested.

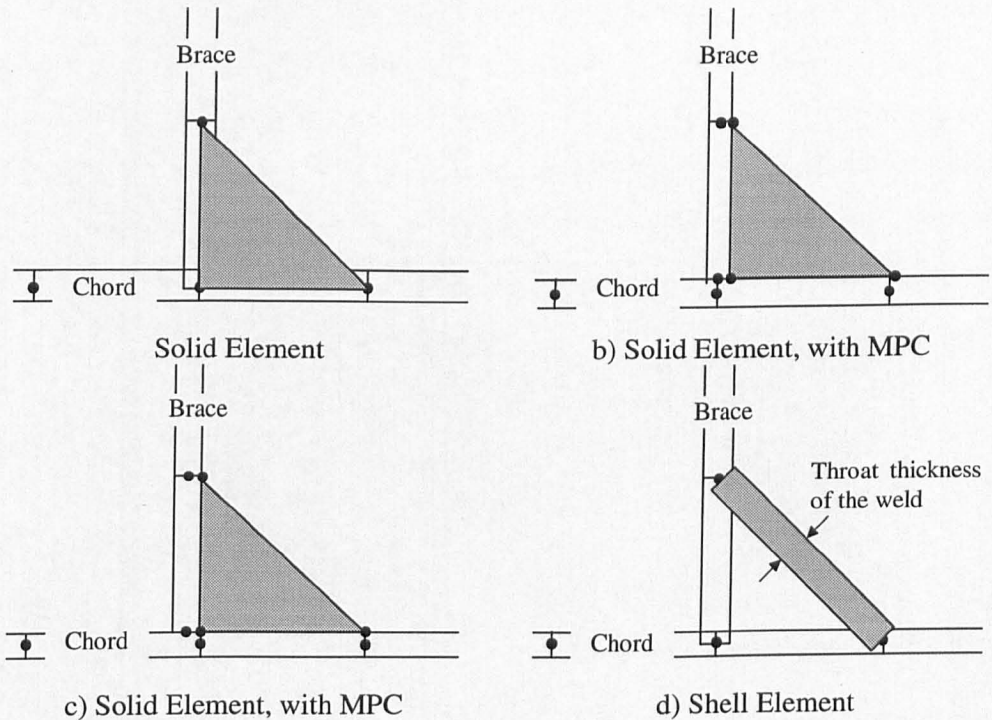


Figure 2.9 Four different forms of weld modelled with 4 node shells elements

Weld case a) 6 node solid element sharing the same nodes as the 4 node shell elements.

Weld case b) 6 node solid element, offset by a distance of $t_1/2$ from the brace and chord, which are 4 node shell elements. There is also a small gap between the brace and chord elements. The directional movements of the nodes on the welds are fixed to adjacent chord/brace nodes by multi-point constraints (MPC).

Weld case c) is the same as for weld case b). However, the node in the chord has been moved from being directly under the centreline of the brace to directly under the nodes of the weld.

Weld case d) models the weld by using a 4 node shell element of the same thickness as the throat of the weld.

Weld cases a) and b) provide a fair representation of the test data, although both finite element load/indentation curves underestimated the resistance of the joint in the elasto-plastic region of the curve. Weld case c) gave better representation of the elasto-plastic region but thereafter overestimate the plastic proportion of the curves by 10% (author's own estimate). Weld case d) overestimated the joint resistant by 25% and was rejected as not worth further study.

When 8 node shells became available this study was repeated to investigate any differences that these new elements may make. Instead of the T joint used previously a T-DT joint was used, MPJT3 where a tensile force is applied to the DT braces of the joint. Crockett reports that Delft University had experienced trouble in calibrating this joint with finite element methods and considered it important that different weld models were tried to improve the results. The four welds investigated are shown in Figure 2.10.

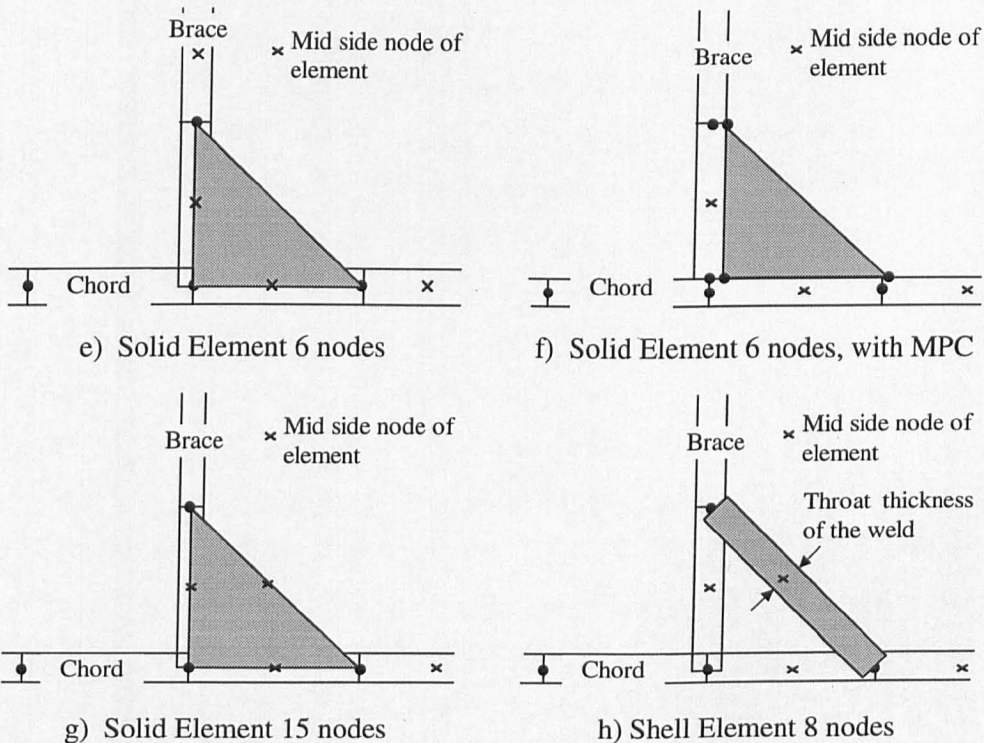


Figure 2.10 Four different forms of weld modelled with 8 node shells elements

Weld case e) 6 node solid element sharing the same corner nodes as the 8 node shell elements.

Weld case f) 6 node solid element, offset by a distance of $t_1/2$ from the brace and chord, which are 8 node shell elements. There is also a small gap between the brace and chord elements. The directional movements of the nodes on the welds are fixed to adjacent chord/brace nodes by multi-point constraints (MPC).

Weld case g) 15 node solid element sharing all the nodes with the adjacent 8 node shell elements representing the chord/brace.

Weld case h) models the weld by using a 8 node shell element of the same thickness as the throat of the weld.

All the load/indentation curves reproduced by finite element analysis in this study underestimated the load/indentation curves obtained from physical tests of the joint. The best comparison is achieved by using a solid 6 node element to model the weld and with an 8 node shell to model the rest of the joint i.e. weld case (f). The finite element load/indentation curves produced for this joint show that the joint strength is underestimated by 8%. In weld case (h) where a shell element is used to model the weld material, the joint strength is underestimated by 12% although in the previous case study this was shown to overestimate the strength of the joint considerably. Weld case g, using a 15 node solid element to model the weld causes the joint strength to be underestimated by 20%. This was attributed to the 15 node solid element being a lot more flexible than the 6 node solid element (or the shell elements) being used before.

This weld case (g) has been used in this thesis to represent all the welds, where the welds have been modelled, although a poor comparison is obtained in this series of analyses when compared to the experimentally tested joints. It is considered that the finite element model of joint MPJT3 as a whole underestimates the strength of the joint being tested and that a good agreement is only achieved with the different weld cases (f and h) is due to the stiffness of the method used to model the weld, contributing towards the strength and stiffness of the joint. This method was chosen because it would probably give a conservative result, the 15 node solid element is more flexible and it is compatible with the 8 node shell elements used to model the rest of the joint (i.e. they both use quadratic interpolation functions). The incompatibility problem of mixing solid and shell elements remains.

Three different ways of modelling the corner of the weld were studied by Crockett, shown below in Figure 2.11. Modelling the full corner shown in Figure 2.11c

consistently provided the best result in all the cases studied and this procedure is used in all the models in this work.

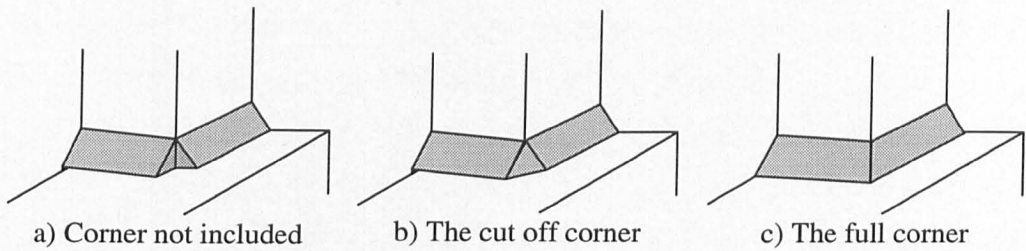


Figure 2.11 3 Methods of modelling the corner of the weld

Different material properties were used to represent the weld material, but increasing the strength by as much as 20% had very little effect on the overall joint resistance. BS 639 states that the ultimate strength expected for the E51 electrode used is significantly larger than the ultimate strength of the steel used in the joints, the yield strengths being approximately equal. However, lack of information about the measured properties of the weld material led Crockett to assume the weld material was the same as the steel and this would not significantly affect the results.

Crockett recognised all the models described have limitations due to the compromises and approximations made. It is possible that there are numerical incompatibility problems between the solid and shell elements used to model the weld that could lead to incorrect stress and strain levels in the vicinity of the weld. These incompatibility problems could be overcome if shell elements are used to represent the weld material. However, as this is the least representative of all the cases, because of the “air gap”. It is considered that the stress and strains then observed in this vicinity would also be inconsistent with the test results.

2.5.1.2 Corner radii

The main problem in modelling the corner radii is that if there is a large curvature across the element, the finite element package rejects the element as being badly deformed. This can be solved by reducing the width of the element however, this causes further problems by creating long thin elements (i.e. with a high aspect ratio) and an increase in the total number of elements. Increasing the number of elements again to decrease the aspect ratio of the curved elements is undesirable as the additional elements further increase the computing time required for the analysis.

A comparison of the results between finite element models with and without the corner radii modelled showed no significant difference up to an indentation of 3% b_0 . For indentations above this level, the corner radii model exhibits a slightly lower joint resistance than the model where no corner radii has been modelled.

Given the problems and the additional computing time required, Crockett concludes that increasing the mesh density in non critical regions in the outreaches of the chord is wasteful, time consuming and beyond a certain refinement does not improve the accuracy of the results any further.

2.5.2 Overlapped K joints in RHS with $\beta = 0.6$

Crockett (1994) in his thesis considers the effects of boundary conditions and the effects of the hidden weld on the strength of partially overlapped K joints. Only the work on joints where the chord width ratio $\beta = 0.6$ is considered, as this is the only chord width ratio examined in this work on K joints .

2.5.2.1 The effects of boundary conditions

Crockett investigates the effects of changing the support arrangement at the ends of the brace and the chord members. All his investigations include changing the sense of the loading, i.e. the through brace loaded in tension and compression in different analyses. He concludes that the boundary conditions do have a significant effect on the joint strength and in particular that:

- changing the restraint supporting the ends of the chord, i.e. fixed or pinned can have a significant effect on the joint strength when the angle between the chord and the brace members θ is small, but this effect decreases as angle θ increases
- when the ends of the brace member were unsupported, then excessively large rotations were observed between the members of the joint and that the joint strength was often severely reduced in these models. He concludes that this is an unreal situation as in a truss the brace members would not be capable of such large rotations
- the more realistic end condition for the braces is supporting the brace end by pinned rollers moving in a direction parallel to the centre line of the member. This boundary condition is used in all further research.

2.5.2.2 The effect of the hidden weld

In fabricating an overlapped K joint in a truss, it is standard practice to tack both the members into position before welding around the outside perimeter. Crockett considers the effects of welding the “through member” completely to the chord, before the overlapping member is placed into position for two different K-joints, where $\theta = 30^\circ$ and 60° . Three different methods of connection are considered, brace and chord nodes being common i.e. joined, brace and chord nodes being separate i.e. no connection between brace and chord members and finally brace and chord nodes being separate with a solid element to represent the weld joining the brace and chord.

When $\theta = 60^\circ$ and the through brace is loaded in tension, there is a significant increase in the joint capacity with the hidden weld included. This is attributed to the fact that when the hidden weld is not included, there is no load transfer to the chord from that face of the brace member and this lack of restraint causes large joint deformations. When the through brace is loaded in compression there is no significant change in the joint capacity.

When $\theta = 30^\circ$ there is very little change in the joint capacity when the through brace was loaded in tension or compression, with or without the hidden weld included. This was shown to be due to the fact that the joint failure occurred elsewhere because the top face of the chord failed under the combined action of the axial load and the bending moment caused by the eccentricity of the joint.

There was no significant difference in the results when the weld was modelled as a solid element or when the weld was represented by the brace and chord nodes being common.

Four different load and boundary conditions were analysed when $\theta = 30^\circ$ and 60° and the hidden weld was represented by the brace and the chord having common nodes. The results presented by Crockett raised the question of whether an angle function was required by CIDECT RHS design codes for K joints, but with the limited amount of information that was available he was not able to be conclusive. This question is taken up in Chapter 7 of this thesis for further study.

2.6 The definition of the ultimate joint capacity

The joint capacity is easy to define when a maximum value is obtained during testing or finite element analysis however, many of the joints examined do not reach a

maximum value. Therefore a method is required to define a load which can be considered as the joint capacity and produces compatible results with those joints where a maximum joint capacity is achieved.

The International Institute of Welding (IIW 1989) defines the working joint (or serviceability) capacity for axially loaded hollow section joints, (where the working joint capacity is taken as approximately $2/3^{\text{rds}}$ the ultimate joint capacity), as being “the deflection in the connection between one bracing and the chord which does not exceed $1\%b_0$ or d_0 ”.

Van der Vegte (1995) uses Yura’s (1980) deformation limits to define failure for both CHS axially loaded joints and joints loaded by bending. Where failure is defined as an indentation of $60f_y d_1/E$ for axially loaded joints and for joints loaded by bending a rotation of $80 f_y/E$. (f_y yield strength of material, d_1 diameter of brace member and E the value of Young’s Modulus)

Korol (1982) suggests, based on a study of RHS T joints, that failure can be defined as 25 times the elastic limit (i.e. $25\delta/\delta_y$ or ϕ/ϕ_y where δ_y and ϕ_y are the yield limit displacement and rotation values respectively) for RHS joints with either an axial load or a moment applied to the branch member.

Lu (1994) examined a wide range of different joint types and methods of loading, where CHS or RHS sections have been used as the chord member and concluded that the local indentation at failure varied between 2.5% and $4\%b_0$ when a maximum load was attained. Therefore she suggests that a local deformation limit of $3\% b_0$ at the intersection of the chord face should be considered to define the joint capacity where no maximum value is attained. This is a conservative estimate as Lu considers that the strength at the deformation limit of $3\%b_0$ gives about 10% lower values than the CIDECT design formula. Care was taken to ensure that so far as possible the ratio between $N_u/N_s < 1.5$, where N_u is the ultimate load (from the test data) and N_s is the serviceability load (from the design codes) was maintained by using this definition of failure. This could not be achieved for RHS joints of a low chord width ratio β and high chord wall slenderness b_0/t_0 values, in which case the strength at the serviceability deformation will be critical. This proposal was accepted by the IIW and incorporated into the design recommendations as IIW Doc. XV-E-94-215.

Lu's recommendations to define the joint capacity has been used in this work to define a joint capacity at failure where a maximum joint capacity is not attained. The precise method in which this is carried out for the different joints is shown later.

3.

Finite Element Modelling

3.1 Introduction

The use of finite element analysis in determining the static strength of structural hollow section joints is now well established and there are many packages available on the market today. No attempt is made in this work to examine the different finite element suites to decide which is the most accurate as the decision on which package to use was limited to those provided at the University of Nottingham.

The finite element package used in this research is ABAQUS. This is widely used in industry and research as a general-purpose finite element program for a wide range of applications and it is commonly used for non-linear work such as the static strength analysis of structural hollow section joints. It is held in high regard for the accuracy of its elements and the simple and efficient way it performs the analysis.

This chapter will examine some of the theory of the finite element method (mainly the basic principles) and how the analysis is performed. Some of the features available in ABAQUS and used in the modelling of the joints in this work will then be examined. Details will be given where these features are unique to the ABAQUS suite of programs, explaining what they do, why they are used and how they work. More general features common to most finite element programs will be discussed in less detail. Finally the general finite element model details will be explained with regard to the type of element used and the manner in which the welds are modelled.

3.2 Finite element programs and the hardware used

The majority of the finite element analyses carried out in this research have been performed on a Dec Alpha cluster of workstations, effectively providing 3 computer processors to do the calculations. The computer facilities provided by the regional computing centre at Manchester and used extensively by Crockett (1994) were investigated, but did not provide the level of post processing facilities needed.

The ABAQUS suite of programs used in this work is updated on a yearly basis by the software company Hibbet, Karlson and Sorenson (HKS) and the research

reported has been carried out on versions 5.2 to 5.5. Extensive use of the restart files available in the ABAQUS package has been made to store all the information generated in the analysis and to produce the graphics used later in this work. The very large files generated by this method have produced storage problems however, these have been overcome with memory upgrades and storing files on tape.

The ABAQUS package provides facilities to construct the mesh for joints of simple geometry, typically most RHS connections, by stipulating key nodes and using a node generation command to create the remainder of the nodes dictated by the mesh. Automatic mesh generation packages have to be used for joints where the geometry is more complex, such as for CHS connections, where the positioning of the nodes at the interconnection of the chord and brace members would require many tedious calculations. Where such joint complexity occurred the mesh generation program FEMVIEW (1989) produced by FEMVIEW Limited was used, so that the basic joint geometry is automatically meshed and translated into a format which can be used in the analysis by ABAQUS.

3.3 The finite element method

Many discrete problems in engineering, such as the structural members in a framework structure, can be solved by using a simplified analytical model. The behaviour of its members, which are readily definable, can be described by simple relationships defined in the model and the properties of the member. The response of the whole structure can then be calculated by considering the accumulated behaviour of all the individual members. The assumptions made in formulating the model may cause inaccuracies in the solution, but if the model has been formulated correctly then validity of the solution should not be affected, as the error should be small.

In the stiffness matrix method, which may be used to solve the example given above, a set of structural equilibrium equations are solved in terms of the unknown nodal deflections from which the internal member forces or stresses can be derived. For low axial forces, causing only elastic deformations, the relationships formed are more or less exact (small changes in the model's geometry will occur) and the only approximations lie in the numerical rounding off in the equation solving process.

For more complex engineering problems involving a continuous structure (the continuum) such as a shaped steel plate, the sub-division of the model is not as readily

definable as in the previous example. However, the same principle can be used by the discretization of the structure, that is dividing the structure into a finite number of different interconnecting parts or elements representing a small portion of the entire structure. The behaviour (i.e. the deformation) of each element or part can still be described mathematically using the stiffness method approach. Providing that conditions of continuity and equilibrium are satisfied, the sum deformation of all the parts or elements describes the behaviour of the whole system. Where the material properties are not linear-elastic, or large deflections effects need to be included then the correct solution will be achieved through an iteration process and the accuracy will depend on the convergence criteria stipulated.

As the size of each element decreases, a better prediction can be made of its deformation and this improves the performance of the whole model, leading to a more accurate solution. The disadvantage to this is that more computational time is required for the solution to be reached, which may be prohibitively expensive, in terms of computing time, when compared to the improvement in the accuracy achieved. Thus each model can only contain a finite number of elements (the exact number depending on the computing power available) for the solution to be achieved economically.

3.3.1 The finite element theory

The finite element method solves the analytical model by finding the displacements of the nodes used to define the elements within the model. To achieve this a series of equations are set up, one for each degree of freedom at every node. The external forces (F_e) acting on each node are known and the stiffness of each element (k_e) can be assessed. The displacement of the nodes (u) can then be found from

$$F_e = k_e u_e \quad \text{Eqn 3.1}$$

Having found the displacement of the nodes, the internal forces acting on the nodes can then be resolved and hence the strains, stresses and any other unknown by manipulation of the displacement data.

3.3.1.1 An example of the construction of the stiffness matrix

Considering a very simple case of a discrete 2 dimensional pin ended linear truss element to explain the finite element process, shown in Figure 3.1. Only one degree of freedom is permitted in this example, that of axial movement.

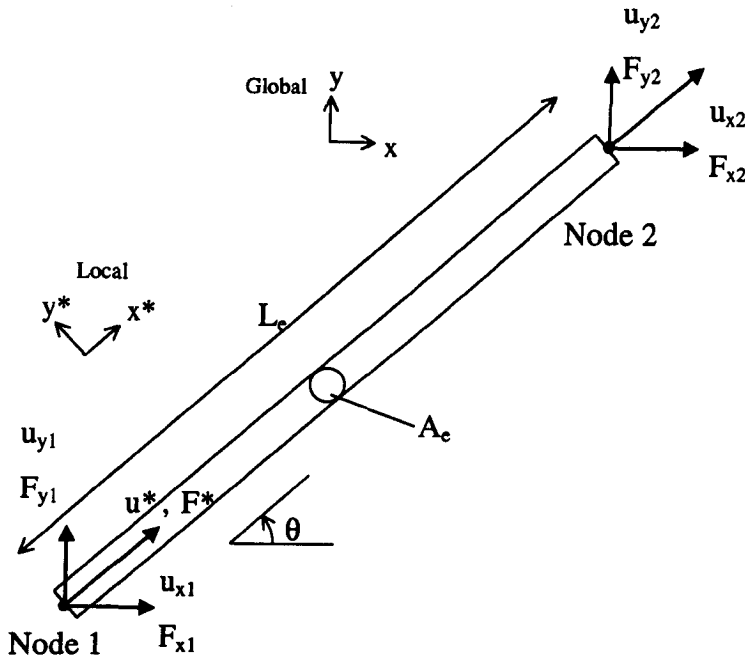


Figure 3.1 A 2-dimensional discrete pin ended element

Where

L_e = the length of the element

A_e = the cross sectional area of the element

x, y = Cartesian (global) co-ordinates

$x^* y^*$ = local directions between nodes 1 & 2

u_x, u_y = global displacements in the x and y directions

u^* = local displacement along the element (in the direction x^*)

F_x, F_y = Global forces in the x and y directions

F^* = Local force along the element (in the direction of x^*)

Expressing the displacement of the two nodes in matrix form where C_1 is the global movement of the element and $C_2 L_e$ is the movement of node 2 in relation to node 1, i.e. C_2 = the strain. Both are unknown constants called trail functions that must satisfy the boundary conditions, at Node 1 ($x=0$) $u=u_1$ and at Node 2 ($x=L_e$) $u=u_2$.

$$\begin{Bmatrix} u_1^* \\ u_2^* \end{Bmatrix} = \begin{bmatrix} 1 & 0 \\ 1 & L_e \end{bmatrix} \begin{Bmatrix} C_1 \\ C_2 \end{Bmatrix} = \mathbf{u}_e = \mathbf{A}\mathbf{C} \quad \text{Eqn 3.2}$$

where \mathbf{u}_e^* is the displacement vector and \mathbf{A} is the coordinate vecor
hence

$$\mathbf{C} = \mathbf{A}^{-1} \mathbf{u}_e^* \quad \text{Eqn 3.3}$$

Resolving the displacements along the direction of the element, the global displacements can be determined as

$$\mathbf{u}_e^* = \begin{Bmatrix} u_1^* \\ u_2^* \end{Bmatrix} = \begin{Bmatrix} u_{x1} \cos \theta + u_{y1} \sin \theta \\ u_{x2} \cos \theta + u_{y2} \sin \theta \end{Bmatrix} \quad \text{Eqn 3.4}$$

substituting this into Eqn 3.3 gives

$$\mathbf{C} = \begin{Bmatrix} C_1 \\ C_2 \end{Bmatrix} = \frac{1}{L_e} \begin{bmatrix} L_e \cos \theta & L_e \sin \theta & 0 & 0 \\ -\cos \theta & -\sin \theta & \cos \theta & \sin \theta \end{bmatrix} \begin{Bmatrix} u_{x1} \\ u_{y1} \\ u_{x2} \\ u_{y2} \end{Bmatrix} \quad \text{Eqn 3.5}$$

The strain along the length of the element C_2 can then be written as

$$C_2 = \epsilon = \frac{1}{L_e} [-\cos \theta \quad -\sin \theta \quad \cos \theta \quad \sin \theta] \begin{Bmatrix} u_{x1} \\ u_{y1} \\ u_{x2} \\ u_{y2} \end{Bmatrix} \quad \text{Eqn 3.6}$$

or in general

$$\epsilon = \mathbf{B} \mathbf{u}_e \quad \text{Eqn 3.7}$$

where $\mathbf{B} = \frac{1}{L_e} [-\cos \theta \quad -\sin \theta \quad \cos \theta \quad \sin \theta]$ is called the strain shape function.

Hooke's law for elastic behaviour can be written in matrix form as

$$\sigma = \mathbf{D} \epsilon \quad \text{Eqn 3.8}$$

where \mathbf{D} is the material properties matrix, in the case of a linear truss element where the force is uniaxial \mathbf{D} takes the value of Young's Modulus E . The stress can be expressed as a function of the displacements by substituting Eqn 3.7 into Eqn 3.8

$$\sigma = \mathbf{D} \mathbf{B} \mathbf{u}_e \quad \text{Eqn 3.9}$$

The "external" forces acting each node can be written in terms of the internal axial force F^*

$$\mathbf{F}_e = \begin{Bmatrix} F_{x1} \\ F_{y1} \\ F_{x2} \\ F_{y2} \end{Bmatrix} = \begin{Bmatrix} -F^* \cos \theta \\ -F^* \sin \theta \\ F^* \cos \theta \\ F^* \sin \theta \end{Bmatrix} \quad \text{Eqn 3.10}$$

which, using the strain shape function \mathbf{B} may be written as

$$\mathbf{F}_e = \mathbf{L}_e \mathbf{B}^T \mathbf{F}^* \quad \text{Eqn 3.11}$$

The element stress is found by dividing the uniaxial force F^* by the element area A_e

$$F^* = A_e \sigma \quad \text{Eqn 3.12}$$

The substituting Eqns 3.12 and 3.9 into Eqn 3.11

$$\mathbf{F}_e = A_e \mathbf{L}_e \mathbf{B}^T \mathbf{D} \mathbf{B} \mathbf{u}_e \quad \text{Eqn 3.13}$$

This however, is usually written in the form of

$$\mathbf{F}_e = \mathbf{k}_e \mathbf{u}_e \quad \text{Eqn 3.14}$$

where $[\mathbf{k}_e]$ is the element stiffness matrix and is equal to

$$\mathbf{k}_e = A_e \mathbf{L}_e \mathbf{B}^T \mathbf{D} \mathbf{B} \quad \text{Eqn 3.15}$$

This process is repeated for all the members in a structure adding each element stiffness matrix \mathbf{k}_e to the global stiffness matrix \mathbf{k} at the appropriate points until the whole structure is included in the model. The global form of Eqn 3.14 ($\mathbf{F} = \mathbf{k} \mathbf{u}$) with the appropriate boundary conditions can then be solved for the displacements at all the nodes from which the internal forces, the stress and strain in each element can be calculated.

3.3.1.2 The alternative energy formulation

Whilst finite element programs could use the equilibrium approach to formulate the stiffness matrix, it is more common to use the energy formulation to derive the stiffness matrix as it is more robust and applies equally to quadratic and cubic elements as well as three dimensional problems.

The total potential energy (TPE) of the element can be written as

$$\text{TPE} = \text{Internal work} - \text{External work}$$

$$\text{TPE} = \int_v \frac{1}{2} \boldsymbol{\sigma}^T \boldsymbol{\epsilon} \, dv - \mathbf{U}^T \mathbf{F}_e \quad \text{Eqn 3.16}$$

where v is the volume and hence $dv = A_e dx^*$. Substituting expressions for σ & ϵ given in Eqns 3.7 and 3.9 into Eqn 3.16 gives

$$\begin{aligned} \text{TPE} &= \int_{L_e} \frac{1}{2} (\mathbf{DB} \mathbf{u}_e)^T (\mathbf{B} \mathbf{u}_e) A_e dx - \mathbf{U}^T \mathbf{F}_e \\ \text{TPE} &= \int_{L_e} \frac{1}{2} A_e \mathbf{DB}^T \mathbf{u}_e^T \mathbf{B} \mathbf{u}_e dx - \mathbf{U}^T \mathbf{F}_e \end{aligned} \quad \text{Eqn 3.17}$$

Then using the principle of minimum total potential energy, the differential of the TPE with respect to the displacement \mathbf{u}_e must be equal to zero (or the lowest possible value)

$$\begin{aligned} \frac{\delta(\text{TPE})}{\delta[\mathbf{u}]} &= 0 = A_e L_e \mathbf{B}^T \mathbf{DB} \mathbf{u}_e - \mathbf{F}_e \\ &= \mathbf{k}_e \mathbf{u}_e - \mathbf{F}_e \end{aligned} \quad \text{Eqn 3.18}$$

Which is the same basic form as Eqn 3.14

3.3.1.3 Shape functions

A shape function is a polynomial expression that relates the displacements that occur at any point within the element to the displacements that occur at the nodes. The number of terms in the general shape function is dependent on the degrees of freedom (DOF) and the order of the element (linear, quadratic etc. depending on the number of nodes on the side of the element) with a term for each possible DOF and order. Each node of an element has a shape function.

In the previous example the shape functions were not considered explicitly as it is a trivial problem however, the general shape function of the linear 2-node beam element with one degree of freedom is

$$N_c(x^*) = a_1 + a_2 x^* \quad \text{Eqn 3.19}$$

where $N_c(x^*)$ is the shape function at node c and a_1 and a_2 are unknown coefficients for the shape function N_c

$$\begin{aligned} N_1(x^*) &= a_1 + a_2 x^* \\ N_2(x^*) &= a_3 + a_4 x^* \end{aligned} \quad \text{Eqn 3.20}$$

When at node 1, $x = 0$, $N_1(x^*) = 1$, $N_c(x^*) = 0$ for all other nodes (node 2 in this case)

and at node 2, $x = L_e$, $N_2(x^*) = 1$, $N_1(x^*) = 0$. Using these conditions the value of the 4 unknowns can be found as

$$a_1 = 1 \quad ; \quad a_2 = \frac{-1}{L_e} \quad ; \quad a_3 = 0 \quad ; \quad a_4 = \frac{1}{L_e}$$

Although expressed differently, this is the same result as Eqn 3.2 using the trial functions.

$$\begin{bmatrix} u_1 \\ u_2 \end{bmatrix} = \begin{bmatrix} 1 & 0 \\ 1 & L_e \end{bmatrix} \begin{bmatrix} C_1 \\ C_2 \end{bmatrix}$$

Solving for C gives

$$C_1 = u_1 \quad \text{and} \quad C_2 = \frac{u_2 - u_1}{L_e}$$

Substituting these values into the general displacement function

$$u^*(x^*) = C_1 + C_2 x^* \quad \text{Eqn 3.21}$$

and rearranging gives

$$u^*(x^*) = \left(1 - \frac{x}{L_e}\right) u_1 + \frac{x}{L_e} u_2 \quad \text{Eqn 3.22}$$

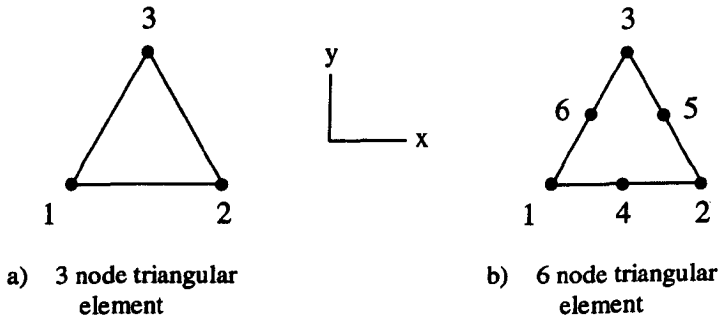


Figure 3.2 Two forms of triangular elements

The general displacement function of a linear 3-node triangular element, with 2 DOF (movement in the x and y direction) shown in Figure 3.2a is

$$u^* = C_1 + C_2 x + C_3 y \quad \text{Eqn 3.23}$$

however the general displacement function of a quadratic 6-node triangular element, with 6 DOF (movement in the x and y direction) shown in Figure 3.2b is

$$u^* = C_1 + C_2x + C_3y + C_4x^2 + C_5y^2 + C_6xy \quad \text{Eqn 3.24}$$

The displacement function can become quite complex if one of the degrees of freedom permitted is a rotation. Returning to the example of the 2-node truss element, shown in Figure 3.1 with the pins removed to allow the transfer of moments between elements. The element, which appears to be a linear element due to the number of nodes, is in fact a cubic element. (Consider the deformed shape of the element when a moment of the same sense is applied to both nodes.) The general displacement function for this element is

$$u^* = C_1 + C_2x + C_3x^2 + C_4x^3 \quad \text{Eqn 3.25}$$

This function permits the displacements u , but not the rotations θ to be expressed. However, as

$$\frac{du}{dx} = \theta \quad \text{Eqn 3.26}$$

$$\theta^* = C_2 + 2C_3x + 3C_4x^2 \quad \text{Eqn 3.27}$$

Using the conditions when $x = 0$, $u^* = u_1$ and $\theta^* = \theta_1$ or $x = L$, $u^* = u_2$ and $\theta^* = \theta_2$ using Eqns 3.25 and Eqn 3.27, the equivalent equation of Eqn 3.3, $[u_e^*] = [A][C]$ becomes

$$\begin{bmatrix} u_1 \\ \theta_1 \\ u_2 \\ \theta_2 \end{bmatrix} = \begin{bmatrix} 1 & 0 & 0 & 0 \\ 0 & 1 & 0 & 0 \\ 1 & L & L^2 & L^3 \\ 0 & 1 & 2L & 3L^2 \end{bmatrix} \begin{bmatrix} C_1 \\ C_2 \\ C_3 \\ C_4 \end{bmatrix} \quad \text{Eqn 3.28}$$

(Similarly with Eqns 3.23 and 3.24)

The shape function can be found from solving for C (i.e. $[C] = [A^{-1}][u_e^*]$ and substituting into the displacement function expressed as

$$u^* = \sum_{c=1}^{c=n} N_c(x, y)(u_i)_c \quad \text{Eqn 3.29}$$

It can be appreciated from these 4 relatively simple examples that an 8-node shell element, with 3 directional and 3 rotational degrees of freedom has very complex shape functions (N_i). However, the reduction in the number of nodes (20 for a quadratic solid element) represents an overall reduction in the number of equations (60-48=12 for each element) to be solved in the analysis.

3.3.1.4 Continuity at the boundaries of the element

When the total energy approach is used to equate the work done on the model by the external forces with the sum total of all the internal work in the elements, it is implicitly assumed that there are no discontinuities at the boundaries of adjacent elements. If such a discontinuity existed, there would be an infinite strain at the boundary causing infinite stresses that would have to be accounted for in Eqn 3.16.

Continuity of displacement at the nodes is ensured in the stiffness matrix however, the displacement along adjacent sides of two elements may not be equal unless the first derivatives of the shape functions N_i of the elements are also equal. This is shown in Figure 3.3 where two elements A and B, with a common boundary 1 – 2, are subjected to a deformation. The deformed shape of the boundaries are defined by N_{Ai} and N_{Bi} , therefore for continuity to exist along the element boundary $\frac{dN_{Ai}}{dx} = \frac{dN_{Bi}}{dx}$.

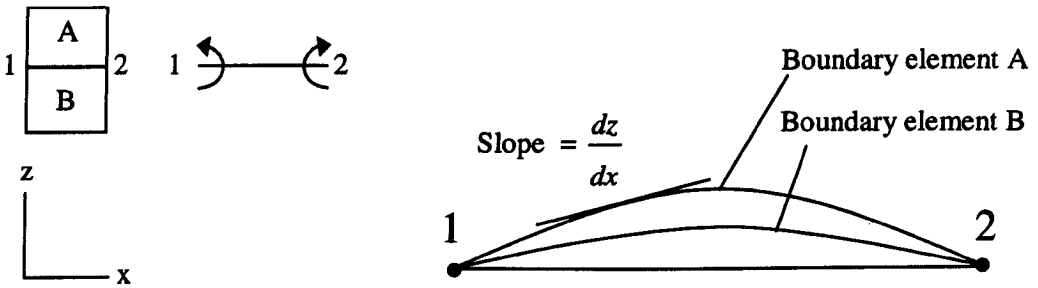


Figure 3.3 Compatibility requirements at inter element boundaries

Elements that have shape functions chosen such that this condition of continuity is complied with are called conforming elements, whilst those elements which do not comply are called non-conforming elements. In order that convergence can be achieved with non-conforming elements, the mesh should be sufficiently fine that the discontinuities at the boundaries of the elements are within acceptable limits.

The patch test is a series of simple tests that can be applied to the mesh in order to check that the discontinuities at the boundaries of the elements are within the prescribe limits and convergence can be achieved for the mesh.

3.3.1.5 Numerical integration

Although there are advantages in using global Cartesian co-ordinates to define the element's shape function, the expressions cannot be easily modified for different element shapes. The alternative is to use a local co-ordinate system where the local axis

have the same polynomial expressions as the shape functions, a process known as isoparametric mapping. The shape functions are then used to define the geometry and the displacement functions of the element. The one disadvantage of this is that very complex integrals have to be solved. However, no attempt is made to solve the integrals analytically, but by using a numerical integration technique.

The trapezoidal rule and Simpson's rules are examples of numerical techniques however, they are only exact when the order of the curve examined is one less than the number of points sampled, usually spaced at equal intervals along the curve. The Gauss quadrature is a very much more accurate method of numerical integration. An exact solution can be found for curves of the order of $2G-1$, where G is the number of points sampled, by choosing specific positions at which the curve should be sampled. Therefore, using 3 points in a single plane, an exact solution can be found when integrating a 5th order polynomial.

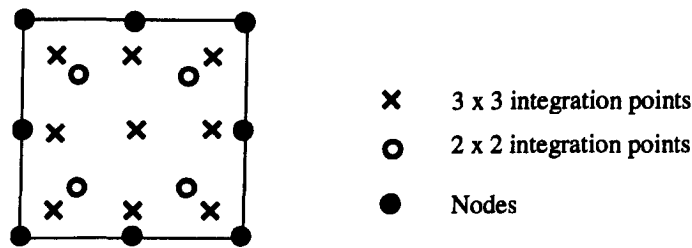


Figure 3.4 A square 8-node element showing two different arrangements of integration points

If full integration were to be calculated for an 8-node shell element, the displaced shape would be sampled at the 9 (i.e. 3 x 3) integration points, shown in Figure 3.4. However, with a small loss of accuracy and a large reduction in the computation required the displaced shape is only sampled at 4 points (2 x 2). Therefore the displaced shape calculated is a 3rd order polynomial in any single direction. The loss in accuracy in using the reduced number of integration points is not the disadvantage it would at first appear. The displacement-based formulation of the stiffness matrix is an upper bound solution to the true stiffness of the element. Therefore underestimating the contribution of the stiffness matrix in the numerical integration will actually give a better result than if the full integration was carried out in most cases.

3.4 Analysis options

ABAQUS being a batch program requires an input data deck that specifies the geometry of the model, the history of the loading pattern and the procedures to be used in the analysis. In non-linear problems the challenge is to obtain a convergent solution in an economic period of computing time and many different methods have been developed to achieve this. A review of the various analysis procedures used in the finite element suite to ensure accurate analyses and efficient use of the computer time is carried out in this section.

3.4.1 Method of loading

Load may be applied to the model in different ways, for example, by load control where the magnitude of the increment of force applied to the loaded member is specified by the operator. Alternatively displacement control may be used where the magnitude of the increment of the displacement of the loaded member can be specified. When load control is used, ascertaining the maximum load and observing post peak behaviour of the model is impossible without subsequent analyses being performed. Displacement control is the preferred approach as the maximum load and the post peak behaviour can be observed although it cannot be used when proportional loads have to be applied to other parts of the model.

The disadvantage of direct control methods is that the operator does not know the response of the model in advance when preparing the analysis and this can be wasteful of the computer time.

3.4.2 The modified RIKS algorithm

In finite element analysis it is often necessary to carry out non-linear static equilibrium solutions for unstable problems, where the resistance may decrease as the analysis progresses. The modified RIKS algorithm used in ABAQUS allows the equilibrium solution to be found, regardless of whether the response of the model is stable or unstable. The basis of the algorithm is a Newton method for determining the path of equilibrium in the analysis. Within each increment the solutions to the non-linear equilibrium equations are solved iteratively by minimising the force residuals so that eventually they are within predefined tolerances (usually the default values) and convergence is achieved. The size of the load increment is determined by the ABAQUS

standard convergence rate dependent, automatic incrementation algorithm for static cases. The convergence of the previous increment determines the size of the initial load increment of the next part of the analysis, although this may be modified if convergence is not achieved. The user can set the size of the initial load increment for the first increment, and limit the maximum and minimum size of further load increments.

This method of controlling the loading of the model has been used in all the analyses as it provides a maximum load, post peak behaviour and uses the computing time efficiently.

3.4.3 Non-linear material behaviour

The stress-strain properties of steel are non-linear. Typically the behaviour is linear and elastic, obeying Hooke's Law, until the yield point is reached, thereafter further increases in strain are non-linear and plastic. These material properties can be modelled in the analysis by ABAQUS using the *ELASTIC and *PLASTIC options. This data is entered, with a unique name, for each material used in the model so that different materials can be used for the chord, brace and weld if so desired.

The simplest form of elastic behaviour is the isotropic case where the material properties are the same in every direction, which is the case with steel. These material properties are then defined by giving the Young's Modulus E and the Poisson's ratio ν in the elastic option.

The plasticity model used by ABAQUS for isotropic materials at low temperatures, relative to the melting point, is the von Mises yield surface model with associated plastic flow rules. This yield surface assumes that the yield of the material is independent of the pressure stresses operating on the material and for the static analysis of SHS joints made with ductile steels, this assumption may be regarded as correct in both tension and compression. The associated plastic flow rule assumes that when the material is yielding, the direction of the deformation is normal to the yield surface at that point. The work hardening of the material on the von Mises yield surface is defined in the input data by giving the values of the uni-axial yield stress as a function of the uni-axial equivalent plastic strains. These stresses and strains for ductile materials such as steel, whose behaviour can exhibit large inelastic strains when yielding, should be entered as the true stress (Cauchy stress) and the (natural) log plastic strains as given by Eqns 3.30 and 3.31.

$$\sigma_{\text{true}} = \sigma_{\text{eng}} (1 + \epsilon_{\text{eng}}) \quad \text{Eqn 3.30}$$

$$\epsilon_{\text{ln}}^{\text{pl}} = \ln(1 + \epsilon_{\text{eng}}) - \epsilon_{\text{el,yield}} \quad \text{Eqn 3.31}$$

where

σ_{true} is the true or Cauchy stress

σ_{eng} is engineering stress or nominal stress

$\epsilon_{\text{ln}}^{\text{pl}}$ is the log plastic strain

ϵ_{eng} is the engineering or nominal strain

$\epsilon_{\text{el,yield}}$ is the elastic strain at yield

3.4.4 The material properties used in this thesis

When comparisons have been made to experimental test joints, the material properties found from tensile test specimens have been used in the manner outlined in the previous section. Details of the materials used are given with the results of the joints tested experimentally.

For the parametric work on the X and T joints the material properties were assumed to be grade 43C steel (S 275 JO) with elastic perfectly plastic material properties. The reasons for the choice of elastic perfectly plastic material properties were:

- to conform with one of the original intentions of the research to compare finite element joint failure with a yield line model for the collapse mechanism. The choice of an elastic perfectly plastic material allowed comparisons to be made on an equal basis
- when loaded in compression that there is only a small difference in the joint capacities between analyses where full work hardening properties are assumed and that of elastic perfectly plastic material properties are assumed
- that the material properties of hollow sections can vary enormously, particularly between hot formed and cold rolled sections. Estimating work hardening properties could lead to an overestimation of the joint capacity where the material properties differed significantly from those assumed, therefore a conservative assumption was made in that the properties were elastic perfectly plastic.

Van der Vegte (1995) reports a comparison between work hardening and elastic perfectly plastic material properties for a CHS uni-planar X joint axially loaded in compression. These results showed that there was a 4.7% difference in the observed collapse loads for the change in the material properties in the same model. This is a little more than the author would have expected, but shows small influence of the work hardening properties on the joint capacity when loaded in compression.

For the work on K joints, originally started by Crockett (Crockett 1994 and Davies et al 1996), the material properties used previously by him were retained so that comparisons could be made with his earlier work. These material properties are given when discussing the K joints in Chapter 7.

3.4.5 Geometric non-linearity

Significant improvements can be made in the accuracy of geometric non-linear problems by updating the stiffness matrix between each load increment to take account of the changes in the geometry that have occurred due to the deformations in the previous increment. The increase in the computing time required to do this is compensated for by the improved accuracy of the analysis. In ABAQUS this option is controlled by the parameter NLGEOM which is used in all the models.

3.4.6 Boundary conditions

Full advantage is taken in all the joints modelled of any planes of symmetry in the geometry and the method of loading to reduce the size of the model. The presence of the rest of the model beyond a plane of symmetry is represented by the boundary conditions at that plane of symmetry. In ABAQUS these boundary conditions are invoked by the commands XSYMM, YSYMM and ZSYMM for symmetry in the x, y and z planes respectively.

3.5 Element types

3.5.1 Shell elements

Shell elements are predominately used in models to find the static strength of structural hollow section joints where typically the thickness of an element may be regarded as low in comparison to its length and breadth.

Two basic assumptions are made in the formulation of the equations governing the shell element that:

- during the deformation of the element, sections normal to the middle plane remain plane during the deformation
- the through thickness stress σ_z are small (i.e. tending to zero) and hence the strain ϵ_z can be neglected, i.e. a plane stress situation

Additionally for thin shells, discussed later, normals to the middle plane remain normal to the middle plane during deformation, therefore assuming that the effects of shear are negligible.

Considerable savings can be made in the computation by using shell elements due to the reduction in the number of nodes that have to be considered even though there are additional degrees of freedom and the governing differential equations are a great deal more complex.

ABAQUS provides two types of shell element, those that use 5 degrees of freedom at each node (3 displacement and 2 rotational components) and those that use 6 degrees of freedom at each node (3 displacement and 3 rotational components). The elements where 5 degree of freedom are allowed can be more economical in terms of computing and storage but elements with 6 degrees of freedom are better able to model the curved surfaces caused by deformation of the model. There are two methods to define the cross sectional behaviour of a shell. When the *SHELL GENERAL SECTION option is used, the linear moment-curvature and the force-membrane relationships are defined and the calculations are carried out in terms of the section forces and moments. When the *SHELL SECTION option is used the cross sectional behaviour of the shell element is calculated by numerical integration at any number of calculation points that may be defined through the thickness of the element. The *SHELL SECTION option is used throughout this work with the number of calculation points through the thickness of the shell element set at five.

In addition to this shell elements may be modelled as thick or thin shells depending on whether transverse shear flexibility, which allows for shear deformations, is provided for. (Thick shells permit this shear deformation.) The ABAQUS user's manual suggests that the transverse shear is only important when the thickness of a uniform material is greater than a 1/15 of the span of the shell elements between supports.

The shell elements provided by ABAQUS which are suitable for the static strength analysis of SHS joints are shown in Figure 3.5 and are:

- S3R 3-node triangular thin or thick shell, finite membrane strain
- STRI65 6-node triangular thin shell, using 5 degrees of freedom per node
- S4R 4-node doubly curved thin or thick shell, reduced integration, hourglass control, finite membrane strains
- S8R 8-node doubly curved thick shell, reduced integration
- S4R5 4-node doubly curved thin shell, reduced integration, hourglass control, using 5 degrees of freedom per node
- S8R5 8-node doubly curved thin shell, reduced integration, using 5 degrees of freedom per node
- S9R5 9-node doubly curved thin shell, reduced integration, using 5 degrees of freedom per node

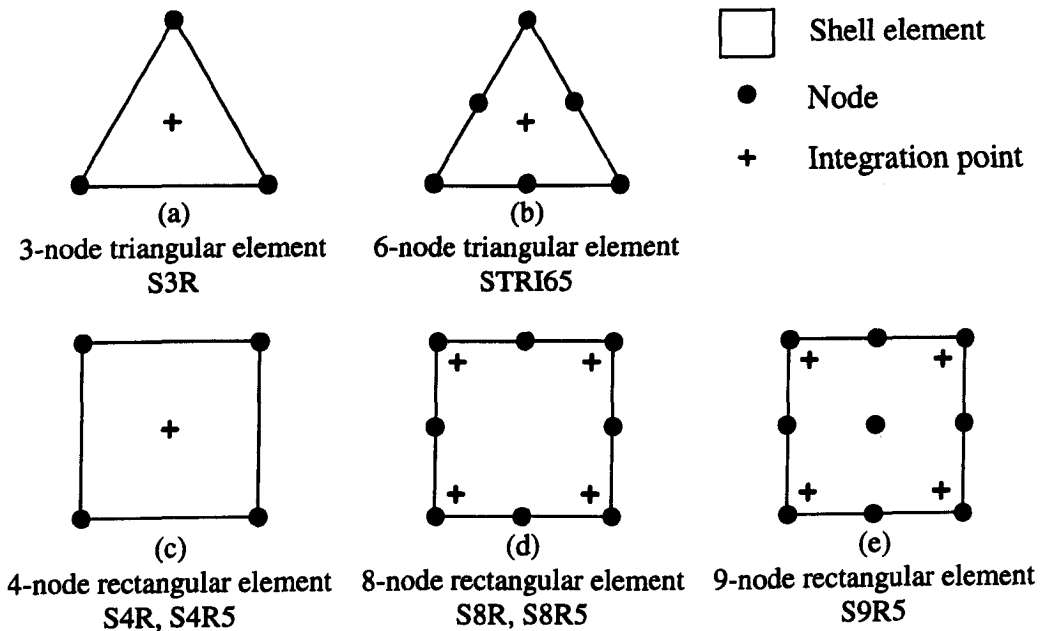


Figure 3.5 The different shell elements available in ABAQUS

Elements S4R5 and S8R5 can be degenerated into triangles. However, element S8R cannot and in which case element STRI65 is used. This causes a conflict in that thick and thin shell are mixed however, the triangular element is only used sparingly to model parts of the chord enclosed by the area of the brace at the intersection of the joint. There is no appreciable deformation in this vicinity and the fact that this triangular element does not calculate the shear deformation within the material is not considered important.

3.5.2 Solid elements

Solid elements are only considered in this work to model the material of a weld at the connection of the brace and chord members. Typically a 15-node quadratic triangular prism C3D15 is used or, occasionally, to fill a hole created in the mesh by the geometry of the weld, a 10-node quadratic tetrahedron C3D10 is required. Both of these elements are shown in Figure 3.6.

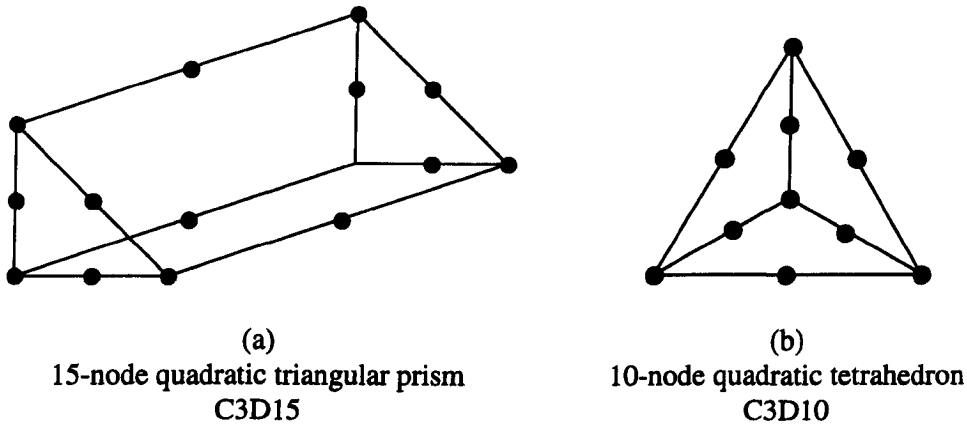


Figure 3.6 Solid elements available in ABAQUS to model the weld material

These elements have 3 degrees of freedom at each node for displacement components only. It is recognised that there are incompatibilities in the degrees of freedom permitted at the nodes between the solid elements when used with shell elements; however, as they are only used to represent the presence of the weld material and the effect that this has on the shell elements in the vicinity, total compatibility is not essential.

3.5.3 Comparison between shell elements

Crockett (1994) compared 4-node (S4R) and 8-node (S8R) elements and concludes that for the cases studied, 8-node elements gave a realistic although conservative prediction of the joint capacity. However, the same number of 4-node elements produced similar results with the benefit of a reduction in the CPU time. He notes that he considers the 8-node shell element to be more accurate than the 4-node shell element but does not explain very clearly why, other than to point out that comparisons of the strains observed between the test joints and the finite analyses were improved.

Van der Vegte (1995) undertook a more serious study of different element types in modelling a simply supported plate with ten elements and a perpendicular force at the

mid point. Van der Vegte concludes that 4-node and 8-node thin shell elements have benefits in the lower storage space and CPU time required, but are less accurate than the 8-node thick shell elements as quadratic interpolation functions have been used to calculate the displacements in the latter. (The author would have expected that quadratic interpolation is used on the 8-node thin shell element as well and that any improvement in the accuracy may be due to the increased number of nodes.)

In a second study of a CHS X joints with 200 elements, the results are shown in Table 3.1. Each of the shell elements he has considered in the finite element program MARC has 4 gauss integration points, each with 7 calculation points at different levels to calculate the effects of the deformation through the thickness of the shell element.

The limiting slenderness of the thin shell element in MARC that van der Vegte gives is $2\gamma = d_0/t_0 > 20$. The slenderness of the chord wall of the joint compared is equal to 40 so it is not surprising that the results of the 8-node thin shell element compare favourably with the thick shell elements. No comparison is made for lower values of 2γ to compare the behaviour of the thin elements when thick shell elements should be used nor are these comparisons compared to a test joint to verify which element is giving the best results. The use of the 8-node thin shell elements demonstrates the large amount of CPU time that can be saved in the analysis when these elements are used.

	Number of elements	Number of nodes	Relative CPU time	Ultimate Load kN	Strength ratio
8-node thick shell elements	200	654	1.00	466.0	1.000
8-node thin shell elements	200	654	0.41	474.0	1.017
4-node thick shell elements	200	227	0.50	511.4	1.097

Table 3.1 A Comparison between three different shell elements, van der Vegte (1995)

Van der Vegte’s conclusion is that thick shell elements are the preferred element, although the 8-node thin shell elements could be considered for models with a large number of elements and where $2\gamma > 20$ to cut down on the computing time. Why he has concluded this from these results is unclear. He however, does note that in multi-planar XX joints where large transverse shear stresses may be expected to occur with equally loaded braces, there could be significant differences if thin shell elements were used instead of thick shell elements, although this is not shown.

3.5.4 The shell elements used in this research

Chord slenderness ratios of $b_0/t_0 = 9.3, 15, 23.8$ and 35.3 are typically used in this research and rather than use different elements to model the behaviour with a possible influence on the results observed, the rectangular 8-node thick shell element S8R and triangular 6-node thin shell element STRI65 with quadratic interpolation have been used throughout. Each of these elements has five calculation points through the thickness of the element at each of the integration points.

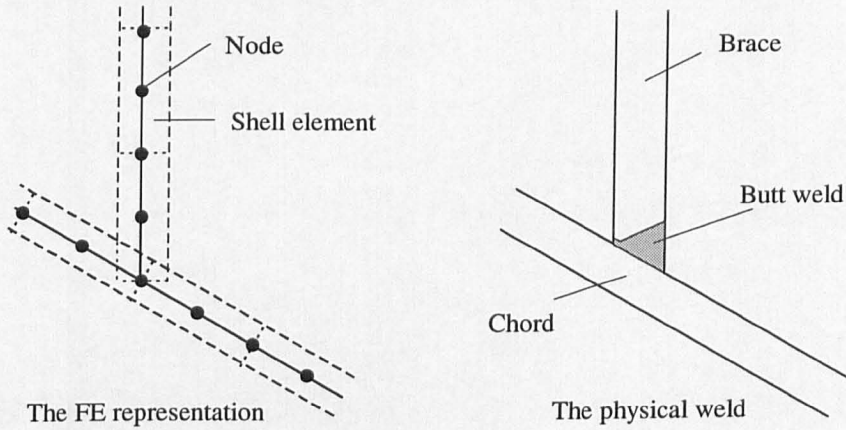


Figure 3.7 Example of the detail when a butt weld is assumed

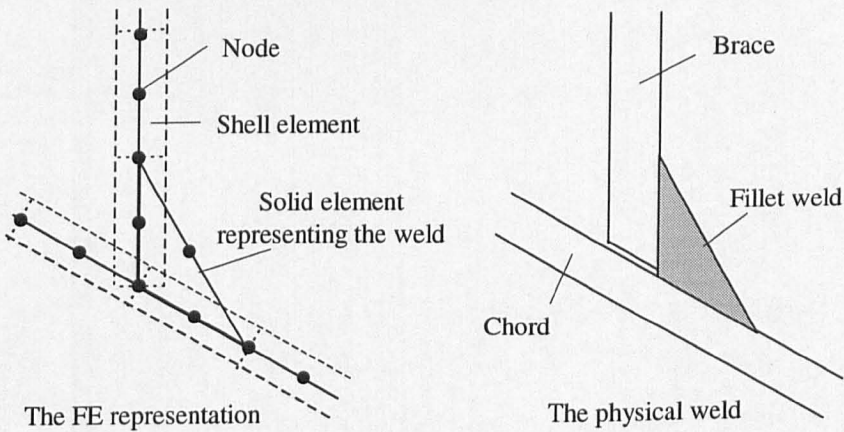


Figure 3.8 Example of the detail when a fillet weld is assumed

3.6 Modelling welds

The literature review in Chapter 2 shows that there are many different ways in which a weld may be modelled. The way this is implemented for the work carried out in this research is discussed in this section.

When a butt weld is assumed, no attempt is made to include the presence of any weld material. Figure 3.7 shows the physical and finite element representation of the connection at a butt weld. When a fillet weld is assumed, then a solid element is used to represent the weld material in the manner shown in Figure 3.8.

3.7 Problems caused by the 3D geometry

Vector geometry has been used extensively in the construction of the model to solve the problems of 3D geometry in the diamond bird beak joints. It was also particularly useful in calculating the angle of rotation of plastic hinges between rigid plates in various yield line models to examining possible collapse mechanisms, although these have since been discarded as unsatisfactory. A simple example of the use of vector geometry in the calculation of the angle between the faces of the brace and chord is shown in the next section.

3.7.1 Calculating the angle between the welded faces

In the diamond bird beak joints, where both the chord and the brace have each been rotated by 45° about their own centre line axes, the angle of intersection between faces can no longer be worked out easily by simple geometry. The most convenient method is to use vector geometry where a normal vector is calculated for the faces of the chord \underline{c} and brace \underline{b} . The angle between these vectors can then be found by the dot product

$$\underline{b} \cdot \underline{c} = |\underline{b}| |\underline{c}| \cos \theta \quad \text{Eqn 3.32}$$

Taking as an example the case where the brace and chord centre lines intersect at 90° , where $\underline{c} = (0i + 0.707j + 0.707k)$ and $\underline{b} = (0.707i + 0j + 0.707k)$ the angle between the normals is $\theta = 60^\circ$ and therefore the angle between the face of the members is 120° .

4.

Member Orientation in X joints

4.1 Introduction

In this Chapter the effects of member orientation will be studied for different forms of orthogonal X joint under axial loading. Diamond and square bird beak X joints will be examined in detail and comparisons made between bird beak X joints and similar X joints in the traditional RHS and CHS configurations.

In order to understand the fundamental behaviour of the diamond bird beak X joints, a detailed study was necessary to develop an understanding of how the failure modes are affected by the section orientation. During the course of the study the parameters for the chord length L_0 , width ratio β , chord slenderness b_0/t_0 and the material yield strength f_y were varied to observe the effect on the joint capacities. A hybrid joint, the square bird beak joint is studied as a comparison to examine the variation of the effect of chord length and the differences in the failure mechanisms.

A limited amount of experimental work has been carried out at Nottingham University by Grunberg (1994) and Fundament (1995), the results of this work are reported and used to validate the models used in the finite element analysis.

In order that comparisons can be made to assess the advantages and disadvantages of the bird beak joint with other joint arrangements, a limited number of traditional RHS and CHS joints were analysed. The differences in the failure modes are discussed and comparisons made between the joint capacities.

4.2 Definition of terms used in this Chapter

To avoid any confusion in the meaning of the terms used in this Chapter, they are defined in this section.

4.2.1 The joint capacity $F_{u,1}$

The joints studied in this Chapter exhibit many different forms of behaviour, in the majority of cases a maximum load is attained. The joint capacity $F_{u,1}$ is defined as the maximum load attained during the test or analysis, or if a maximum load is not attained then the load reached with an indentation of $3\%b_0$.

4.2.2 Load deformation curves

In order to assess the stiffness and joint load capacity of the finite element models or experimentally tested joints, load/indentation curves and load/lozengeing curves are examined. The indentation is taken as the change in the distance between a point on the brace (approximately a distance of b_1 from the toe of the brace) to the middle corner of the chord. The lozengeing is the change in the overall width of the section measured cross the chord at a point directly under the centre line of the brace as shown in Figure 4.1.

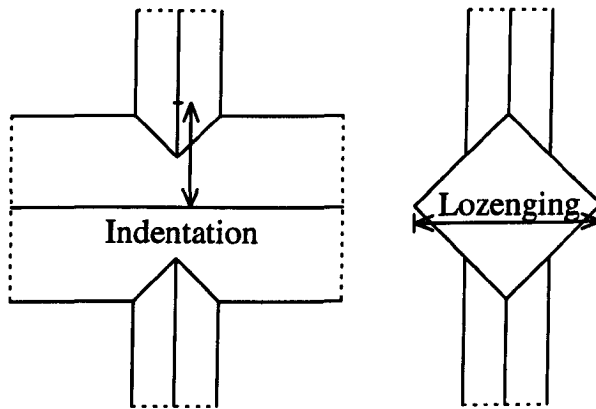


Figure 4.1 The definition of datum lengths for “indentation” and “lozengeing”

4.2.3 Descriptions of chord failure

The term “crushing” is used in reference to the failure of the chord when there is a decrease in the vertical dimension along the whole length of the chord. The term “lozengeing” is used only when the deformation occurs in the vicinity of the brace and the cross section shape at the end of the chord remains unchanged.

4.2.4 The Chord length, L_0

The chord length refers to the whole length of the chord, shown in Figure 4.2a and not the length of the chord in the finite element models.

4.2.5 Chord width ratio β

In the square bird beak joint, the chord width ratio is still defined as b_1/b_0 , even though the orientation of the chord means that this not the true width ratio of the joint. (The width of the brace is b_1 , whilst the width of the chord is $b_0/\sin 45^\circ$)

4.3 The model details for the X joints studied

The X joints considered in this Chapter and the method of loading are shown in Figure 4.2. In the diamond bird beak joint both the chord and brace members are rotated through 45° about their own centreline axes. The square bird beak joint, where only the chord is rotated by 45° about its own centre line axis, is studied as it may be a necessary hybrid joint in some structural situations. Studying the behaviour of this joint may also extend our understanding of the diamond bird beak joint system. Traditional RHS and CHS X joints formed in the conventional way are studied to provide bench marks for comparison with bird beak joints and consequently are not examined in such great detail.

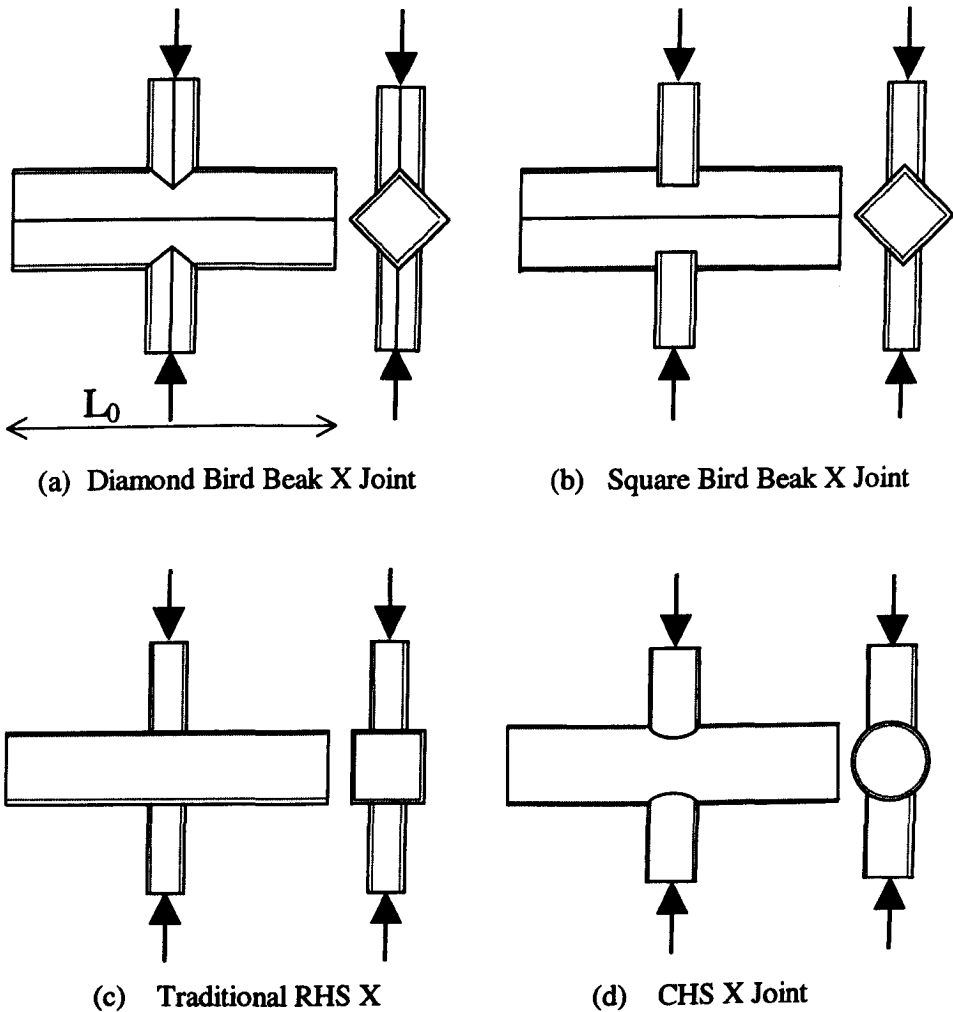


Figure 4.2 The different forms of X joint studied in this Chapter

4.3.1 The finite element meshes

X joints with only axial forces applied to the brace members have three planes of symmetry. By taking advantage of this symmetry only an eighth of the joint need be modelled, with the rest of the joint represented by the boundary conditions imposed at the planes of symmetry. An example of some of the meshes used for these finite element models, representing the different forms of X joint analysed, are shown in Figure 4.3.

All the elements used in the X joint models are 8-node thick shell elements, ABAQUS element S8R described in Chapter 3.

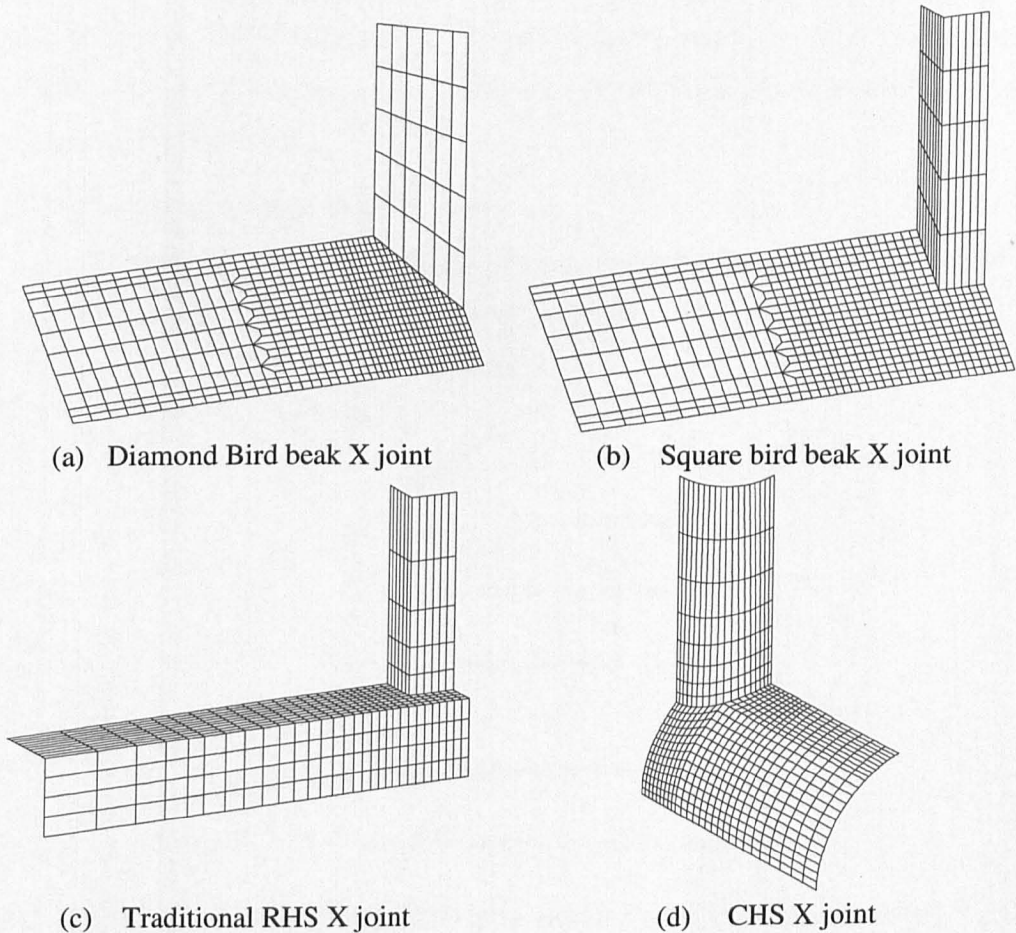


Figure 4.3 Examples of the finite element meshes for the X joints considered

The distribution of the shell elements was determined by running simple models to determine the stress gradients and the forms of failure that occurred along the chord as the length was increased. This led to a very high mesh density in the vicinity of the

brace and very few elements at the end of the chord for very long joints (not shown above).

4.3.2 Mesh connectivity and weld considerations

Due to the different joint types considered in this Chapter, alternative solutions have had to be found to connect the meshes for the brace and the chord. In the following sections the methods used to connect the meshes are described, recognising that in the design guide recommendations, fillet welds are not permitted in all cases.

It is appreciated that the presence of a fillet weld can significantly affect the strength of some joints and that this effect will vary between the different joint types considered. When the fillet weld influences the joint strength, the total joint capacity becomes dependent on the size of the weld chosen, as the effective branch/chord width ratio varies in such cases.

4.3.2.1 The diamond bird beak X joints

The method used to connect the brace to the chord for the diamond bird beak can be seen in Figure 4.3 and in greater detail in Figure 4.4.

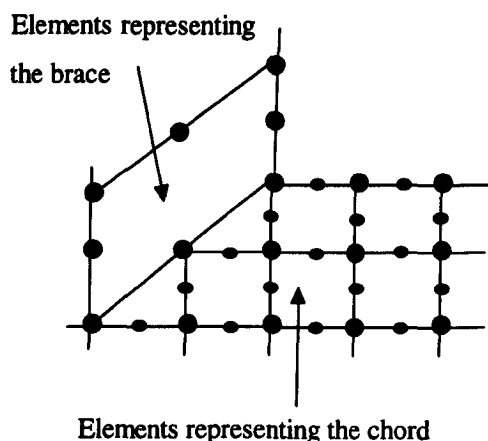


Figure 4.4 The connection between brace and chord elements

When a solid element representing the material of a fillet weld was added to this mesh, the sloping faces of the brace and chord distorted the solid element to such an extent that the analysis could not be performed. For this reason no fillet welds were modelled in the diamond bird beak X joints and a butt weld connection was assumed. The validity of this approach can in some way be justified by the fact that:

- the angle between the face of the brace and the chord is 120^0 , which is also the limiting angle, above which fillet welds are not recommended. (Packer et al 1992)(IIW 1989)
- fillet welds are generally used only up to a throat thickness of 8mm, whereafter butt welds are recommended (IIW 1989)
- that when using grades of steel higher than 43C and thicknesses greater than 8mm, preheating of the joint for a fillet weld may be required, making butt welds more economic.
- this study is considering the fundamental behaviour of the bird beak joints and the presence of weld material may obscure a failure mechanism and the true strength of the joint.

The geometry required for fillet and butt welds in this joint is shown in Figure 4.5. Where “L” is the leg length and “a” is the throat thickness of the fillet weld and is calculated as the greater of

$$a = \frac{\text{Capacity}}{\text{Weld strength} \cdot \text{Weld Length}} \quad \text{Eqn 4.1}$$

or

$$a = \text{Load function} \times \frac{\text{Material strength}}{\text{Weld strength}} \times t_1 \quad \text{Eqn 4.2}$$

where the load function is the greater of

$$\frac{\text{Applied factored load}}{\text{Members tension capacity}} \quad \text{or} \quad \frac{\text{Applied factored load}}{\text{Joint Capacity}}$$

Assuming that the welded joint is to have a tensile strength equal to the joint capacity this gives a throat thickness of 8.06mm for S 275 J0 (Grade 43C) steel 90x90x6.3mm branch member and E43 21R electrode.

The design strength of the butt weld may be taken as the strength of the brace, providing that the electrodes used have at least the same yield and tensile properties as the steel used in the brace.

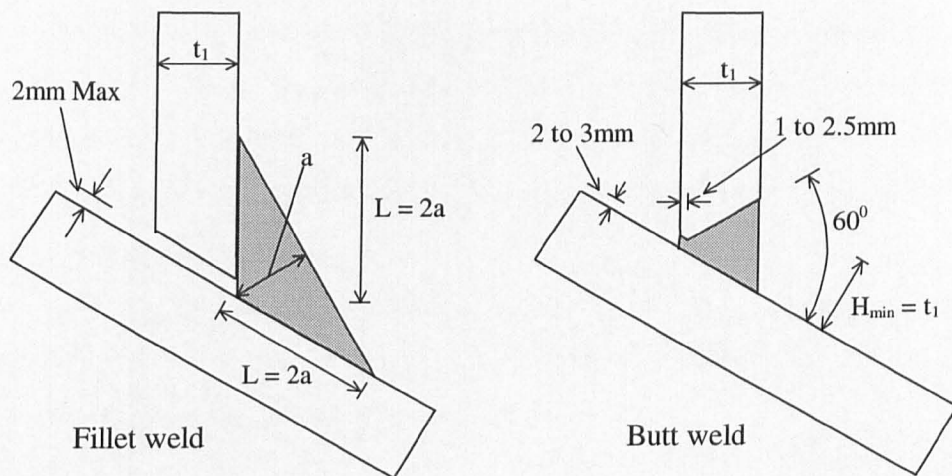


Figure 4.5 Examples of the different types of weld

4.3.2.2 Square bird beak X joint

Due to the orthogonal nature of the geometry of this joint there were no problems fitting the brace member to the chord and the finite element analysis could be performed using solid elements to model the weld material. Fillet welds may be used for the sides of the brace members perpendicular to the longitudinal axis of the chord where the angle of intersection between the faces is 90° . However, for the sides parallel to the longitudinal axis of the chord where the angle of intersection is 135° , butt welds are recommended by the design codes as the angle is greater than 120° .

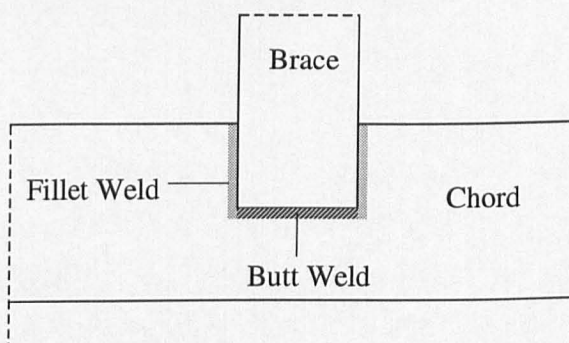


Figure 4.6 Recommended positioning of fillet and butt weld on the square bird beak joint

4.3.2.3 Traditional RHS X joints

Due to the simple orthogonal nature of the geometry of the traditional RHS X joints where $\theta=90^\circ$, the angle between all the faces of the brace member and the chord is a right angle. Therefore there are no problems in connecting the elements in the brace and the chord and adding solid elements to represent the fillet weld material.

The preferred method of welding a traditional RHS X joint is to use a fillet weld providing it is within the design recommendations' limits, as it is usually more economic than a butt weld. In addition to this the presence of a fillet weld can significantly increase joint capacity by increasing the effective width ratio of the joint.

4.3.2.4 CHS X joints

The complex connection between brace and the chord members is achieved using an automatic mesh generation program, FEMVIEW (1989), that calculates all the intersection points at the connection.

The angle of intersection between the walls of the chord and the brace members varies around the joint and (with the possible exception of small width ratio joints ($\beta < 0.5$) where the angle of intersection everywhere is less than 120° when $\theta=90^\circ$), fillet/butt or butt welds are the recommended methods of welding CHS sections. For the width ratio considered in this Chapter ($\beta=0.6$) fillet/butt or plain butt welds should be used.

4.3.3 The type of weld assumed in the finite element models

In the previous four sections, the reasons why fillet welds cannot be used for some of the welded joints are discussed. In addition to these reasons the designer or the prefabricator may have a preference for a butt weld, as a large fillet weld is unsightly and difficult to manufacture in terms of quality.

Assuming fillet welds for all the welded connections could lead to an overestimation of the joint capacity and be against the recommendations in the design guidance in some cases. Assuming a mixture of fillet welds and butt welds in line with the design guidance has the problem that true comparisons of the joint capacity cannot be made between the joints where different welding techniques are used. In addition to this, should a fillet weld be replaced by a butt weld for whatever reason, then the joint capacity will be overestimated. If all the welds are assumed to be butt welds then true comparisons can be made between the different joint types because they are all welded in the same manner and if a butt weld is replaced by a fillet weld then the joint capacity will be underestimated, a safer alternative.

Due to problems of modelling the weld material for a fillet weld in the diamond bird beak models discussed in section 4.3.2.1 and so that comparisons can be made of the true strength of all the joint configurations considered, no welds were modelled in

any of the models, i.e. butt welds were assumed throughout. The only exception to this are the traditional RHS joint where the increase in the strength of the joint with a weld was investigated as it is unlikely that this type of joint will be butt welded.

4.3.4 The material properties used in the analysis

To facilitate the theoretical analysis of bird beak joints, which was the original intention of this research, elastic perfectly plastic material properties were assumed in all the models. The only exceptions to this are the joints used for benchmark validation of the finite element work where the material properties of the test joints themselves were simulated. This is unlikely to make a large difference to the joint capacity when loaded in compression as the strain hardening of the steel at joint failure will be low.

The material used in the analyses was assumed to be S 275 J0H, Grade 43C steel with Young's Modulus $E = 207 \text{ kN/mm}^2$ and a yield stress $f_y = 275 \text{ N/mm}^2$.

4.3.5 Method of loading

An axial compressive force is applied to the brace members of all the X joints analysed in this Chapter. The load is applied uniformly to all the nodes at the end of the brace, with only half the load applied to the nodes lying on the planes of symmetry.

4.3.6 Convergency tests

In order to achieve the optimum efficiency in the analysis of the models, balancing accuracy and CPU time, the appropriate mesh size of the models was investigated. One external factor which was considered important was that the analysis of all the models could be completed within two CPU hours on the DEC Alpha workstations at Nottingham University, to avoid the slow turn around of the twenty four CPU hour queue. The reason for the selection of each mesh is briefly discussed in the following sections.

4.3.6.1 Diamond bird beak X joint

Examples of the meshes used in the convergency study for the diamond bird beak joint are shown in Figure 4.7. The load/indentation curve, shown in Figure 4.8, for the coarse mesh shows the joint strength to be 2% greater than the medium mesh. There is a small decrease (1%) in the joint strength of the fine mesh however, the CPU time increased from 1.75hrs to 4hrs.

This decrease in the joint capacity, indicating an improvement in the accuracy, does not justify the increase in the CPU time required to analyse the model. The medium mesh is used in all further analyses.

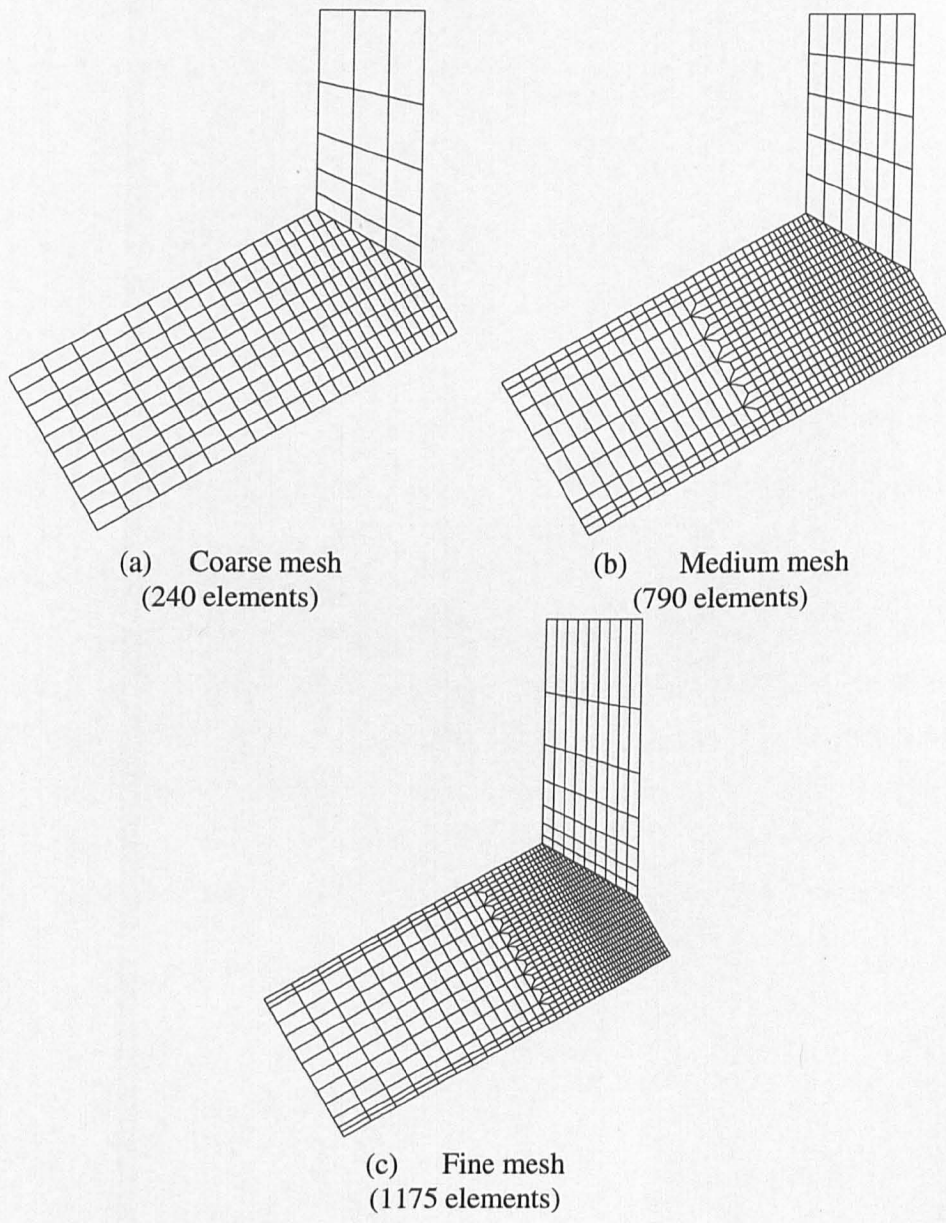


Figure 4.7 The three diamond bird beak meshes used in the convergence study

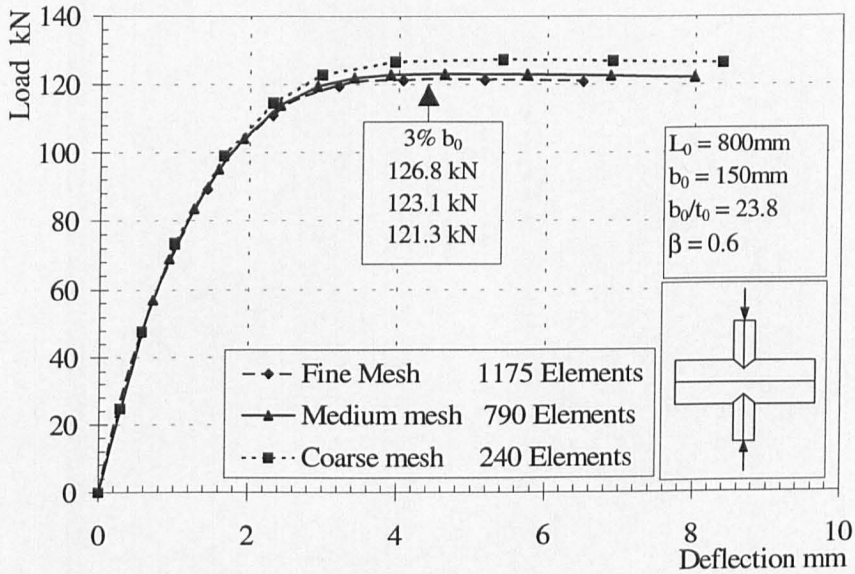
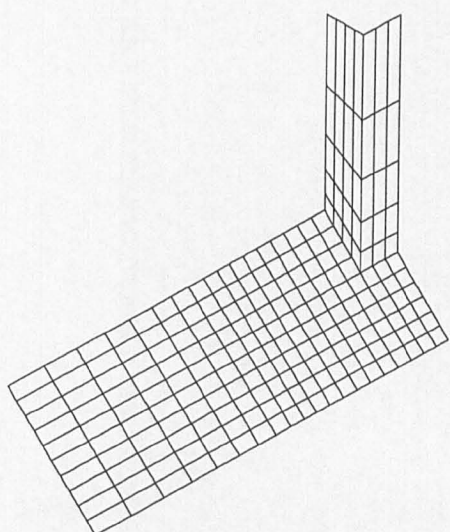


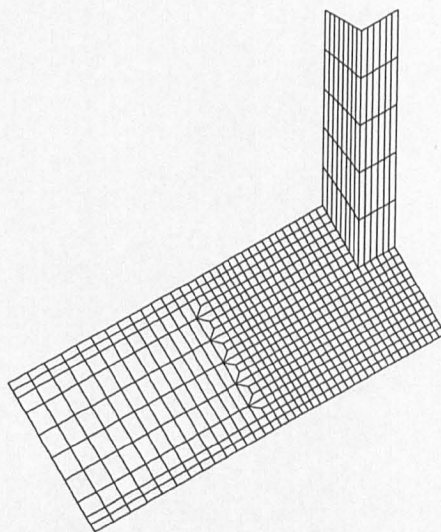
Figure 4.8 The results of the convergency study for the diamond bird beak X joint

4.3.6.2 Square bird beak X joint

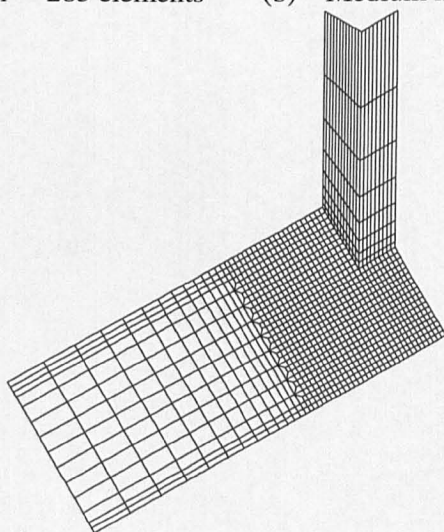
The three meshes used in the convergency study are shown in Figure 4.9. The load/indentation curve for the coarse mesh, shown in Figure 4.10 differs from the medium and fine meshes by a considerable amount (15%) and it may be reasonable to assume that increasing the element size significantly affects the failure mechanism. There is however, only a very small difference between the medium and the fine meshes (<1%), therefore it is justifiable to use the medium mesh for further analyses.



(a) Coarse mesh - 285 elements



(b) Medium mesh - 870 elements



(c) Fine mesh - 1294 elements

Figure 4.9 The three square bird beak meshes used in the convergency study

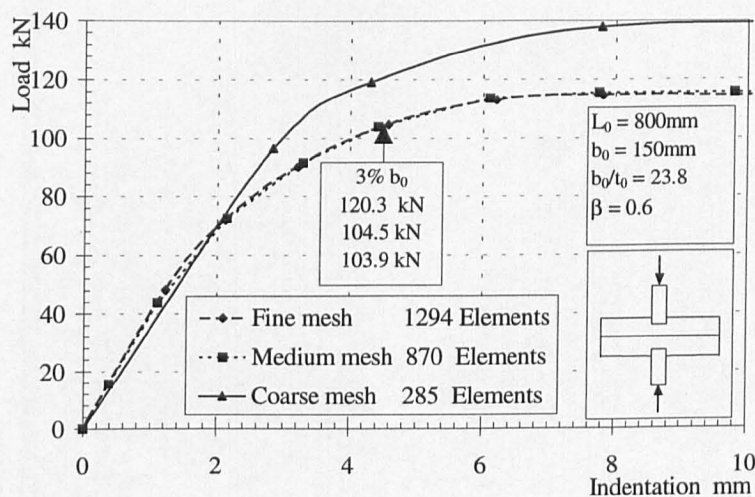


Figure 4.10 The results of the convergency study for the square bird beak X joints

4.3.6.3 CHS X joint

The meshes used in the convergency study are shown in Figure 4.11. The load/indentation curves shown in Figure 4.12 for the two different meshes used in this study gave virtually identical curves. It was not thought necessary to run a fine model as the results were only being used to compare with the bird beak joints. The coarse mesh is used in the comparisons.

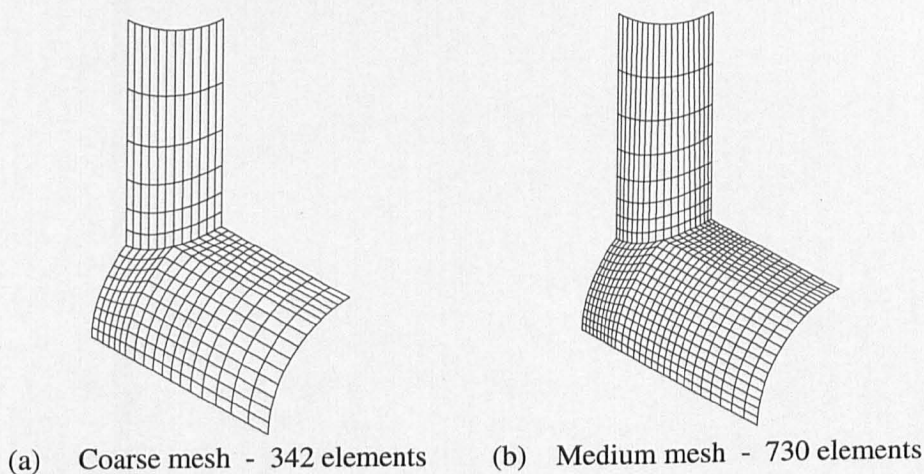


Figure 4.11 The two CHS meshes used in the convergency study

In the light of further experience it is regretted that the mesh for these analyses was not further refined.

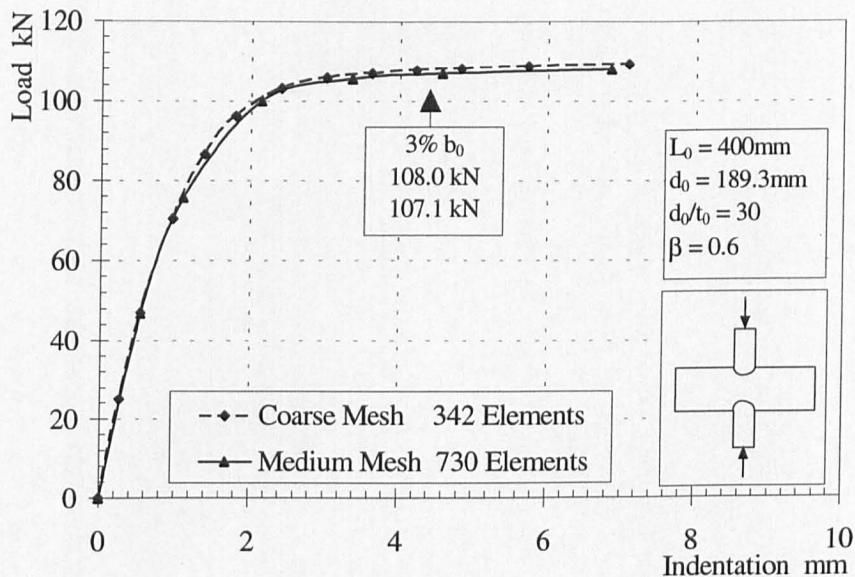


Figure 4.12 The results of the convergency study for the CHS X joints

4.3.6.4 Traditional RHS X joint

The variation of the joint capacities from the load/indentation curves shown in Figure 4.13 between the three models (Figure 4.14) used in the convergence study is not as conclusive as some of the previous studies.

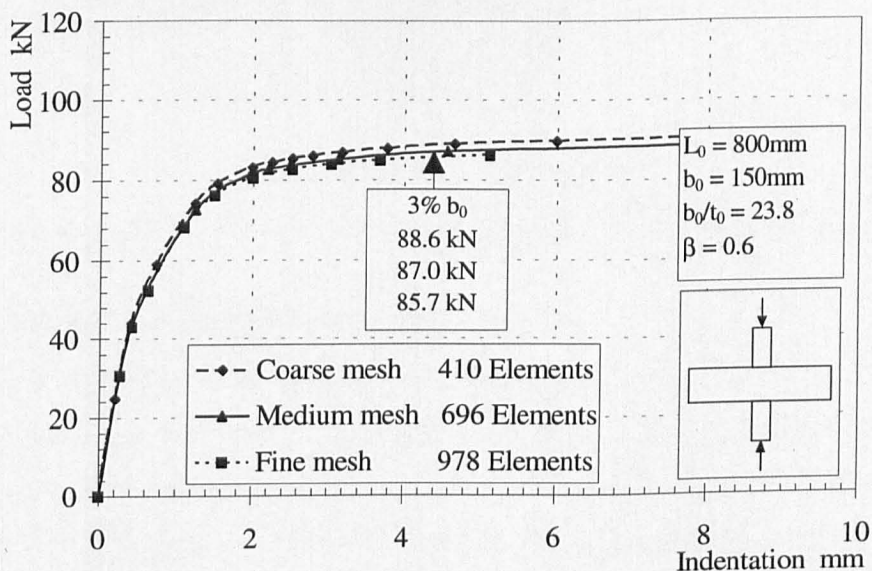


Figure 4.13 The results of the convergency study for the traditional RHS X joints

Although the difference in joint capacities between the coarse-medium and the medium-fine mesh is tending to converge, true convergence is not achieved. However,

the CPU time for the fine mesh has increased to 2.8hrs, so a trade off in the accuracy of the joint capacity against the CPU time taken resulted in the medium mesh joint being used in further analyses.

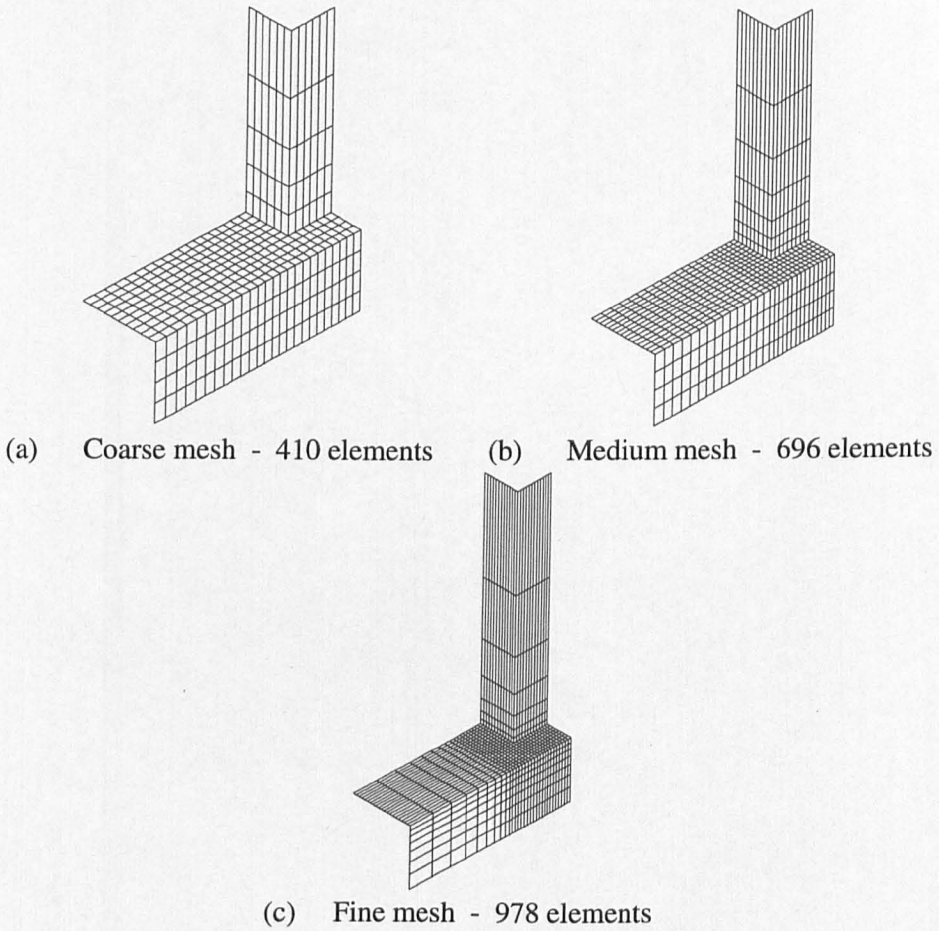


Figure 4.14 The three traditional RHS meshes used in the convergency study

4.3.7 Validation of the bird beak models

Although finite element analysis is a very useful and accurate tool for analysing joint strength, it is important to validate the finite element models to ensure that the joint capacity and failure mechanism are correctly predicted in the analysis. Using the physical data from the joints tested by Grunberg (1994) and Fundament (1995) in the civil engineering laboratories at Nottingham University, four finite element models were analysed to compare the results and validate the finite element models. The details of the joints tested are given in Table 4.1 and the engineering material properties in Figure 4.15. The experimental joints tested were fabricated using fillet welds around the brace members.

	Chord Length L_0 mm	Chord Size b_0 mm	Brace Size b_1 mm	β b_1/b_0	Chord Thickness t_0 mm	Brace Thicknes s t_1 mm
Diamond bird beak X joint	520	149	90	0.6	6.2	6.25
Diamond bird beak X joint	1000	149	90	0.6	6.2	6.25
Square bird beak X joint	520	149	90	0.6	6.2	6.25
Square bird beak X joint	1000	149	90	0.6	6.2	6.25

Table 4.1 Details of the joints tested by Grunberg (1994) and Fundament (1995)

Brace				Chord			
Stress N/mm ²	Strain	True Stress N/mm ²	True Plastic Strain	Stress N/mm ²	Strain	True Stress N/mm ²	True Plastic Strain
0	0	0.0	-	0	0	0.0	-
400	0.00193	400.8	0	320	0.00153	320.5	0
400	0.04159	416.6	0.03882	333	0.02240	340.5	0.02061
486	0.110	539.5	0.10243	400	0.05115	420.5	0.04834
486	0.260	612.4	0.22918	462	0.110	512.8	0.10281
360	0.310	471.6	0.26809	462	0.270	586.7	0.23747
				350	0.310	458.5	0.26848

Table 4.2 The stress/strain relationship of the test joints

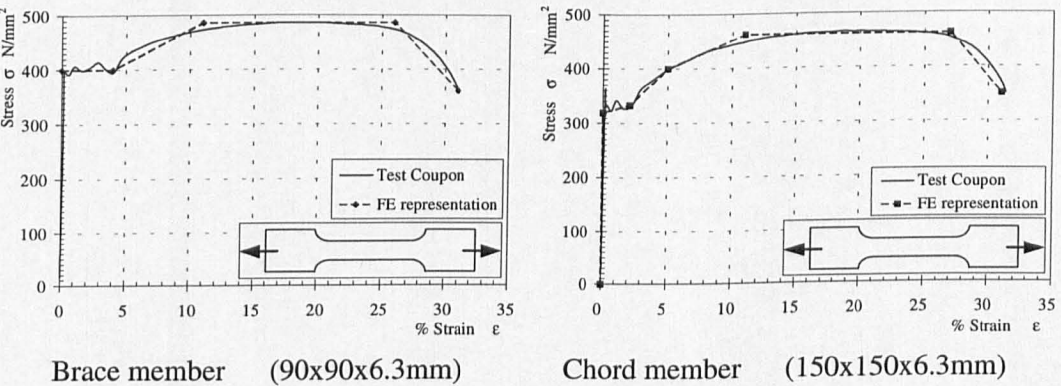


Figure 4.15 The engineering material properties of the joints tested

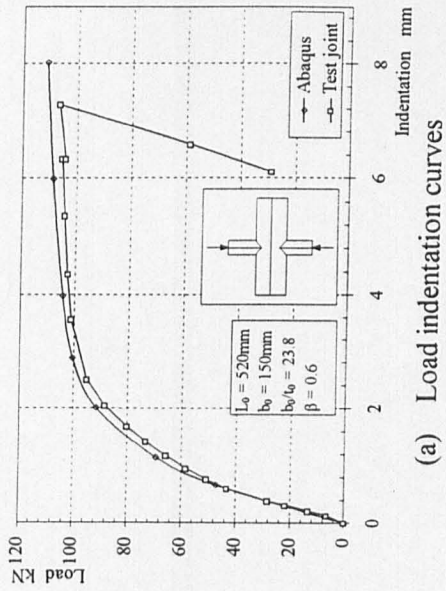


Figure 4.16 Validation curves for the diamond bird beak X joint $L_0=520\text{mm}$

(b) Load lozenging curves

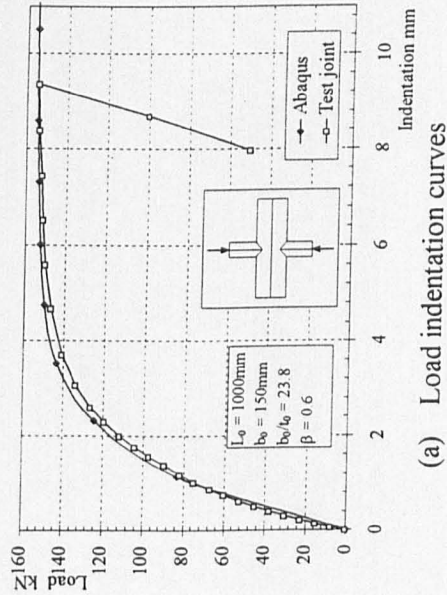
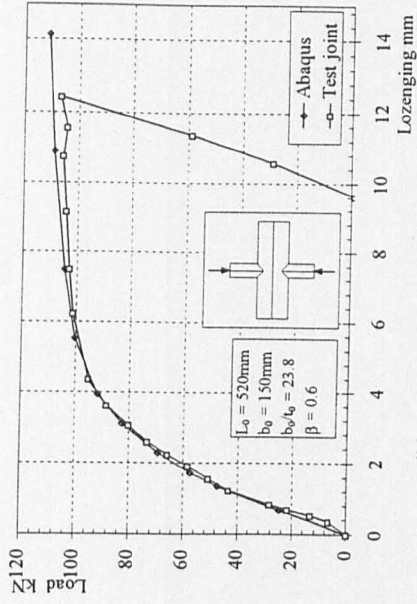
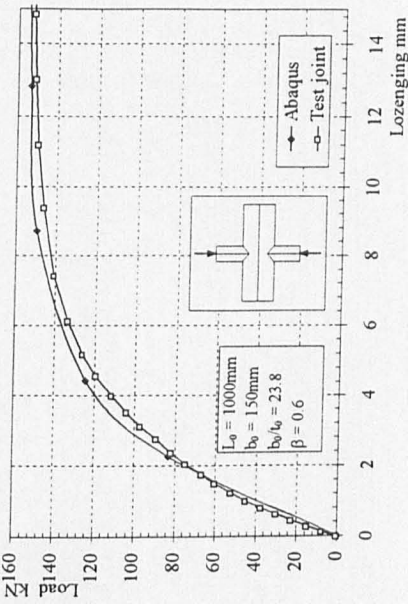
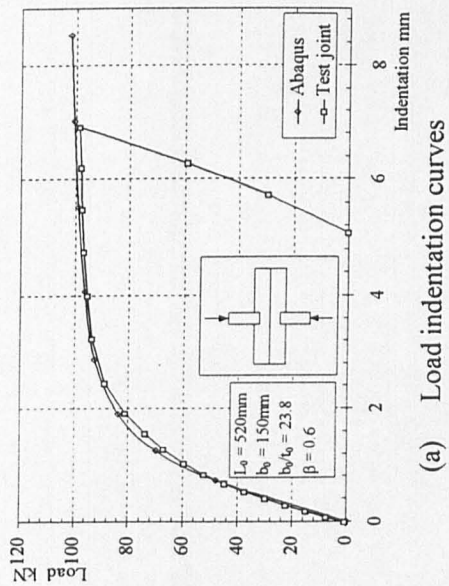


Figure 4.17 Validation curves for the diamond bird beak X joint $L_0=1000\text{mm}$

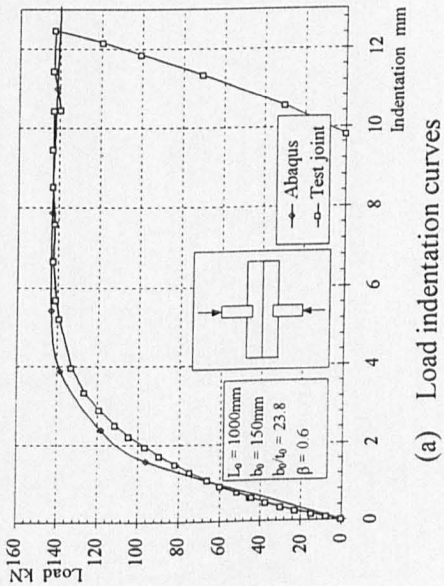
(b) Load lozenging curves



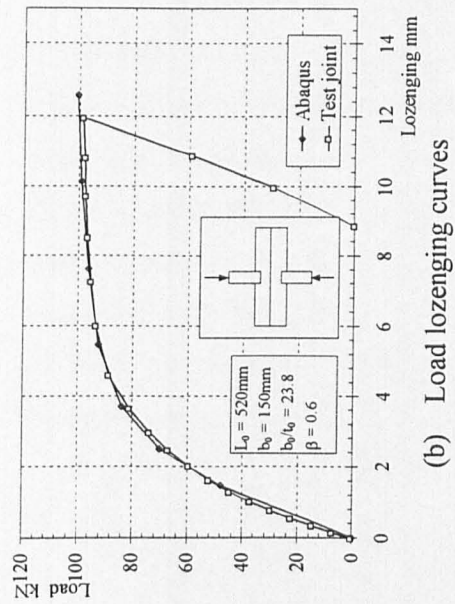


(a) Load indentation curves

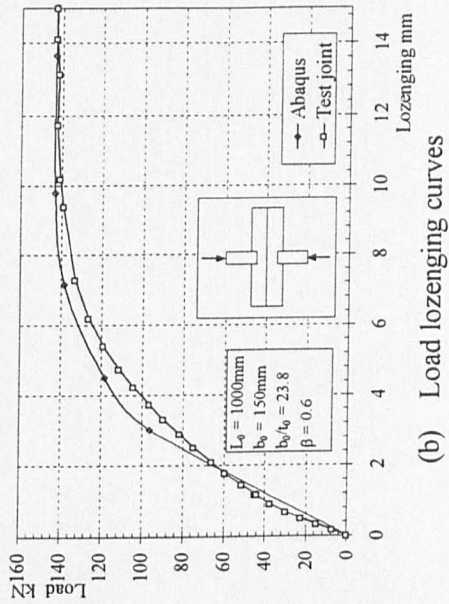
Figure 4.18 Validation curves for the square bird beak X joint $L_0=520\text{mm}$



(a) Load indentation curves



(b) Load lozengeing curves

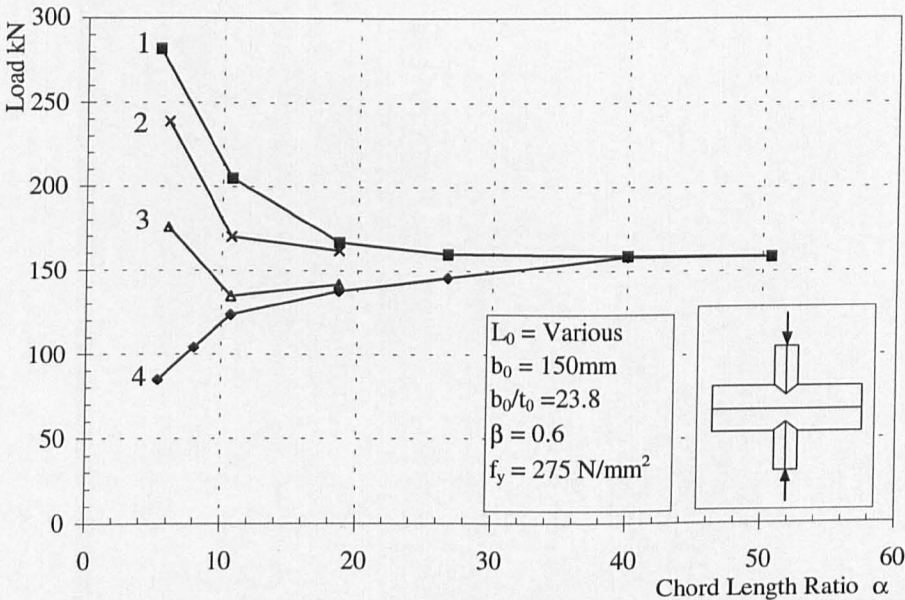


(b) Load lozengeing curves

Figure 4.19 Validation curves for the square bird beak X joint $L_0=1000$

The comparison between the finite element analyses and the experimental test joints is made in terms of the average indentation across the chord (by dividing the measured deflection by 2) and the lozenging of the chord.

The load/indentation and lozenging curves can be seen for the diamond bird beak X joint in Figure 4.16 and Figure 4.17, and for the square bird beak X joint in Figure 4.18 and Figure 4.19. Although the finite element models did not have any weld material modelled there is a very good correlation between the test joints and the finite element models. The joint capacity in most cases is correctly predicted and a good estimate of the stiffness of the joint is achieved. On the basis of the fair comparison of these results, it is considered that the finite element models are validated even though no welds were modelled and that they can be expected to give reasonable estimate of the physical joint capacity.



	Degree of freedom permitted to the nodes at the end of the chord
1	Encastré, i.e. no movement or rotation permitted
2	Freedom to move in the longitudinal direction of the chord
3	Freedom to move in the longitudinal direction of the chord and rotate about any axis
4	None i.e. complete freedom

Figure 4.20 The effect of length and boundary conditions on the joint capacity for the diamond bird beak X joint

Model	Chord				Brace		Boundary	Failure load
	L_0 mm	α $2L_0/b_0$	b_0 mm	t_0 mm	b_1 mm	t_1 mm	Condition	$F_{u,1}$ kN
B45V10	400	5.3	150	6.3	90	6.3	1	282.2
B45V17	800	10.6	150	6.3	90	6.3	1	205.0
B45V16	1400	18.7	150	6.3	90	6.3	1	167.0
B45V14	2000	26.7	150	6.3	90	6.3	1	160.3
B45V19	3800	50.7	150	6.3	90	6.3	1	158.5
B45V9	450	6.0	150	6.3	90	6.3	2	239.0
B45V30	800	8.0	150	6.3	90	6.3	2	170.0
B45V32	1400	18.7	150	6.3	90	6.3	2	162.3
B45V8	450	6.0	150	6.3	90	6.3	3	176.0
B45V31	800	8.0	150	6.3	90	6.3	3	134.8
B45V33	1400	18.7	150	6.3	90	6.3	3	142.5
B45V5	400	5.3	150	6.3	90	6.3	4	85.0
B45V12	600	8.0	150	6.3	90	6.3	4	104.5
B45V3	800	10.7	150	6.3	90	6.3	4	123.5
B45V7	1400	18.7	150	6.3	90	6.3	4	138.8
B45V2	2000	26.7	150	6.3	90	6.3	4	146.0
B45V15	3000	40.0	150	6.3	90	6.3	4	158.6
B45V4	3800	50.7	150	6.3	90	6.3	4	158.6
B45V1	6000	80.0	150	6.3	90	6.3	4	158.6
B45V34	450	6.0	150	6.3	90	6.3	5	85.3
B45V35	800	10.6	150	6.3	90	6.3	5	124.9
Boundary conditions at the nodes at the end of the chord								
1	Encastré, i.e. no movement or rotation permitted							
2	Freedom to move in the longitudinal direction of the chord							
3	Freedom to move in the longitudinal direction of the chord and rotate about any axis							
4	None i.e. complete freedom							
5	Symmetrical boundary conditions, i.e. restrained from moving in the longitudinal direction of the chord and rotating about the two axes perpendicular to this							

Table 4.3 The variation of joint capacity with chord length and boundary conditions for the diamond bird beak X joint

4.4 The numerical results for the diamond bird beak X joints

The main part of this investigation on bird beak joints has involved the diamond bird beak. The results of the finite element investigation are reported in this section and discussed in the next.

4.4.1 The effect of chord length L_0 and boundary conditions on the strength of diamond bird beak joints

During the initial investigations it was found that the chord length and the boundary conditions at the end of the chord had a significant effect on the joint capacity. This effect has also been observed in CHS joints (van der Vegte 1995). The results of the analyses for variation of chord length and the boundary conditions at the end of the chord are given in Table 4.3 and shown in Figure 4.20.

4.4.2 The effect of changing the chord width ratio β and the chord wall slenderness ratio on the strength of diamond bird beak joints

In this part of the investigation the chord length is kept constant $\alpha = 40$ ($L_0 = 3000\text{mm}$), whilst the parameters for chord slenderness b_0/t_0 , chord width ratio β , yield stress f_y and brace thickness t_1 are varied. The results of the finite element analyses are given in Table 4.4.

Model	Chord thickness	Chord slenderness ratio	Brace width	Chord width ratio	Yield stress	Joint capacity
	t_0 mm	$2\gamma = b_0/t_0$	b_1 mm	$\beta = b_1/b_0$	f_y N/mm ²	$F_{u,1}$ kN
6BETA3	4.25	23.8	45	0.3	400	88.9
6BETA4	4.25	23.8	60	0.4	275	69.9
6BETA6	4.25	23.8	90	0.6	275	83.0
6BETA8	4.25	23.8	120	0.8	275	110
BETA3	6.3	23.8	45	0.3	275	126
BETA4	6.3	23.8	60	0.4	275	135
BETA5	6.3	23.8	75	0.5	275	144
BETA6	6.3	23.8	90	0.6	275	158.5
BETA7	6.3	23.8	105	0.7	275	176
BETA8	6.3	23.8	120	0.8	275	200
BETA9	6.3	23.8	135	0.9	275	225
BETA10	6.3	23.8	150	1.0	275	336
1BETA5	6.3	23.8	75	0.5	400	198
1BETA9	6.3	23.8	135	0.9	400	310
1BETA3	10.0	15.0	45	0.3	400	369
1BETA6	10.0	15.0	90	0.6	400	472
1BETA4	12.5	12.0	90	0.4	400	540
2BETA3	10.0	15.0	45	0.3	275	261
2BETA5	10.0	15.0	75	0.5	275	310
2BETA7	10.0	15.0	105	0.7	275	367
2BETA9	10.0	15.0	135	0.9	275	462
4BETA3	12.5	12.0	45	0.3	275	386
4BETA5	12.5	12.0	75	0.5	275	446

4BETA7	12.5	12.0	105	0.7	275	526
4BETA9	12.5	12.0	135	0.9	275	649
5BETA5	16.0	9.4	75	0.5	275	676
5BETA7	16.0	9.4	105	0.7	275	814

Table 4.4 The finite element results of the parameter study, chord length $\alpha = 40$

The variation in the brace thickness t_1 and low width chord ratio β joints are considered separately in Table 4.6.

There is no restraint on the end of the chord in these analyses. However, this should not affect the joint capacity as can be seen in Figure 4.20 at $\alpha = 40$, that the boundary conditions no longer affect the joint capacity.

Model	Chord thickness	Yield stress	Joint capacity	$\frac{4 F_{u,1}}{t_0^2 f_y}$	$\frac{4 F_{u,1}}{t_0^{1.6} f_y}$
	t_0 mm	f_y N/mm ²	$F_{u,1}$ kN		mm ^{0.4}
6BETA3	4.25	400	88.9	49.22	87.80
6BETA4	4.25	275	69.9	56.29	100.41
6BETA6	4.25	275	83.0	66.84	119.23
6BETA8	4.25	275	110	88.58	158.01
BETA3	6.3	275	126	46.18	96.42
BETA4	6.3	275	135	49.47	103.30
BETA5	6.3	275	144	52.77	110.19
BETA6	6.3	275	158.5	58.09	121.29
BETA7	6.3	275	176	64.50	134.68
BETA8	6.3	275	200	73.30	153.04
BETA9	6.3	275	225	82.46	172.17
BETA10	6.3	275	336	123.14	257.11
1BETA5	6.3	400	198	105.54	104.16
1BETA9	6.3	400	310	165.25	163.09
1BETA3	10.0	400	369	53.67	92.69
1BETA6	10.0	400	472	68.65	118.56
1BETA4	12.5	400	540	78.55	94.92
2BETA3	10.0	275	261	37.96	95.36
2BETA5	10.0	275	310	45.09	113.26
2BETA7	10.0	275	367	53.38	134.09
2BETA9	10.0	275	462	67.20	168.80
4BETA3	12.5	275	386	35.93	98.69
4BETA5	12.5	275	446	41.52	114.03
4BETA7	12.5	275	526	48.97	134.48
4BETA9	12.5	275	649	60.42	165.93
5BETA5	16.0	275	676	38.41	116.43
5BETA7	16.0	275	814	46.25	140.20

Table 4.5 The normalised joint capacities of the parameter study

4.4.3 The effect of brace thickness t_1 on the strength of diamond bird beak joints

The effect of changing the brace thickness have been separated out from the main parameter study because the joint capacity is only affected at very low chord width ratios and the different nature of the failure which can be seen in Figure 4.22. The results of the finite element analyses are shown in Table 4.6.

Model	Chord thickness	Chord thickness ratio	Brace width	Chord width ratio	Brace thickness	Failure load
	t_0 mm	$2\gamma = b_0/t_0$	b_1 mm	$\beta = b_1/b_0$	t_1 mm	$F_{u,1}$ kN
BETA1	6.3	23.8	15	0.1	6.3	60.5
BETA2	6.3	23.8	30	0.2	6.3	123
2BETA1	10.0	15.0	15	0.1	5.0	48.0
2BETA2	10.0	15.0	30	0.2	6.3	118
3BETA1	6.3	23.8	15	0.1	5.0	48.0
3BETA5	6.3	23.8	75	0.5	5.0	144
3BETA7	6.3	23.8	105	0.7	5.0	173

Table 4.6 The finite element results of the parameter study for the change in brace thickness with the chord length L_0 constant ($\alpha = 40$)

4.5 Discussion of the results for the diamond bird beak X joint

Using the information from contoured stress plots, displaced shape diagrams and load/indentation curves the results given in Tables 4.3, 4.4 and 4.6 are examined and discussed to analyse the different forms of failure which may be occurring.

4.5.1 The presence of yield lines at the corners of the chord

The presence of yield lines at the corners of the chord is verified by the example shown in Figure 4.21 for joint B45V7 ($\alpha=18.6$), where the transverse stress across the chord are shown for three different levels through the thickness of the shell element. (Where the blue areas indicate a compressive stress, the green areas indicate low tensile or compressive stresses (approximating to zero) and the red areas a tensile stress.) Forming a stress block for the different stress levels shown for the three different levels reveals the presence of a plastic or elasto-plastic hinge, an example of which is also shown in Figure 4.21 for the top corner of the chord

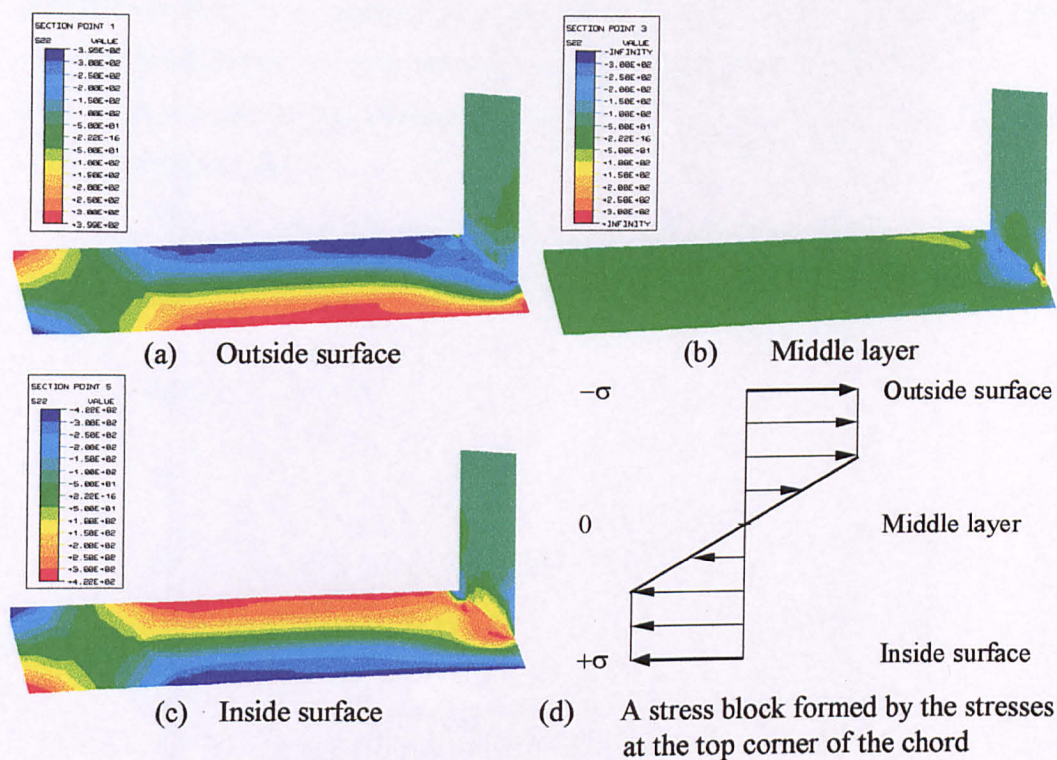


Figure 4.21 Transverse stress in B45V7 at maximum load (138.8 kN) showing the presence of yield lines

4.5.2 The effect of changing the chord width ratio β and the chord wall slenderness ratio on the strength of diamond bird beak joints

The effect of changing the brace width ratio β , chord wall slenderness b_0/t_0 and the yield stress f_y are considered in this section. The effect of changing the brace wall thickness is considered separately in the next section. The chord length ratio $\alpha = 40$, so the asymptotic strength of the joint is observed, removing any influence caused by the chord length and the boundary conditions at the end of the chord. The results of the investigation are given in Table 4.4.

The effect of the variation of the chord width ratio β on the joint capacity is illustrated by a series of finite element analyses carried out for the diamond bird beak joint where $b_0/t_0 = 23.8$ shown in Figure 4.22. Examination of Figure 4.22 reveals that there are three different regimes of failure, when $\beta \leq 0.2$, $0.2 \leq \beta \leq 0.9$ and $\beta \geq 0.9$. For the range $0.2 \leq \beta \leq 0.9$ the failure mechanism is the same as that examined previously, a general plasticification of the chord walls. For the nearly full width joint, when $\beta \geq 0.9$ the increase in the joint capacity is attributed to the crushing of the brace

members as they are compressed together. The toe of the brace shows considerable yielding and deformation as the brace members transfer the axial load directly to each other. This is a very complex failure mechanism and no further work has been done to estimate design guidance.

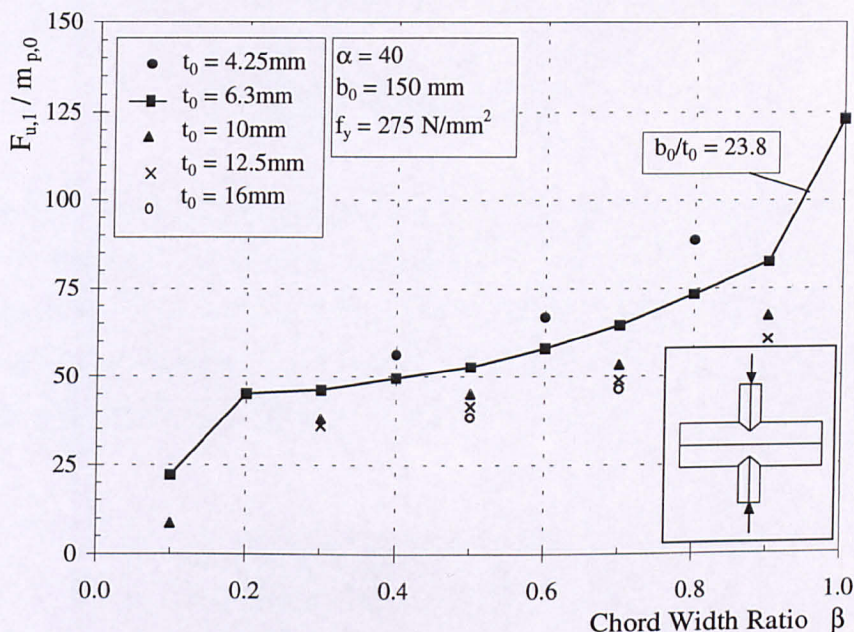


Figure 4.22 The variation of the joint capacity with chord width ratio β and chord wall thickness, normalised by the plastic moment capacity per unit length of the chord wall m_p

Figure 4.22 shows the variation of the normalised joint capacity with chord width ratio β for all the results where the yield stress $f_y = 275 \text{ N/mm}^2$. (N.B. some of the results from Table 4.6 have been included into this figure to demonstrate the change in behaviour at low chord width ratio values β .) These results are normalised against the chord wall plastic moment capacity per unit width $m_p = t_0^2 f_y / 4$, with the values given in Table 4.5, on the assumption that the failure mechanism is principally dependent on chord wall flexure. The spread of the results in Figure 4.22 suggests that this assumption is not correct as it can be seen that increasing the chord wall thickness decreases the non-dimensional strength. It was observed that if the chord thickness t_0 is raised to the power 1.6 then all the results converge to a single curve in the range $0.2 \leq \beta \leq 0.9$. This is a clear indication that the failure mechanism cannot be attributed to a single mode of failure, but is a combination of different modes such as membrane or shear yielding ($f(t_0)$), plastic failure of the chord wall ($f(t_0^2)$) and possibly the rotational stiffness of the chord wall ($f(t_0^3)$).

4.5.2.1 The variation of the joint capacity with the chord width ratio β and chord wall slenderness b_0/t_0

Analysing the results from the range $0.2 \leq \beta \leq 0.9$ and $9.4 \leq b_0/t_0 \leq 35.3$ the expected joint capacity for a diamond bird beak X joint is given in Newtons by

$$F_{u,1} = \frac{2.6}{1-0.6\beta} 275 \left(\frac{f_y}{275} \right)^{0.8} t_0^2 \left(\frac{b_0}{t_0} \right)^{0.4} \quad \text{Eqn 4.3}$$

The fit of the predicted joint capacities by Eqn 4.3 against the normalised results can be seen in Figure 4.23. Where the curve has been normalised by $t_0^{1.6}$ (representing the influence of the chord wall thickness t_0 and $275(f_y/275)^{0.8}$ (representing the influence of the change in yield stress f_y). These are based on 25 sets of data points, yielding a mean of 1.029, with a Coeff. of Correlation of 1.000 and a Coeff. of Variation of 0.0704.

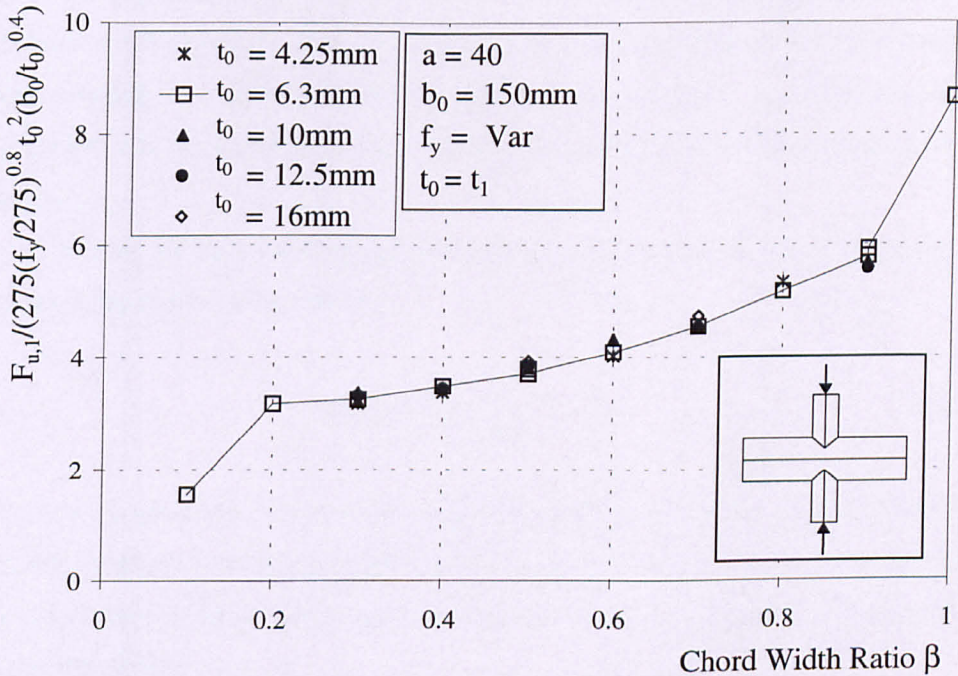


Figure 4.23 The fit of the predicted joint capacities against the normalised results

4.5.3 The effect of changing the brace thickness t_1 on the strength of diamond bird beak joints

For joints with a very low chord width ratio, $\beta \leq 0.2$, the failure mechanism is much simpler to understand than those studied previously. With the low chord width

ratio of the brace member it may be expected that failure could be attributed to punching shear of the chord, in which case the joint capacity could be estimated as follows (where $4\sqrt{1.5} b_1 t_0$ is the perimeter of the brace on the chord and $\frac{1}{\sin 45^\circ}$ allows of the inclination of the chord wall thickness).

$$F_{u,1} = \frac{4\sqrt{1.5} b_1 t_0}{\sin 45^\circ} \frac{f_y}{\sqrt{3}}$$

$$F_{u,1} = \frac{\sqrt{8} b_1 t_0 f_y}{\sin 45^\circ} = \sqrt{16} b_1 t_0 f_y \quad \text{Eqn 4.4}$$

However, examination of Table 4.7, which shows the punching shear capacity of the chord wall, the brace shear capacity and the joint failure load, reveals that for $\beta = 0.1$ and for $t_0 = 6.3$ (3BETA1) and 10mm (2BETA1) the joint capacity is 48.0 kN in both cases. Clearly then these results are either wrong or there is a different failure mechanism operating as Eqn 4.4 has a term for t_0 although the joint capacity does not change.

In fact the joint capacity is determined by shear of the brace member and the joint capacity can be estimated by

$$F_{u,1} = 4 b_1 t_1 \frac{f_y}{\sqrt{3}} \quad \text{Eqn 4.5}$$

and given the same values for t_0 and t_1 , Eqn 4.5 gives a lower joint capacity. Therefore punching shear of the chord (as predicted in Eqn 4.4) is unlikely to occur as the chord wall thickness should always be greater than the brace wall thickness (as advised by Packer et al 1992).

Model	Chord thickness	Chord punching shear capacity	Brace width	Brace thickness	Brace shear capacity	Failure load
	t_0	shear capacity	b_1	t_1	capacity	$F_{u,1}$
	mm	kN	mm	mm	kN	kN
BETA1	6.3	120.1	15	6.3	60.0	60.5
BETA2	6.3	240.1	30	6.3	120.0	123
2BETA1	10	190.5	15	5.0	47.6	48.0
2BETA2	10	381.0	30	6.3	120.0	118
3BETA1	6.3	120.1	15	5.0	47.6	48.0
3BETA5	6.3	599.9	75	5.0	300.0	144
3BETA7	6.3	840.2	105	5.0	420.0	173

Table 4.7 A comparison between the chord punching shear capacity and the brace capacity to the joint capacity

The question of why should the brace fail in shear still remains? This can be answered when the deformation of the joint is considered. As a compressive load is applied to the chord by the brace members the chord lozenges (i.e. flattens and widens). If the chord and the brace were not attached and the chord is free to deform without restraint from the brace member, then the projected shape of the brace on the chord changes. This is shown in Figure 4.24, where the drawing on the right shows both the original and the deformed outlines of the brace on the chord.

In a joint where the brace and the chord are attached, the brace acts to restrain the deformation of the chord and it is this action which causes the shearing of the brace. This is confirmed by finite element analyses where the brace thickness has been varied, shown in Table 4.7 where all the results shown agree very closely with the predicted shearing of the brace values. The only exceptions are the larger width ratio joints (3BETA5 and 3BETA7) where the strength of the joint is almost independent of the brace thickness. This can be seen by comparing joints BETA5 (144 kN) and BETA7 (176 kN) given in Table 4.4, with 3BETA5 (144kN) and 3BETA7 (173kN) given in Table 4.7, where the only difference is the brace thickness t_1 .

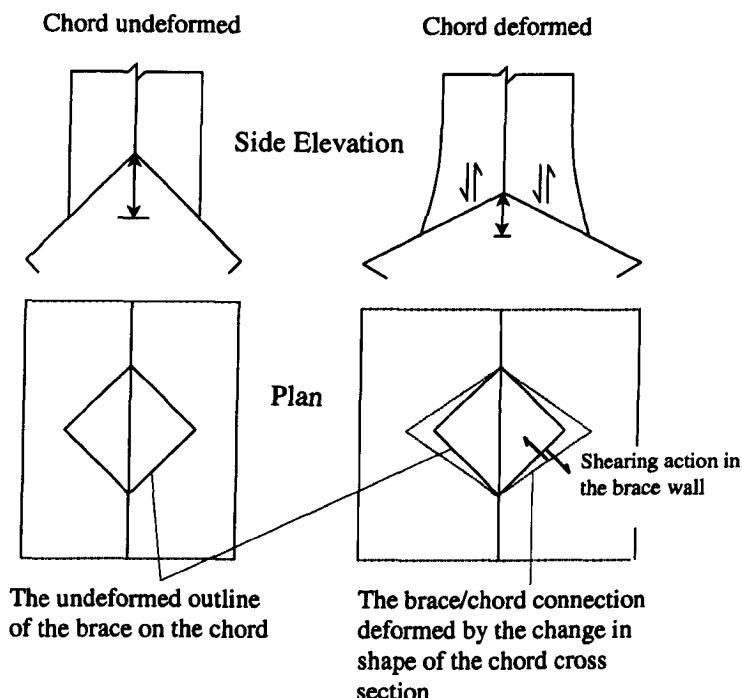


Figure 4.24 The cause of the shear action in the brace

In the series of finite element analyses where the variation of the joint capacity with the width ratio β is observed the brace wall thickness is maintained at $t_1 = 6.3\text{mm}$, unless otherwise stated, so that the effect of the restraint of the brace on the chord remains constant for the size of the section. This has led to some theoretical stocky sections being used for the brace member. Should more realistic (of normal slenderness) sections be used, then shearing of the brace member would be more likely to occur. It is therefore recommended that all brace members should be checked to ensure that their shear capacity is greater than the joint capacity and not to rely on shear failure only occurring at a value of $\beta \leq 0.2$.

4.5.4 The effect of chord length L_0 and boundary conditions on the strength of diamond bird beak joints

Examination of Figure 4.20 shows that the variation of joint capacity with chord length for the diamond bird beak X joints can be divided into three different groups according to the chord length:

- short joints ($5 \leq \alpha < 10$) where the rate of change of joint capacity with chord length is rapid and uniform

- medium joints ($10 \leq \alpha < 40$) where the rate of change of the joint capacity with chord length is approximately uniform and with a lower rate of change than the short joints
- long joints ($\alpha \geq 40$) where the joint capacity is constant with increasing chord lengths

Figure 4.20 shows four different boundary conditions applied to the ends of the chord and the increase in the joint capacity observed as more restraint is applied to the ends of chord can be clearly seen. The intermediate boundary conditions (2 & 3) are not chosen to represent any particular physical condition, but to show how the joint capacity observed may vary between the extremes of fully encastred and complete freedom.

Figure 4.25 shows the simplified behaviour of the failure of the chord when there is no restraint at the end of the chord. When $\alpha < 10$ there is an overall crushing of the chord and when $\alpha > 10$ there is only lozenging of the chord at the centre line of the joint. (This form of behaviour can be seen in the displaced shape diagrams in Figure 4.26 and Figure 4.29.) It is therefore concluded that when $\alpha > 10$ the chord can support the load applied to the brace without a failure of the end of the chord in a crushing mode.

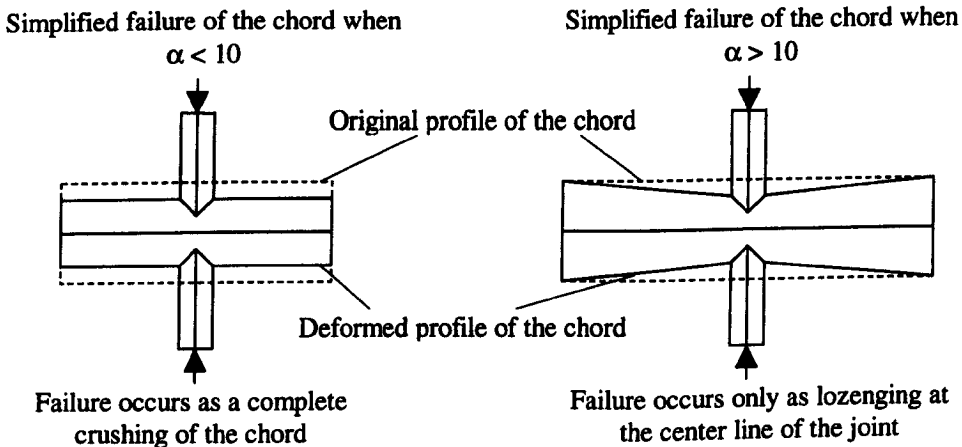


Figure 4.25 The deformation apparent in the failure of the chord with no restraint at the ends

The increase in joint capacity for short chord length joints ($\alpha < 10$), when the ends of the chord are held encastred is due to the restraint offered by the support conditions resisting the overall crushing of the chord (example shown in Figure 4.27)

and the membrane action in the chord walls caused by the deformation of the joint as the brace members are forced into the chord. This effect is most pronounced in short chord lengths ($\alpha = 5.3$), decreasing as the chord length increases. At $\alpha = 10.6$ the encasté boundary conditions at the end of the chord no longer resist the overall crushing of the chord as the chord can support the load without a crushing failure when there is no restraint at the ends of the chord.

The decrease in the joint capacity when $\alpha = 10.6$ for boundary condition 3, which then increases as the chord length increases is again attributed to the influence of the boundary conditions at the shorter chord lengths. When the chord length $\alpha < 10$, the joint capacity is increased as the ends of the chord are prevented from being crushed by the boundary conditions. When the chord length is $\alpha > 10$ the fact that ends of the chord are prevented from being crushed is no longer important as the models with no restraint (i.e. boundary condition 4) no longer exhibit any crushing at the end of the chord. Thus the joint capacities for boundary conditions 3 & 4 are very similar at this and larger chord lengths. A similar trend of the joint capacity decreasing and then increasing again with increasing chord length can be seen later in Chapter 6 in Figure 6.25 for CHS T joints (when load by the method shown in CHS3) and Figure 6.31 for diamond bird beak T joints.

Models were analysed with symmetrical boundary conditions (i.e. with the nodes restrained from moving in the longitudinal direction of the chord and rotating about the two axes perpendicular to this) at the end of the chord to represent the presence of an identical joint a chord length away from the analysed joint. (Note that there is no restraint preventing the cross sectional deformation of the chord.) With these chord end conditions, there was a minimal increase in the joint capacity when compared to joints where there is no restraint at the ends of the chord. (These results shown in Table 4.3, are not shown in Figure 4.20 as results are virtually coincident with each other).

At chord length of $\alpha > 10$ the boundary conditions at the end of the chord still affect the joint capacity although to a lesser extent. Although Figure 4.25 assumes that there is no deformation at the end of the chord this is only due to the simplification. At a chord length of $\alpha = 18.6$, Figure 4.20 shows that the restraint offered by boundary condition 3 in resisting the cross sectional deformation at the end of the chord is

minimal, so that the increase in joint capacity for boundary condition 2 must come from resisting the rotation of the nodes at the end of the chord.

4.5.4.1 Displaced shape diagrams and contoured stress plots

The contoured stress plots of the models where the ends of the chord have no restraint and chord length ratio $5 < \alpha < 10$, an example shown in Figure 4.26, indicates that yielding occurs at the corners of the chord for the entire length of the chord,. This is consistent with the deformed shape diagrams, where the faces of the chord can be seen to have rotated, causing the crushing of the chord and it is reasonable to assume that the joint capacity is a direct function of the length of the plastic hinge and the angle of rotation of the hinge. This is the reason why the rate of increase in joint capacity is rapid and uniform in Figure 4.20 for short chord length joints with no restraints at the ends of the chord. The contoured stress plot where the ends of the chord are held encastré (shown in Figure 4.27), reveals the wide spread yielding of the chord walls particularly at the end of the chord caused by the restraint of the boundary conditions resisting the deformation of the joint.

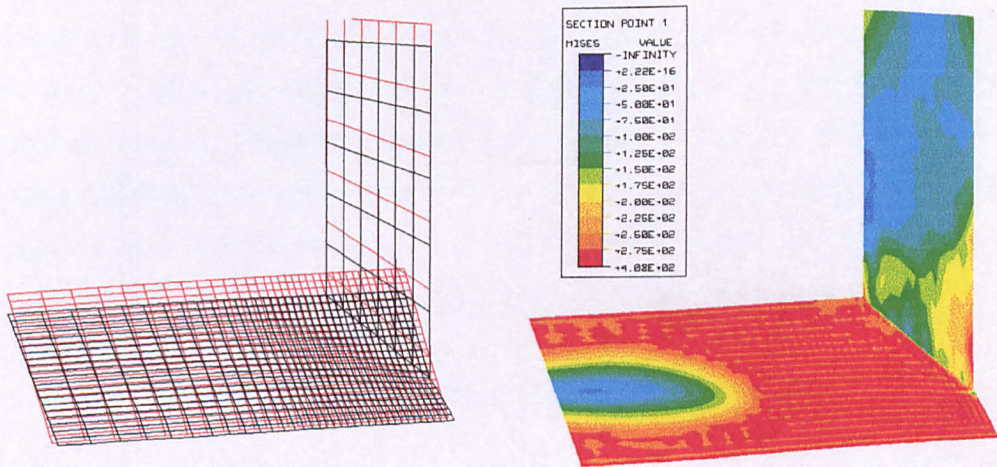


Figure 4.26 The deformed shape and von Mises contoured stress plot (outside surface, maximum load) of a X joint B45V12 where $\alpha = 8$ and there is no restraint at the end of the chord

The widespread yielding of the chord wall material in the vicinity of the brace member, common to both cases, is due to the presence of the brace member stiffening the chord wall locally and the deformation of the material in this area that is required, so that compatibility is maintained with the deformed shape of the rest of the chord.

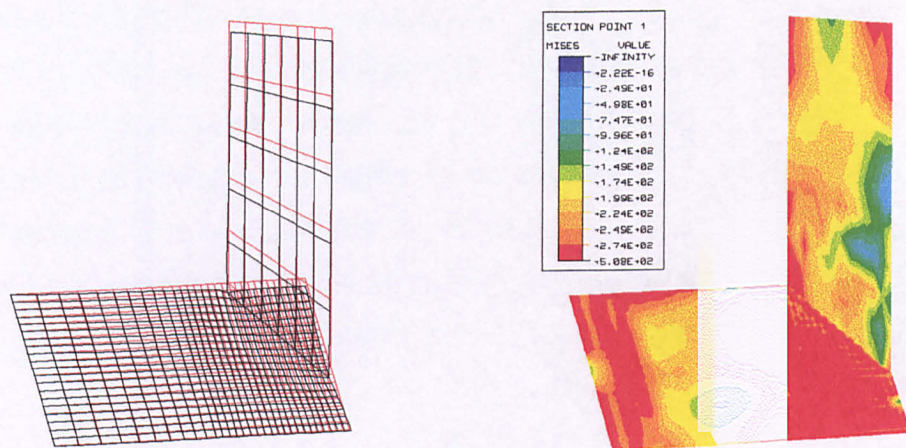


Figure 4.27 The deformed shape and von Mises contoured stress plot (outside surface, maximum load) of a diamond bird X joint B45V10 where $\alpha = 5.33$ and the ends of the chord are held encastré

For the medium length joints where $10 < \alpha < 40$ the displaced and contoured stress plots are shown just prior to and at maximum load in Figure 4.29. In the contoured stress plots the yield lines can be identified at the corners of the chord section but there is an interesting phenomenon in the stress distribution at the end of the chord, where there appears to be a different form of mechanism operating. Examination of the displaced shape diagram shows that this part of the chord is actually deformed in the opposite sense to the rest of the model having passed through a point of zero deformation, where the original cross section shape of the chord is maintained. Figure 4.28 shows the exaggerated deformation of the three cross sections from Figure 4.29c.

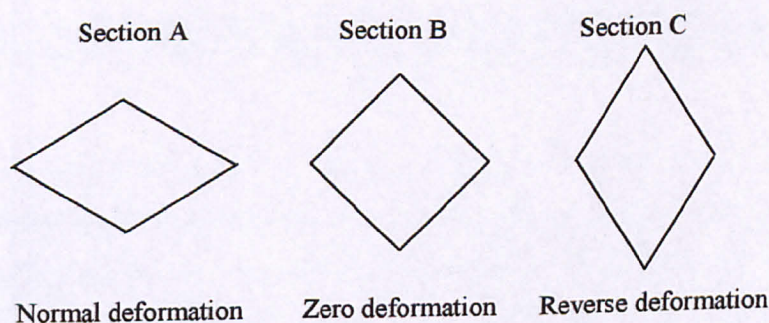


Figure 4.28 Three cross section of the chord shown in Figure 4.29c

Comparing the diagrams just before the maximum load and at the maximum load, it can be seen that a large amount of deformation occurs for a very small load

step. The yield lines have not increased in length and the stress concentration at the end of the chord has increased dramatically. The reason for this is that just before the maximum load the plastic mechanism, i.e. in-plane yielding in the vicinity of the brace and the yield lines at the corners of the section, is fully developed and no further increase in the joint capacity can be obtained from this mechanism. The small increase in the joint capacity observed comes from the deformation at the end of the chord in resisting the deformation caused by the plastic mechanism to maintain continuity.

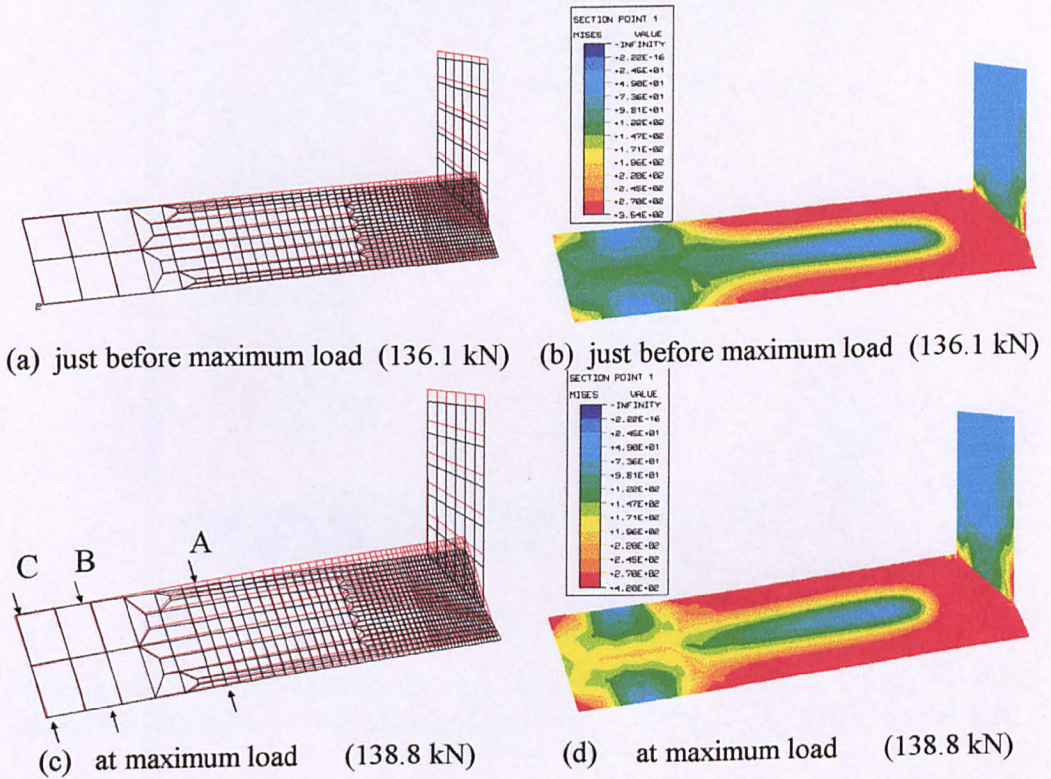


Figure 4.29 The deformed shape and von Mises contour stress plot of the outside layer of a diamond bird beak X joint B45V7, where $\alpha = 18.7$ and there is no restraint at the end of the chord

In the long joints, where $\alpha > 40$ ($L_0 = 3000\text{mm}$) the joint strength is constant with increasing chord length, referred to as the asymptotic joint strength and the effect of the boundary conditions at the end of the chord is no longer important. Regrettably due to the size of the model not much detail can be shown. The deformed shape diagram shown in Figure 4.30 reveals that most of the deformation is confined to the first 900mm from the brace member. The contoured stress plots display the same form of yielding pattern seen in the previous contoured stress plots shown in Figure 4.29, although the stress distribution is not confused by the presence of the end of the chord.

of yielding pattern seen in the previous contoured stress plots shown in Figure 4.29, although the stress distribution is not confused by the presence of the end of the chord.

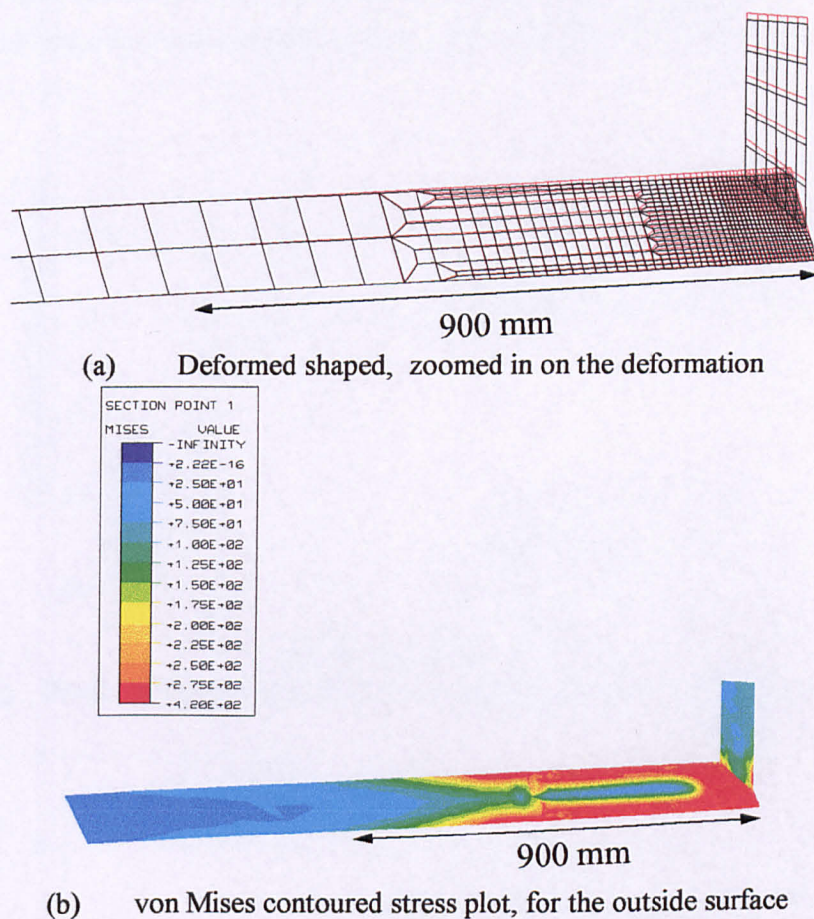
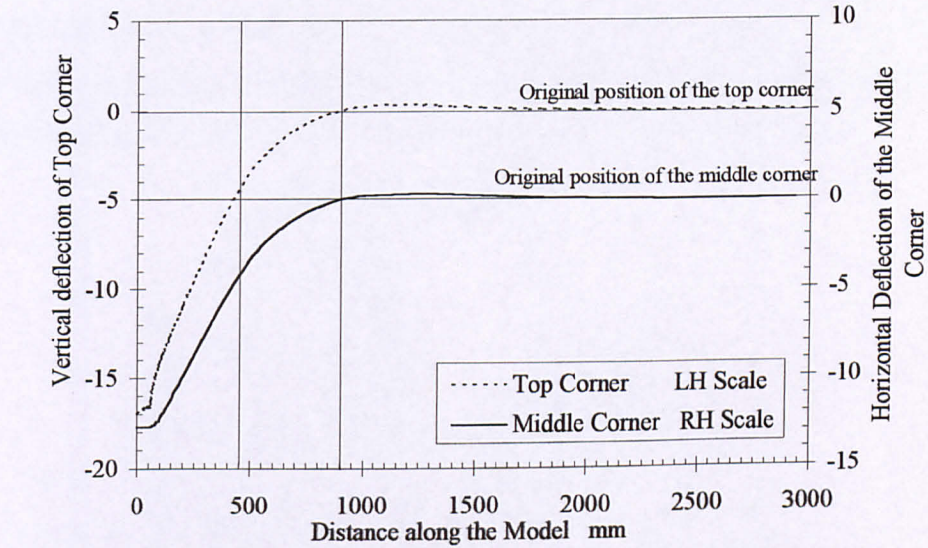


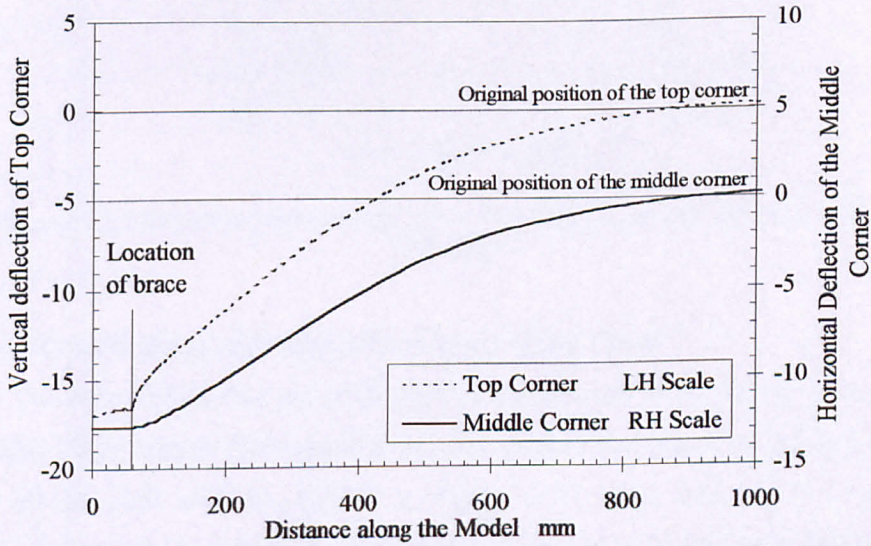
Figure 4.30 Deformed shape and von Mises contour stress plot of a long diamond bird beak X joint B45V15 where $\alpha = 40$ and at maximum load of 158.6kN. There is no restraint at the end of the chord

Figure 4.31 shows the vertical and horizontal deformation of the top and middle corners of the chord respectively along the length of the chord. The deformation of the top corner of the chord is considerable at the brace member and for the next 50mm. At the brace there is a considerable discontinuity in the rate of indentation indicating local failure possibly due to punching shear. The stiffness of the corners of the chord and brace attract a larger proportion of the axial load transmitted from the brace to the chord. This can be verified by examining all the contoured stress plots where the stress concentration at the corners of the brace member indicates a significantly greater extent of yielding than the rest of the brace member. It is interesting to note that there is a clear change in the gradient of the slope at a point

approximately 450mm ($3b_0$) along the chord from the centre line. The middle corner of the chord exhibits a smooth curve all the way along the length to the point where no deformation occurs, with a similar change in the gradient at 450mm from the centre line.



(a) Profile of the corners of the chord along the entire length of the joint



(b) The deformed profile of the corners of the chord for the 1st 1000mm

Figure 4.31 Deformed profile of the top and middle corners of the chord for the joint B45V1

At a distance of 900mm ($6b_0$) a point of zero deformation is reached, after which the deformation can clearly be seen to be reversed, tending towards zero as the chord length increases. Examining the data for the deformation reveals that the

deformation continues to oscillate between positive and negative deformation, although this effect is too small to be seen in the figure.

Figure 4.32 shows the deformation of the chord wall for the joint B45V1 at the last load measured (151.5kN), at different cross sections along the length of the chord from the centre line of the joint. The restraint offered by the brace member on the chord wall can clearly be seen in the first three cross sections and the twisting nature of the deformation of the remainder of the chord wall in the other cross sections.

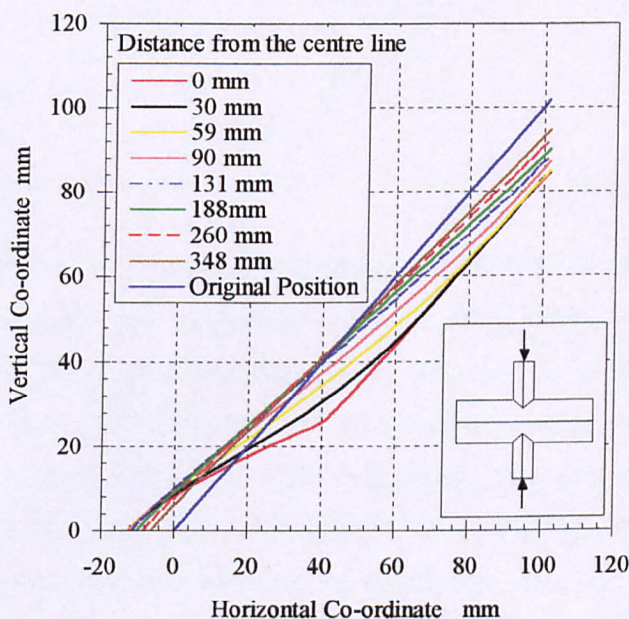


Figure 4.32 Cross section deformation of the chord in joint B45V1 at last recorded load (151.5 kN)

4.5.4.2 Moment along the hinge at the corner of the chord

In order to calculate the magnitude of the moment at the middle corner along the length of the chord, the transverse stresses (across the chord) at the five different levels in the shell element, shown in Figure 4.33, were summed up using the relationship expressed in Eqn 4.6. The basis of the formulation of this equation is only approximate. However, if it is simplified it then approximates to the elastic and plastic chord wall moment capacities of $t_0^2 f_y / 6$ and $t_0^2 f_y / 4$ respectively.

Due to the nature of the finite element program ABAQUS, the stresses at the different levels can only be obtained at the integration points rather than the nodes. The exact position of the integration points is not known however, it is thought that

they lie close to the edge of the elements. The information used to plot Figure 4.34 is derived from the integration points closest to the corner of the chord.

$$M = \frac{3}{64}(\sigma_1 + \sigma_2)t_0^2 + \frac{1}{48}\sigma_2 t_0^2 - \frac{1}{48}\sigma_4 t_0^2 - \frac{3}{64}(\sigma_4 + \sigma_5)t_0^2 \quad \text{Eqn 4.6}$$

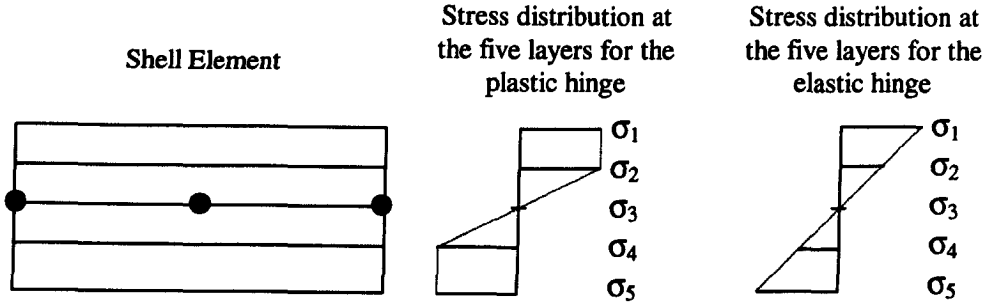


Figure 4.33 The stress distribution through the shell element

Figure 4.34 shows the magnitude of the moment acting along the middle corner of the chord for joint B45V15. The plastic and elastic moments (2728 N/mm² and 1819 N/mm² respectively) are drawn on the figure to provide a reference which define the type of moment acting in the chord wall, plastic, elasto-plastic or elastic.

Considering the chord between 0 - 450mm (3b₀) from the centre line of the brace where a plastic moment is acting in the chord wall, the value of the moment (approx. 2950 N/mm²) is above the plastic moment because of a von Mises effect which allows the stress to reach a maximum value of 317.5 N/mm² when the yield stress is 275 N/mm².

When considering the deflected profile of the top and middle corners of the chord shown in Figure 4.31, it was noted that at 450mm (3b₀) there was a distinct change in the profile of the deformed section. Examination of Figure 4.34 reveals that this is also the limit of the plastic hinge. The influence of the corner of the brace can be seen by the small reduction in the moment acting at the corner of the chord directly below it. An elasto-plastic moment is acting in the chord wall between 450 - 600mm (3 - 4 b₀) from the centre line of the brace. The rate of decrease in the magnitude of the moment acting in the chord wall is approximately uniform between plastic moment capacity and zero, at 400 and 900mm (2.7 - 6 b₀) respectively. There is an elastic moment acting in the chord wall from 600mm to the end of the chord, positive between 600 - 900mm (4 - 6 b₀) and negative between 900 - 1500mm (6 - 10 b₀).

This agrees with Figure 4.31 where the point of zero deformation was noted to be at 900mm (6 b_0) and the deformation of the section reversed thereafter.

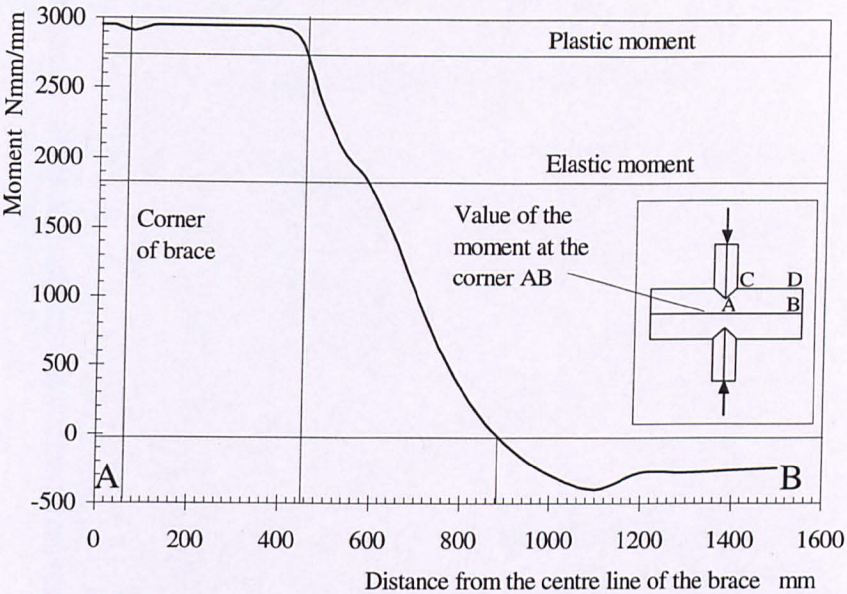


Figure 4.34 The magnitude of the moment along the middle corner of the chord of the joint B45V15 at maximum load 158.5kN

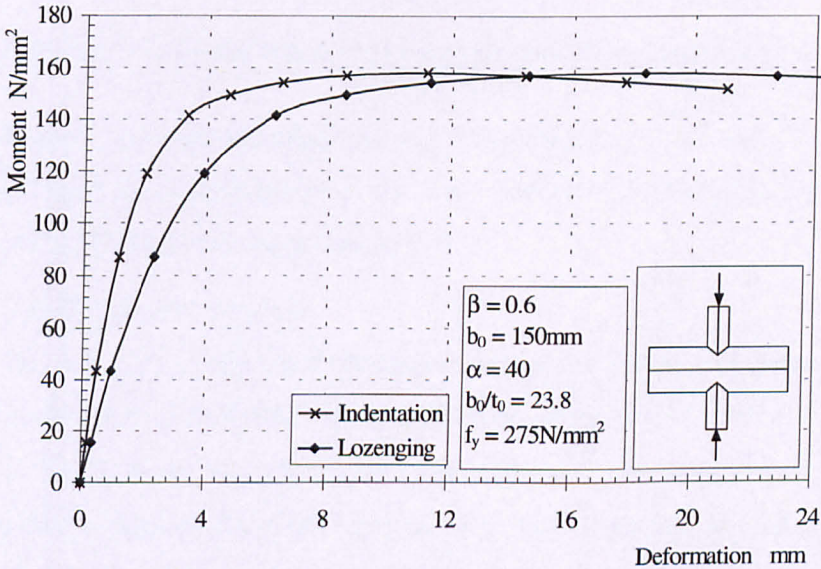


Figure 4.35 A comparison between the load/indentation curve and load/lozenging curve for the joint B45V15

4.5.4.3 Load/lozenging curves

When the load/indentation and the load/lozenging curves shown in Figure 4.35 and the relationship between the indentation and the lozenging shown in Figure 4.36 are compared it is revealed that there is not a constant relationship between the

indentation and the lozenging. Figure 4.36 shows the relationship between the theoretical value of the lozenging and the observed value of the lozenging, where the theoretical value has been calculated by simple geometry.

$$\text{Lozenging} = 2 \sqrt{b_0^2 - \left(\frac{b_0}{\sqrt{2}} - \text{indentation} \right)^2} \quad \text{Eqn 4.7}$$

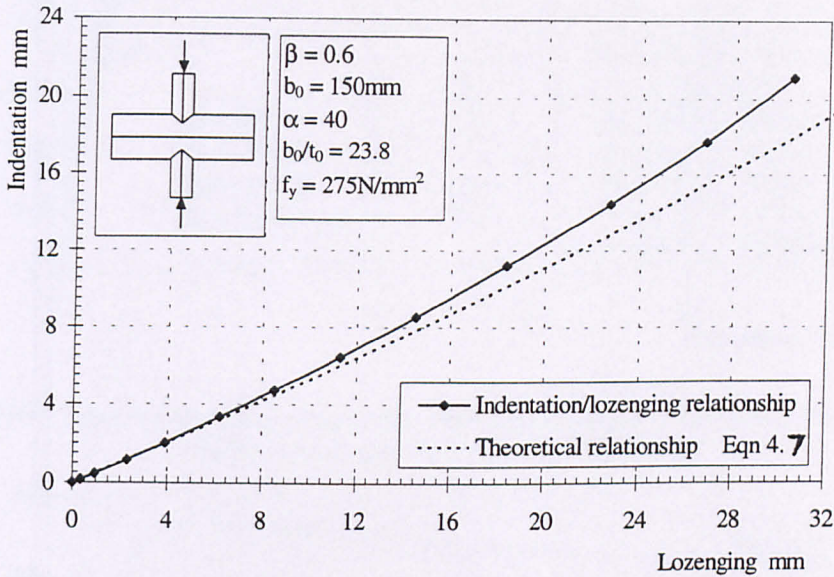


Figure 4.36 The relationship between the indentation and the lozenging at the centre line of the joint B45V15

The difference between the observed and theoretical values of the lozenging are attributed to the restraining action of the brace and the Z shaped deformation of the chord walls, which can be seen in Figure 4.32.

4.5.4.4 Load/indentation curves

The variation in the load/indentation curves for joints with different chord lengths where there is no restraint on the end of the chord can be seen in Figure 4.37. All the curves show the same approximate initial stiffness, although when $\alpha = 80$ there is a marginal increase in the initial stiffness. It is very noticeable that when $\alpha < 10.6$ none of the curves reach a maximum load, but continue to gain strength due to the presence of the brace member restraining the lozenging of the chord. When $\alpha \geq 10.6$ all the curves reach a maximum load, although the curve shape differs considerably. At $\alpha = 10.6$ failure occurs rapidly, possibly due to the formation of the plastic hinges at the corners of the chord section, whereas when $\alpha = 80$ the failure occurs gradually and at a much larger indentation than for the shorter joints.

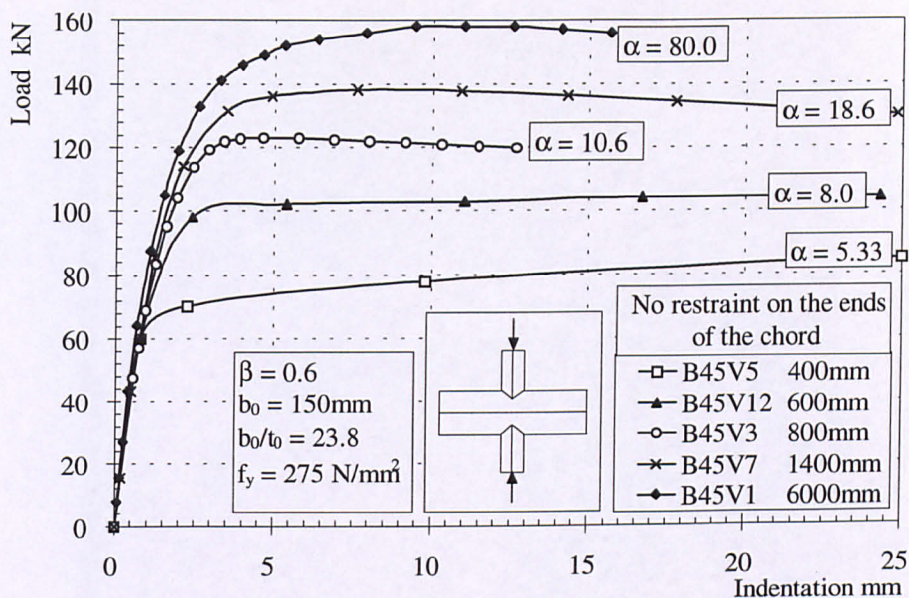


Figure 4.37 Load indentation curves for the diamond bird beak X joints of different chord lengths and no restraint on the chord ends

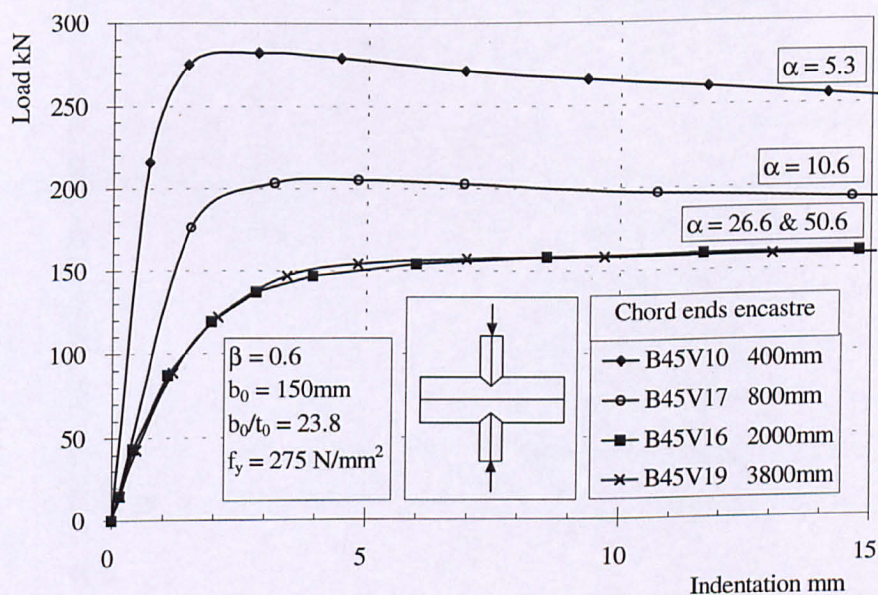


Figure 4.38 Load/Indentation curves for the Diamond bird beak X joint, chord ends held encastré

Figure 4.38 shows the load/indentation curves when the ends of the chord are held encastré. The encastré end conditions stiffen the models considerably and increases the joint capacity. In the short model $\alpha = 5.3$ (joint B45V10) where this effect is most pronounced, it can be seen that this curve reaches a maximum, has the highest initial stiffness and the largest joint capacity. This is completely the opposite

to the curves in Figure 4.37 for the chord length of $\alpha = 5.3$ (joint B45V5) which did not reach a maximum and had the lowest joint capacity. As the chord length increases so the initial stiffness and the joint capacity decrease until the asymptotic strength is attained when the curve for the load/indentation is almost identical to those curves for similar length joints when the ends of the chord have no restraint.

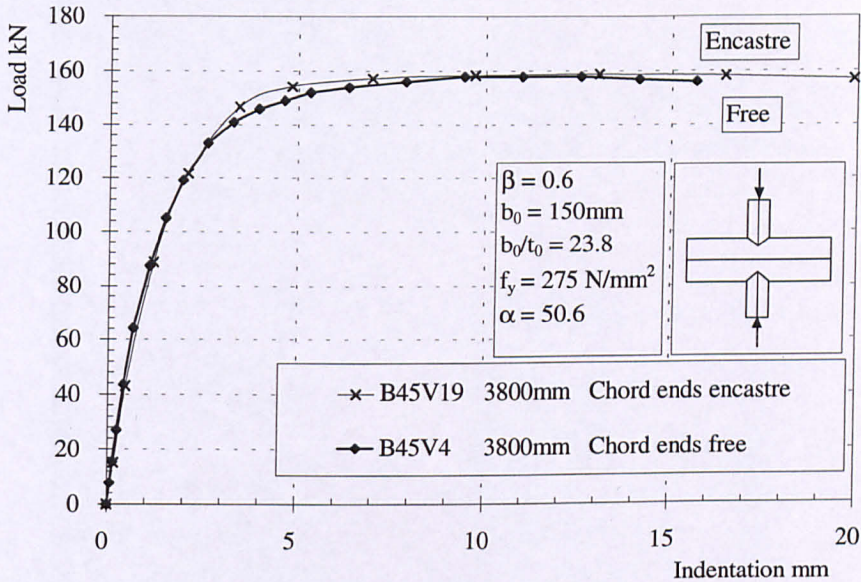


Figure 4.39 A comparison between long diamond bird beak X joints of the same length with different chord end boundary conditions

A comparison of these long joints with different chord end conditions is shown in Figure 4.39. The load/indentation curves are very nearly identical. However, there is a distinct increase in stiffness before and after the maximum load in the model where the ends are held encastré. This shows that the boundary conditions at the end of the chord may still affect the behaviour of the joint even through the joint capacity is constant.

4.5.4.5 Determining the joint capacity when the chord length is varied for the diamond bird beak X joint

It is appreciated that the range of data is very limited however, for the joints analysed in this section, the variation of joint capacity with chord length can be predicted as:-

for no restraint at the end of the chord

$$F'_{u,1,\text{length}} = F_{u,1,\text{asymptotic}} - 124.7e^{-0.106\alpha} \quad \text{Eqn 4.8}$$

and for the ends of the chord encastré

$$F'_{u,1,length} = F_{u,1,asymptotic} + 334.4e^{-0.186\alpha} \quad \text{Eqn 4.9}$$

where the asymptotic strength $F_{u,1,asymptotic}$ is determined by Eqn 4.3

when $\beta = 0.6$, $b_0 = 150\text{mm}$ $t_0 = 6.3\text{mm}$ and $f_y = 275\text{N/mm}^2$

The fit of these predictions against the finite element results can be seen in Figure 4.40

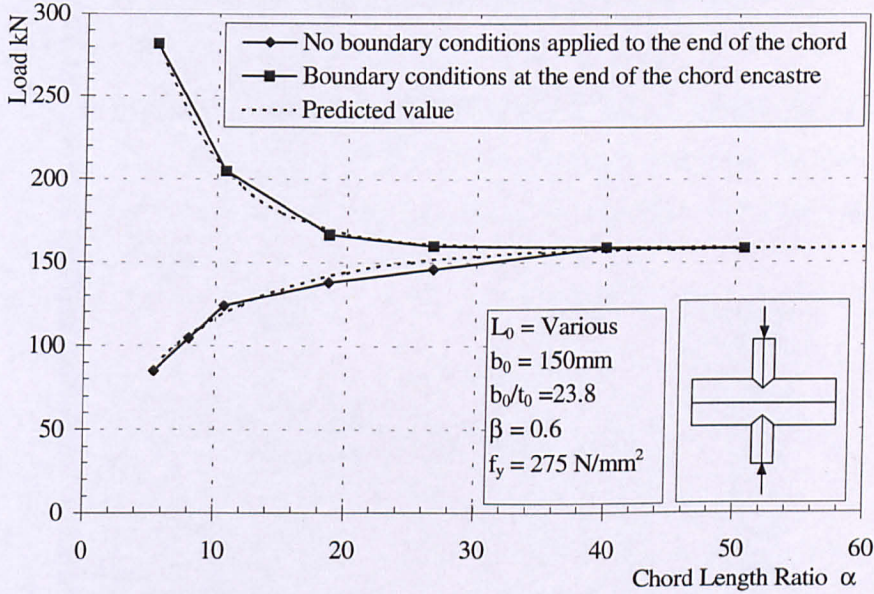


Figure 4.40 The predicted joint capacity against chord length for the diamond bird beak X joint

4.5.4.6 Comparisons with the work of Ono, Iwata and Ishida

The work carried out by Ono et al (1991) and Ishida (1993) was on T joints where $\alpha = 6$ (i.e. very short to prevent chord failure by bending). No reference is made to the method of supporting the joint during the test, although it appears from the drawings shown in Figure 2.5 that the ends of the chord are supported in some sort of cradle. The minimum restraint on the chord imposed by this form of support would be similar to boundary condition 3 describe in Figure 4.20, although there are likely to be additional restraints imposed by the support in addition to this. Should the same behaviour that has been observed in the X joints, i.e. the joint capacity is increased for a short chord lengths and additional restraints on the end of the chord, then it is possible that Ono et al (1991) may have overestimated the strength of the bird beak T joints that they have tested.

4.6 The numerical results for the square bird beak X joints

The use of a hybrid joint such as the square bird beak joint is considered a possibility in a structure where the traditional and bird beak configurations interconnect. As a hybrid joint, the square bird beak X joint has not been studied in as great a detail as the diamond bird beak X joint.

4.6.1 The effect of chord length L_0 and boundary conditions on the strength of square bird beak X joints

In this section the behaviour of the square bird beak X joint is investigated to examine what effect the change of the orientation of the brace member has on the joint capacity, when the parameters of chord length L_0 and boundary conditions at the end of the chord are varied.

Model	Chord				Brace		Boundary Condition	Failure load
	L_0	α	b_0	t_0	b_1	t_1	End of	$F_{u,1}$
	mm	$2L_0/b_0$	mm	mm	mm	mm	Chord	kN
B90V11	400	5.3	150	6.3	90	6.3	None	70.0
B90V20	600	8.0	150	6.3	90	6.3	None	93.3
B90V10	800	10.6	150	6.3	90	6.3	None	115.6
B90V28	1400	18.7	150	6.3	90	6.3	None	128.6
B90V12	2000	26.7	150	6.3	90	6.3	None	138.8
B90V13	3000	40.0	150	6.3	90	6.3	None	104.1
B90V26	3800	50.7	150	6.3	90	6.3	None	143.5
B90V1	6000	80.0	150	6.3	90	6.3	None	143.5
B90V22	400	5.3	150	6.3	90	6.3	Encastré	263.8
B90V23	800	8.0	150	6.3	90	6.3	Encastré	191.5
B90V30	1400	18.7	150	6.3	90	6.3	Encastré	167.0
B90V24	2000	26.7	150	6.3	90	6.3	Encastré	145.1
B90V25	3000	40.0	150	6.3	90	6.3	Encastré	144.2
B90V31	3800	50.7	150	6.3	90	6.3	Encastré	143.5

Table 4.8 The results of the finite element investigation on the effects of chord length and boundary conditions on the square bird beak X joint.

The results of the finite element analyses are shown in Table 4.8. The variation of the joint capacity with chord length and the different boundary conditions are plotted in Figure 4.41 and compared to the behaviour of the diamond bird beak joint plotted as the dotted line.

4.7 Discussion of the results for the square bird beak X joint

The variation of the joint capacity caused by the change of orientation of the brace member is discussed in this section using the displaced shape diagrams, the von Mises contoured stress plots and the load/indentation curves to observe any differences between the diamond and square bird beak X joints.

4.7.1 The effect of chord length L_0 and boundary conditions on the strength of square bird beak X joints

Examining Figure 4.43 it can be seen that the general behaviour of the square bird beak X joints is very similar to diamond bird beak joints and that the joint capacity is a little reduced throughout the entire range of chord lengths considered. The same classification used for the diamond bird beak X joints (short, medium and long) may also be applied to the square bird beak X joints with similar transition points.

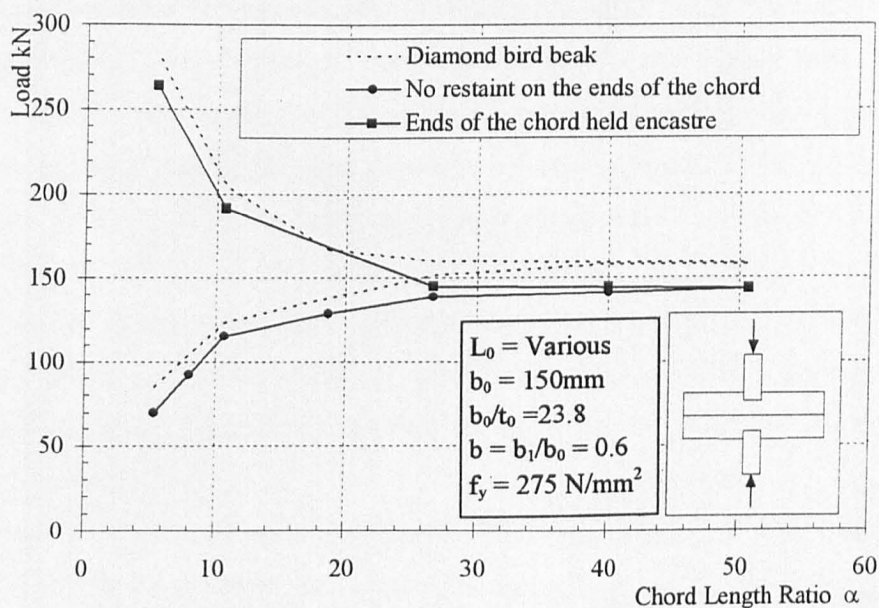


Figure 4.43 The effect of length and boundary conditions at the end of the chord on the joint capacity for the square bird beak joint

The short chord length joints ($5 < \alpha < 10$) exhibit the same form of behaviour as the diamond bird beak joints and it may be assumed suffer the same form of failure, i.e. yield lines forming at the corners of the chord leading to a crushing of the chord. This assumption is based on the fact that the gradient of the lines is approximately the same and over the same chord length as the diamond bird beak joints. Also, the

restraint offered by the ends of the chord when held encasté strengthen the chord by approximately the same amount. (When $\alpha = 5.3$, diamond bird beak difference = 197.0kN, square bird beak difference = 193.8kN and when $\alpha = 10.7$ the difference is 81.5kN and 75.9kN respectively)

The medium chord length joints ($10 < \alpha < 50$) exhibit a similar form of behaviour to the diamond bird beak joints. The joints converge to an approximate asymptotic strength at a chord length of $\alpha = 26.7$ but true convergence does not occur until $\alpha = 50.7$.

The long chord length joints ($\alpha > 50$) show the same behaviour in that an asymptotic strength is achieved.

4.7.1.1 Displaced shape diagrams and contoured stress plots

Examination of the displaced shape and contoured stress plots also show similarities and subtle differences between the diamond and square bird beak X joints.

Examining the displaced shape diagrams and the von Mises contoured stress plots shown in Figure 4.42 it can be seen that they are generally the same as for the diamond bird beak X joints. One very noticeable difference is the area of low (i.e. zero) stress under the toe of the brace. This would indicate that this area is deforming in the same manner as the rest of the chord face, in that a yield line has formed at the toe of the brace and rotated in respect to a yield line at the corner of the chord immediately below it.

Figure 4.43 shows the von Mises contoured stress plots of the middle layer at maximum load for the diamond and square bird beak X joints. The stresses in the middle layer indicate where the in-plane yielding due to the membrane action of the chord walls is occurring (red colour). It can be seen that there is very little membrane action in the shorter joints, but that this increases as the chord length increases and that there is more membrane action in the diamond bird beak joints than the square bird beak joints.

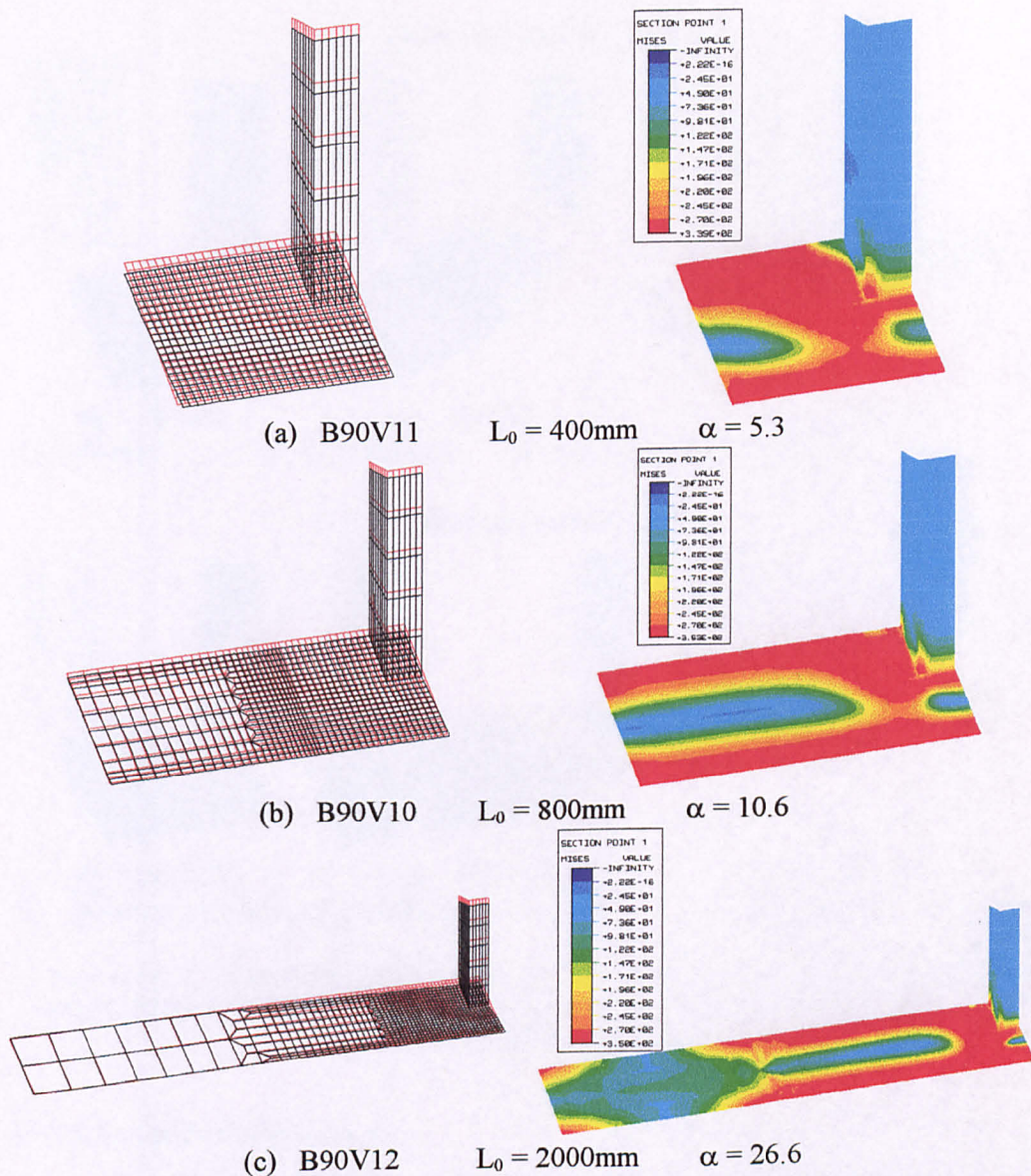
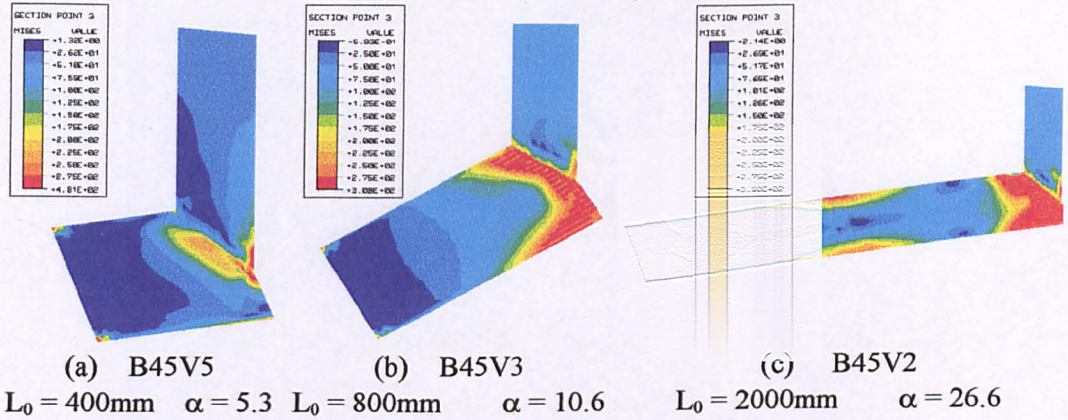


Figure 4.42 The displaced shape and von Mises contoured stress plots for the square bird beak joint for the outside surface at maximum load and no restraint at the end of the chord

This is attributed to the orthogonal geometry of the square bird beak joint which allows the chord face to deform with less membrane action in the chord walls. This may account for the fact that all the square bird beak joints have a joint capacity below that of the equivalent diamond bird beak joint.

Diamond bird beak X joints



Square bird beak X joints

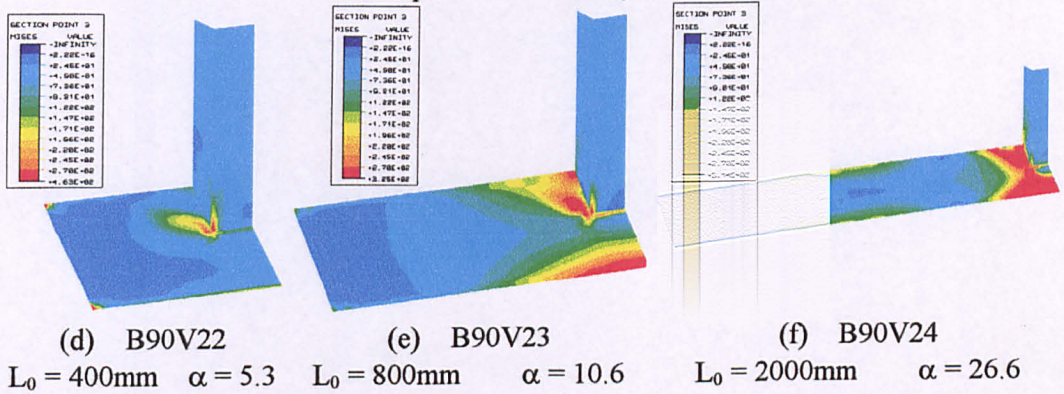


Figure 4.43 A contrast in the von Mises contoured stress plots between the diamond and square bird beak X joints for the middle layer at maximum load and no restraint at the end of the chord

4.7.1.2 Load/indentation curves

The load indentation curves for the square bird beak X joints with no restraint at the end of the chord shown in Figure 4.44, are very similar to those for the diamond bird beak X joints shown in Figure 4.37. Both sets of curves exhibit the behaviour for the different chord lengths. The initial stiffness is approximately the same for both the diamond and square bird beak joints.

Examining the load/indentation curves for the square bird beak joints with the ends held encastré shown in Figure 4.45, it can be seen that all the joints achieve a maximum strength and that the shorter joints have a higher initial stiffness than those which attain the asymptotic strength. Comparing these curves with those for the diamond bird beak joint, shown in Figure 4.38, where the ends of the chord is also

held encastré the curves again show a similar behaviour and each curve, for a particular chord length, have the same approximate initial stiffness.

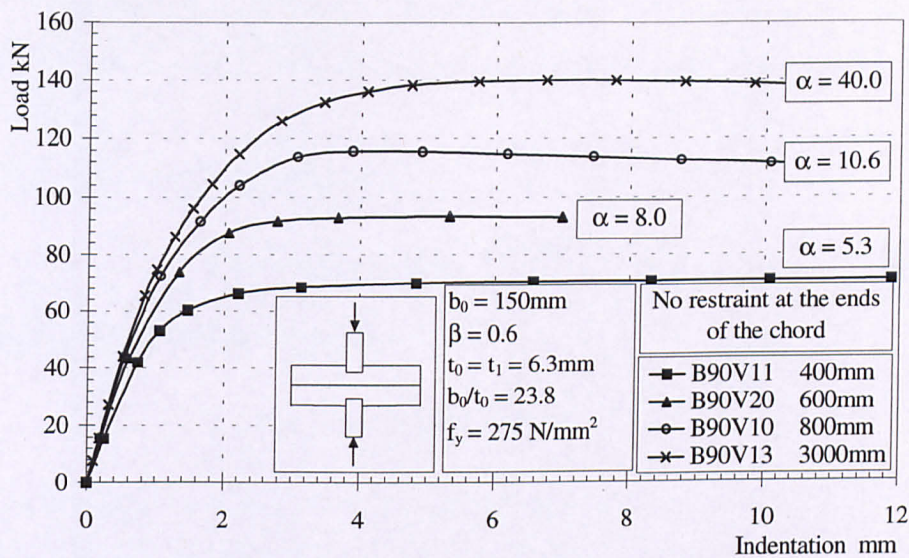


Figure 4.44 Load indentation curves for square bird beak cross joint with no restraint on the ends of the chord

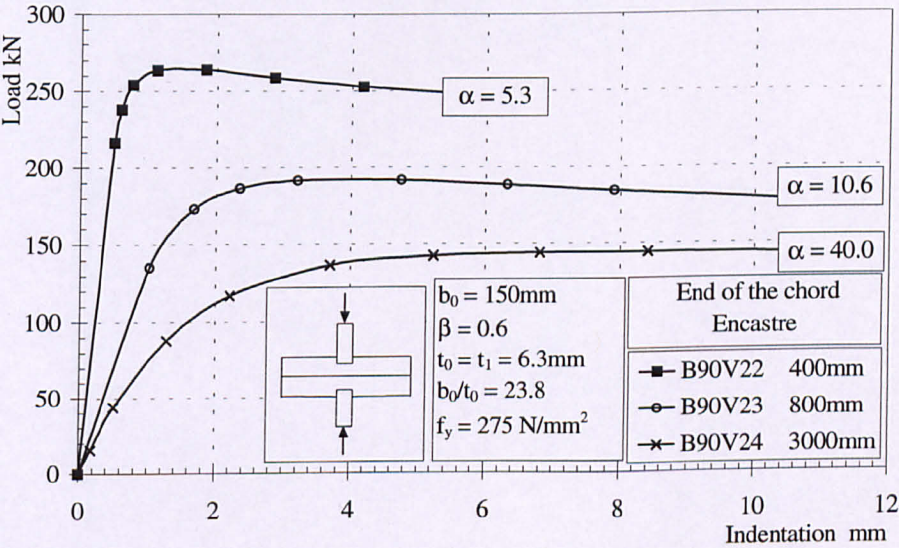


Figure 4.45 Load indentation curves for square bird beak X joint with the ends of the chord held encastré

4.7.2 Determining the joint capacity when the chord length is varied for the square bird beak X joint

It is appreciated that the range of data is very limited however, for the joints analysed in this section the variation of joint capacity with chord length can be estimated as:-

for no restraint at the end of the chord

$$F'_{u,1,length} = F_{u,1,asymptotic} - 159.2 e^{-0.147\alpha} \tag{Eqn 4.10}$$

and for the ends of the chord encasté

$$F'_{u,1,length} = F_{u,1,asymptotic} + 304.0 e^{-0.174\alpha} \tag{Eqn 4.11}$$

when $\beta = 0.6$, $b_0 = 150\text{mm}$ $t_0 = 6.3\text{mm}$ and $f_y = 275\text{N/mm}^2$

The fit of these predictions against the finite element results can be seen in Figure 4.46.

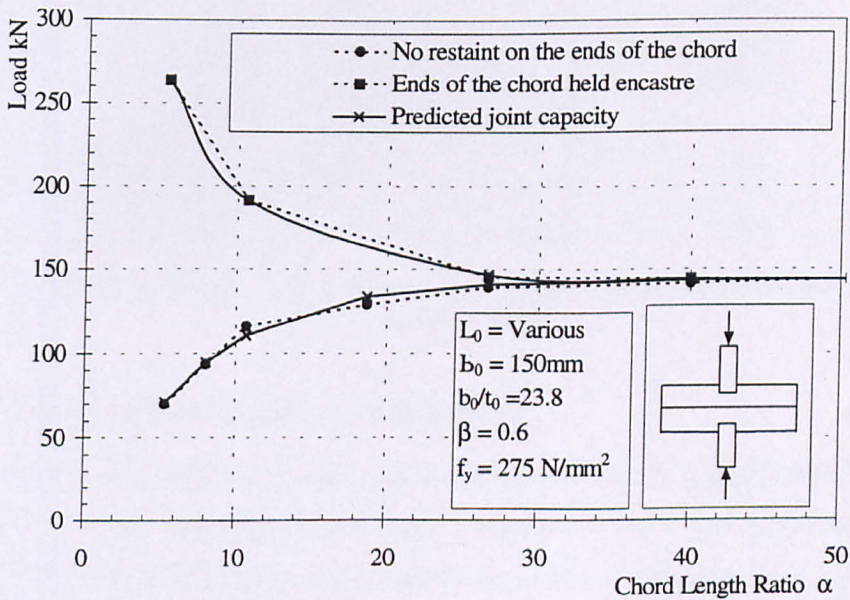


Figure 4.46 The estimated joint capacity against chord length for the square bird beak X joint

4.8 Traditional RHS X joints

The results given in this Section on RHS and the next Section on CHS are only reported so that comparisons can be made with the bird beak joints.

4.8.1 The numerical results for the traditional RHS X joints

The results of the analyses for variation of chord length and the boundary conditions at the end of the chord are given in Table 4.9. The yield stress in all models is 275 N/mm².

Due to the large increase in the joint capacity when a fillet weld is included in a traditional RHS joint, the effect of including a weld is investigated. When a weld has been modelled it has the same properties as the parent material and a throat thickness equal to the brace thickness t_1 .

Model	Chord				Brace		Boundary Condition	Failure Load
	L_0 mm	α $2L_0/b$ 0	b_0 mm	t_0 mm	b_1 mm	t_0 mm	End of Chord	$F_{u,1}$ kN
No weld included in the model								
RHS200	400	5.3	150	6.3	90	6.3	None	92.0
RHS300	600	8.0	150	6.3	90	6.3	None	91.8
RHS400	800	10.7	150	6.3	90	6.3	None	91.7
FRHS200	400	5.3	150	6.3	90	6.3	Encastré	91.8
FRHS400	800	10.7	150	6.3	90	6.3	Encastré	91.9
Weld included in the model								
WRHS200	400	5.3	150	6.3	90	6.3	None	119.5
WRHS400	800	10.6	150	6.3	90	6.3	None	119.8
WRHS850	1700	10.6	150	6.3	90	6.3	None	119.7

Table 4.9 The variation of joint capacity with chord length and boundary condition for the traditional RHS X joint

4.8.2 Discussion of the traditional RHS X joints

There is no significant variation in the joint capacity for a traditional RHS X joint when the chord length or the boundary conditions at the end of the chord were changed. All the load/indentation curves obtained were coincident to each other, an example load/indentation curve obtained for one joint RHS400, without a fillet weld, is shown in Figure 4.47.

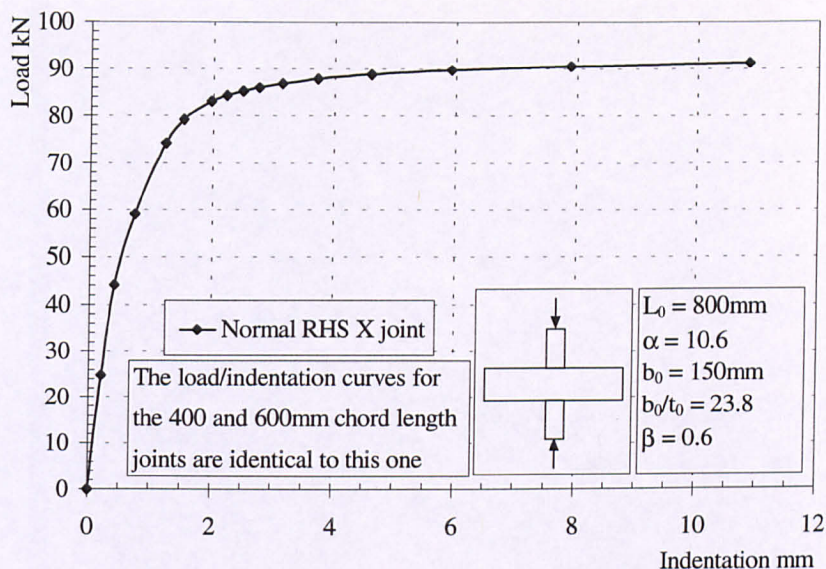


Figure 4.47 Load/indentation curve for the traditional RHS X joint

The fact that the joint capacity does not vary with chord length or boundary conditions can be easily explained by considering the yield line failure mechanism of the traditional RHS joints. Plasticification is assumed to occur in the chord wall along yield lines, which act like stiff hinges, in a pattern similar to the one shown in Figure 4.48. The internal work to rotate these yield lines can easily be calculated and hence the external work and then the joint capacity. Providing the chord is long enough for these yield lines to form, further increases in chord length or a change in the boundary conditions at the end of the chord do not affect the failure mechanism.

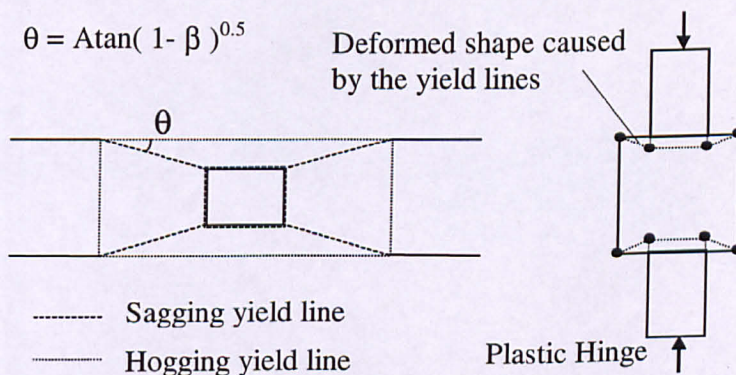


Figure 4.48 The yield line failure mechanism in RHS X joints

The lack of stiffness of the top and bottom faces of the chord in resisting the load imposed on the brace leads to the relatively low joint capacity for the traditional RHS X joints. If a yield line collapse mechanism is assumed, as opposed to the

collapse of the side walls of a slender chord section, a maximum load will never be achieved for this form of joint. (This behaviour can be seen in the load/indentation curve shown in Figure 4.47.) This behaviour can be explained by considering the deformation of the joint. The brace members punch into the chord as the load is applied, forming the yield line pattern. The increase in area of this yield line pattern as the joint deforms causes further internal work to be done in stretching the connecting face of the chord wall. The plastic nature of the yield lines mechanism supports a constant load as the brace members are punched further into the chord. However, the membrane action in the chord wall will support a small increase in the load as further deformation occurs, thus a maximum load will never be attained for this form of joint.

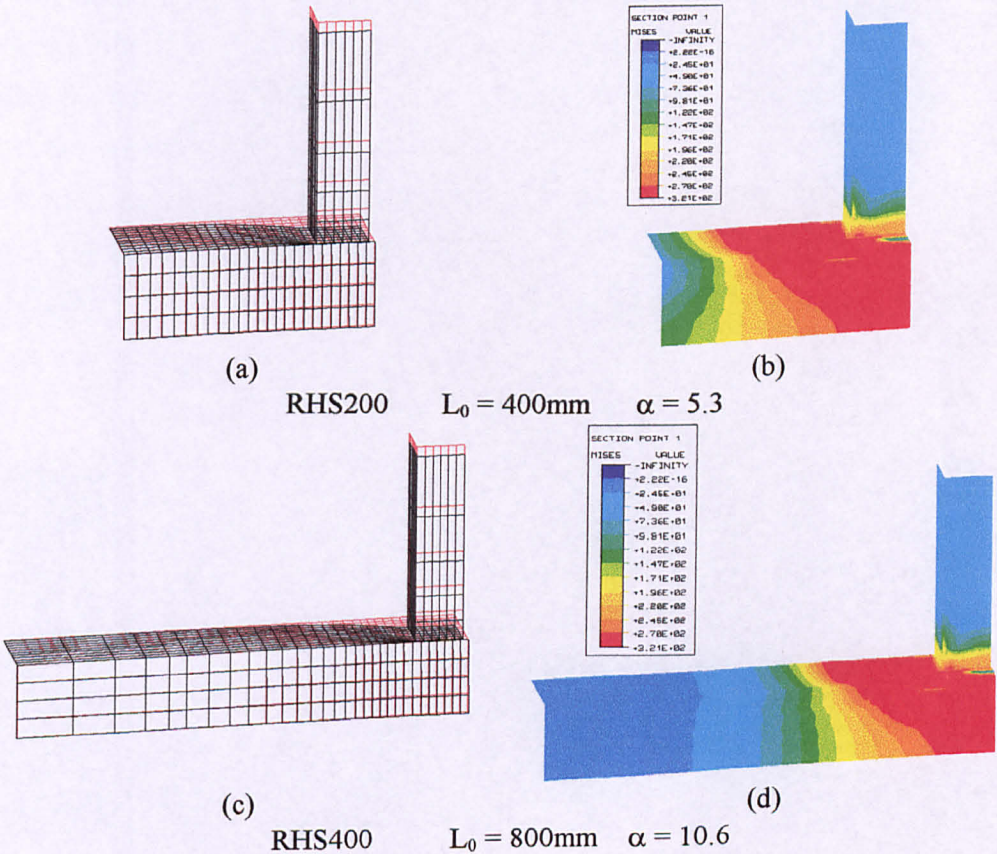


Figure 4.49 The deformed shape diagrams and the von Mises contoured stress plots for the traditional RHS X joints at the joint capacity and for the outside surface

The deformation of the top face of the chord caused by the yield line mechanism can be seen in the displaced shape diagrams shown in Figure 4.49. The contoured stress plots for the different chord lengths show that the area of yielded material in the chord wall is virtually identical in all the joints which is a further

indication of the independence of the joint capacity and chord length. The presence of the yielded material in the chord side wall of the finite element model indicates that some of the rotation attributed to the yield line at the corner of the chord section does in fact occur in the side wall. This does not affect the operation of the mechanism as it can be shown that any rotation in the chord side wall is equivalent to a rotation at the corner of the chord.

4.9 The numerical results for the CHS X joints

In order that comparisons can be made with the rectangular sections used in the previous sections, the circular section was sized to keep the wall thickness and cross sectional area the same. In this manner the plastic moment capacity of the chord wall per unit length (m_p), the membrane action effect of the chord wall and the volume of steel per metre is kept the same for the circular and the rectangular sections. The circular sections used in the finite element models therefore is $d_0=189.2\text{mm}$, $t_0=6.3\text{mm}$, $d_0/t_0=30.0$, $d_1=113.5\text{mm}$, $\beta=0.6$. The same material properties are also used in the circular section $f_y=275\text{N/mm}^2$.

Model	Chord				Brace		Boundary Condition End of Chord	Failure Load $F_{u,1}$ kN
	L_0 mm	α $2L_0/d_0$	d_0 mm	t_0 mm	d_1 mm	t_0 mm		
CHS200	400	4.2	189.2	6.3	113.5	6.3	None	108.6
CHS300	600	6.3	189.2	6.3	113.5	6.3	None	139.2
CHS400	800	8.5	189.2	6.3	113.5	6.3	None	146.2
CHS700	1400	14.8	189.2	6.3	113.5	6.3	None	160.9
CHS1000	2000	21.6	189.2	6.3	113.5	6.3	None	166.5
CHS1500	3000	31.7	189.2	6.3	113.5	6.3	None	166.5
FCHS200	400	4.2	189.2	6.3	113.5	6.3	Encastré	226.6
FCHS400	800	8.3	189.2	6.3	113.5	6.3	Encastré	193.3
FCHS700	1400	14.8	189.2	6.3	113.5	6.3	Encastré	167.4
FCHS1000	2000	21.6	189.2	6.3	113.5	6.3	Encastré	166.5

Table 4.10 The variation of joint capacity with chord length and boundary condition for the CHS X joint

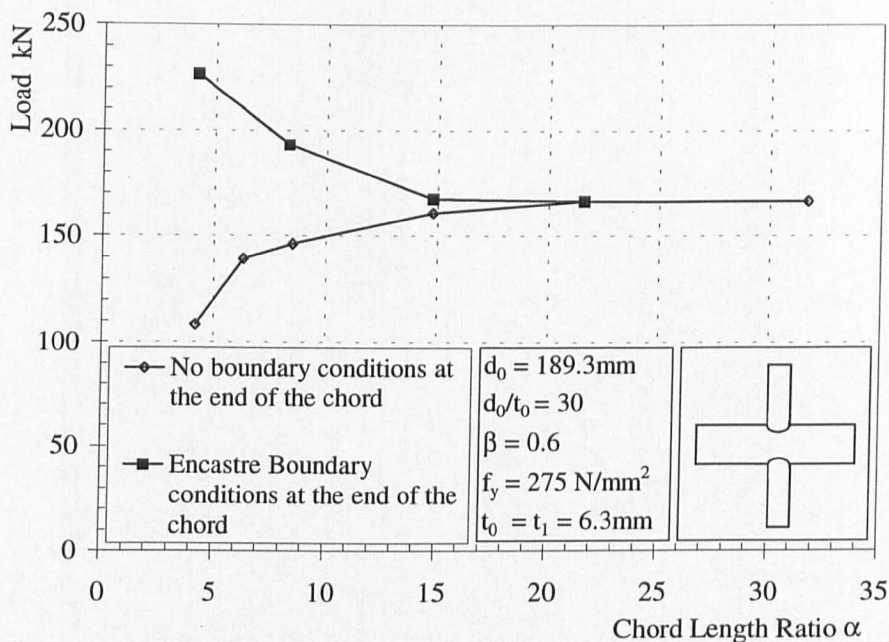


Figure 4.50 The variation of joint capacity with chord length for the CHS X joint

The results of the finite element investigation to study the effects of chord length and the change in boundary conditions on the joint capacity for CHS X joints are given in Table 4.10. The variation of chord length L_0 , and the different boundary conditions considered are shown in Figure 4.50.

4.10 The discussion of the results for the CHS X joints

Van der Vegte (1995) reported the variation of joint capacity with chord length, although he did not investigate the effects of holding the ends of the chord encasté or identify an asymptotic strength. He does note however, that the joint capacity increases very little after the chord length ratio $\alpha > 11.5$ for the CHS X joints that he investigated. The results reported in this section confirm van der Vegte's work and also show the effects of holding the ends of the chord encasté.

A similar behaviour to that of the bird beak X joints is shown in Figure 4.50 for the CHS X joints, that is when the ends of the chord are held encasté the joint capacity is increased for the shorter joints, which then decreases to the asymptotic strength as the chord length increases. When the ends of the chord have no restraint then the joint capacity increases with chord length until the asymptotic strength is reached. The asymptotic strength of the joint is achieved when the chord length ratio $\alpha = 21.6$.

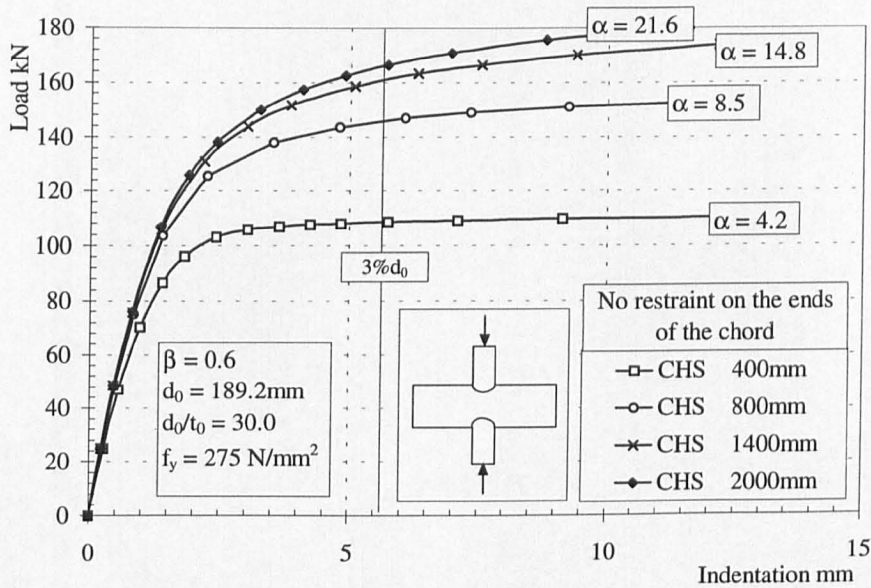


Figure 4.51 Load indentation curves for the CHS X joints

4.10.1 Load/indentation curves

In order that the joint capacity can be easily defined a failure criteria of 3% d_0 was used to determine failure. This can be seen in the load/deflection curves shown in Figure 4.51. None of the models for the CHS X joints reached a maximum value although the shorter chord length appears to reach a limiting value.

It was noted in the section on convergency tests that van der Vegte (1995) reported that for $\alpha > 6$ he obtained a maximum joint capacity for similar analyses and that the mesh used for these analyses is overly stiff. Therefore, it is considered that detailed comments on the shape of the load/indentation curves are invalid until more work is done on validating the mesh used.

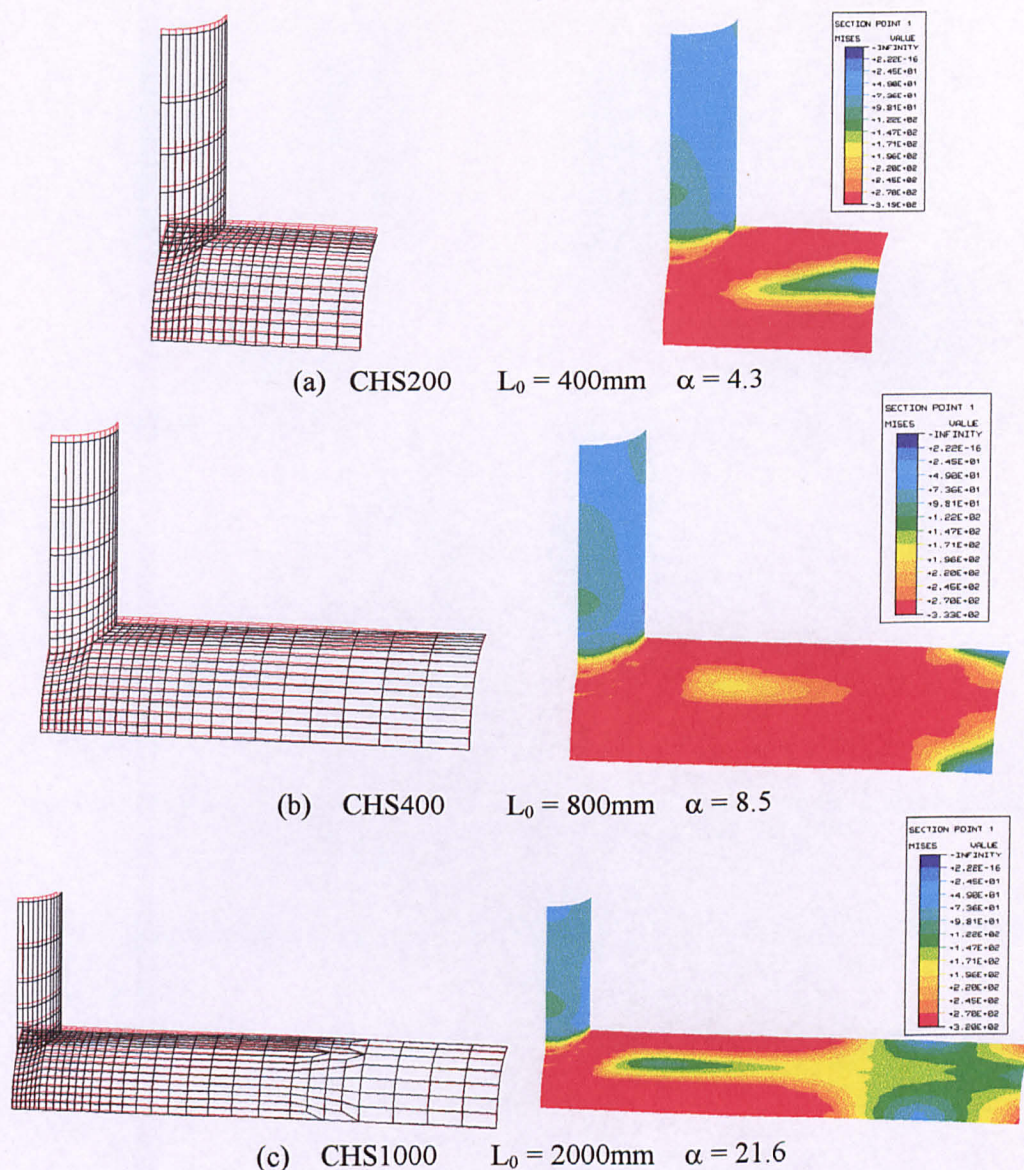
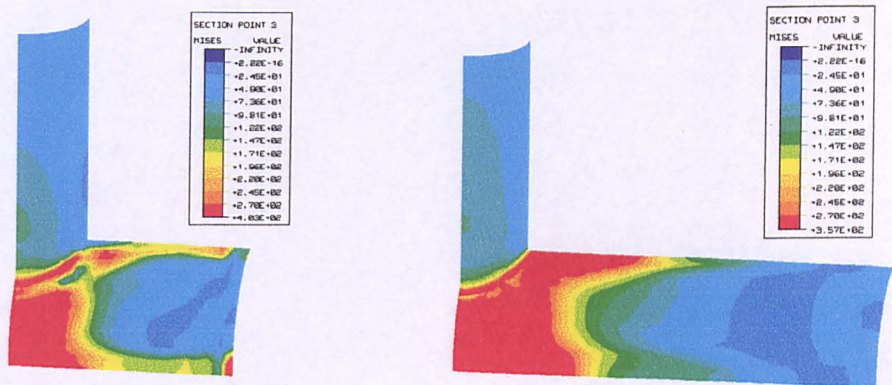


Figure 4.52 The displaced shape diagrams and the von Mises contoured stress plots for the CHS X joints at maximum load and the outside surface, no restraint at the end of the chord

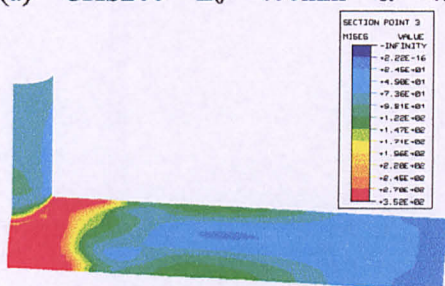
4.10.2 Displaced shape diagrams and contoured stress plots for the CHS X joints

Examination of the displaced shape diagrams shown in Figure 4.52 reveals that failure occurs due to the chord crushing when $\alpha = 4.3$, whilst in the longer joints $\alpha \geq 8.5$, the chord can support the load applied to the brace without failing in a crushing manner. There is considerably more membrane action in the vicinity of the brace member in the longer joints to accommodate the deformation of the chord, indicated by the von Mises contoured stress plots of the middle layer at the joint capacity which can be seen in Figure 4.53.

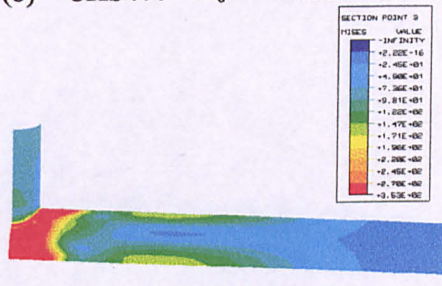


(a) CHS200 $L_0 = 400\text{mm}$ $\alpha = 4.3$

(b) CHS400 $L_0 = 800\text{mm}$ $\alpha = 8.5$



(c) CHS700 $L_0 = 1400\text{mm}$ $\alpha = 14.8$



(d) CHS1000 $L_0 = 2000\text{mm}$ $\alpha = 21.6$

Figure 4.53 The von Mises contoured stress plots for the CHS X joints at maximum load at the middle layer, no restraint at the end of the chord

4.10.3 Determining the joint capacity when the chord length is varied for the CHS X joints

Van der Vegte (1995) reports the variation of joint capacity against chord length with no restraint on the end of the chord to be

$$F'_{u,1,\text{length}} = \frac{12.5\alpha}{11.5(1+\alpha)} F_{u,\alpha=11.5} \quad \text{Eqn 4.12}$$

where $F_{u,\alpha=11.5}$ is the joint capacity of a joint with a chord length of $\alpha = 11.5$.

Eqn 4.12 when applied to van der Vegte's results produces a very poor fit at low values of α , in most cases overestimating the strength of the finite element analyses. (This can be seen in Vegte (1995) and in Figure 4.54 where Eqn 4.12 is applied to the results obtained in this work.) Due to the formulation of Eqn 4.12 a maximum value will never be achieved, although it is accepted that for practical circumstances this effect is not significant.

Again it is appreciated that the range of data is very limited. However, for the joints analysed in this section the variation of joint capacity with chord length can be predicted as:-

for no restraint at the end of the chord

$$F'_{u,length} = F_{u,asymptotic} - 181.2e^{-0.276\alpha} \quad \text{Eqn 4.13}$$

and for the ends of the chord encasté

$$F'_{u,1,length} = F_{u,1,asymptotic} + 157e^{-0.224\alpha} \quad \text{Eqn 4.14}$$

when $\beta = 0.6$, $d_0 = 189.26\text{mm}$ $t_0 = 6.3\text{mm}$ and $f_y = 275\text{N/mm}^2$

The fit of these predictions against the finite element results and van der Vegte's prediction can be seen in Figure 4.54.

It is suggested from these results that the use of an exponential function to base the formulation of the variation of joint capacity against chord length is better able to replicate the type of curve produced (i.e. to tend towards an asymptotic value and predict the strength of the very long and very short chord lengths).

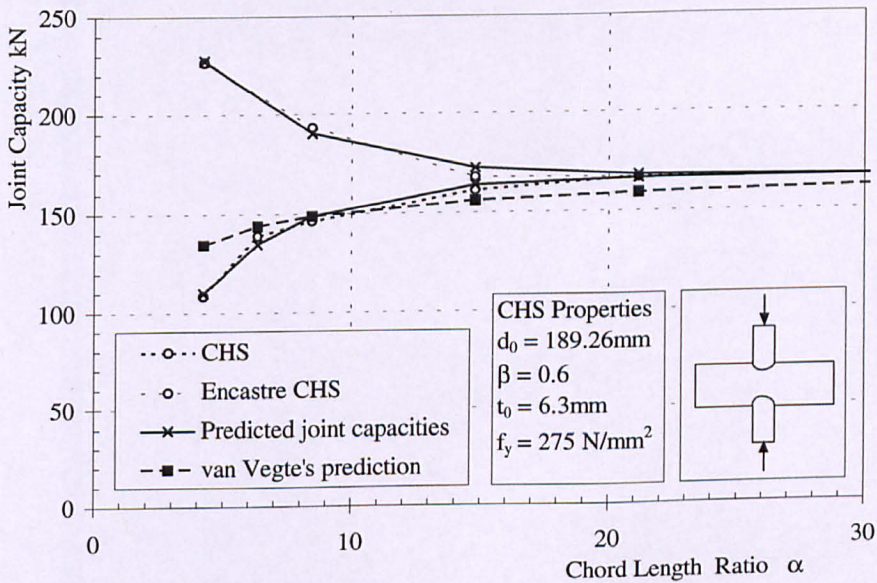


Figure 4.54 The predicted joint capacity against chord length for CHS X joint

4.11 Comparisons between the joint types

Each form of joint configuration has been studied, some in more detail than others. The similarities and differences of all the joints systems will now be examined.

4.11.1 The variation of joint capacity with chord length

It has been shown in this Chapter that the joint capacity of all the X joints studied varies to some extent with chord length and the boundary conditions at the end of the chord, with the exception of the traditional RHS X joints. Figure 4.55 shows how the relationships between joint capacity, chord length and boundary conditions vary between the different joint configurations. From this figure we can see that:

- the traditional RHS X joint is the not affected by chord length, although the increase in joint capacity by the inclusion of the weld material is significant.
- of the remaining joints the CHS X joint is the least affected by chord length, where the asymptotic strength is achieved practically at $\alpha = 14.8$ and actually at $\alpha = 21.6$.
- the diamond bird beak X joint is the most affected by chord length not attaining the asymptotic strength until $\alpha = 40.0$.
- the square bird beak joint is the somewhere in between in that the practical asymptotic strength is achieved at $\alpha = 26.6$, although actual convergence is not achieved until $\alpha = 50.0$.

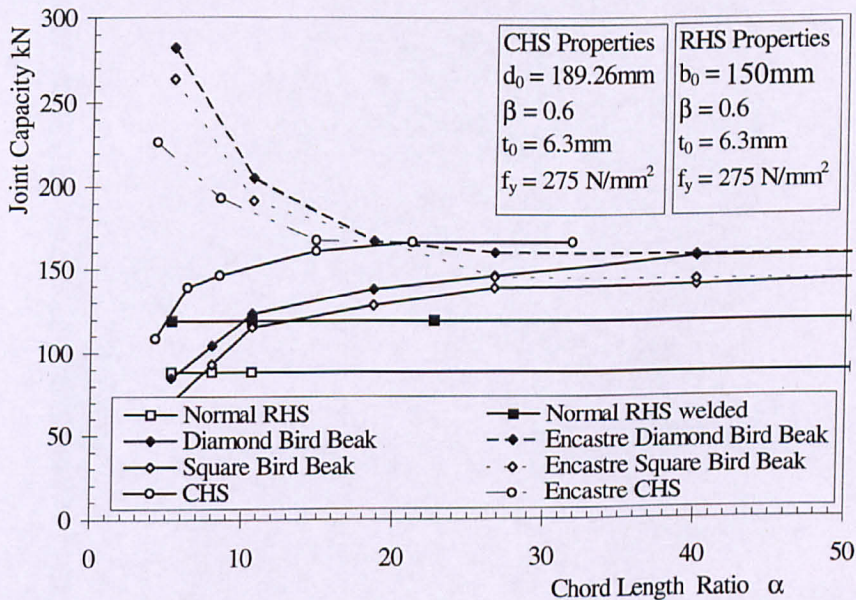


Figure 4.55 A comparison of joint capacity with chord length and boundary conditions at the end of the chord for all the joints studied

All the joints where the joint capacity is affected by chord length are in turn affected by the boundary conditions at the end of the chord. Imposing encastré boundary conditions at the end of the chord increases the joint capacity, particularly for the shorter chord length joints. The CHS X joint shows the least increase in strength, whilst the square and diamond bird beak joints both demonstrate a larger increase, the magnitude of which is approximately equal.

When the ends of the chord have no restraint on them, short joints (for the CHS joints $\alpha \leq 6.3$ and for the bird beak joints $\alpha \leq 10.6$) failure was attributed to the crushing of the chord. When the ends of the chord were held encastré, the restraint offered by the support conditions in resisting this deformation causes a dramatic increase in the joint capacity observed.

4.11.2 Load/indentation curves

The load/indentation curves studied in this Chapter have exhibited a wide variety of different behaviours. The traditional RHS and the CHS X joints consistently did not reach a maximum value. However, it is regrettable that the CHS X joint load/indentation curves have to be considered unreliable in this respect. Ideally it would be useful to further develop the CHS model to see if it can be improved and verify whether these curves are correct or incorrect.

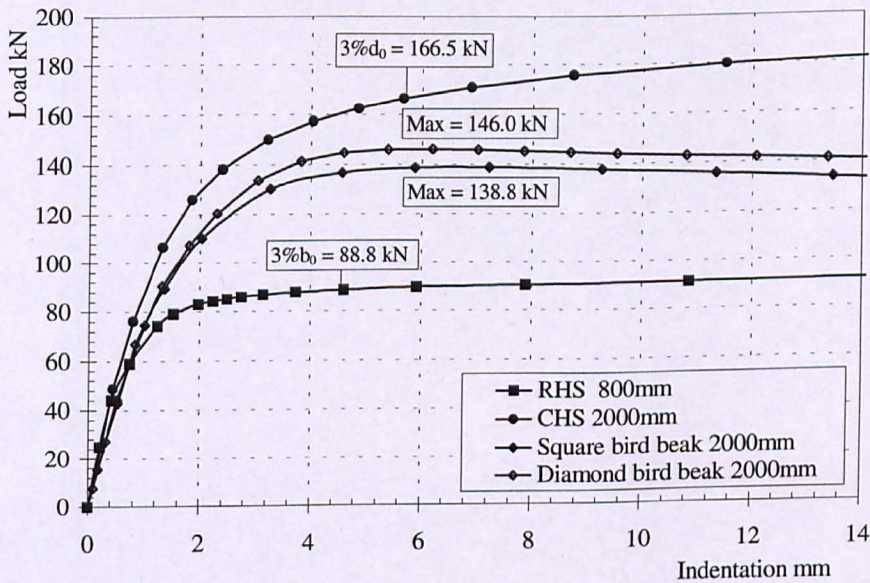


Figure 4.56 A comparison of some the load/indentation curves of the various joints studied

The load/indentation curves for the bird beak joints usually reach a maximum with the exception of the diamond bird beak when $\alpha \leq 8.0$ and the square bird beak when $\alpha = 5.3$ when there is no restraint at the end of the chord. The reason for this is attributed to the membrane action of the chord wall, due to the deformation of the joint. The indentation at which the maximum joint strength occurred, increased as the chord length increased and the indentation at the maximum load where the asymptotic strength is reached was in the order of $5\%b_0$

Figure 4.56 shows an example of the load/indentation for each joint configuration at the same chord length (for all the RHS configurations $\alpha=26.7$ and for the CHS $\alpha=21.1$) so that they can be compared. The traditional RHS load/indentation curves were identical for all chord lengths, so a chord length of 800mm can be regarded as equivalent to a 2000mm chord length.

4.11.3 Failure mechanisms

It would appear from the contoured stress plots that the CHS and bird beak X joints have failure mechanisms that are very similar to each other, in that yield lines appear to occur at similar points, i.e. the top, middle and the bottom of the section running in direction parallel to the centre of the chord. In the bird beak configuration the discontinuity at the corners of the chord provide a natural weakness in the section which causes lozenging (or in some circumstances crushing) of the section.

The in-plane yielding due to the membrane action within the chord walls, required to permit the deformation of the joint is evident in all the CHS, diamond and square bird beak X joints, although it is most notable in the CHS sections

The traditional RHS X joint has a failure mechanism which is unique to itself, in that the yield lines can be assumed to occur on the connecting face of the chord in a manner described previously in the Section 4.8.2.

4.12 Summary

The behaviour of the X joints with the variation of chord length identified in this Chapter is very important as it has influenced much of the research that followed. With the exception of the traditional RHS X joint and joints where the asymptotic strength is attained, the joint capacity is dependent on:

- the length of the chord

- the boundary conditions at the end of the chord

In addition to this:-

- that when there is no restraint at the end of the chord, the joint capacity increases with increasing chord length
- that when the ends of the chord are held encastré, the joint capacity decreases with increasing chord length

The asymptotic strength was obtained in the joints studied when $\alpha > 40$ for diamond bird beak X joints, $\alpha > 50$ for square bird beak X joints and $\alpha > 21.6$ for CHS X joints. Further increases in chord length or changes in the boundary conditions did not affect the joint capacity observed.

The failure mechanisms observed for X joints studied can be classified according to the joint chord length and with the exception of the traditional RHS X joints, failure occurs for:

- short chord length joints as a crushing of the chord, with yield lines running the length of the chord
- medium chord length joints as a lozenging of the chord. The chord can support the load applied to the brace without complete failure at the end of the chord. The yield lines do not run for the full length of the chord and the moment in the chord wall decreases to an elasto-plastic or an elastic moment (+ve or -ve) with increasing length
- long chord length joints as a lozenging of the chord. However, the length of the chord is sufficient for the reverse deformation, apparent in the medium length joints to tend towards zero and the asymptotic strength of the joint is achieved

In addition to the plastic moment acting in the chord walls, the amount of membrane action that occurs as the joint deforms also contributes to the joint capacity. The medium and long chord length joints particularly exhibited large amounts of membrane action.

The traditional RHS X joint was unique in that the failure mechanism can be represented by a yield line mechanism and providing that the length of the chord is sufficient for this mechanism to form, then the joint capacity is independent of chord length.

For the diamond bird beak joint where a parametric study was carried out it was established that altering the design parameters for the chord width ratio β , and chord slenderness $\tau=b_0/t_0$ in the range of $0.2 \leq \beta \leq 0.9$ and $9.4 \leq b_0/t_0 \leq 35.3$ the joint capacity for the asymptotic strength can be determined by:

$$F_{u,1} = \frac{2.6}{1-0.6\beta} 275 \left(\frac{f_y}{275} \right)^{0.8} t_0^2 \left(\frac{b_0}{t_0} \right)^{0.4}$$

for the range of yield stress of $275 \leq f_y \leq 400 \text{ N/mm}^2$

In addition to these formulae a separate failure mechanism was identified in that the brace could fail in shear and this could be a lower bound value to the joint capacity when there was either a low chord width ratio β or a high brace slenderness value b_1/t_1

$$F_{u,1} = \frac{4}{\sqrt{3}} b_1 t_1 f_y$$

5.

The Analysis of the Bird Beak X joint

5.1 Introduction

One of the original intentions of this research was to formulate a yield line model to represent the failure mechanism of bird beak joints. However, due to the complex nature of the failure mechanisms it has not been possible to complete this. This Chapter will examine these failure mechanisms and attempt to assess their relative importance to the collapse mechanism.

The best analysis models replicate the collapse mechanism and produce a similar form of deformation. Using the deformation of the chord wall and the contoured stress plots examined in Chapter 4, the collapse mechanisms for long, medium and short chord length joints are examined in this Chapter. The failure mechanism for a short chord length is relatively simple and can be fully explained, whereas those for the medium and long joints are more complex and cannot be completely explained. The nature of the collapse mechanism of the long chord length is studied in detail and a plastic collapse mechanism, based on the effective length of the yield lines is suggested. The deformed shape of the chord wall is then examined and an alternative method where two semi-rigid mechanisms are identified in addition to the plastic mechanisms. The contribution of all these mechanisms to the final collapse load is then investigated.

5.2 The plastic mechanisms operating in the bird beak X joints

In a simple yield line model the deformation, which may occur over a large area, is assumed to be confined to the rotation of yield lines that form between rigid plates. If the rotation of the yield lines produces a similar form of deformation to that actually observed, then equating the internal work done in the plastic hinges and with the work done by the external force leads to a fair estimate of the collapse load for that mechanism. This will be an upper bound solution to the true collapse load.

In addition to this, the internal work done due to the in-plane yielding of the material may be included into the calculation to satisfy compatibility requirements. However, due to the interaction of the stresses between the different mechanisms the

estimation of the collapse load may not be as good as when a pure flexural yield line mechanism is considered.

5.2.1 Yield lines at the corners of the chord section

The presence of yield lines at the corners of the chord section was clearly demonstrated in Chapter 4 in the contoured stress plots, by the nature of the deformation of the chord section and Figure 4.34 reproduced here as Figure 5.1. The distribution of the moment along CD is similar to that along AB, although it has irregularities caused by the presence of the brace and the shape of some of the elements.

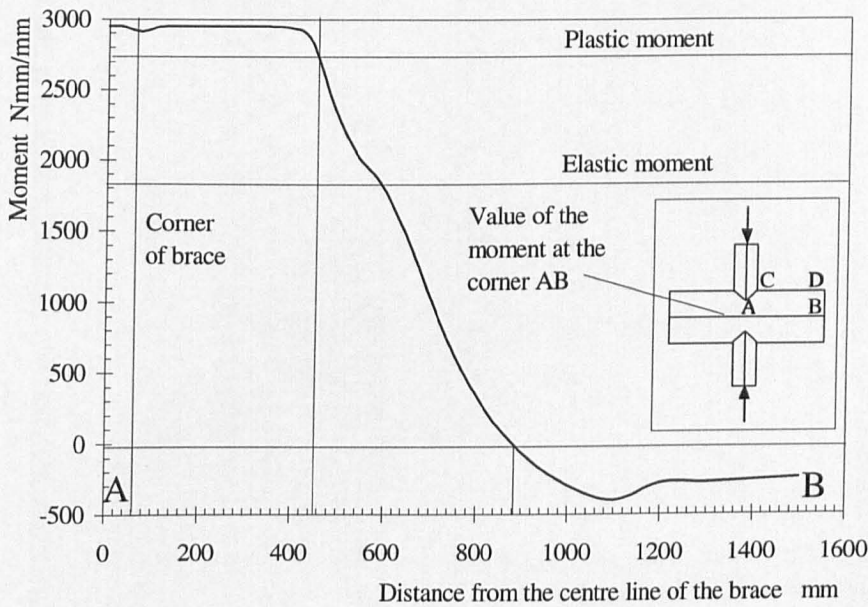


Figure 5.1 The magnitude of the moment along the middle corner AB of the chord of the joint B45V15 at maximum load 158.5kN

Hence, a yield line model representing the collapse mechanism would have yield lines at the corners of the chord section in the manner shown in Figure 5.2 and would assume the faces of the chord section to be rigid plates.

The angle of rotation of the yield line (θ) can be determined from the geometry of the joint and the indentation (δ) of the load. However, problems arise in defining the length of the yield lines (L) and the value of the moment operating in the chord wall (m_p) at the corner of the chord section, but if values are assumed the collapse load $F_{u,1}$ can then be estimated by

$$\text{External work} = \text{Internal work}$$

$$F_{u,1} \delta = 4(2L m_p \theta) + \text{other internal work} \quad \text{Eqn 5.1}$$

The term of “other internal work” arises through the need to satisfy compatibility requirements which is discussed next. This term will be used to include the work done by various different mechanisms discussed in this Chapter, such as the in-plane yielding of the chord wall, the twisting and the in-plane bending of the chord faces.

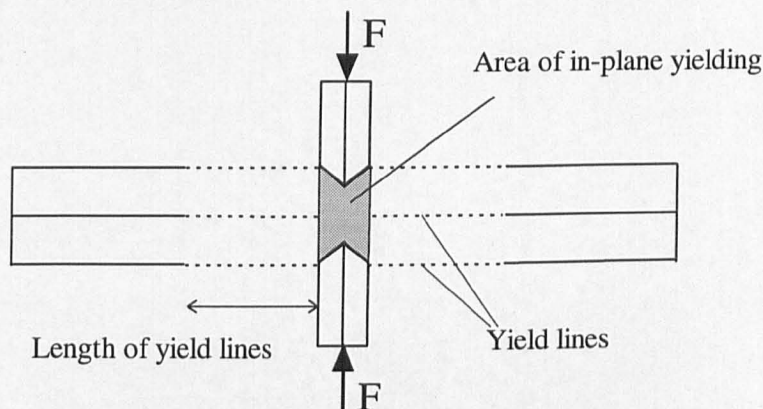


Figure 5.2 A yield line model of the collapse mechanism

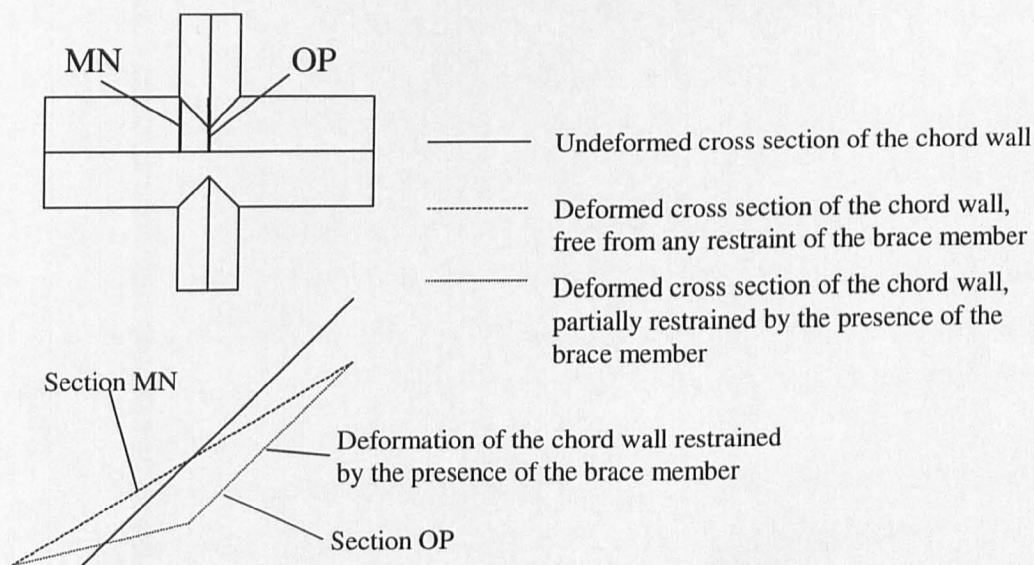


Figure 5.3 The effect of the restraint of the brace member on the deformation of the chord wall

5.2.2 Membrane action in the chord walls

The restraint offered by the brace in resisting the deformation of the chord wall, shown in Figure 5.3 and in any of the displaced shape diagrams in Chapter 4, causes considerable yielding of chord wall so that compatibility in the deformation is

maintained between the restrained and unrestrained regions. The area affected is shown as the shaded area in Figure 5.2. A considerable amount of internal work is done in this area and this must be accounted for when the internal work of the collapse mechanism is assessed. The internal work done by the in-plane yielding of the chord walls is entered in Eqn 5.1 as “other internal work” as a function of δ , the indentation assumed in the calculation of the external work done.

The restraint offered by the brace is likely to be independent of the chord length and its contribution to the strength of the joint will depend on the width ratio β , the chord width b_0 and thickness of the chord t_0 .

5.3 Short chord length joints

Chapter 4 showed that, short chord length joints ($5 \leq \alpha \leq 10$ for bird beak joints) yield lines were found to run along the full length of the chord. This can be seen in the contoured stress plots and the deformed shape diagrams, shown in Figure 4.26, where the chord was crushed (i.e. the same vertical displacement along the length of the chord) when there was no restraint at the end of the chord. This is also confirmed in Figure 5.1, which shows that the value of the plastic moment m_p in the chord wall is approximately constant at a value of 2950 Nmm/mm over a length of 0 - 400mm (i.e. $\alpha = 10.6$). However, a value for the plastic moment of $m_p = t_0^2 f_y / 4 = 2728$ Nmm/mm ($f_y=275\text{Nmm}^{-2}$ and $t_0=6.3\text{mm}$) will be used in all the following calculations.

In this section on short chord length joints the angle of rotation of the yield lines θ is assumed to be constant along the length of the yield line, which is the case if the chord is crushed. This is not quite the case and is discussed later, but for short chord length this is a reasonable assumption.

The two mechanisms discussed previously are initially assumed to be operating independently of each other to form the collapse mechanism are shown in more detail in Figure 5.4. This figure shows that:

- the chord wall free of the restraint of the brace member (Area ABDE) is assumed to be a yield line mechanism where the angle of rotation of the plastic hinge (θ) is constant along the length of the yield line (L) and the chord wall behaves as a rigid plate. The internal work done by the yield line mechanism can be calculated by

$$\text{Internal work} = 4(2L m_p \theta) \quad \text{Eqn 5.2}$$

- the chord wall beneath the brace member (Area AGCD) is assumed to deform by in-plane yielding in such a manner that the deformation at the connection between the mechanisms is compatible. The internal work done by this mechanism cannot be calculated directly, but is arrived at by empirical methods.

Figure 5.5 shows the variation of joint capacity with chord length for the diamond bird beak X joints with no restraint at the end of the chord. The load supported by the internal work of the yield line mechanism, calculated by Eqn 5.2 is shown as a dashed line and it is noticeable that it is parallel to the short chord length joint capacities. It therefore appears that the additional work - probably associated with in plane yielding - is constant with changing chord length up to $\alpha = 10$ (and in this case the correction term is equivalent to 56δ . With more data it should be possible to derive an empirical expression to estimate this term.) Substituting this value into Eqn 5.1, the results are plotted as the solid thick line.

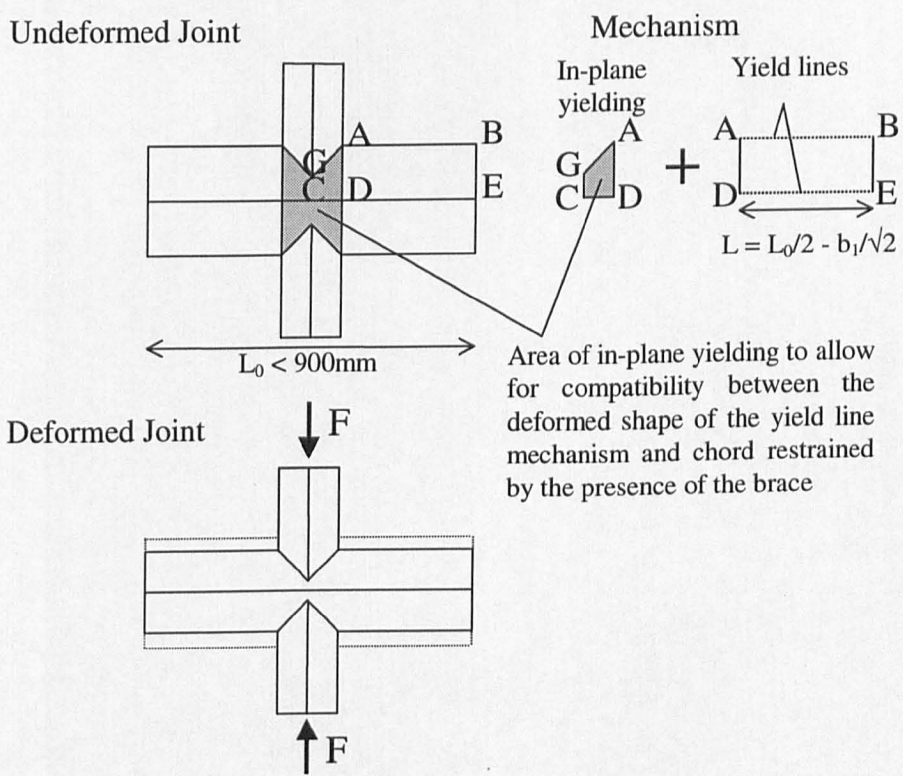


Figure 5.4 The assumed deformation and the yield line mechanism for short chord length joints

If the same procedure is followed for the square bird beak X joints, then the internal work done to cause in-plane yielding in the vicinity of the brace is 42δ . The results of

combined yield line and in-plane yielding mechanism compared against the finite element joint capacities for the square bird beak joint with no restraint at the end of the chord can be seen in Figure 5.6.

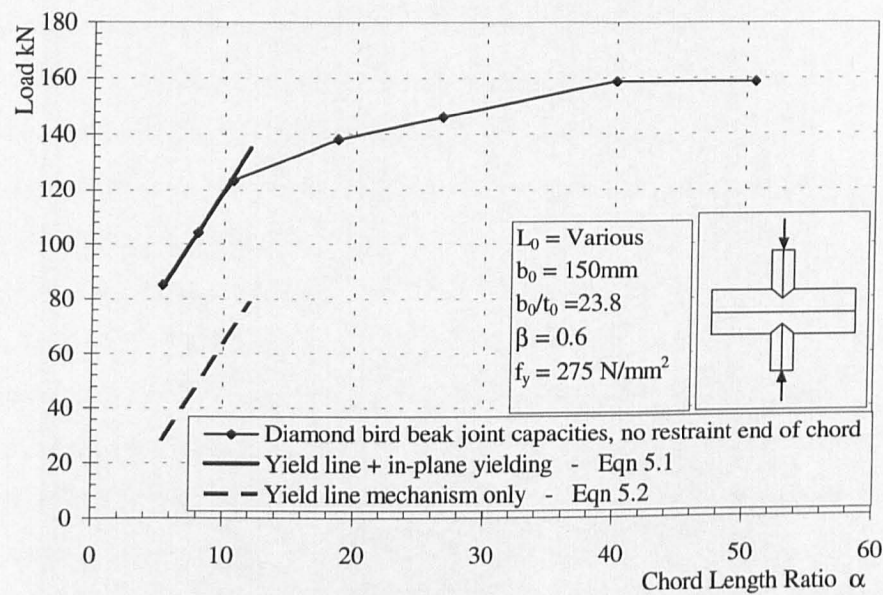


Figure 5.5 A comparison between the finite element joint capacity and the analytical capacity for short chord length diamond bird beak X joints

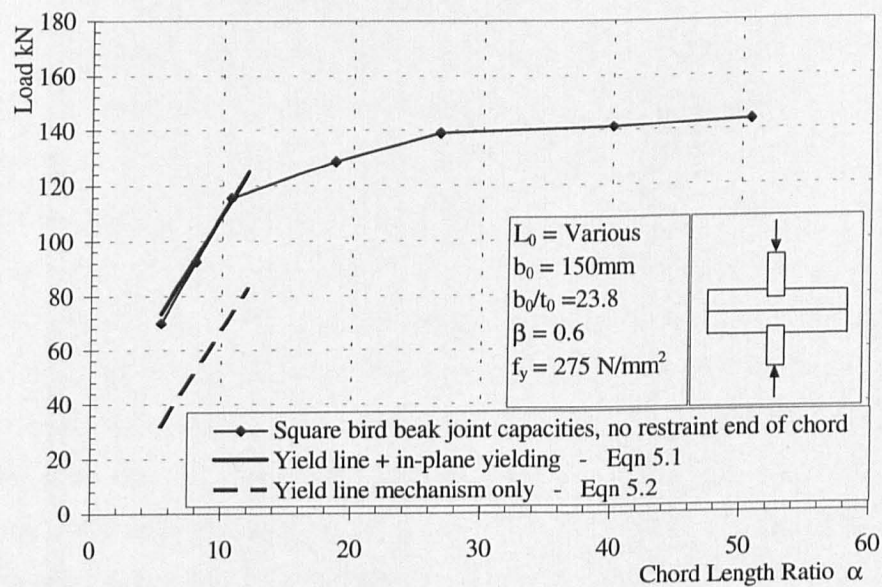


Figure 5.6 A comparison between the finite element joint capacity and the analytical capacity for short square bird beak X joints

In this section it has been assumed that the angle of the rotation of the plastic hinge is constant and that the two mechanisms are independent of each other, these two assumptions will now be examined more carefully. Examination of Figure 4.26 shows that the indentation is not quite constant along the length of the chord and therefore the angle of rotation of the plastic hinge will not be constant along the length of the chord. This will result in less work being done by the plastic hinge at the end of the chord section where the angle of rotation is less than θ . However, examination of Figures 4.44 a & b, that show the von Mises contoured stress plots of the middle layer of the joint and give an indication of the amount of in-plane yielding present, reveals that the amount of in-plane yielding increases with increasing chord length. For this chord wall slenderness at least, it is apparent that the increase in the work done by the in-plane yielding is equal to decrease in the work done by the rotation of the plastic hinges when the angle of rotation is not considered constant along the length of the chord. Therefore the assumptions made initially can be seen to be reasonable, although further work is required to ascertain whether these assumptions are true for other chord wall slenderness values.

5.4 Medium chord length joints

It was shown in the contoured stress plots in Chapter 4 that for medium chord length joints (for the diamond bird beak $10 < \alpha < 40$ or $800 < L_0 < 3000\text{mm}$) the yield lines did not run the full length of the chord. This was confirmed when the magnitude of the moment acting in the chord wall was plotted for the joint B45V15 where $\alpha = 40$, shown in Figure 5.1. This figure shows that moment in the chord wall changes from plastic to elasto-plastic at 450mm ($3b_0$), from elasto-plastic to elastic at 600mm ($4b_0$) and becoming negative at a distance of 880mm ($\approx 6b_0$) from the centreline of the joint.

Clearly then plastic theory which has been used for the short chord length joints is no longer suitable and alternative methods should be sought which would account for all the internal work done. In the plastic theory, the moment acting in the chord wall is considered to act as a stiff hinge requiring a moment of $M_p (= L t_0^2 f_y / 4)$ to turn it. For given values of the length of the yield line L , the section thickness t_0 and the yield stress f_y , the work done by the yield line is directly proportional to the angle of rotation of the yield line θ .

In bird beak joints there is a limiting value to the length of the yield lines, shown by the fact that all medium and long chord length joints reach a maximum load shown in Figure 4.36. If this were not the case, then a further displacement of the external force would cause the yield lines to increase in length, supporting a larger load. This limit to the yield line's length can be seen in Figure 5.7 and Figure 5.8 which shows the deformed shape of the top corner of the chord for different load levels. Observing the "point of zero deformation" will indicate any change in the length of the mechanism operating at the corner of the chord.

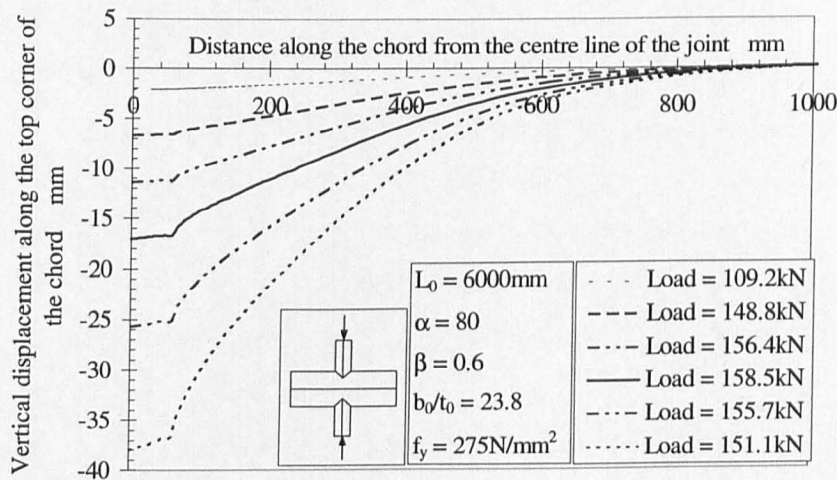


Figure 5.7 The deformed shape of the top corner of the chord for joint B45V1 for successive load levels

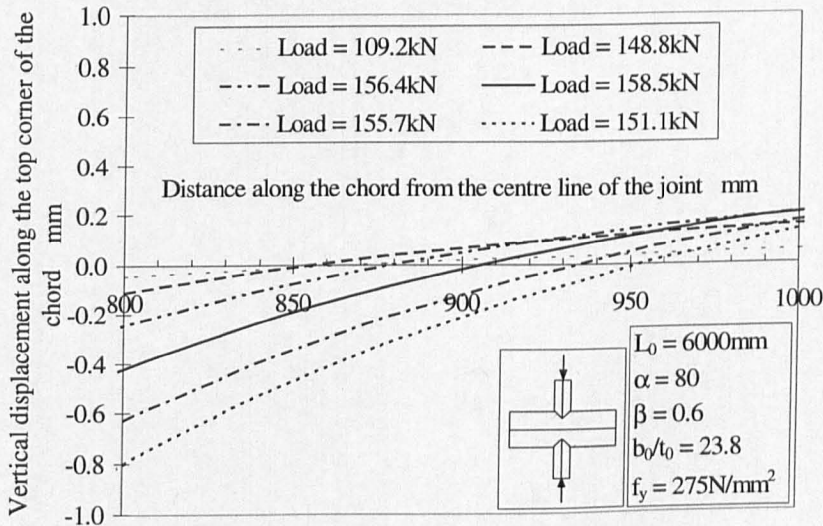


Figure 5.8 The deformed shape of the top corner of the chord for joint B45V1 for successive load levels, zoomed in on the point of zero deformation

Figure 5.7 shows the deformations that occur under the brace of the joint and how the point of zero deformation appears to be stationary with increasing load on the brace. Figure 5.8 shows that the point of zero deformation changes from 907mm at maximum load, to 952mm from the centre line of the joint for the last load recorded. However, given the large changes in geometry and the overall length of the deformation this may be considered as a constant length.

When similar curves were drawn for the middle corner of the chord, the deformed shape varied due to the absence of the brace member (shown in Figure 4.31), but the equivalent figure to Figure 5.8 was identical.

Therefore, when the yield line is fully developed (i.e. the length attained at the maximum load) the value of the moment acting at any particular point along the length of the mechanism can be assumed to be constant with increasing displacement of the external force. (Even when there is an elasto-plastic or elastic moment acting in the chord wall.) If a hinge is then considered to operate at the corner of the chord, of varying stiffness according to the moment acting in the chord at that point, the work done by the rotation of the hinge can be calculated.

In this model the face of the chord will not be considered as rigid, but allowed to twist along its length. In this way the angle of rotation at the centre line of the joint is θ and 0 at the point of zero deformation. The angle of rotation is assumed to change linearly between θ and 0 along the length of the yield line. The effect of allowing the chord face to be twisted instead of rigid will be investigated in the next section when long chord length joints are examined.

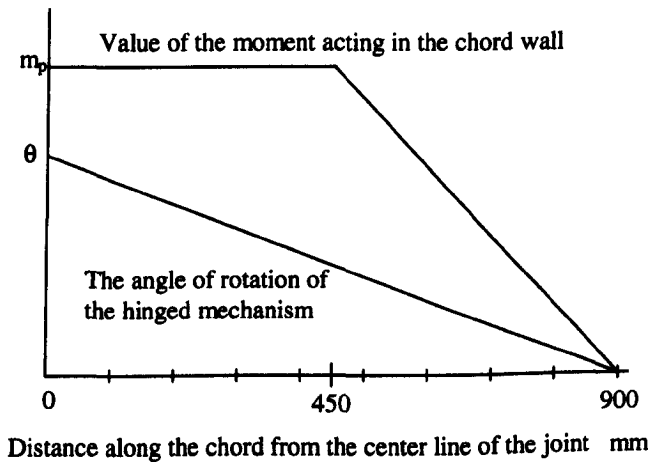


Figure 5.9 The assumed relationship between the moment and the angle of rotation of the yield line along the length of the chord

Figure 5.9 shows the assumed relationship of the moment and the angle of rotation along the length of the chord. If the length of the mechanism is assumed to be L , then summing the work done in the first part of the chord from the centre line to 450mm (0 to $L/2$), the internal work done is

$$= 8 \int_0^{L/2} m_p \left(\frac{L - x}{L} \right) \theta dx + \text{other internal work} \quad \text{Eqn 5.3}$$

However, from the work on short length joint it is known that the total internal work is 135.1δ (yield lines= 79.1δ and in-plane yielding= 56δ) when $\alpha=12$ ($L_0=900\text{mm}$).

Summing the work done by the second part of the mechanism from 450mm to a point A between 450mm and 900mm, the internal work is

$$= 8 \int_{L/2}^A \left(\frac{2(L-x)}{L} \right) m_p \left(\frac{L - x}{L} \right) \theta dx \quad \text{Eqn 5.4}$$

When $A = 900\text{mm}$ the expression becomes

$$= \frac{2}{3} m_p \theta L \quad \text{Eqn 5.5}$$

If the length of the mechanism is assumed to be 900mm, then the total work done by this mechanism, using Eqn 5.5 is 15.3δ . Plotting the values of Eqn 5.4 for the range of chord lengths L_0 (i.e. $\approx 2L$) 900mm to 1800mm ($10.6 < \alpha < 21.2$) and adding them to Figure 5.5 gives the results shown in Figure 5.10.

Examining Figure 5.10 it is observed that whilst the curve produced by Eqn 5.4 has a limiting value and is approximately the shape that should be expected, the predicted capacity of the asymptotic strength is underestimated and the increase in the joint capacity with chord length is overestimated.

This method has tried to calculate the internal work of the failure mechanism by considering the moment acting in the chord wall and an assumed rotation of that moment, with an allowance made for the in-plane yielding observed in the vicinity of the brace. As the asymptotic joint capacity was underestimated and the assumptions made are considered to be reasonable, there must be additional mechanisms operating in the collapse mechanism as this is an upper bound method of calculating the collapse

load. One of these has already been identified as the twisting of the chord wall to allow the angle of rotation to vary between 0 and θ and is discussed in the next section as a semi rigid mechanism.

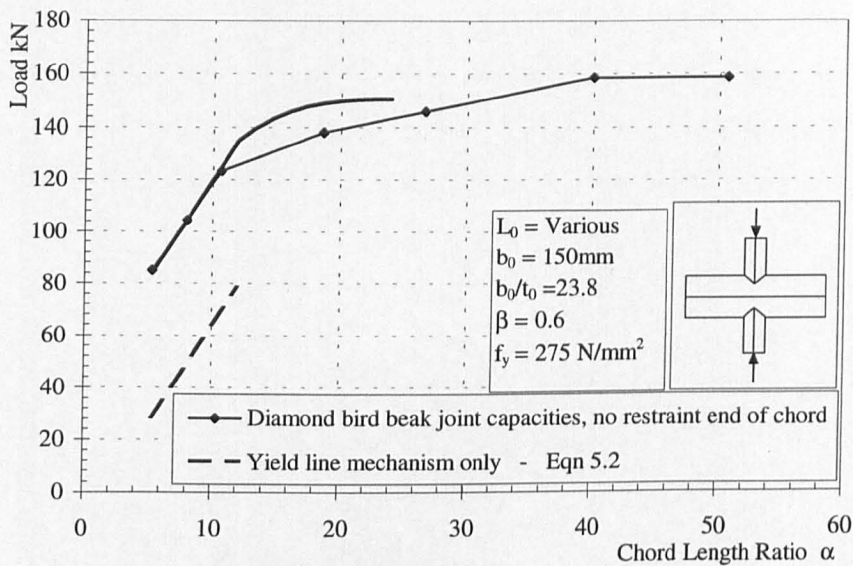


Figure 5.10 A comparison between the finite element joint capacity and the analytical capacity for medium chord length diamond bird beak X joints

5.5 Long chord length joints

This section will consider both plastic and semi-rigid mechanisms which are thought to operating in the collapse mechanism of long chord length joints ($\alpha > 40$ for diamond bird beak joints) and which may be used to estimate the asymptotic collapse load.

5.5.1 Yield line and in-plane yielding mechanisms

This model will use some of the mechanisms identified in the previous sections, but will only consider how the asymptotic collapse load can be determined using plastic mechanisms. Yield line and in-plane yielding mechanisms clearly operate in the collapse mechanism of long chord length joints and this is confirmed by the contoured stress plots shown in Chapter 4 (Figures 4.24 and 4.44 for example) and Figure 5.1. The question remains how can the yield line mechanism be incorporated into an analytical theory to predict the joint capacity?

Togo (1967) used a ring model to describe a yield line mechanism for CHS joints where the yield lines are assumed to have an effective length and run in a direction parallel to the centre line of the chord member, shown in Figure 5.11. The effect of transferring this model directly to the diamond bird beak joint can be seen in Figure 5.12. However, comparisons with the contoured stress plots shown in Chapter 4 (Figure 4.24 for example) reveal that the yield lines are clearly in the wrong position in this model, running along the middle of the chord face instead of at the corners of the chord.

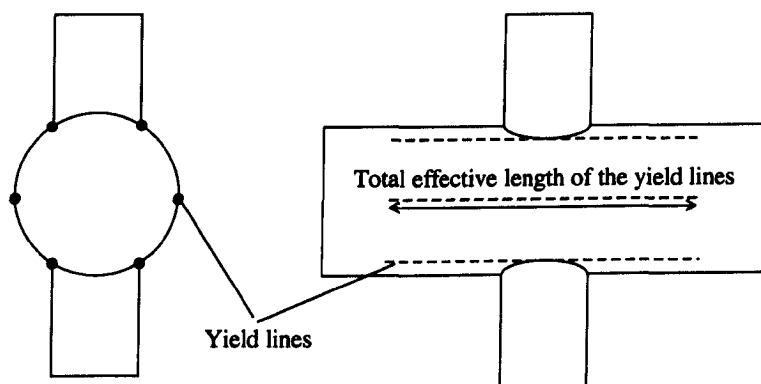


Figure 5.11 Togo's ring model for CHS X joints

This modified ring model is felt to represent the collapse mechanism with a reasonable accuracy with the following exceptions:

- compatibility is not maintained at the end of the mechanism with the undeformed parts of the chord
- the faces of the chord are assumed to be rigid plates and because of this the angle of rotation along the length of the yield lines is constant. This is not the case, a fact which can be established from Figure 5.7 where the deformation varies along the length of the chord and hence the angle of rotation.

Combining the yield line failure mechanism for the short chord length joints with the Togo's ring model produces a modified ring model shown in Figure 5.13. The yield lines are correctly positioned at the corners of the chord and the restraint offered by the brace on the chord is accounted for by the in-plane yielding. The effective length of the yield lines can be calculated by Eqn 5.1, where the asymptotic strength of the diamond bird joint is 158.5 kN, the work done by the in-plane yielding is 568 kNmm

and $m_p = 2728 \text{ Nmm/mm}$. The effective length of the yield lines is then 500mm which is in close agreement with the length of the yield lines observed previously.

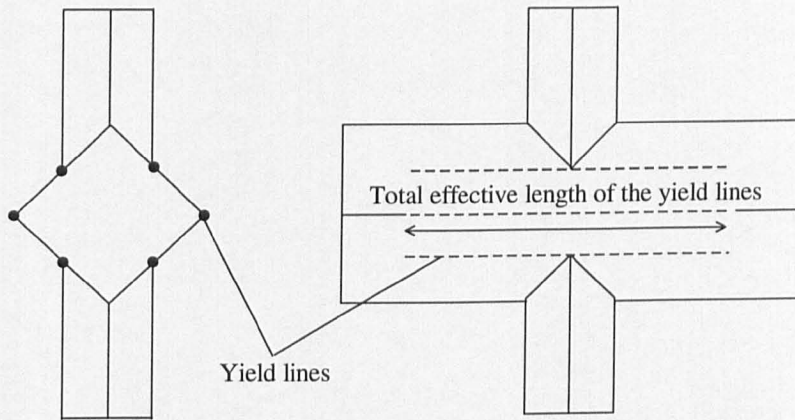


Figure 5.12 Togo's ring model applied to the diamond bird beak X joint

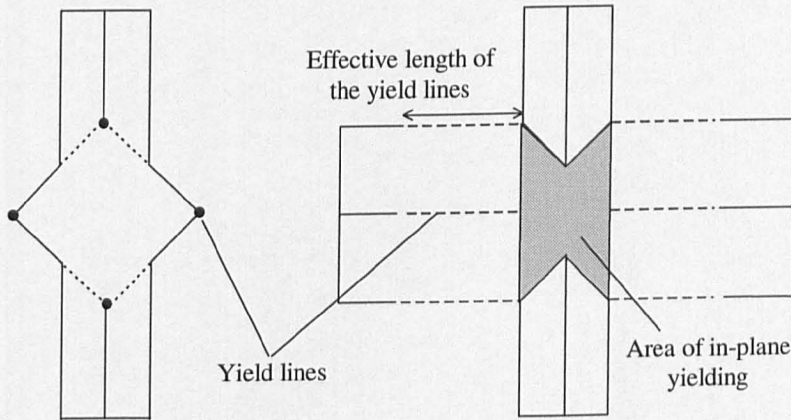


Figure 5.13 Modified ring model for the diamond bird beak X joint

5.5.2 Semi-rigid mechanisms

This section examines some of the semi-rigid mechanisms identified from the deformation of the chord walls and an attempt is made to assess their contribution to the collapse mechanism. The work done in the short and medium chord length joints and identified in Sections 5.3 & 5.4 is included to assess the total work done at the asymptotic joint capacity. (Short chord length, yield line $(L_0/2 - b_1/\sqrt{2} = 386\text{mm}) = 79.1\delta$, in-plane yielding = 56δ and the moment rotation of the medium length joints = 15.3δ .) It is totally independent of the plastic mechanisms discussed in the previous section, 5.5.1.

In order to define the work done by a semi-rigid mechanism at the collapse load, failure is defined as an indentation of $3\%b_0$ (which is the definition used in Chapter 4 to

define the joint capacity when a maximum load was not attained) as the load supported by the semi-rigid mechanism increases with the deflection assumed, shown in Figure 5.14. The semi-rigid internal work is then calculated by $\frac{1}{2} F \delta$, and is entered in Eqn 5.1 as “other internal work” in addition to the work done by the in-plane yielding.

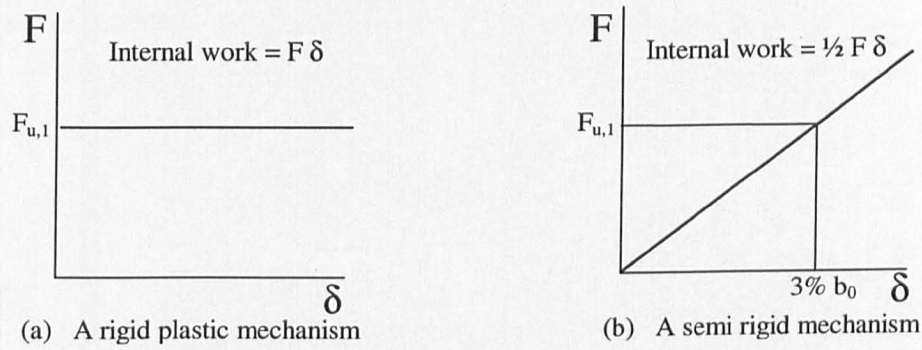


Figure 5.14 Comparisons of plastic and semi-rigid load/deflection curves

5.5.2.1 The twisting of the chord walls

The twisting nature of the deformation of the chord walls can be seen in the series of chord cross sections shown in Figure 4.31 and in a simplified finite element model where the brace was removed and replaced by a single point force acting on the chord shown in Figure 5.15.

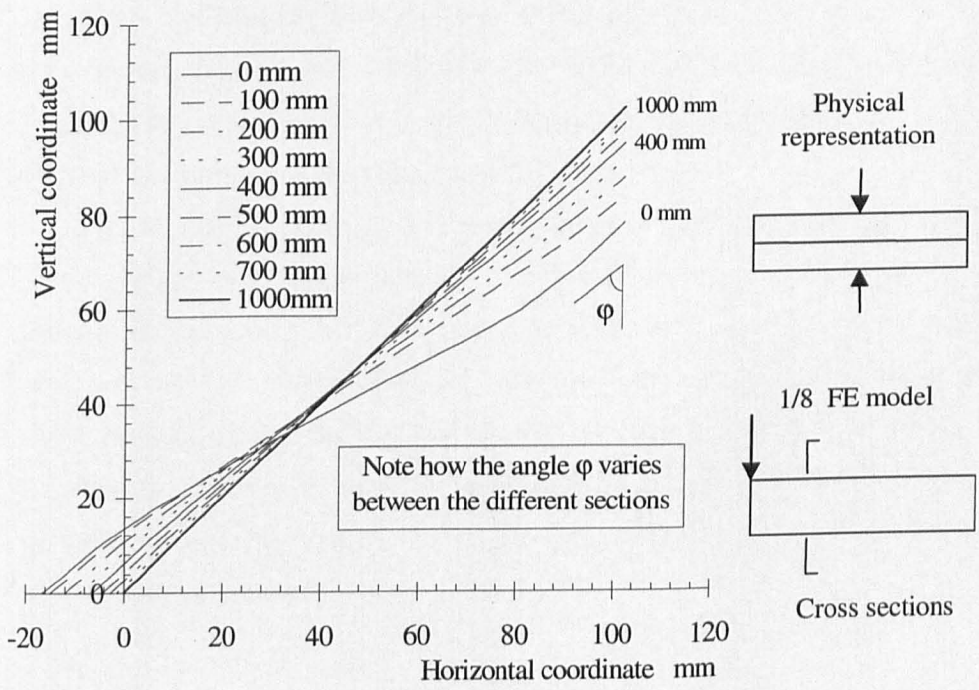


Figure 5.15 Cross section profiles along the length of the model without a brace present

The twisting of the chord face was considered as part of the yield line model instead of the rigid plates when medium chord length joints were discussed. This section will consider the internal work done in twisting the chord face and the effect that it may have on the collapse load. This may be significant in determining the joint capacity when t_0 is large as the internal work done by twisting the chord face is a function of t_0^3 .

The internal work done by this mechanism can be calculated from

$$\frac{1}{2} T \Phi = 4 \left(\frac{1}{2} \frac{G J \Phi^2}{L} \right) \quad \text{Eqn 5. 6}$$

where

T = the applied torque

Φ = the angle through which the chord face is twisted, when a indentation of $3\%b_0$ was imposed on the chord

G = the torsional rigidity modulus

L = the length of the chord face which is considered to be twisted

J = The torsional constant of the chord face $\approx \frac{b_0 t_0^3}{3}$

The internal work done by the twisting mechanism is relatively low. When $t_0=6.3\text{mm}$, $b_0=150\text{mm}$, $G=80\text{kN/mm}^2$, $\Phi=0.042\text{rads}$ and $L=900\text{mm}$ was used for the length of the chord twisted, the internal work done by the twisting of the chord is 2δ . It is therefore considered that this mechanism is of minor importance in determining the collapse load but does help with the resolution of compatibility problems.

If the face of the chord is considered to be twisted, then the angle of rotation varies along the length of the yield line. This rotation has been assumed to vary linearly with the distance along the chord in this work however, the variation could be non-linear with distance. Examination of the deformed shape of the chord, shown in Figure 5.7 for example, reveals that deformation at points of 0mm, 450mm and 900mm from the centre line of the joint is approximately 1δ , 2δ and zero respectively. It is therefore expected that for small changes in geometry that the angle of rotation of the yield line varies linearly with length.

5.5.2.2 The bending of the chord walls

Considering the twist of the chord walls is not a complete mechanism in terms of compatibility of the deformation, as there has to be an additional mechanism for the bending of the chord face about an axis perpendicular to that face. This can be seen in Figure 5.16 which shows a simplified version of the cross section profiles shown in Figure 5.15.

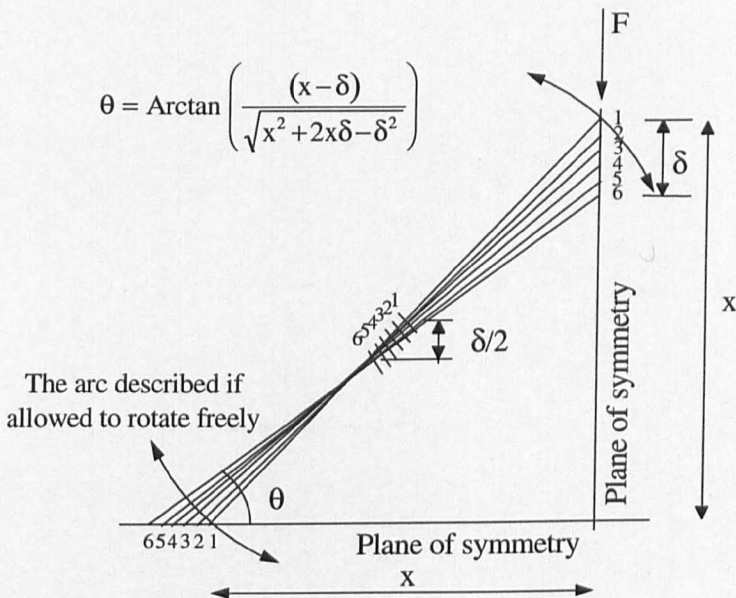


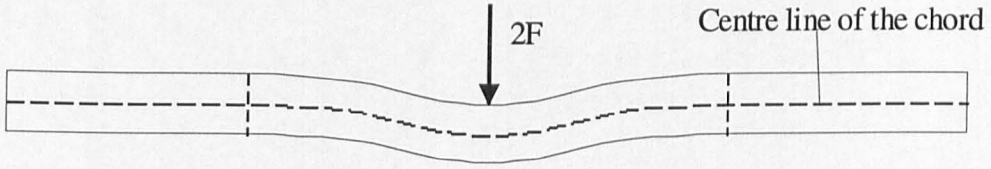
Figure 5.16 A simplified view of the cross section profiles along the length of the model

Each of the profiles is considered as a straight line with a cross at the mid point. If the chord face is subjected to a twisting action only, then there would be no displacement of the crosses at the mid point and the edges of the face would describe an arc shown in the figure. However, due to the boundary conditions the movement of the crosses numbered 1 - 6 indicate the deflection of the centre line of the chord face as the face is twisted. Using simple geometry, the deflection of the chord face in the plane of the face is approximately $\delta / \sqrt{2}$, where δ is the indentation of the chord.

The first assumed shape of the chord face subjected to this bending action is shown in Figure 5.17, where continuity dictates that there is no rotation of the chord face at the ends of the mechanism about an axis perpendicular to the face. The compatibility between the twisting action and the assumed shape of the chord for bending action shown in this figure is not known however, the compatibility at the ends of the mechanism is maintained with adjacent parts of the chord and it is possible that

the angle of twist Φ per unit length is not uniform along the length of the chord face as discussed previously.

The assumed deformation of the chord face due to the bending action only,
viewed perpendicular to the face



The assumed boundary conditions acting at either end of
the deformed part of the centre line of the chord face

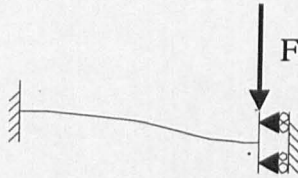


Figure 5.17 The first assumed shape of the chord face under the bending action

The internal work done in the in-plane bending of the chord face in this manner
is

$$\frac{1}{2}Fd = 4 \left(\frac{1}{2} \frac{12EI d^2}{L^3} \right) \quad \text{Eqn 5. 7}$$

where

d = the assumed deflection of the chord face, ≈ 0.7 of the indentation of the chord, δ

E = Young's Modulus ($=207\text{kN/mm}^2$)

I = the second moment of area of the chord face $= t_0 b_0^3/12$

L = the length of the mechanism where the deformation occurs.

If values of $L = 900\text{mm}$, $d = 0.7 \times 4.5\text{mm} = 3.15\text{mm}$ and $t_0 = 6.3\text{mm}$ and $b_0 = 150\text{mm}$ are assumed, then the internal work of this semi-rigid mechanism is 76δ . Adding this into Eqn 5.1 (including terms for the work done by the short and medium length joints) gives a total joint strength of 226.3kN compared to that of 158.5kN obtained from the finite element analysis.

However, it is possible that a different form of bending of the chord face is taking place. One possible alternative is that a plastic hinge forms in the centre of the chord face in the vicinity of the brace member. The work required to rotate this hinge is already accounted for in the in-plane yielding that occurs in this area to maintain continuity between the deformed shapes of the different mechanisms.

The assumed deformation of the chord face due to bending action only,
viewed perpendicular to the face

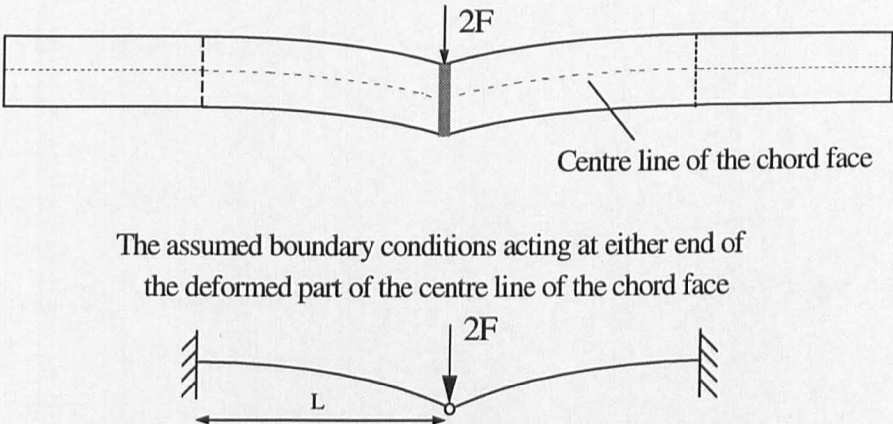


Figure 5.18 The second assumed shape of the chord face under the bending action

The internal work done in the bending of the face of the chord in this manner is

$$\frac{1}{2} Fd = 4 \left(\frac{1}{2} \frac{3EI d^2}{L^3} \right) \quad \text{Eqn 5. 8}$$

Using the same figures as before, the work done by this mechanism is exactly a quarter of that predicted by Eqn 5.7 so that internal work done by this semi rigid mechanism is 198. Adding this into Eqn 5.1 (including terms for the work done by the short and medium length joints) gives a total joint strength of 169.3kN compared to that of 158.5kN obtained from the finite element analysis.

It is likely that the work done by the bending of the chord face lies between these two models however, it is considered that the value tends towards that predicted by Eqn 5.8.

Examination of Eqns 5.7 and 5.8 reveals that the internal work done by the bending of the chord face is a function of b_0^3 in the same manner as the twisting of the chord face was a function of t_0^3 . The work done in bending the chord face is an

important term (whereas the twisting was of minor importance unless t_0 was very large) and the calculated joint capacity will be a function of b_0^3 .

If the same procedure is followed for the square bird beak joints the calculated asymptotic strength is 159.2kN compared to the finite element analysed capacity of 143.5kN. (Calculated by yield line and in-plane yielding 124.9δ, rotation of the moment in the elasto plastic and elastic regions 15.3δ and bending of the chord face 19δ.)

5.6 Discussion

This Chapter has examined the deformed shape of the diamond bird beak X joint and estimated the internal work required to produce each form of deformation observed. Many assumptions have been made during the course of this analysis and the total effect of all these assumptions is not known. The biggest failing is that all the mechanisms examined in this Chapter have had to use prior knowledge of the failure of the joint in order to assume the length of yield lines and the internal work done by the in-plane yielding mechanism. In addition to this, for the semi-rigid mechanisms of the long chord length joints, the indentation at the maximum joint capacity and the length of the mechanism have had to be assumed as well.

Increasing the database of the results for the variation of joint capacity with chord length whilst parameters such as chord width and chord thickness are varied would help establish the relationship between these parameters. It has been shown that the joint capacity is likely to be function of t_0 , t_0^2 , t_0^3 , b_0 and b_0^3 and that complex interaction between the failure mechanisms can be expected as these parameters are varied. However, using the approaches outlined in this Chapter it is likely that a empirical yield line model could be developed.

Two different models were considered to estimate the asymptotic strength of the long chord length joints. In the plastic model the effective length of the yield line was determined however, the deformation assumed is not compatible with the rest of the chord and does not represent the deformation actually observed. This will inevitably cause problems when trying to establish the total effective yield line length for different chord width and slenderness ratios. Regrettably there is insufficient data to establish the in-plane yielding constant of other joints with different parameters where the asymptotic strength is known, so no relationship to determine the total effective yield line length can be made.

The second method using a combination of plastic and semi rigid mechanisms required extensive knowledge of the length of the mechanisms involved however, summing the internal work of the various mechanisms provided a very good estimation of the total work done. It is considered that this mechanism is an impractical method of determining the collapse load of the joint, unless relationships can be established to determine the length of the plastic and semi rigid mechanisms. However, it does provide a good model showing all the mechanisms involved and how the joint capacity may vary as the parameters are changed.

One problem common to both methods is to establish a relationship for the in-plane yielding of the chord material in the vicinity of the brace. It is considered that with a larger database of results this could be easily established. This would also enable the joint capacity of short chord length joints to be determined using the yield line model describe previously.

5.7 Summary

In this Chapter various plastic and semi-rigid mechanisms were examined to assess their contribution to the total collapse mechanism. The classification of the joint according to the length of the chord has helped in identifying the different mechanisms operating in the collapse mechanism.

A plastic collapse mechanism was suggested for short chord length joints, combining a yield line mechanism and in-plane yielding of the chord walls. In the yield line mechanism, the yield lines are positioned at the corners of the chord section and run along the length of the chord free of any restraint from the brace member. The angle of rotation of the yield lines was assumed to be constant along the length of the yield lines. The in-plane yielding of the chord walls is caused by the restraint offered by the brace member in resisting the deformation of the chord. Considerable in-plane yielding of the chord walls is required so that there is compatibility of the deformation in the chord wall between deformation caused by the restraint of the brace member and the yield line mechanism. This is accounted for in the collapse mechanism as an empirical allowance, estimated from the difference between the joint capacity observed and the load supported by the yield line mechanism.

The joint capacity of the medium chord length joints was estimated by considering the work done by the rotation of the moment at the corner of the chord

section in addition to the in-plane yielding in the vicinity of the brace. The result underestimated the work done at the asymptotic strength which was taken as evidence of additional mechanisms operating in the collapse mechanism.

A plastic collapse mechanism was suggested for long chord length joints to calculate the asymptotic strength of the bird beak joints, based on Togo's ring model for CHS joints. This model was then modified to place the yield lines at the corners of the chord and to allow for the restraint offered by the brace. The effective yield line length and the restraint from the brace member had to be estimated by empirical means.

A combination of semi-rigid and plastic mechanisms based on the known deformation of the chord walls was then examined to further the understanding of the collapse mechanism. The plastic mechanism remained the same as for the short chord length joints, whilst the additional work done by the semi-rigid mechanisms was estimated by assuming an indentation at which failure occurred. The internal work done in twisting the chord was found to be of minor importance to the strength of the joint, whilst the work done in bending the chord face about an axis perpendicular to that face was found to be significant, although the strength of the joint was overestimated.

No method was identified in this Chapter in which the strength of the joint could be calculated from the joint's physical specification, all the methods relied on empirical observations to assess the length of the yield line, the length affected by the semi-rigid mechanisms and the restraint offered by the brace. With a larger database of joint capacities obtained from further research it is felt that empirical formula could be established to estimate these unknown quantities.

5.8 Conclusion

It should be recognised that many of the conclusions made here are tentative, with empirically based assumptions and are consequently not proven. This Chapter and the conclusions reached, do however convey to the reader how the failure mechanism is thought to operate and should provide a good starting point for further investigations.

For the long chord length bird beak joints analysed, it has been shown that a reasonable upper bound estimation of the asymptotic joint strength can be made by calculating the internal work done by:

- the yield lines, with a linear variation of the angle of rotation along the length of the yield line

- the in-plane yielding of the chord wall in the vicinity of the brace member
- the rotation of the moment in the elasto plastic and elastic regions
- the bending of the chord face about an axis perpendicular to the face of the chord when a plastic hinge of negligible stiffness is formed at the centre of the chord face

The work done in twisting the chord face was found to be of minor importance and for this and most other chord thicknesses and it can be ignored.

Good estimates can be made for short chord length joints by calculating the internal work done by:

- the yield lines
- the in-plane yielding of the chord wall in the vicinity of the brace member

The estimation of the joint capacity for the medium length joints underestimated the asymptotic strength and overestimated the joint capacity with increasing chord lengths. Obviously there is some degree of bending of the chord face, which has been considered for the long chord length joints, but this could not be incorporated into this model as the end of the mechanism cannot be assumed to be held encastré.

6.

The effect of member orientation in T joints

6.1 Introduction

The effect of the orientation of the members of T joints will be discussed in this Chapter by examining traditional RHS and diamond bird beak T joints, where $\theta = 90^\circ$ and the brace member is axially loaded. The results of the finite element analyses for these joints are presented and compared to establish what effect the orientation of the chord has on the joint capacity. The variation of the joint capacity with the chord length is then investigated for both the traditional RHS and the bird beak T joints.

In traditional methods of T joint design, the local joint capacity is found from the design recommendations in the appropriate design code which have been established from physical tests. The moment capacity of the chord is then checked separately. However, the interaction between the local joint failure and the overall chord failure is liable to have an effect on the capacity of the connection itself leading to a possible overestimate (or underestimate) of the capacity of the connection. In this Chapter the interaction method, first proposed by van der Vegte (1994b) will be used where all the factors which affect the strength of a T joint, including the moment acting in the chord, are combined into one diagram. The interaction relationship is established by considering the local joint capacity, i.e. the joint capacity when the bending moment in the chord at the joint is zero and the moment capacity of the chord reduced to allow for the effects of shear in the vicinity of the brace member. The interaction between the joint strength and the moment operating in the chord is then defined by

$$\frac{\text{The joint capacity}}{\text{The local joint capacity}} \quad \text{and} \quad \frac{\text{The moment operating in the chord}}{\text{The reduced moment capacity of the chord}}$$

In this Chapter the interaction relationship is established by examining T joints of different chord lengths whilst the parameters of chord slenderness and width ratio are varied to find how the joint capacity is affected by the moment acting in the chord. Then local joint capacity for each combination of chord slenderness and width ratio examined previously, is found by analysing a series of T joints where the effects of

chord bending have been eliminated by applying a moment to the chord such the bending moment under the brace is zero. Finally the reduced moment capacity of the chord is calculated theoretically. These results are plotted on the interaction diagram in the manner shown in Figure 6.1.

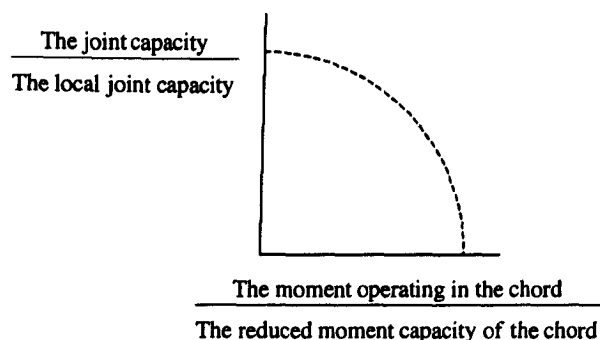


Figure 6.1 An example of the interaction diagrams consider in this Chapter

The method by which van der Vegte determined the local joint strength without the effects of chord bending will be examined and improvements to the method suggested. As a comparison to the bird beak joints, similar traditional RHS T joints are examined in the same manner and the differences between the interaction diagrams of the traditional RHS T joints in this work and those published by Yu (1996) will be noted. Finally the different interaction curves for the traditional RHS, CHS and diamond bird beak T joints will be compared and discussed to establish the variation in the behaviour of the various joint configurations.

A limited amount of experimental testing of diamond bird beak T joints was carried out by Steller (1996) in the Civil Engineering laboratory at Nottingham University. The results from this work are reported and are used to validate the models used in this Chapter.

6.2 The model details of the T joints studied

The general arrangement of the traditional RHS and the diamond bird beak T joints considered in this Chapter are shown in Figure 6.2. The diamond bird beak T joint is formed by rotating the brace and the chord members through 45° about their own centre line axes. The square bird beak T joint is not considered in this Chapter as it is expected that its behaviour will be very similar to the diamond bird beak T joint. The traditional RHS T joint is formed in the traditional manner.

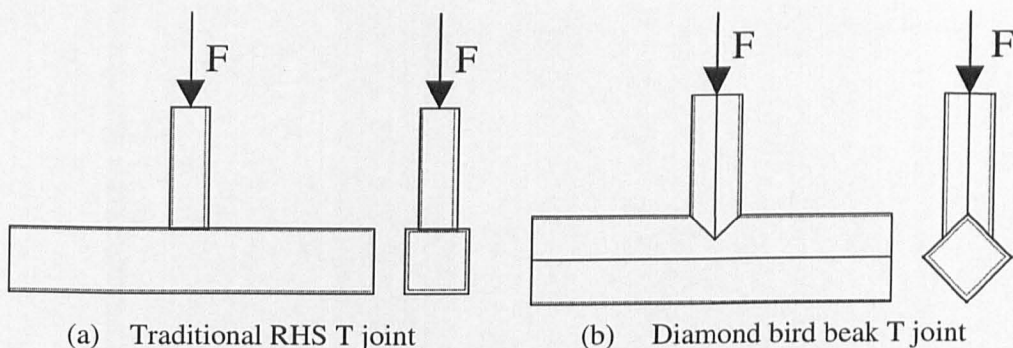


Figure 6.2 The traditional RHS and diamond bird beak T joints studied

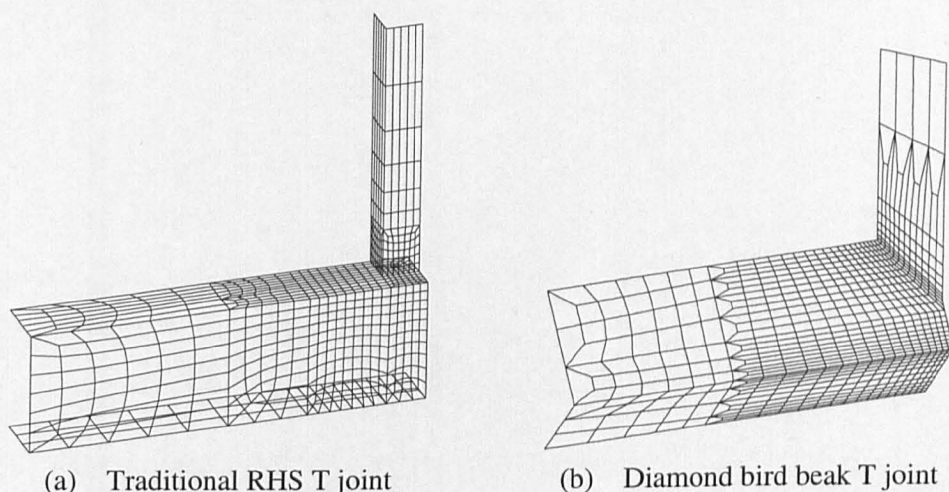


Figure 6.3 Examples of the finite element mesh for the traditional RHS and diamond bird beak T joint

T joints with an axial force applied to the brace member have two planes of symmetry, so that only one quarter of the joint need be modelled. The rest of the joint is represented by the symmetrical boundary conditions on the planes of symmetry. Examples of the finite element meshes used to represent the different forms of T joint analysed in this Chapter are shown in Figure 6.3

6.3 The method of loading

All the joints analysed in Section 6.10, where the effects of chord bending are considered, have been loaded by an axially compressive force applied to the brace member only. The load is applied uniformly to all the nodes at the end of the brace with the exception of the nodes on the planes of symmetry, where only half the load is applied. This is shown in Figure 6.4a. Later in this Chapter, in Section 6.11, the effects of chord bending will be removed to find the local joint strength by loading the joint in

the manner shown in Figure 6.4b. This is described in more detail later however, it is important not to confuse the two methods of loading.

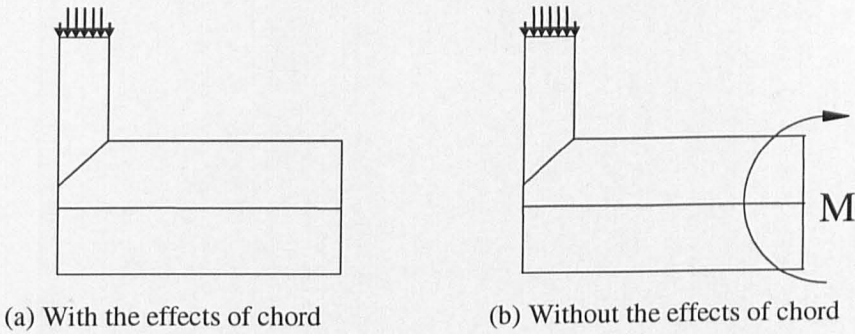


Figure 6.4 The two methods of loading the diamond bird beak T joint

6.4 The material properties

The same properties used in Chapter 4 are also used in this Chapter, that is an elastic/perfectly plastic material with Young's Modulus $E = 207 \text{ kN/mm}^2$ and a yield stress of $f_y = 275 \text{ N/mm}^2$. The reason for this choice is to aid the analytical analysis of the failure mechanisms, which are discussed in Chapter 5.

6.5 The method of supporting the chord

Traditionally T joints are tested with a thick diaphragm plate on the end of the chord to transfer the reaction from the chord to the base of the test machine. However, in Chapter 4 it was established that the boundary conditions at the end of the chord influenced the behaviour of the X joint and its capacity. An example of how the boundary conditions at the end of the chord affect the behaviour of the T joint occurs when the models loaded without the effects of chord bending are analysed with a thick plate supporting the end of the chord and is discussed in more detail in Section 6.5. Chord lengths longer than $\alpha = 12$ could not be analysed without the calculation becoming unstable, i.e. the load increment tending to zero at a relatively low load. To overcome this problem the nodes at the end of the chord were supported in a vertical direction only for all the models considered. This is shown in Figure 6.5 where the nodes at the end of the chord are allowed every degree of freedom except that of vertical displacement.

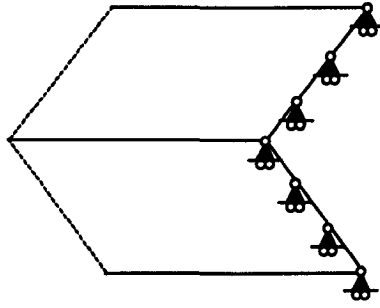


Figure 6.5 The method of supporting the end of the chord

It is acknowledged that this method of support cannot be replicated in the laboratory or in a structure however, it does have the advantage that a minimum amount of restraint is applied to the end of the chord. This is important as it has been established in Chapter 4 that the shorter chord length joints will be strengthened by any restraint imposed at the end of the chord. It is unfortunate that imposing a vertical restraint at the end of the chord has the most influence on the joint capacity however, this is unavoidable when analysing T joints.

6.6 The type of weld assumed

A butt weld was assumed for all the joints analysed in this Chapter, for similar reasons to those discussed in Chapter 4. These were:

- the angle of intersection between the faces of the chord and the brace members for the diamond bird beak joint is 120° , the limit for considering fillet welds
- the distorted shape of the elements to model the weld material, caused by the geometry of the joint could not be analysed
- the strength of the weld does not mask the natural strength of the joint and so true comparisons can be made between different joint configurations

6.7 The method of measuring the indentation

As models with different chord lengths are analysed, it is not very useful to observe the deflection of the brace, as all that is measured is the stiffness of the chord. To overcome this problem the indentation is observed between a point on the brace close to the chord (approximately a distance of $0.75b_1$ from the toe of the brace) and the bottom corner of the chord, shown in Figure 6.6. The load/indentation curves achieved by this method reflect the stiffness of the whole joint.

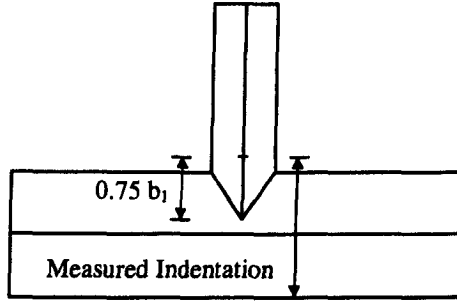


Figure 6.6 The datum point for the measuring the indentation of the diamond bird beak T joint

6.8 The moment capacity of the chord

The elastic moment capacity of the chord when a square section is used for a traditional RHS T joint is

$$M_e = \frac{2 I f_y}{b_0} \quad \text{Eqn 6.1}$$

and when an identical section is used for the diamond bird beak T joint it is

$$M_e = \frac{\sqrt{2} I f_y}{b_0} \quad \text{Eqn 6.2}$$

where the value for the second moment of area I is the same in both configurations because the product moment $I_{xy} = 0$ due to the symmetry of the section.

It can be seen from Eqns 6.1 and 6.2 that the elastic moment capacity of the chord in the traditional RHS chord section is higher than the diamond bird beak section and hence yielding will occur first in the diamond bird beak section.

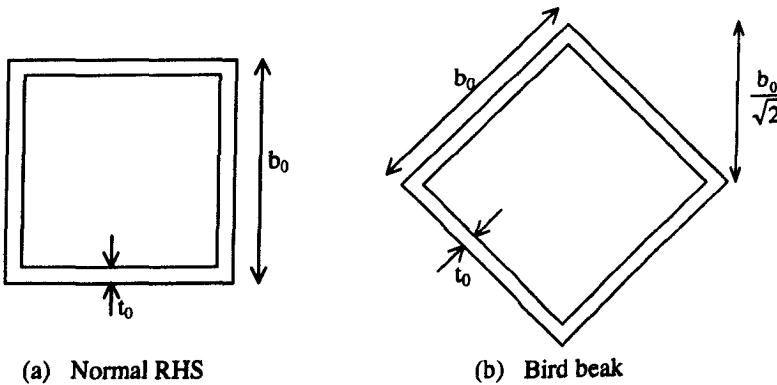


Figure 6.7 The orientation of the chord in the traditional RHS and bird beak joints

The approximate plastic moment capacity of the chord when used for traditional RHS joints can be estimated from

$$M_p = 1.5b_0^2 t_0 f_y \quad \text{Eqn 6.3}$$

but is calculated exactly from (ignoring the corner radii)

$$M_p = \left[\frac{b_0^2}{2} + (b_0 - t_0)(b_0 - 2t_0) \right] f_y t_0$$

$$M_p = 1.5 \left(b_0^2 t_0 - 2b_0 t_0^2 + \frac{4}{3} t_0^3 \right) f_y \quad \text{Eqn 6.4}$$

when allowances are made for the corners of the section.

The approximate plastic moment capacity of the chord when used in diamond bird beak joints can be estimated from

$$M_p = \sqrt{2} b_0^2 t_0 f_y \quad \text{Eqn 6.5}$$

However, a better estimate can be made from

$$M_p = \sqrt{2} (b_0 - t_0)^2 t_0 f_y$$

$$M_p = \sqrt{2} \left(b_0^2 t_0 - 2b_0 t_0^2 + t_0^3 \right) f_y \quad \text{Eqn 6.6}$$

The exact value of the plastic moment capacity can be obtained by calculus

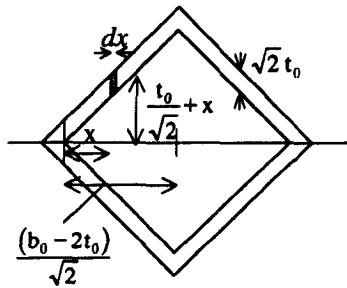


Figure 6.8 Calculation of the plastic moment of the chord for a diamond bird beak joint by calculus

$$M_p = 4 \left[\frac{(\sqrt{2}t_0)^2}{2} \frac{\sqrt{2}t_0}{3} f_y + \int_0^{\frac{(b_0-2t_0)}{\sqrt{2}}} \sqrt{2}t_0 f_y \left(\frac{t_0}{\sqrt{2}} + x \right) dx \right]$$

$$M_p = \sqrt{2} \left(b_0^2 t_0 - 2b_0 t_0^2 + \frac{4}{3} t_0^3 \right) f_y \quad \text{Eqn 6.7}$$

Comparing the plastic moment capacities of the two different sections using Eqns 6.4 and 6.7 it can be seen that the plastic moment capacity of the traditional RHS configuration is only slightly larger (1.5 opposed to 1.414) and so it will be expected that the diamond bird beak configuration will fail plastically at a slightly lower moment. Examining Eqn 6.6 and Eqn 6.7 it is found that the difference between these two equations is only $\approx \frac{1}{2} t_0^3$ and for all practical purposes Eqn 6.6 can be used to calculate the plastic moment of the diamond bird beak section.

Sections with corner radii will have different values for the moment capacities, which would have to be calculated by numerical integration techniques. This difference may be particularly significant if cold rolled sections are considered with their larger corner radii.

6.9 Validation of the model

To ensure optimum meshing of the model, a convergency test was carried out to establish the number of elements and their best arrangement. Then to ensure that the failure modes are accurately reproduced in the finite element model, a comparison is made between physical tests carried out in the civil engineering laboratories at Nottingham University by Steller (1996) and the finite element analyses of the models.

6.9.1 Convergency tests

In the convergency tests three different models were analysed, coarse, medium and fine (280, 546 and 845 elements respectively). The results of these analyses are given in Table 6.1 and the load/indentation curves are shown in Figure 6.9. The CPU time required for the analysis of the fine mesh was 1.75hrs, which when extra elements were added to lengthen the chord, was thought to be the optimum number of elements that could be used so that the analysis was completed in the 2hr CPU queue.

During the convergency test it was realised that the elements could be rearranged to improve the mesh density in areas of stress concentrations. This was done in model TB45V5 and resulted in a decrease of the joint capacity of 8kN (3.2%). It was not thought necessary to repeat the convergency tests as the optimum number of elements had been determined for the 2hr CPU time queue and there was a convergency between the fine and medium meshes with the original mesh.

Model	Number of Elements	Maximum Load kN
TB45V2	280	284.7
TB45V3	546	257.6
TB45V4	845	257.0
TB45V5	881	249.0

Table 6.1 The results of the convergency test

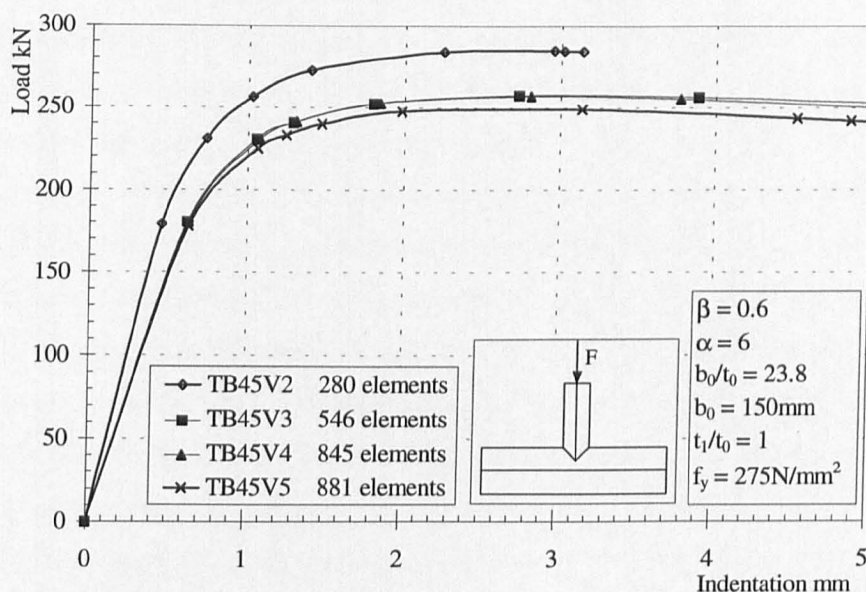


Figure 6.9 The load/indentation curves for the convergency tests

		T1	T2	T3
Chord length	L_0	450mm	900mm	1350mm
Chord length ratio	α	6	12	18
Chord breadth (Nom.)	b_0	150x150mm	150x150mm	150x150mm
Brace breadth (Nom.)	b_1	90 x 90mm	90 x 90mm	90 x 90mm
Wall thickness (Nom.)	t_0 & t_1	6.3mm	6.3mm	6.3mm

Table 6.2 The nominal dimensions of the diamond bird beak T joints tested by Steller (1996)

6.9.2 Validation of the finite element models

In order that the results from the finite element models may be considered valid they need to be compared with physical test results. Steller (1996) tested three diamond bird beak T joints in the Civil Engineering laboratories at Nottingham University with the nominal dimensions given in Table 6.2 and the measured values given in Table 6.5.

6.9.2.1 Introduction

The experimental tests carried out by Steller (1996) used cold rolled sections which have two appreciable differences to hot formed sections used previously in the X joint tests and assumed in all the finite element models - the material properties and the cross section profile.

The material properties of a cold formed section are changed due to the cold working of the RHS section as it is manufactured and rolled from a circular to a rectangular section. The work hardening and subsequent loss in ductility caused by this deformation is not removed by heat treatment. The effect of this on the stress strain relationship is to decrease the elongation at failure and to mask the true yield strength of the material. (The design yield stress of the material is then taken as the 0.1% proof stress, which may lead to an increase in the yield stress used in the design process). These material properties can be determined by tensile test coupons cut from the side walls of the section being tested. The problem in modelling a cold formed section is that the corners of the section, which have been deformed to a greater extent than the sides will have different material properties, due to the extra work hardening that has taken place and that this change in the properties is not known. It is likely that the design yield stress (0.1% proof stress) in corners of the section has been increased up to a value approaching the ultimate tensile stress of the material. This will significantly affect the strength of bird beak joints, which are formed on the corners of the sections and derive much of their strength from the stiffness of the corners.

Section	Hot Finished		Cold Formed	
	Maximum ¹	Actual	Maximum ²	Actual
90x90x6.3mm	12.6mm	7.5mm	18.9mm	18.0mm
150x150x6.3mm	12.6mm	7.1mm	18.9mm	12.0mm

1 Defined in BS4848 as 2.0t

2 Defined in BS6363 as 3.0t

Table 6.3 The outside corner radii of the hot rolled and cold formed sections used in the validation of the X and T joints respectively

The second major difference of cold formed sections, is the cross sectional profile of the section. In order that the residual stresses and the loss in ductility is not excessive, the cold formed RHS are produced with larger corner radii than the hot finished sections. The differences in corner radii are shown in Table 6.3, where the

maximum is defined in the respective British Standard. The values for the actual corner radii are from the tested joints, hot finished sections being used for the testing of the X joints described in Chapter 4 and cold formed sections being used in the testing of T joints described in this section. It can be seen that there are appreciable differences between the two sections formed by different processes, particularly in the case of the 90x90x6.3mm section.

No corner radii have been modelled for the majority of joints in this thesis and Crockett (1995) found there was little to be gained from modelling the corner radii in RHS section for traditional RHS joints. However, the effect of the larger corner radii of cold formed sections on the bird beak joints is likely to be completely different because:

- the bird beak joints are formed on the corners of the section and this will affect the transference of the load from the brace to the chord member
- when considering the yield line failure model of a traditional RHS joints it makes no difference if the yield line is assumed at the corner of the chord section or in the chord wall
- of the change in the moment capacity of the chord when considering bird beak T joints due to change in the cross section profile

In order to investigate the effect of the corner radii and to model the test joints as closely as possible, corner radii were modelled in some of the joints used for the comparisons with the experimental results and compared to models where the corner radii was not modelled. The same material properties were used in all the models.

6.9.2.2 The general arrangement of the joint

The reaction from the load applied to the brace of the T joint is transferred to the base of the testing machine by a 15mm plate, welded to the ends of the chord and a roller bearing under the plate. This arrangement is shown in Figure 6.10. This was modelled in the finite element representation as a roller bearing at the bottom of the plate, which should be an accurate representation providing there is no friction in the physical roller bearing.

Regrettably, in order to measure the lozenging of the chord, a hole was flame cut in the 15mm plate to provide access into the inside of the chord section. This is also reproduced in the finite element model as accurately as possible however, due to

the irregularities of the edges of the hole, errors may be expected in estimating the stiffness and strength of the end plate. After testing the first T joint ($\alpha = 12$), the end plate was noticeably deformed and in the remainder of the tests ($\alpha = 6$ and 18) the end plate was reinforced by two steel bars 38x25mm in the manner shown in Figure 6.11.

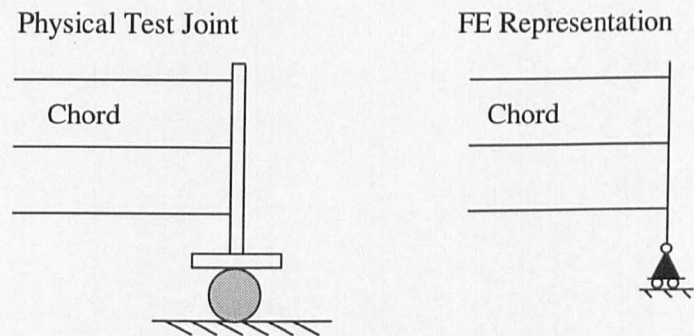


Figure 6.10 The support arrangements at the ends of the chord

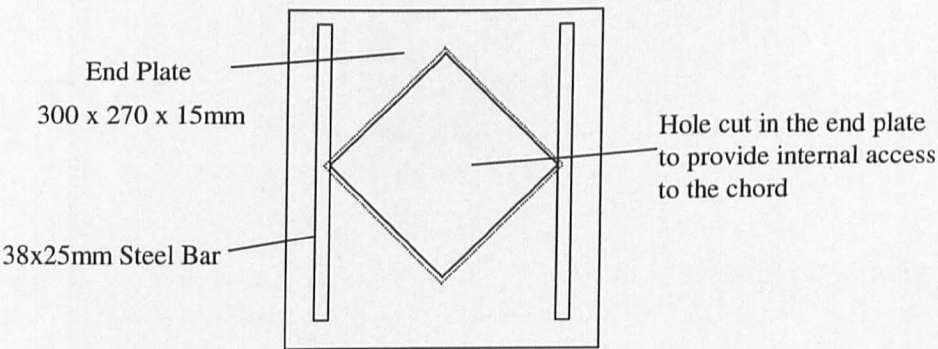


Figure 6.11 The plate at the end of the chord

The deformation of the end plates in the first test demonstrates the importance of the chord end conditions in assessing a joint’s strength. Doubtless the failure of the end plate affected the failure capacity of the joint tested. Although all these factors are represented in the finite element models as accurately as possible, estimates have had to made of the material properties of the end plate and the reinforcing bars as they were not derived from tensile test coupons. The accuracy of these estimates will affect the accuracy of the joint strength comparison and the reliability that can be placed on the results because unfortunately the strength of the support arrangement used was not sufficient and influences the strength of the T joint observed.

6.9.2.3 The material properties

The material properties of the sections used for the chord and brace were found by tensile test coupons cut from the sides of the respective section. The material properties found during the tensile test are given in Table 6.4 and shown in Figure 6.12 where the stress and strain relationship is given as an engineering stress/strain relationship. (This is changed to a true stress/strain relationship using Eqns 3.1 and 3.2 before it is entered into the finite element models.)

Chord		Brace	
Stress N/mm ²	Strain	Stress N/mm ²	Strain
0	0.0000	0	0.0000
420	0.0021	360	0.0017
440	0.0026	380	0.0023
460	0.0037	400	0.0031
480	0.0084	440	0.0085
500	0.0196	462.5	0.0395
520	0.0471	460	0.14
524	0.0796		
520	0.12		
518	0.14		

Table 6.4 Engineering stress/strain relationship of the test joints and used in the finite element analyses to validate the diamond bird beak T joint models

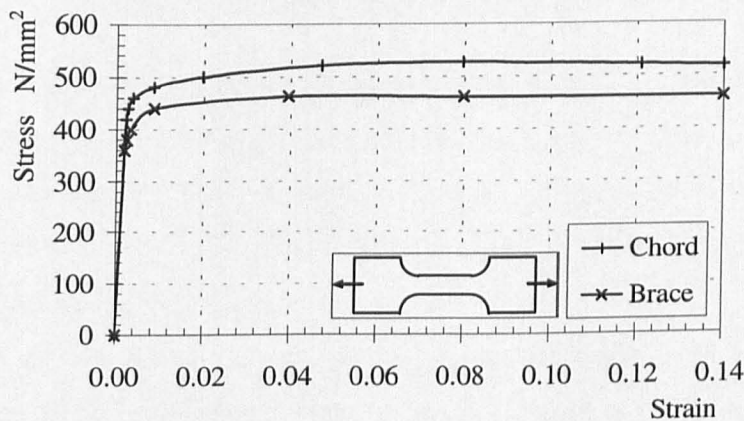


Figure 6.12 Engineering stress/strain relationship of the test joints and used in the finite element analyses to validate the diamond bird beak T joint models

6.9.2.4 The physical properties

The physical properties of the joints tested reported by Steller (1996) are given in Table 6.5 and were used in the construction of the models used to validate the finite element work. During the work on the validation of the models, both straight corner models and radii corner models are considered. The straight corner models had no corner radii modelled and are identical to the parametric models used in this Chapter, whereas the radii corner models had the radii modelled but are otherwise identical to the straight corner models considered in this validation procedure. (All the joints had the same material properties, that of the cold formed section.) The inclusion of the corner radii necessitated the inclusion of 125 extra elements so that the curvature of the corner radii could be modelled without the elements being considered unduly distorted.

		Chord mm		Brace mm
Outside dimensions	b_0	152.5	b_1	94
Wall Thickness	t_0	5.77	t_1	5.89
Outside Radius	-	12.0	-	16.13
Inside Radius	-	4.41	-	10.5
		N/mm ²		N/mm ²
0.1% Proof stress	f_y	445.5	f_y	387.1
UTS		524		462

Table 6.5 Physical properties of the test joints and used in the finite element analyses to validate the diamond bird beak T joint models

Fillet welds were modelled in these finite element models to represent the weld material in the physical joint. The welding of the joints was very irregular and untidy due to the slope of the weld surfaces of the joint. However, observations made indicated a throat thickness of 6.2mm, which is used in the models.

6.9.2.5 Comparison of the results

The load/indentation and the load/lozenging curves for the test joints and the finite element models representing them are given in Figure 6.13. These results are summarised in Table 6.6, giving the maximum joint capacity observed and the initial stiffness of the load/deflection curves. (The initial stiffness has been calculated by considering the deflection observed at approximately 40% of the maximum load and assuming that the joint behaves elastically in this range.)

The finite element analysis predicts the maximum joint capacity with reasonable accuracy for all the radii corner models (3.3%, 0.2% and 1.8% when $\alpha = 6$, 12 and 18 respectively) however, the straight cornered models overestimated the maximum joint capacity (7.6% and 7.9% when $\alpha = 6$ and 18 respectively).

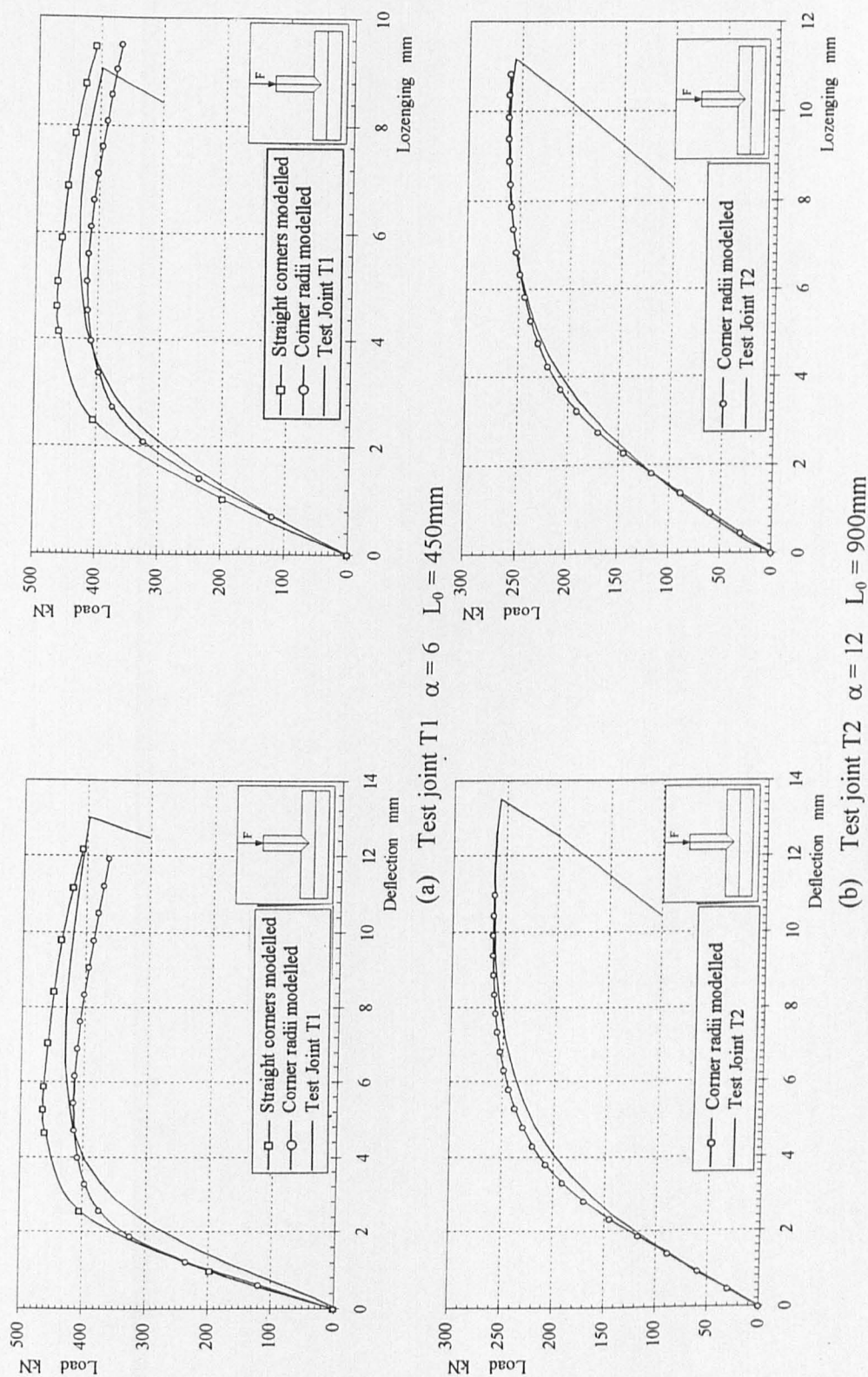


Figure 6.13 Load deflection and load lozenge curves for the diamond bird beak T joints used to validate the finite element models

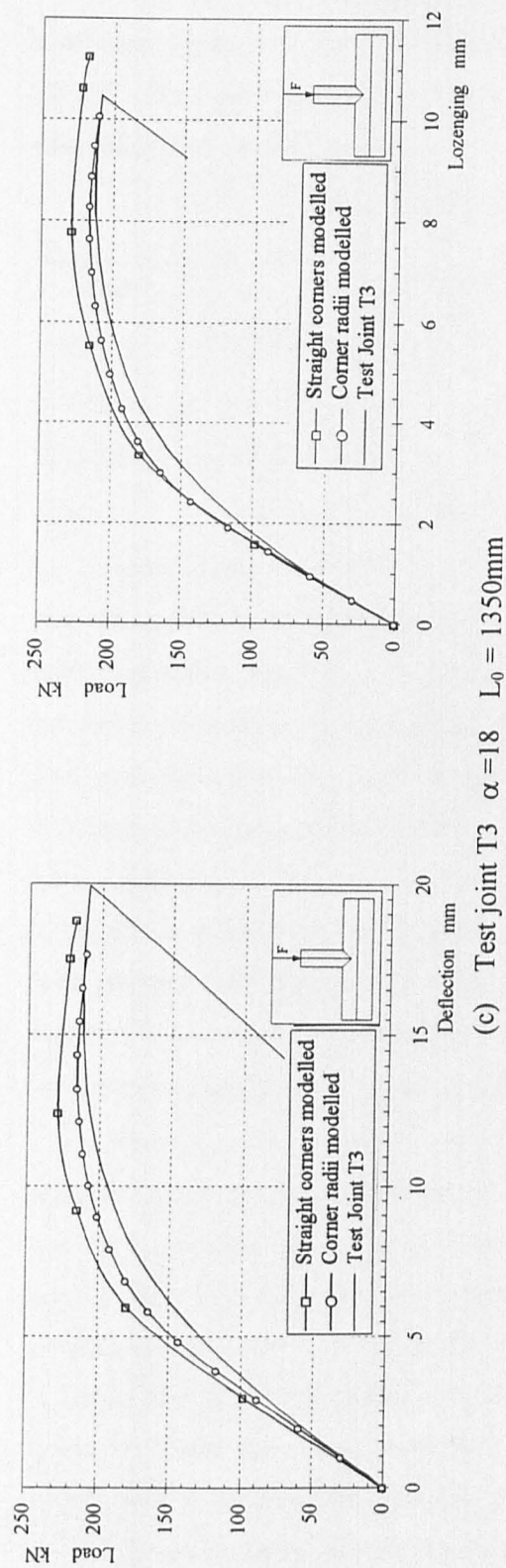


Figure 6.13 (cont.) Load deflection and load lozenging curves for the diamond bird beak T joints used to validate the finite element models

	Straight cornered models		Corner radii models		Test Joint	
	Initial stiffness kN/mm	Max Load kN	Initial stiffness kN/mm	Max Load kN	Initial stiffness kN/mm	Max Load kN
T1	198.3	463.6	188.7	416.4	140.1	430.7
T2	-	-	62.6	261.2	59.6	260.6
T3	33.3	228.9	30.4	216.2	24.3	212.2

Table 6.6 A comparison of the initial stiffness and maximum joint capacity for the validation of the diamond bird beak T joint models

The deformation at the maximum load predicted by the finite element models in all cases under-estimated the deformation observed in the physically tested joints by 15-25%. This may be seen in Table 6.7 where the deformation observed at the maximum joint capacity is given.

		Corner radii model		Straight corner model		Physically tested joints	
Model	α $2L_0/b_0$	Load kN	Deflect. mm	Load kN	Deflect. mm	Load kN	Deflect. mm
T1	6	416.4	5.45	463.6	5.27	430.7	7.35
T2	12	261.2	9.93	-	-	260.6	11.68
T3	18	216.2	14.45	228.9	12.45	212.2	16.89

Table 6.7 The deflection at maximum joint capacity

Considering the results of each joint shown in Figure 6.13 in turn, it can be seen that in addition to these general observations that when $\alpha = 6$ in joint T1, there are significant differences between the load/deflection curves for the physically tested joint and those predicted by finite element analysis. This is thought to be due to the end plate and the reinforcing bars at the end of the chord influencing deformation behaviour of the joint (the effect of which is not entirely known). The load/lozengeing curve, which is not influenced by the conditions at the end of the chord to the same extent, shows a better correlation between the curves. The joint capacity predicted by finite element analysis based on straight cornered models is 11% greater than that predicted for the corner radii models, showing that for the bird beak joints there may be a substantial difference in the joint capacity depending on the type of section used.

When $\alpha = 12$ in joint T2, there appears to be good agreement between the predicted curves and those observed for the physical test. In this particular joint there were no reinforcing bars on the end plate of the chord and at the maximum joint capacity there was considerable deformation of the end plate. This in turn caused considerable deflections at the centre of the chord with little change in the load recorded. This appears to make the comparison between the curves better than it should be. Table 6.6 shows that there is a large difference in the deflection at maximum joint capacity, but as there is little difference in the load applied to the brace, this cannot be seen in the load deformation curves shown in Figure 6.13b.

When $\alpha = 18$ in joint T3, there is again a substantial difference between the predicted load deformation curves and those observed for the physical test. There are reinforcing bars on the end plate of the chord for this joint however, they should affect the joint strength less because of the longer chord length and the lower joint capacity observed, although this cannot be seen by comparing Figure 6.13 a & c. The load/lozenging curves show a better correlation between the predicted and the observed deformation than the load/deflection curves although there are still significant differences in the stiffness of the joints. The difference between the finite element analysis prediction of the straight cornered model and the corner radii model joint capacity is reduced to 6% as the mode of failure becomes that of a chord bending failure due to the longer chord length.

6.9.2.6 Conclusions

From the examination of these results, it is concluded that:

- when the physically tested joints are compared against the finite element models with corner radii modelled there is a good agreement between the predicted and observed joint capacities. However, the experimental deformation (deflection or lozenging) is underestimated in all the finite element models by approximately 20% at maximum load.
- when the physically tested models are compared against the finite element models with straight corners the joint capacity is overestimated by 7 - 8%. Again the experimental deformation is underestimated by approximately 25% at maximum load in the finite element models.
- there are appreciable differences in the joint strength in the finite element model depending on whether straight or radii corners are used to form the joint and that the cause of this difference is the shape of the cross section profile as the same material properties have been used.

6.10 Diamond bird beak T joint with the effects of chord bending

The variation of the joint capacity including the effects of chord bending (loaded in the manner shown in Figure 6.4a) with chord length will be examined in this section. The moment operating in the chord at failure will be examined and compared to the calculated plastic moment capacity to establish how the chord may be expected

to fail when the chord wall thickness and chord length are varied. The displaced shape diagrams, von Mises contoured stress plots, the load/indentation curves and the moment/deflection curves are then studied to show what effect the variation of chord length has on the respective diagrams for those joints where $b_0/t_0=23.8$.

The joint capacities predicted by the equation published by Ishida et al (1993) are then compared to joint capacities predicted by finite element methods to establish the accuracy of the Ishida's equation and using the results contained in this work a different equation is presented to estimate the joint capacity of the diamond bird beak T joint. Finally, the design methods used at present are examined to study how the variation in chord length and the effect that this has on the joint capacity is allowed for in the design recommendations. The joint capacities estimated from the design codes for various chord lengths are then compared to the finite element joint capacities.

Model	Chord Length L_0 mm	α $\frac{2L_0}{b_0}$	t_0 mm	$\frac{b_0}{t_0}$	$F_{u,1}$ kN	$F_{u,1}$ kN (With end plate)	$\frac{F_{u,1} L_0}{4M_{p, chord}}$	$\frac{F_{u,1} (L_0 - \sqrt{2} b_0)}{4M_{p, chord}}$
TBV8	450	6	4.25	35.3	104.8	(132.9)	0.426	0.241
TBV5	450	6	6.3	23.8	202.5	(249.0)	0.450	0.478
TBV9	450	6	10.0	15	407.7	(495.0)	0.601	0.657
TBV10	450	6	16.0	9.4	786.8	(915.7)	0.792	0.879
TBV20	900	12	4.25	35.3	86.81	(102.2)	0.556	0.323
TBV19	900	12	6.3	23.8	161.3	(183.6)	0.717	0.616
TBV21	900	12	10.0	15	322.5	(342.5)	0.951	0.835
TBV22	900	12	16.0	9.4	601.8	(607.4)	1.211	1.006
TBV16	1350	18	4.25	35.3	75.52	(80.5)	0.725	0.432
TBV12	1350	18	6.3	23.8	138.2	(140.9)	0.921	0.817
TBV17	1350	18	10.0	15	247.2	(247.6)	1.094	0.991
TBV18	1350	18	16.0	9.4	415.2	(415.4)	1.254	1.051
TBV13	2700	36	4.25	35.3	48.0	(47.0)	0.922	0.568
TBV11	2700	36	6.3	23.8	79.2	(76.2)	1.056	1.040
TBV14	2700	36	10.0	15	124.6	(124.3)	1.103	1.136
TBV15	2700	36	16.0	9.4	202.1	(201.5)	1.220	1.163

Table 6.8 The finite element analysis results of bird beak T joints with the effects of chord bending, width ratio $\beta = 0.6$

6.10.1 The results of the finite element analyses for the diamond bird beak T joint with the effects of chord bending

In order to investigate the effects of chord bending in detail, a series of analyses were performed where the parameters of chord length and slenderness are varied. The results of the finite element analyses with the effects of chord bending for a chord width ratio of $\beta = 0.6$ and the method of support shown in Figure 6.5 are given in Table 6.8.

The values of the same joints analysed with a thick plate (40mm) supporting the end of the chord are also given in brackets so that the increase in the observed joint capacity can be seen. These results are not used in any further analyses of the joint capacities, as the joints to which they are to be compared, loaded without the effects of chord bending, do not have an end plate. Comparing two different joints with and without an end plate would cause significant differences to be observed in some of the shorter joints, which would be due to the presence of the end plate alone. This trend can be seen by comparing the joint capacities shown in Table 6.8 with and without the end plate. The lower joint capacities with the end plate when $\alpha = 36$, contrary to what may be expected, is not considered significant and is attributed to differences which may be expected in solving the analyses.

To increase the database of results, further joints were analysed where the parameters of chord length, chord wall slenderness and the chord width ratio were varied. The results for these joints where the chord width ratio $\beta = 0.2, 0.4$ and 0.8 are given in Table 6.9.

6.10.2 The variation of joint capacity with chord length with the effects of chord bending.

6.10.2.1 Introduction

When considering the effect of changing the chord length L_0 on the joint capacity $F_{u,1}$ for a diamond bird beak T joint, there are two different effects which may influence the joint capacity. The first effect applies to all T joints in that as the mode of failure changes from a local joint failure for short chord lengths to an overall chord bending failure for the longer joints, the capacity of the joint can be expected to decrease with increasing chord length.

The second effect is specific to those joint configurations where the joint capacity of the X joint varied with changing chord length. It is possible that a similar effect may influence the strength of diamond bird beak T joint, particularly at short chord lengths where there may be an increase or decrease in the joint capacity depending on the boundary conditions at the end of the chord.

Model	Chord Length L_0 mm	α $\frac{2L_0}{b_0}$	β $\frac{b_1}{b_0}$	t_0 mm	$\frac{b_0}{t_0}$	$F_{u,1}$ kN
TBV54	900	12	0.2	4.25	35.3	68.2
TBV50	450	6	0.2	6.3	23.8	144.4
TBV51	900	12	0.2	6.3	23.8	122.9
TBV52	1350	18	0.2	6.3	23.8	112.7
TBV53	2700	36	0.2	6.3	23.8	68.02
TBV55	1350	18	0.2	10	15.0	203.3
TBV57	2700	36	0.2	10	15.0	112.1
TBV56	900	12	0.2	16	15.0	459.9
TBV44	900	12	0.4	4.25	35.3	80.94
TBV45	1350	18	0.4	4.25	35.3	72.38
TBV40	450	6	0.4	6.3	35.3	189.1
TBV41	900	12	0.4	6.3	23.8	150.1
TBV42	1350	18	0.4	6.3	23.8	132.2
TBV43	2700	36	0.4	6.3	23.8	77.47
TBV46	450	6	0.4	10	15.0	362.7
TBV47	1350	18	0.4	10	15.0	238.9
TBV48	900	12	0.4	16	9.3	554.5
TBV49	2700	36	0.4	16	9.3	207.6
TBV34	450	6	0.8	4.25	35.3	130.5
TBV35	900	12	0.8	4.25	35.3	101.5
TBV35A	1350	18	0.8	4.25	35.3	85.07
TBV30	450	6	0.8	6.3	23.8	231.9
TBV31	900	12	0.8	6.3	23.8	185.9
TBV32	1350	18	0.8	6.3	23.8	151.1
TBV33	2700	36	0.8	6.3	23.8	77.96
TBV38	450	6	0.8	16	9.4	887.7

Table 6.9 The finite element analysis results of diamond bird beak T joints with the effects of chord bending for all other chord width ratios

6.10.2.2 The influence of the chord length on joint capacity $F_{u,1}$

The effect of the chord length on the joint capacity can be seen in Figure 6.14, where identical joints with the same chord wall thickness were tested with different

chord lengths. All the joints demonstrate a decrease in joint capacity with increasing chord length as expected.

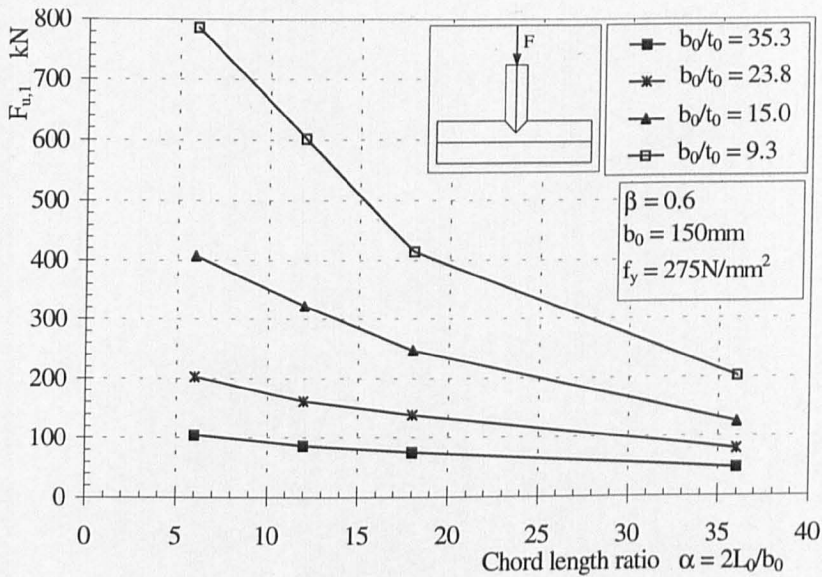


Figure 6.14 The effect of chord length on the joint capacity when $\beta = 0.6$ for various chord thicknesses

However, all the joints where $b_0/t_0 \leq 23.8$ ($t_0 \geq 6.3\text{mm}$) show a definite change in the rate of decrease of the joint capacity with chord length at some point in the range of chord lengths plotted. Whether this decrease is due to the change in the failure mode from a local joint failure to an overall chord bending failure or a change in the local joint failure capacity, or a combination of both, cannot be ascertained from this figure.

6.10.2.3 The influence of the chord length on the moment acting in the chord

The variation in the chord moment at the joint with the chord wall thickness t_0 is shown in Figure 6.15 where the chord width ratio is $\beta=0.6$. The plastic moment capacity at which the joints may be expected to fail by overall chord failure has been calculated in two ways, using Eqns 6.5 and 6.7 with the latter being the more accurate method.

When $\alpha = 6$ the joints can be seen to be failing by a local joint failure and can be considered to be largely independent of the plastic capacity of the section for all of the chord wall thicknesses considered. As the chord length increases, the moment acting in the chord also increases. It would be expected that the value described by the plastic moment calculated by Eqn 6.7 would be the limiting value however, Figure

6.15 shows that this value is exceeded by the longer chord length and the stockier chord sections.

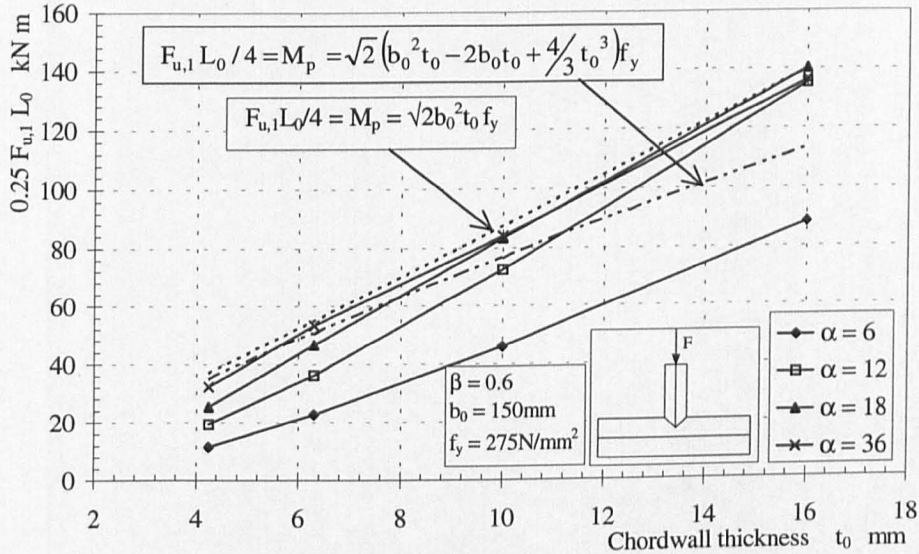


Figure 6.15 The variation of the moment at the joint with chord wall thickness when $\beta=0.6$

It is interesting to note that as the chord length increases, the moment in the chord at which joint failure occurs, tends towards the plastic moment capacity calculated by Eqn 6.5, which is the least accurate way of determining the moment capacity. No explanation can be given for this other than coincidence as Eqn 6.5 clearly overestimates the plastic moment capacity by considering the corners of the section twice in the calculation. It is possible that it might be due to a von Mises effect due to the tri-axial stress operating in the corner of the section.

Figure 6.16 shows the variation in the normalised moment acting in the chord with chord length. The moment $M_{u,0}$ is calculated at a point in the chord free of any restraint or stiffening effect from the brace member and is considered the most likely place where the chord will fail due to a plastic hinge forming. The plastic moment M_p is calculated using the Eqn 6.7. If the failure is to be attributed to overall chord failure, then the normalised moment acting in the chord should be constant and equal to 1. The following points can be made from examination of Figure 6.16:

- for very short chord length joints, where $\alpha = 6$, the value of the normalised moment is significantly less than 1, so the failure mode is predominately that of a local joint

failure. However, the chord bending may still influence the joint capacity, as the moment acting in the chord is still significant

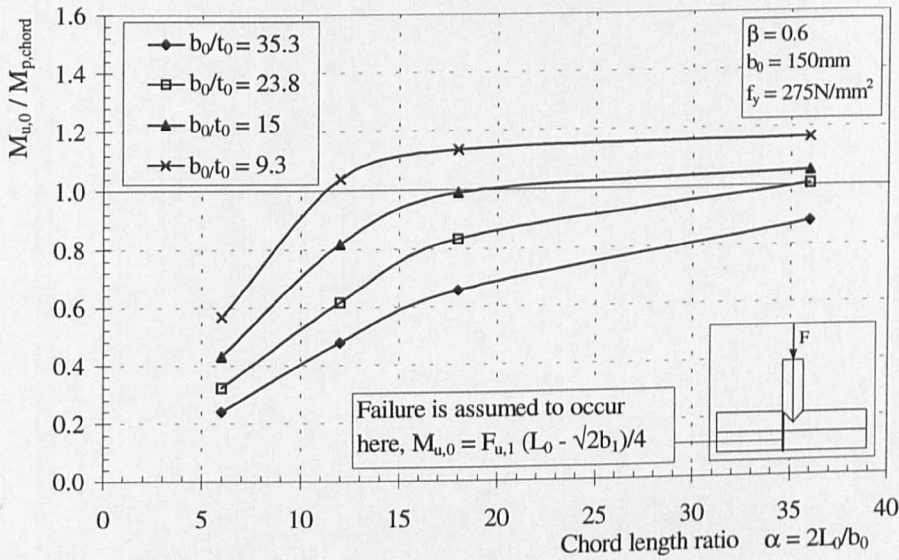


Figure 6.16 The variation in the normalised moment in the chord with the chord length when $\beta=0.6$ and the failure is assumed to occur in the chord free of the influence of the brace member (M_p using Eqn 6.7)

- the normalised moment acting in the chord increases as the chord length increases, tending to a limiting value of about one, suggesting that in these joints the dominant failure mechanism is an overall chord bending failure
- the magnitude of the moment acting in the chord when $\alpha > 18$ for the joints where $b_0/t_0 = 15$ and 9.3 ($t_0 = 10$ or 16mm) is clearly above the plastic moment capacity of the chord. It would also appear that the plastic moment capacity of the chord is exceeded in those joints where $b_0/t_0 = 35.3$ and 23.8 ($t_0 = 4.25$ and 6.3mm) as the chord length increases beyond the range of chord lengths considered
- the normalised moment acting in the chord increases with chord wall thickness.

6.10.2.4 Von Mises contoured stress plots and displaced shape diagrams

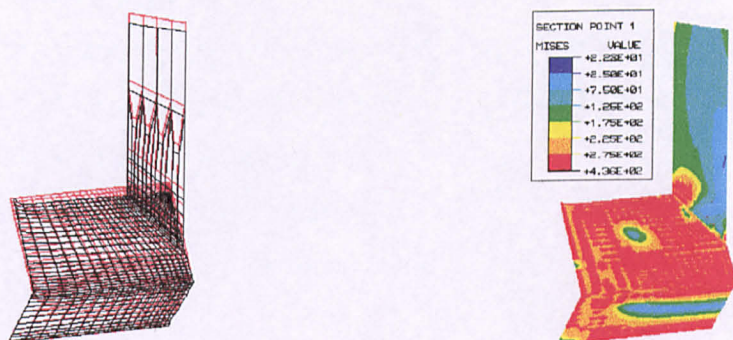
The contoured stress plots shown in Figure 6.17 for similar diamond bird beak T joints with varying chord length show the transition from a local joint failure when $\alpha = 6$ to an overall chord bending failure when $\alpha = 36$. This is best observed by examining the stress levels on the lower face of the chord at the centre line of the joint. When $\alpha = 6$ the stress level is relatively low in the centre of the face and clear of the

yield lines forming at the corners of the chord section, but as the chord length increases so the level of stress in this area increases.

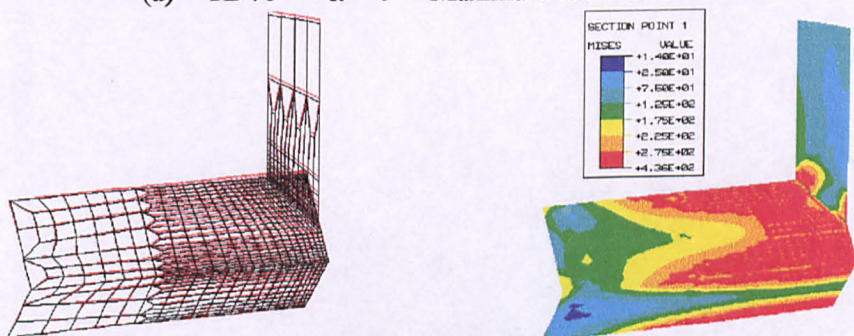
For the longest joint, when $\alpha = 36$, all the material in the vicinity of the centre line of the joint has yielded indicating the formation of a plastic hinge in the chord member under the brace.

Examining Figure 6.17 in more detail it can be seen that:

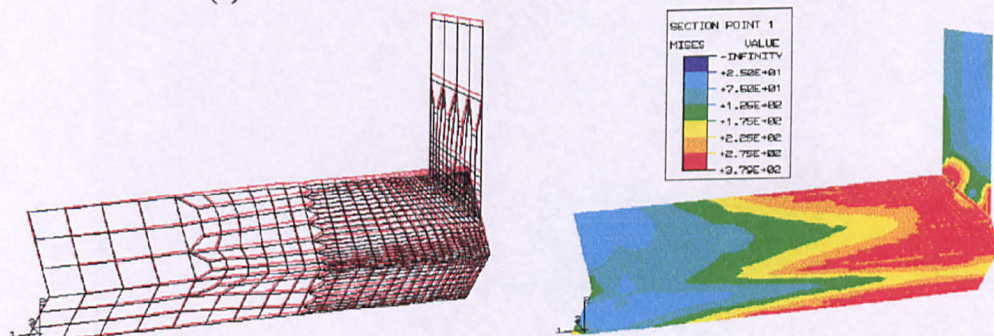
- when $\alpha = 6$ the material in the upper face of the chord has undergone widespread yielding as would be expected with a local joint failure. There is further yielding of the material at the end of the chord due to the restraint offered by the boundary conditions. These two areas of yielded material have merged together and it is not possible to differentiate how much yielding is caused by either mechanism. Further evidence of the effect of the restraint at the end of the chord can be seen in the displaced shape diagram at the end of the chord where the local deformation of the top corner of the chord shows the influence of the restraint. The stress distribution in the brace member indicates that the majority of the load is transferred into the chord at the top corner of the chord.
- when $\alpha = 12$ and 18 the mode of failure is a combination of local joint failure and overall chord bending failure. There is evidence of yield lines forming at the top, middle and bottom corners of the chord section. The support conditions at the end of the chord do not unduly appear to affect the failure of the joint.
- when $\alpha = 36$ the mode of failure is predominately that of overall chord bending failure. It is interesting to note that there is no evidence of a yield line forming at the middle corner of the chord when $\alpha = 36$, although a yield line can be identified at the middle corner of the joints where $\alpha = 12$ and 18. Examination of the stress distribution in the brace member indicates that the load transference into the chord is more evenly distributed through the brace member.



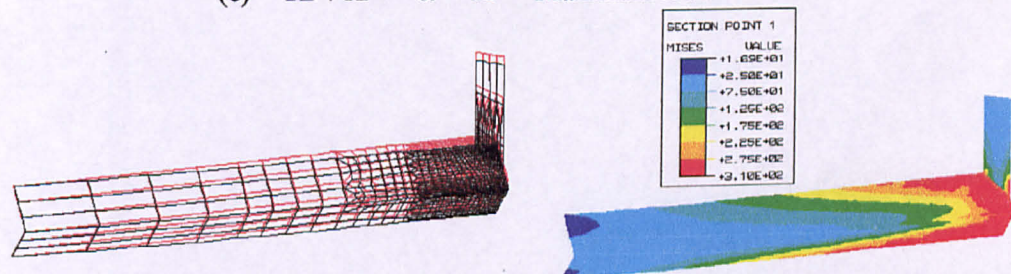
(a) TBV5 $\alpha = 6$ Maximum load 202.5kN



(b) TBV19 $\alpha = 12$ Maximum load 161.5kN



(c) TBV12 $\alpha = 18$ Maximum load 138.2kN



(d) TBV11 $\alpha = 36$ Maximum load 79.2kN

Figure 6.17 Displaced shape diagrams and von Mises contoured stress plots for the diamond bird beak joint with the effects of chord bending at maximum load on the outside surface

6.10.2.5 Load indentation curves

The load/indentation curves for the same joints shown in contoured stress plots are shown in Figure 6.18. Examining this figure it can be seen that:

- as would be expected, the maximum load decreases with increasing chord length
- all the joints, regardless of the chord length, attain a maximum load although the indentation at which this occurs varies widely, from $3\%b_0$ when $\alpha = 6$ to $0.6\%b_0$ when $\alpha = 36$
- the restraint offered by the support conditions increases the initial stiffness when $\alpha = 6$

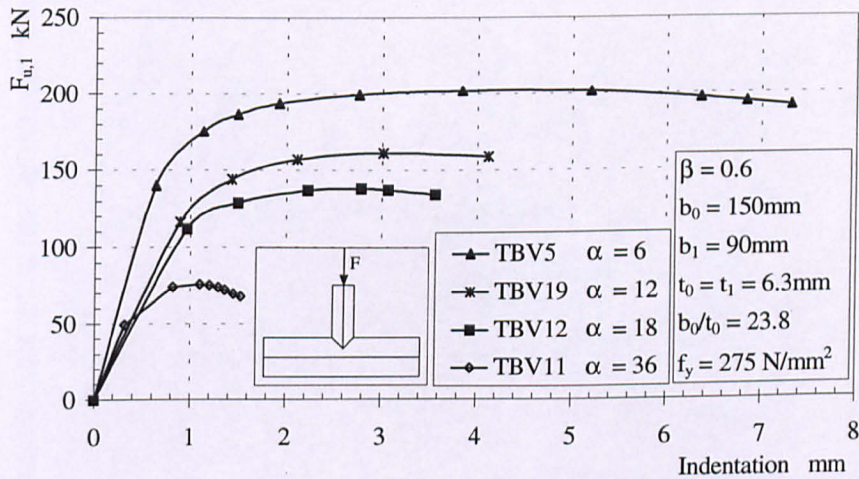


Figure 6.18 Load indentation curves for the diamond bird beak T joint with the effect of chord bending

The load/indentation curves shown in Figure 6.18 give an indication of how the stiffness of the joint changes as the chord length is varied, whilst the moment/deflection curves shown in Figure 6.19 show how the stiffness of the chord changes as chord length is varied. The moment has been calculated at a point in the chord free of any restraint from the brace and is considered the most likely place for the plastic hinge to form.

Comparing the moment/deflection curves for TBV5 and TBV19 where $\alpha = 6$ and 12 respectively, the initial slopes of the curves are virtually identical and the curves are similar in shape. The moment in TBV19 (31.2kNm) is virtually twice that of TBV5 (16.3kNm) as would be expected as the chord length has been doubled. The initial slope of TBV12 is less than that of TBV5 and TBV19 and the moment at failure

(42.2kNm) is not quite three times that of TBV5. The moment in TBV12 is at 85% of the moment capacity of the chord (50.6kNm) and it can be expected that chord bending is becoming more dominant in the failure mechanism when $\alpha = 18$. In joint TBV11 where $\alpha = 36$ the curve is very different to that seen in the previous three curves discussed. The initial slope is significantly less and the moment in the chord is no longer related to the length of the chord and is 97% the moment capacity of the chord. The dominant mechanism in the failure of the joint is obviously chord bending.

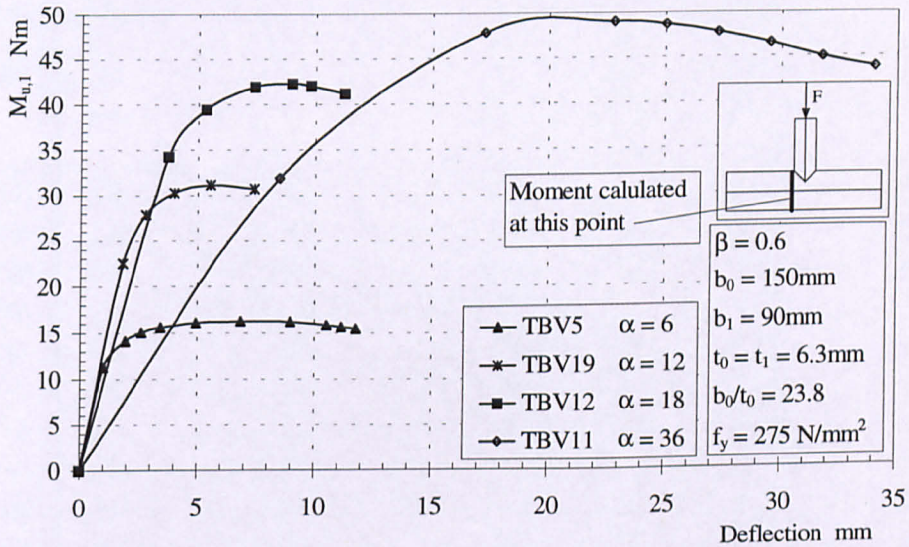


Figure 6.19 Moment/deflection curves for the diamond bird beak T joint with the effect of chord bending

6.10.3 Calculation of joint strength for the diamond bird beak T joints

Ono et al (1991) suggested that the joint capacity of a diamond bird beak T joint can be estimated from Eqn 6.8 based on a series of experimental test joints where $\alpha = 6$. The joint capacities predicted by Eqn 6.8 are compared against those finite element results where $\alpha = 6$ and are shown in Table 6.10.

$$F_{u,1} = t_0^2 f_y \left(\frac{1}{0.211 - 0.147\beta} + \frac{1}{1.794 - 0.942\beta} \cdot \frac{b_0}{t_0} \right) \quad \text{Eqn 6.8}$$

Examination of the predicted joint capacities against the finite element results show that Eqn 6.8 overestimates the expected capacity considerably. The reason attributed to this large discrepancy is the method of restraining the chord used in experimental tests.

This was discussed in Chapter 4, where a large increase in the X joint capacity was noted when the ends of the chord were restrained for short chord length joints. The precise method used to support the ends of the chord in the experimental tests performed by Ono et al (1991) is not known (see Figure 2.5) however, it is thought that the conditions resemble that of the chord ends held encastré.

In view of these results, the design equation established by Ishida et al (1993) and published in the CIDECT design guide (Packer et al 1992) should be used with caution until further work has been done on this type of joint configuration.

Model	b ₀ mm	t ₀ mm	β	b ₀ /t ₀	f _y N/mm ²	FE analysis kN	Ishida et al Eqn 6.8 kN	% Difference
TBV50	150	6.3	0.2	23.8	275	144.4	222.0	54
TBV40	150	6.3	0.4	23.8	275	189.1	255.1	35
TBV46	150	10	0.4	15.0	275	362.7	471.8	30
TBV8	150	4.25	0.6	35.3	275	104.8	183.1	75
TBV5	150	6.3	0.6	23.8	275	202.5	300.4	48
TBV9	150	10	0.6	15.0	275	407.7	559.6	37
TBV10	150	16	0.6	9.4	275	786.8	1110.4	41
TBV34	150	4.25	0.8	35.3	275	130.5	221.2	70
TBV30	150	6.3	0.8	23.8	275	231.9	366.3	58
TBV38	150	16	0.8	9.4	275	887.7	1389.2	56

Table 6.10 A comparison between Ishida et al design equation for diamond bird beak T joints and similar finite element results where α = 6

Using the T joint results where α = 6 analysed with the effects of chord bending that may be used to establish the joint strength. Longer joints, when α ≥ 12, cannot be used as the mode of failure will include a significant amount of chord bending failure. However, using the few results that are available the mean joint strength can be estimated empirically by

$$F_{u,1} = 4 f_y t_0^2 \sqrt{\beta^{0.5} \frac{b_0}{t_0}}$$

Eqn 6.9

for the range of parameters 0.2 ≤ β ≤ 0.8, 9.4 ≤ b₀/t₀ ≤ 35.3, b₀ = 150mm and f_y = 275 N/mm². Using the results given in Table 6.10 (which have a wide variation of parameters) giving a Coeff. of Correlation of 0.999 so that a mean of 1.034 and CoV. of 0.0505 enables Eqn 6.9 to be used with confidence when α = 6.

6.10.4 A comparison of the results to current design methods

In the design methods used at present for the design of T joints the local joint strength is derived from design equations based on the physical tests of short chord length joints. (Typically $\alpha \approx 6$.) The chord is then checked separately to ensure that the moment capacity of the chord at the joint and the shear capacity at the supports is not exceeded.

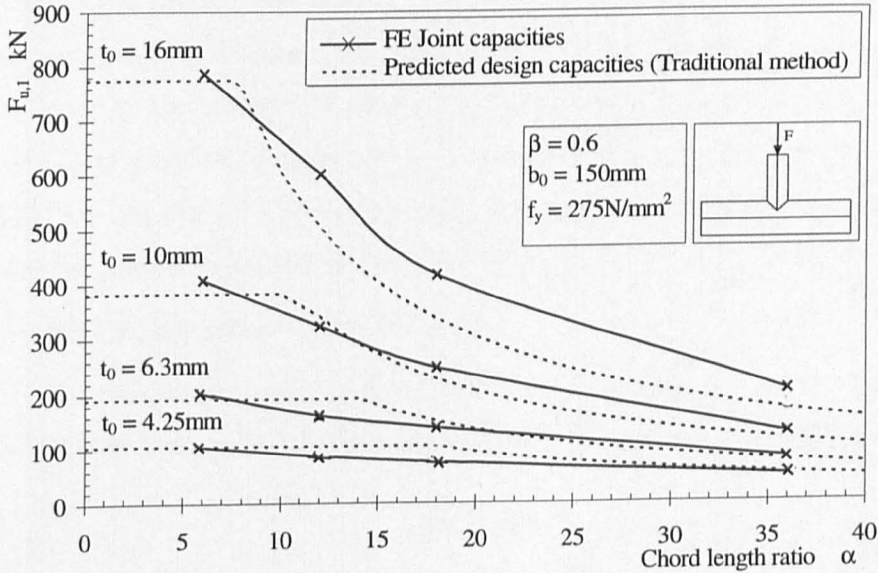


Figure 6.20 A comparison between the observed finite element and the predicted joint capacities

The joint capacities calculated using this method (the joint capacities at $\alpha = 6$ are calculated using Eqn 6.9) are compared against the observed finite element joint capacities in Figure 6.20 and examining this figure it can be seen that:

- for very slender joints when $t_0 = 4.25\text{mm}$ ($b_0/t_0 = 35.2$) the design guidance will overestimate the joint strength by up to 25% $F_{u,1,\alpha=6}$
- for stocky sections when $t_0 = 16\text{mm}$ ($b_0/t_0 = 9.3$) the design guidance will substantially underestimate the joint strength by up to 12% $F_{u,1,\alpha=6}$
- that the assumption that the local joint capacity is independent of the effects of chord bending is not correct

Clearly then there is a need to consider the length of the chord (and hence the moment acting in the chord), when considering the design strength of the joint. An alternative method (i.e. the interaction method) will be considered later in this Chapter where the

effect of the co-existing moment acting in the chord is considered in the design procedure for the diamond bird beak T joints.

6.11 Diamond bird beak joints without the effects of chord bending

This section discusses how the local joint strength without the effects of chord bending $F_{u,1,loc}$ is found using finite element methods. There were problems in applying the moment to the chord for the bird beak T joints in the same manner as van der Vegte (1994a). In order to confirm van der Vegte’s work and to examine possible improvements to the method of loading the chord with a moment, a series of CHS joints similar to those analysed by van der Vegte are examined. The improvements to the method of loading the chord with the moment suggested by this study are then applied to the diamond bird beak joints with improved results.

6.11.1 Removing the effects of chord bending

The method used to remove the effects of chord bending is to apply a moment to the chord, such that the bending moment at the joint is zero, shown in Figure 6.21.

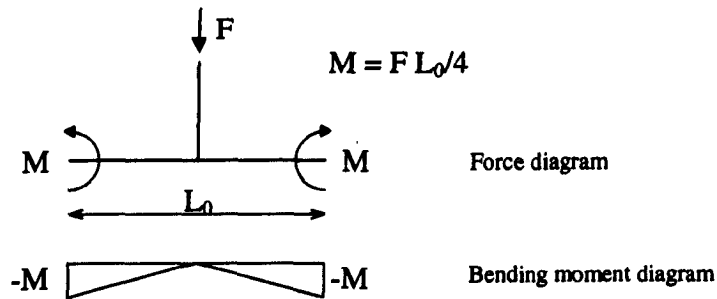


Figure 6.21 The method used to remove the effects of chord bending

It is considered that the most likely place for a plastic hinge to form in the chord is next to the brace, where the chord is free of any restraint from the brace. In the case of a diamond bird beak T joint, the moment that should then be applied to the chord to remove the effects of chord bending is

$$M = \frac{F(L_0 - \sqrt{2}b_1)}{4}$$

Eqn 6. 10

and the effect of this is shown in Figure 6.22.

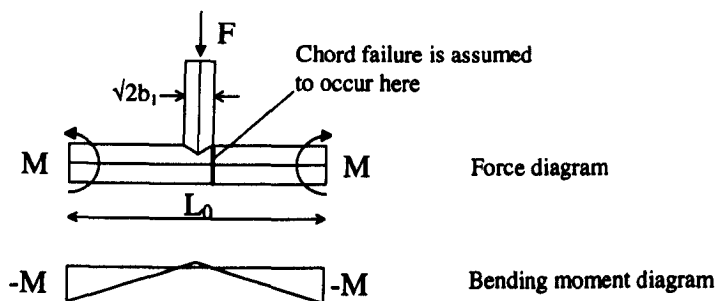


Figure 6.22 Removing the effects of chord bending from a diamond bird beak T joint

When this method was used to remove the effects of chord bending in the diamond bird beak T joints, consistent results could not be obtained as the local joint capacity $F_{u,1,loc}$ still varied with chord length and in the longer joints the failure was due to chord bending failure at the end of the chord due to the size of the moment applied. In order to investigate this and to verify how van der Vegte (1995) obtained his results for the local joint capacity $F_{u,1,loc}$, similar CHS T joints were analysed and are reported in the next section.

6.11.1.1 Removing the effects of chord bending from CHS T joints

When van der Vegte (1994a and 1995) used this technique to remove the effects of chord bending to CHS T joints, he applied a single moment to the end of the chord. He was able to show that for chord lengths of $\alpha = 12$ and 18 there was no significant difference in the local joint strength, 1621kN and 1615kN respectively, when $d_0 = 406.4\text{mm}$, $t_0 = 16\text{mm}$, $d_1 = 244.5\text{mm}$ and $t_1 = 16\text{mm}$. To achieve this result, van der Vegte states that “to avoid plasticification of the chord end, the yield strength of the elements over a small distance of the chord, adjacent to the ends of the chord have been increased” without saying over what distance and by how much the yield strength had been increased.

In this study three different methods of applying the moment to the chord have been investigated, which are shown in Figure 6.23. In all these cases the moment has been applied to the chord as a series of longitudinal forces (in the form of a plastic moment distribution) producing a couple equal to the moment acting in the chord due to action of the load on the brace. In the model series CHS2 the moment is applied to the end of the chord only. However, in the model series CHS3 the moment is applied in several small increments in the manner shown in Figure 6.24.

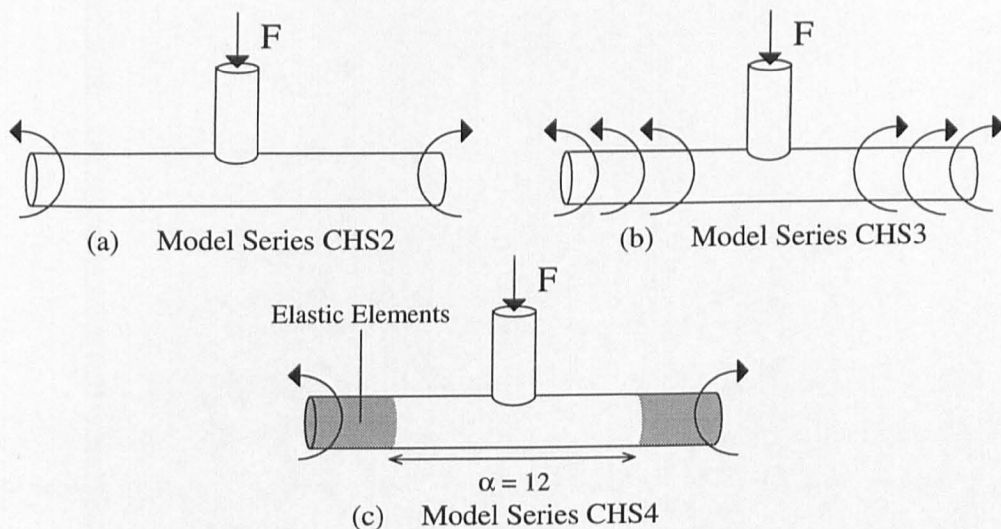


Figure 6.23 Three different methods of applying the moment to the chord

The moment is applied by a single couple at the end of the chord in the series CHS4 (i.e. the same as the CHS2 series) however, the elements at the end of the chord shown as the shaded area in Figure 6.23c, are purely elastic with no plastic properties at all, to prevent yielding and premature failure. The elements in the middle of the chord over a length equivalent to $\alpha = 12$ have both elastic and plastic properties to assess the local joint strength.

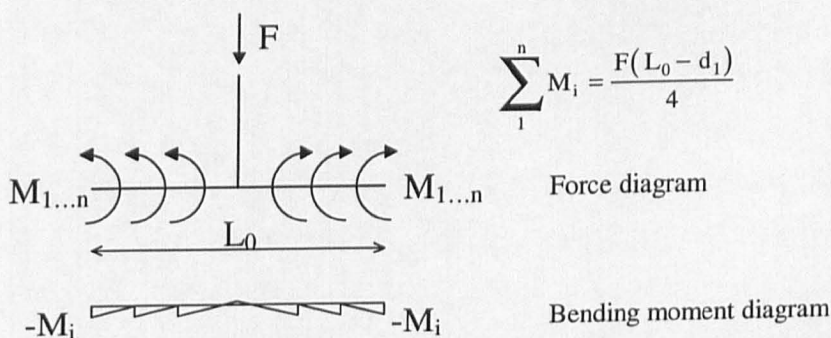


Figure 6.24 The method of applying moment in the model series CHS3

The joint parameters used in the analysis of the CHS T joints are $d_0 = 406.4\text{mm}$, $t_0 = 16\text{mm}$, $d_1 = 244.5\text{mm}$ and $t_1 = 16\text{mm}$, where $\beta = 0.6$ and $d_0/t_0 = 25.4$. The material properties used, estimated from van der Vegte's data and are given in Table 6.11. The Young's Modulus was taken to be 207 kN/mm^2 .

Stress N/mm ²	Plastic Strain
355	0.00
355	0.02
440	0.05
510	0.10

Table 6.11 The material properties used in the CHS T joints

The results of the CHS finite element models analysed are given in Table 6.12 and shown in Figure 6.25. Examples of the von Mises contoured stress plots for the different methods of applying the moments are shown in Figure 6.26 for the CHS T joints where $\alpha = 24$.

Examining the data shown in Table 6.12 and Figure 6.25 and using the contoured stress plots to interpret this information it can be seen that:

- the values of $F_{u,1,loc}$ for the model series CHS2 are not constant with increasing chord length. Examination of the von Mises contoured stress plot reveals that the size moment applied to the chord is causing the chord to fail by bending at the end.
- the values of $F_{u,1,loc}$ for the model series CHS3 are constant with increasing chord length when the chord length ratio $\alpha \geq 18$. Examination of the von Mises stress plot shows that the failure occurs in the chord locally about the brace member
- the values of $F_{u,1,loc}$ for the model series CHS4 are approximately constant with increasing chord length for the range of $12 \leq \alpha \leq 24$. The values of $F_{u,1,loc}$ are marginally higher than for the model series CHS3 reflecting the increase in the joint capacity by removing the plastic properties from the elements at the end of the chord. When the chord length increases to $\alpha = 36$ a fall in the value $F_{u,1,loc}$ can be observed as the elastic part of the chord begins to deform and so provide less support for the central part of the joint where the elements have the elastic and plastic properties. Examination of the von Mises contoured stress plot shows that the areas of high stress are not confined to the chord in the vicinity of the brace member but extend the whole length of the chord. The failure of the joint cannot be considered to be localised in the vicinity of the brace member and total failure of the chord is only prevented by removing the plastic properties of the elements at the end of the chord

- comparing joints CHS2-12 and CHS4-18, i.e. similar to the joints van der Vegte used to establish that the local joint capacity $F_{u,1,loc}$ was independent of chord length, it can be seen that similar values of $F_{u,1,loc}$ are obtained for these joints (1550 and 1537kN respectively).

Model	L_0 mm	α	$F_{u,1,loc}$ kN
CHS2-6	609.6	6	1535
CHS2-12	1219.2	12	1550
CHS2-18	1828.8	18	1376
CHS2-24	2438.4	24	1034
CHS2-36	3657.6	36	742
CHS3-6	609.6	6	1535
CHS3-12	1219.2	12	1489
CHS3-18	1828.8	18	1511
CHS3-24	2438.4	24	1510
CHS3-36	3657.6	36	1510
CHS4-18	1828.8	18	1537
CHS4-24	2438.4	24	1548
CHS4-36	3657.6	36	1485

Table 6.12 The results of the finite element analyses for the CHS T joints without the effects of chord bending.

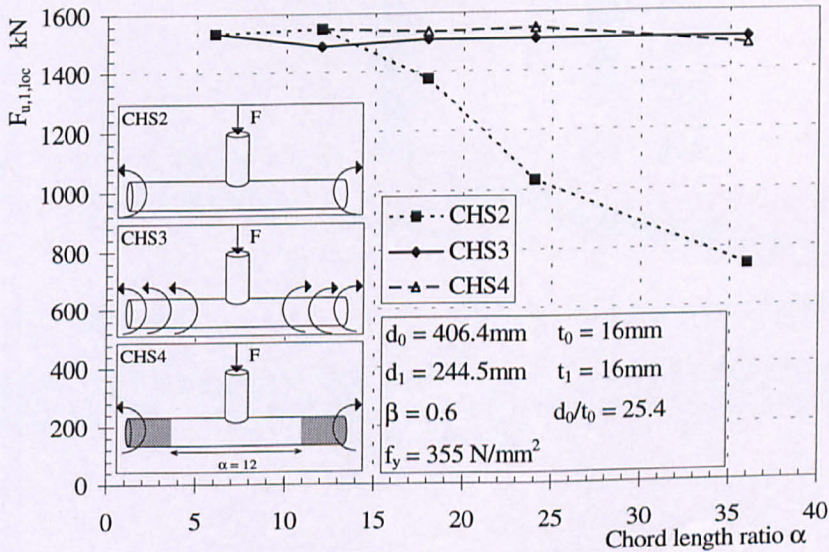
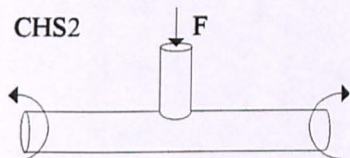
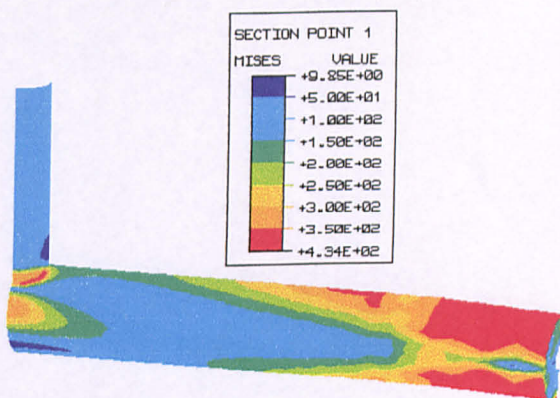


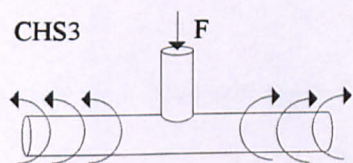
Figure 6.25 The comparison between the different methods of eliminating the chord bending effects for the CHS T joints



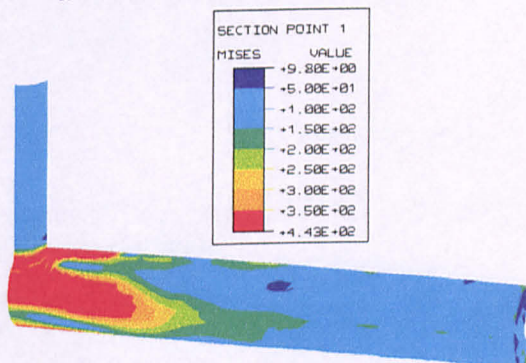
(a) CHS2-24



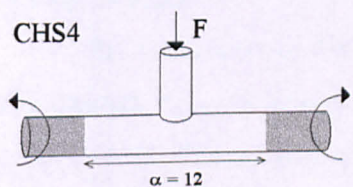
$\alpha = 24$ Maximum load = 1034kN



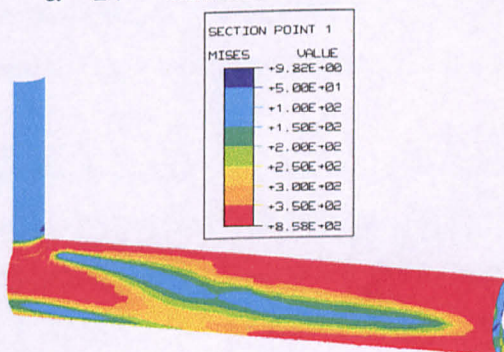
(b) CHS3-24



$\alpha = 24$ Maximum load = 1510kN



(b) CHS4-24



$\alpha = 24$ Maximum load = 1548kN

Figure 6.26 Examples of the von Mises contoured stress plots for the different methods of applying the moment to remove the effects of chord bending, shown for the outside surface at the maximum load

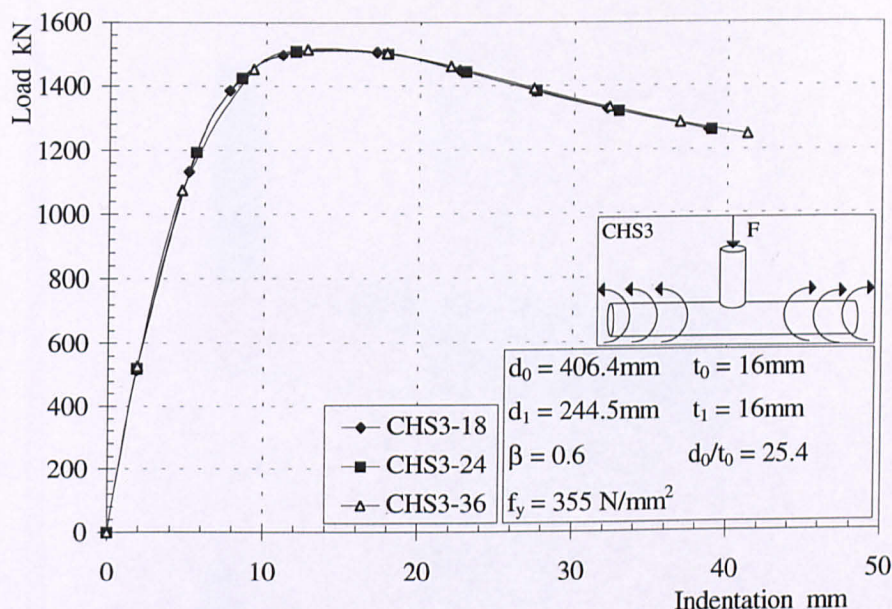


Figure 6.27 Load indentation curves for the model series CHS3, CHS T joint loaded without the effects of chord bending

The load/indentation curves and the von Mises contour stress plots shown in Figure 6.27 and Figure 6.28 respectively for series CHS3 show how identical the failure is regardless of the length of the chord. The load/indentation curves are coincident and the stress distribution shown in the von Mises contoured stress plots are virtually identical.

The conclusion of this investigation is that the best way of finding the local joint strength $F_{u,1,loc}$ is to apply the moment to the chord in incremental steps as shown in Figure 6.24. This method produces the most consistent results particularly when $\alpha \geq 18$ and does not change the properties of any part of the model, ensuring that the true local joint strength is observed.

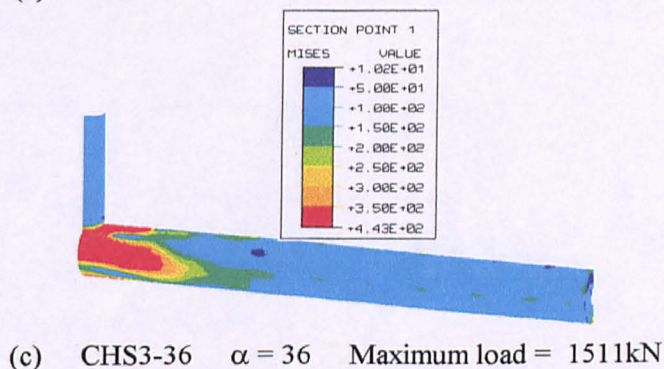
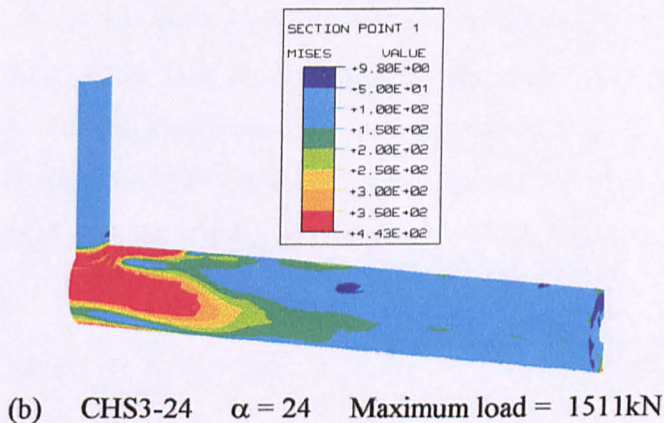
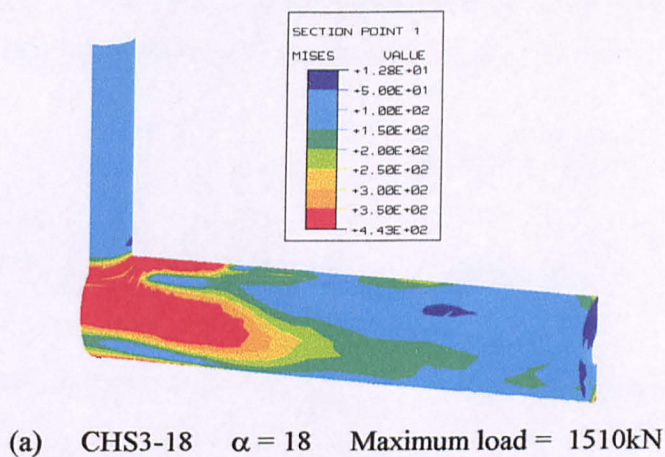


Figure 6.28 Von Mises contoured stress plots for different chord lengths for model series CHS3 for the outside surface at maximum load

6.11.1.2 Removing the effect of chord bending from diamond bird beak T Joints

The effect of removing the influence of chord bending is now examined by applying a moment to the chord as a series of incremental steps according to the relationship shown in Figure 6.29. The distribution across the section of the longitudinal forces that cause the moment is shown in Figure 6.30. Applying the

moment in the form of an elastic moment distribution was investigated however, this caused significantly higher stresses at the top and bottom of the chord section.

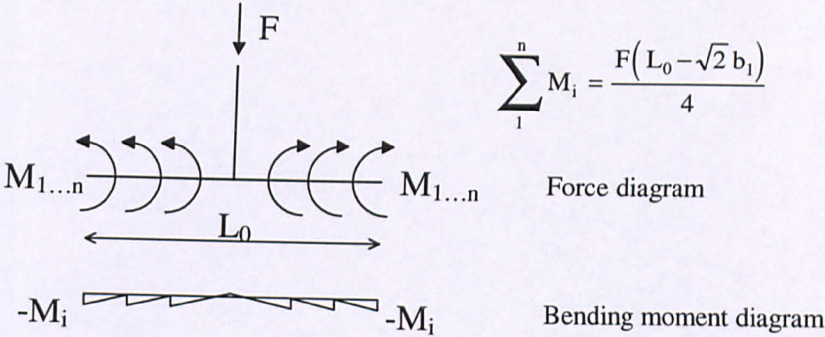


Figure 6.29 The method of applying moment to the diamond bird beak joint

The variation in the local joint capacity $F_{u,1,loc}$, with chord length when the moment is applied in this manner and all the other parameters remain constant, is given in Table 6.13 and shown in Figure 6.31. It can be seen that a consistent value can be obtained for the local joint strength $F_{u,1,loc}$ when the chord length ratio $\alpha \geq 24$.

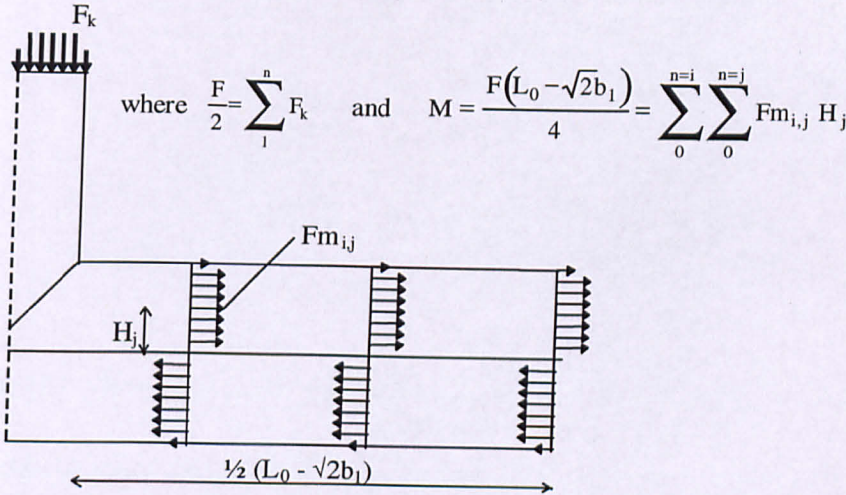


Figure 6.30 The axial forces applied to the chord in the finite element model to cause a moment in the chord

Furthermore when $\alpha \leq 24$ the joint capacities of diamond bird beak T joints can be seen to be dependent on the length of the chord, although this effect is small and is normally masked by the effects of chord bending. Comparing the results of the model series CHS3 shown in Figure 6.25 with Figure 6.31 a similarity in the curves is noted. Comparing these values relatively to the asymptotic value, both curves show an increased value for $F_{u,1,loc}$ when $\alpha = 6$, a decrease in the value $F_{u,1,loc}$ when $\alpha = 12$ and a

constant asymptotic value when $\alpha \geq 18$ for the CHS T joints and $\alpha \geq 24$ for the diamond bird beak T joints.

Model	L_0 mm	α	b_0 mm	β	b_0/t_0	t_1 mm	$F_{u,1,loc}$ kN
TBMV5	450	6	150	0.6	23.8	6.3	253.8
TBMV19	900	12	150	0.6	23.8	6.3	224.0
TBMV12	1350	18	150	0.6	23.8	6.3	232.7
TBMV23	1800	24	150	0.6	23.8	6.3	242.1
TBMV11	2700	36	150	0.6	23.8	6.3	243.7
TBMV24	3600	48	150	0.6	23.8	6.3	243.5

Table 6.13 The variation of local joint capacity $F_{u,1,loc}$ with chord length α for diamond bird beak T joints without the effects of chord bending

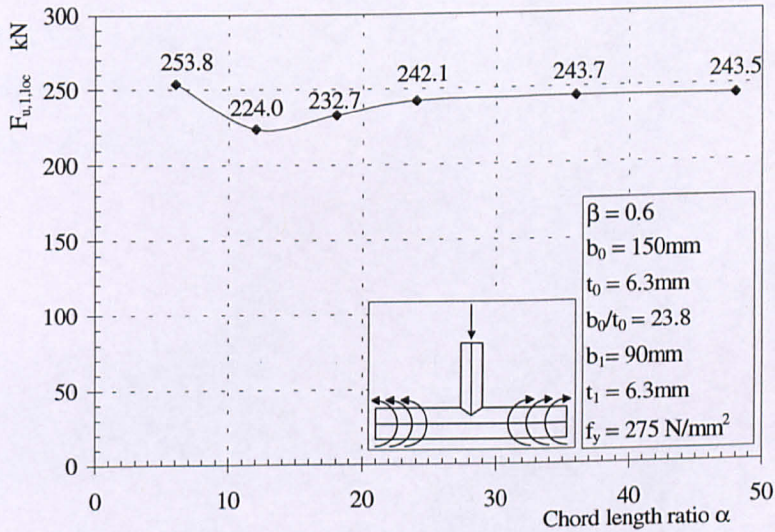


Figure 6.31 The variation of joint capacity with chord length without the effects of chord bending

The restraint offered by the boundary conditions at the end of the chord can be seen to increase the joint capacity above the asymptotic strength when $\alpha = 6$. As the chord length is increased, then the boundary conditions no longer affects the strength of the joint to the same extent and the joint capacity drops below the asymptotic joint strength for $\alpha = 12$ and 18 . This form of behaviour was noted for the X joints for boundary condition 3 shown in Figure 4.20, where the cross sectional shape of the end of the chord was maintained and is similar to the boundary conditions used for the diamond bird beak T joints. So it is concluded that the strength of diamond bird beak T joints is affected by the boundary conditions at the end of the chord in the same way as the diamond bird beak X cross joints.

6.11.1.3 Displaced shape diagrams and von Mises contoured stress plots

Figure 6.32 shows the displaced shape diagrams and von Mises contoured stress plots for the range of chord lengths considered in ascertaining a constant local joint strength $F_{u,1,loc}$ for diamond bird beak T joints without the effects of chord bending. A comparison of this figure with Figure 6.28 (which shows the von Mises contoured stress plots for the CHS T joints studied) shows that the area of material affected by the joint failure in the CHS T joints is much more localised than with the diamond bird beak joint. For the CHS T joints the material failure on the surface is confined to a chord length equivalent to $\alpha \approx 9$ whilst in the diamond bird beak joints the material failure on the surface extends to a chord length equivalent to $\alpha \approx 18$. This will account for the fact that a larger chord length ratio needs to be considered for the diamond bird beak T joint ($\alpha = 24$) than for the CHS T joints ($\alpha = 18$) before a constant value of the local joint strength $F_{u,1,loc}$ is ascertained.

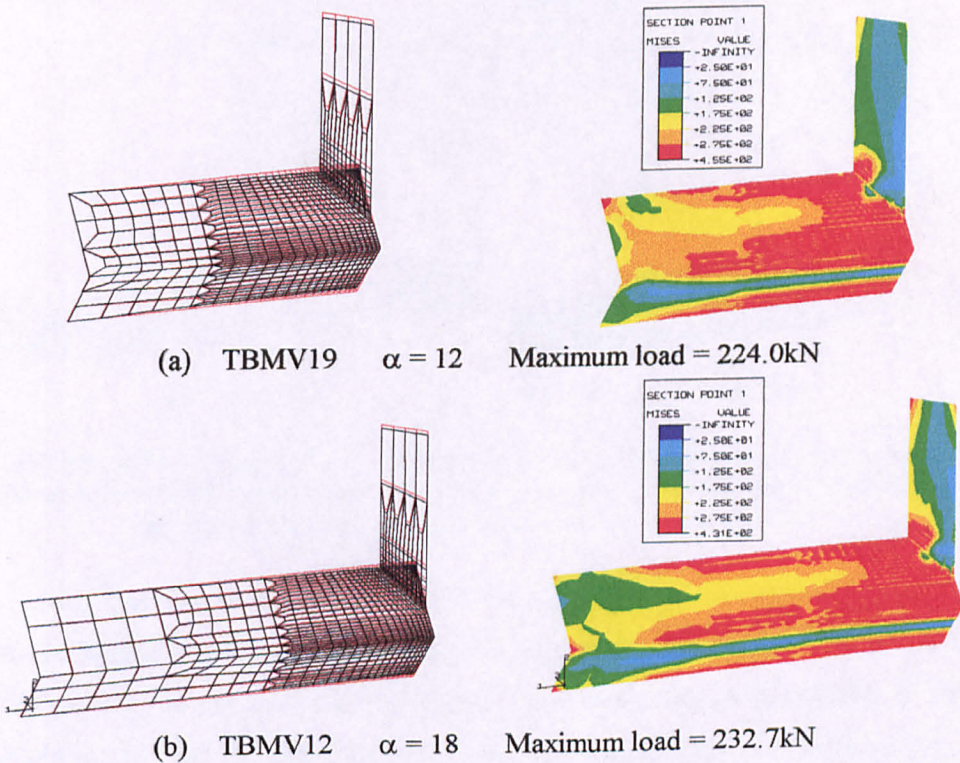
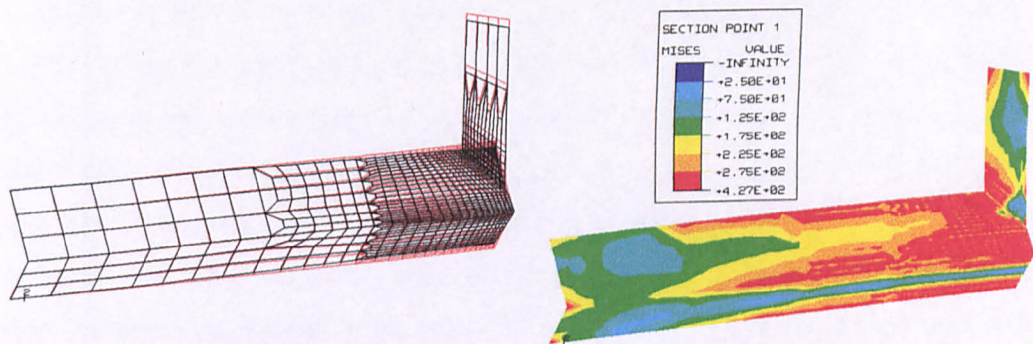
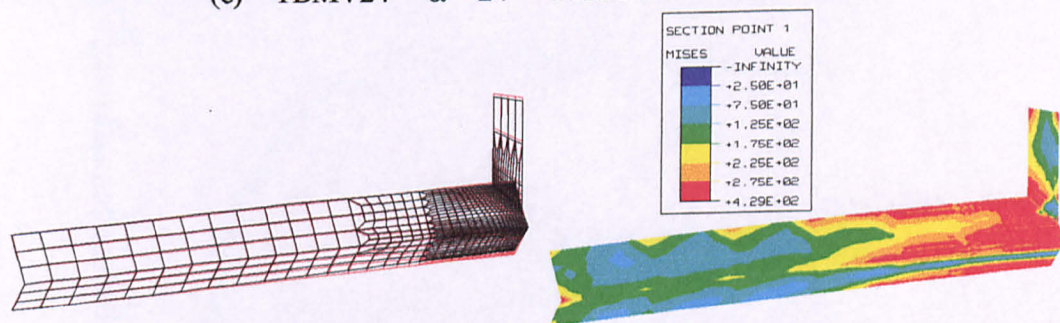


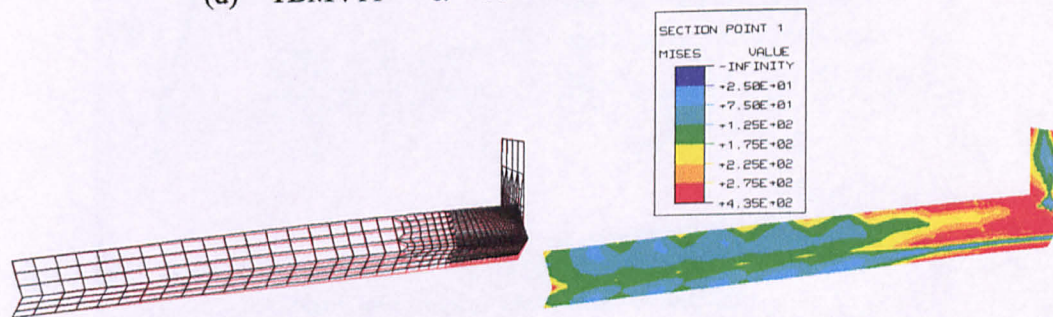
Figure 6.32 Displaced shape diagrams and von Mises contoured stress plots for the diamond bird beak T joints without the effects of chord bending for identical joints with differing chord lengths for the outside surface at maximum load



(c) TBMV24 $\alpha = 24$ Maximum load = 242.1kN



(d) TBMV11 $\alpha = 36$ Maximum load = 243.7kN



(e) TBMV12 $\alpha = 48$ Maximum load = 243.5kN

Figure 6.32 (cont.) Displaced shape diagrams and von Mises contoured stress plots for the diamond bird beak T joints without the effects of chord bending for identical joints with differing chord lengths for the outside surface at maximum load

The presence of yielding material at the corners of the chord section evident in all the contoured stress plots would indicate the presence of yield lines in same manner shown to exist in the bird beak X joints. Examination of all the displaced shape diagrams shows that the cross sectional height of the chord has been reduced and the width increased in the vicinity of the joint, this deformation is attributed to the plastic hinges occurring in the chord wall at the corners of the section. The effect of this deformation is that the moment applied to the chord to remove the effects of chord bending is also reduced according to the change in the cross sectional height of the

chord. Hence the loading of the joint is no longer balanced to produce a zero bending moment under the crown of the brace. It would therefore be expected that the chord should sag as the moment supplied by the force acting on the brace (sagging) is greater than the moment acting on the deformed chord to remove the effects of chord bending (hogging). Why the chord can be clearly seen to be hogged in the longer chord length joints can only be explained by the accumulation of all the small hogging moments acting on the chord, shown in Figure 6.29. This effect is small and is not thought to affect the joint capacities observed.

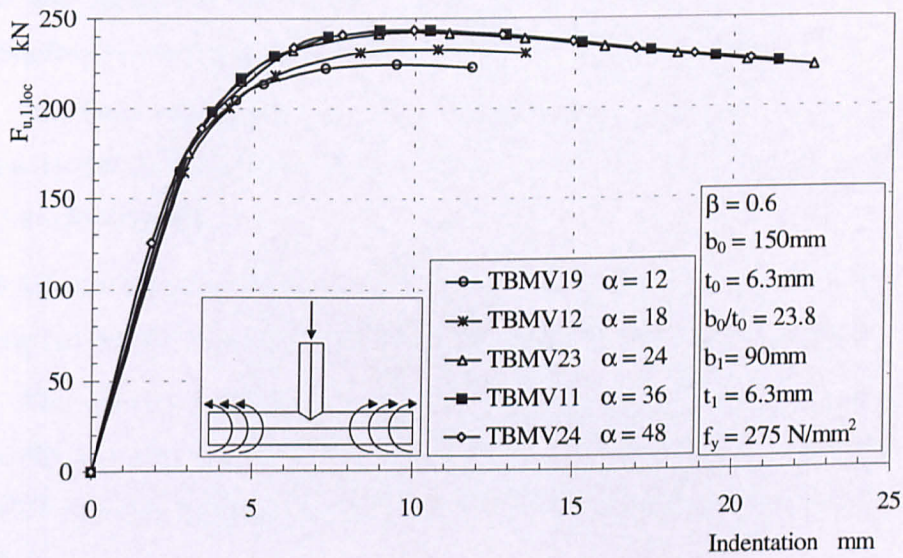


Figure 6.33 Load indentation curves of the diamond bird beak T joints without the effects of chord bending for different chord lengths

6.11.1.4 Load/indentation curves for the diamond bird beak T joints without the effects of chord bending

The variation in the load/indentation curves with chord length can be seen in Figure 6.33 for the diamond bird beak T joints without the effects of chord bending. All the joints attain a maximum load at an indentation of $\approx 7\%b_0$. The joints TBMV19 and TBMV12 where $\alpha = 12$ and 18 do not attain the asymptotic local joint strength. The joints where $\alpha \geq 24$ attain the asymptotic joint strength with all the curves being virtually coincident with each other.

6.11.1.5 Conclusions

Section 6.5.1 has shown that the effects of chord bending can be eliminated from diamond bird beak T joints and that a constant value for the local joint strength

$F_{u,1,loc}$ can be achieved when $\alpha \geq 24$. The best way of achieving this is to apply the moment incrementally along the chord. As a result of this investigation a chord length of $\alpha = 36$ is used to find the local joint strength $F_{u,1,loc}$ for all the joints where the effects of chord bending have been eliminated.

When the effects of chord bending have been removed, it can be seen that the strength of the T joints is dependent on the length of the chord (when $\alpha < 24$) in a similar manner to the X joints studied in Chapter 4.

6.11.2 The results of the finite element analyses without the effects of chord bending for the diamond bird beak T joints, for various β and b_0/t_0 values

The finite element analysis results represented in Table 6.14 are obtained from T joints loaded in the manner shown in Figure 6.29 and Figure 6.30 to remove the effects of chord bending.

6.11.3 Discussion of the finite element analyses without the effects of chord bending for the diamond bird beak T joints, for various β and b_0/t_0 values

The results of the finite element analyses given in Table 6.13 are shown graphically in Figure 6.34 and Figure 6.35. These figures indicate that the local joint capacity $F_{u,1,loc}$ is principally a function of chord wall thickness t_0 and the chord width ratio β .

Analysis of this data gives an empirical formula to predict the local joint capacity of diamond bird beak T joints without the effects of chord bending of

$$F_{u,1,loc} = 5.7 f_y t_0^2 \sqrt{\beta \frac{b_0}{t_0}} \quad \text{Eqn 6.11}$$

for the range of parameters $f_y = 275\text{N/mm}^2$, $b_0 = 150\text{mm}$, $0.2 \leq \beta \leq 0.6$ and $4.25 \leq t_0 \leq 16\text{mm}$. The data for Eqn 6.11 was derived from 14 results with a Coeff. of Correlation of 0.9962, a mean of 1.0267 and CoV. of 0.0669, enabling this equation to be used with confidence.

Model	α	b_0 mm	β	t_0 mm	b_0/t_0	$F_{u,1,loc}$ kN
TBMV50	36	150	0.2	4.25	35.3	84.0
TBMV51	36	150	0.2	6.3	23.8	150.7
TBMV52	36	150	0.2	10	15.0	288.9
TBMV53	36	150	0.2	16	9.4	501.7
TBMV40	36	150	0.4	4.25	35.3	112.6
TBMV41	36	150	0.4	6.3	23.8	213.8
TBMV42	36	150	0.4	10	15.0	433.2
TBMV43	36	150	0.4	16	9.4	829.5
TBMV25	36	150	0.6	4.25	35.3	120.5
TBMV23	36	150	0.6	6.3	23.8	243.7
TBMV26	36	150	0.6	10	15.0	496.6
TBMV27	36	150	0.6	16	9.4	979.9
TBMV30	36	150	0.8	4.25	35.3	148.9
TBMV31	36	150	0.8	6.3	23.8	265.8

Table 6.14 The local joint capacities $F_{u,1,loc}$ for diamond bird beak T joints without the effects of chord bending

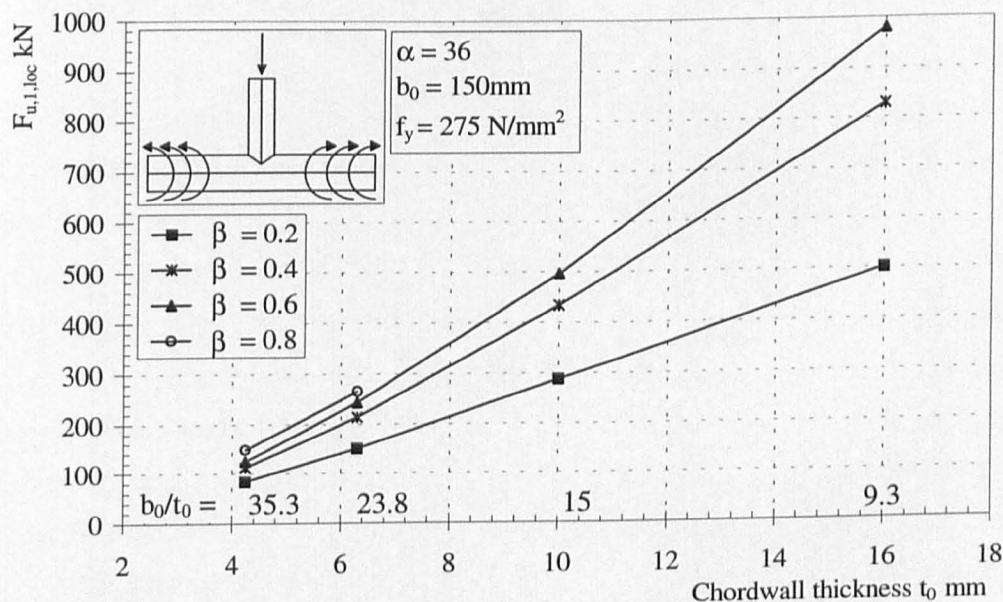


Figure 6.34 The variation in local joint capacity $F_{u,1,loc}$ with the chord wall thickness t_0 for diamond bird beak T joints without the effects of chord bending

The fit of these predictions against the results from the finite element analyses can be seen in Figure 6.35. Generally there is a good fit between the actual and the predicted results with the exception of the joint TBMV53 where $\beta = 0.2$ and $b_0/t_0 = 9.3$

where there is a possibility of a different form of failure. Careful examination of this joint reveals that the brace may have failed in shear (discussed in Chapter 4 for the X joints) before the expected joint capacity could be attained.

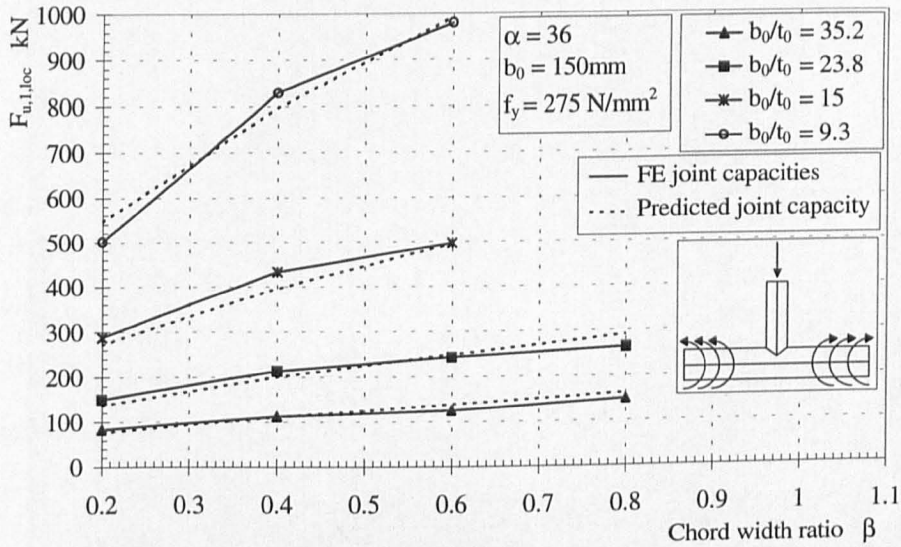


Figure 6.35 The variation in local joint capacity $F_{u,1,loc}$ with the chord width ratio β for diamond bird beak T joints without the effects of chord bending

When joints where $\beta = 0.8$ and a chord wall slenderness of $b_0/t_0 = 15$ and 9.3 or $\beta = 1$ were considered, the moment applied to the chord to remove the effects of chord bending exceeded the plastic moment of the chord section. Hence the moments applied to the chord become unbalanced, thus the bending moment at the centre line of the joint was no longer zero. Attempts were made to solve this problem by decreasing the size of the moment applied to the chord and increasing the number of moment increments to compensate. This resulted in a small increase in the value of $F_{u,1,loc}$. However, no consistent value could be found for the local joint capacity. Further changes in the increment size resulted in further increases in the value of $F_{u,1,loc}$. It was concluded that for full width or nearly full width joints the failure mechanism was principally that of a chord bending failure and the local joint capacity is of minor importance. This can be confirmed by examining the joint capacity of TBV38 = 887.7kN, shown in Table 6.9 where $\alpha = 6$, $\beta = 0.8$ and $t_0 = 16\text{mm}$. The load at which this joint can be expected to fail by a plastic moment at the centre line of the joint is 993kN which indicates the dominance of the chord bending in the failure mechanism.

6.12 The interaction curve method

This section will show how the reduced moment capacity $M_{p,v,0}$ of the chord is calculated to allow for the effects of shear caused by the load applied to the brace. This information together with the values of the joint strength $F_{u,1}$ and the local joint strength $F_{u,1,loc}$ obtained by finite element analyses in the previous sections will then be used to produce an interaction curve between the load applied to the brace and the moment acting in the chord to provide the designer with a better model to estimate the design strength of T joints of different chord lengths.

6.12.1 Introduction

Van der Vegte (1995) suggested an approach for CHS T joints considering the interaction between the force applied to the brace and the moment acting in the chord. The force applied to the brace $F_{u,1}$ is normalised by the local joint capacity $F_{u,1,loc}$ of similar T joint determined by finite element analysis, where all the effects of chord bending have been eliminated. The moment acting in the chord $M_{u,0}$ is normalised by the reduced plastic moment capacity of the chord $M_{p,v,0}$ which allows for the reduction in the moment capacity caused by the shear action of the brace on the chord. When these values are determined, then the load applied to the brace and the moment acting in the chord can be related to each by a normalised interaction curve defined by

$$\frac{F_{u,1}}{F_{u,1,loc}} \text{ and } \frac{M_{u,0}}{M_{p,v,0}}$$

where

$F_{u,1}$ is the maximum axial force applied to the brace which causes a local joint failure and/or a chord bending failure.

$M_{u,0}$ the moment acting in the chord due the action of the axial force applied the to brace $F_{u,1}$.

$F_{u,1,loc}$ the local joint capacity, found by analysing the joint without the effects of chord bending.

$M_{p,v,0}$ the theoretical moment capacity of the chord reduced to allow for the effect of shear caused by the load acting to cause the plastic collapse of the chord.

6.12.2 The theoretical determination of the reduced plastic moment capacity due to coincident shear

It was noted at the beginning of this section that the reduced moment capacity of the chord $M_{p,v,0}$ needed to be calculated so that moment capacity of the chord is accurately determined for all joint conditions. The moment capacity of the chord needs to be reduced to allow for the presence of shear caused by the axial load on the brace when a chord bending failure contributes to the failure mechanism. This term is a constant dependent on the cross sectional dimensions, the yield stress f_y and the length of the chord in the T joint considered.

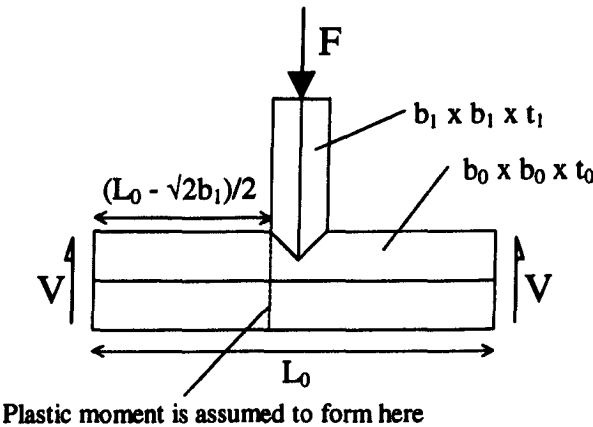


Figure 6.36 The loading of the diamond bird beak T joint with the effects of chord bending

In this calculation the chord plastic hinge is assumed to form under the crown of the brace member where the chord is free of any restraint from the brace, shown as a dotted line in Figure 6.36. It is recognised that the plastic hinge could form anywhere under the brace, but this position is considered most likely as the chord is not stiffened by the presence of the brace which will act to restrain the rotation of the hinge. Van der Vegte assumes that the relationship between the moment and the shear in the (CHS) chord is of the form

$$1 = \left(\frac{M}{M_p} \right)^2 + \left(\frac{V}{V_p} \right)^2 \tag{Eqn 6.12}$$

(Van der Vegte gives this relationship in his work with no further explanation. This formula actually represents the interaction between the bending moment and the shear

of a circular hollow section calculated theoretically based on an assumed distribution of the normal stress and shear stress, Wardenier (1982). A different assumption of the distribution normal stress and shear stress gives the same formula for a solid rectangular beam.) Assuming the same relationship for the shear and the moment for RHS in a diamond configuration as Wardenier does for either a solid rectangular beam or a CHS hollow section provides a means to calculate the reduced plastic moment capacity in the presence of shear. As no better relationship is available it is reasonable to assume that this relationship is correct, but to be aware of its possible limitations.

When the brace is axially loaded by a force F , the shear V and the moment M in the chord in the cross section under the crown of the brace are given by

$$V = \frac{1}{2} F \quad \text{Eqn 6.13}$$

$$M = \frac{1}{4} F (L_0 - \sqrt{2} b_1) \quad \text{Eqn 6.14}$$

and V_p and M_p , the plastic capacities for the shear and moment in the chord respectively, are given by

$$V_p = \frac{4(b_0 - t_0)t_0 f_y}{\sqrt{2}\sqrt{3}} \quad \text{Eqn 6.15}$$

$$M_p = \sqrt{2}(b_0 - t_0)^2 t_0 f_y \quad \text{Eqn 6.16}$$

Substituting Eqns 6.13 to 6.16 into Eqn 6.12 and solving for $F_{p,v,0}$, the assumed force in the brace when the chord failures by a combination of shear and bending, the value F , now called $F_{p,v,0}$, is found to be

$$F_{p,v,0} = \frac{8(b_0 - t_0)^2 t_0 f_y}{\sqrt{6(b_0 - t_0)^2 + 2(L_0 - \sqrt{2}b_1)^2}} \quad \text{Eqn 6.17}$$

The value of $M_{p,v,0}$, the moment capacity of the chord with shear present, can be found by substituting the value of $F_{p,v,0}$ into Eqn 6.14

$$M_{p,v,0} = \frac{2(b_0 - t_0)^2 t_0 f_y (L_0 - \sqrt{2}b_1)}{\sqrt{6(b_0 - t_0)^2 + 2(L_0 - \sqrt{2}b_1)^2}} \quad \text{Eqn 6.18}$$

6.12.3 Interaction curves for the diamond bird beak T joints

The results presented for the joint capacity $F_{u,1}$ in Table 6.8 & 6.9 and for the local joint capacity $F_{u,1,loc}$ in Table 6.14 are reproduced in Table 6.15. The values of $M_{u,0}$ and $M_{p,v,0}$ have been calculated using Eqns 6.14 & 6.18 respectively. This information is then used to produce the interaction diagram shown in Figure 6.37. The point labelled TBV56 can be discounted as examination of this point revealed that in the model TBMV53 used to find the local joint strength $F_{u,1,loc}$, the brace failed by shear before the expected joint capacity was attained.

A circular arc is drawn in Figure 6.37 to provide a basis for comparison of the finite element results and a possible relationship of

$$\left(\frac{F_{u,1}}{F_{u,1,loc}} \right)^2 + \left(\frac{M_{u,0}}{M_{p,v,0}} \right)^2 = 1 \quad \text{Eqn 6.19}$$

which is of a similar form to the Eqn 6.12. The spread of the finite element results, however, rules out any relationship of this kind.

Lines connecting joints of the same chord length ratio α but different chord slenderness b_0/t_0 , where $\beta = 0.6$, are drawn as an example to establish the relationship between chord length and slenderness. The chord slenderness of the joints on each line decreases from left to right along the line, as indicated on Figure 6.37.

Model	α $2L_0/b_0$	$\frac{b_0}{t_0}$	$F_{u,1}$ kN	$F_{u,1,loc}$ kN	$\frac{F_{u,1}}{F_{u,1,loc}}$	$M_{u,0}$ kNm	$M_{p,v,0}$ kNm	$\frac{M_{u,0}}{M_{p,v,0}}$
TBV54	12	35.3	68.2	84	0.812	14.6	33.7	0.434
TBV59	18	35.3	44.1	84	0.525	29.3	35.0	0.838
TBV50	6	23.8	144.4	150.7	0.958	14.7	43.2	0.341
TBV51	12	23.8	122.9	150.7	0.816	26.3	48.6	0.542
TBV52	18	23.8	112.7	150.7	0.748	36.8	49.7	0.741
TBV53	36	23.8	68.02	150.7	0.451	45.2	50.4	0.897
TBV55	18	15.0	203.3	288.9	0.704	43.6	73.4	0.594
TBV57	36	15.0	112.1	288.9	0.388	74.5	75.9	0.981
TBV56	12	9.3	459.9	501.7	0.917	98.6	107.9	0.914
TBV44	12	35.3	80.94	112.6	0.719	16.5	33.5	0.492
TBV45	18	35.3	72.38	112.6	0.643	22.9	34.4	0.665
TBV40	6	23.8	189.1	213.8	0.884	17.3	41.8	0.413
TBV41	12	23.8	150.1	213.8	0.702	30.6	48.4	0.632
TBV42	18	23.8	132.2	213.8	0.618	41.8	49.6	0.842
TBV43	36	23.8	77.47	213.8	0.362	50.6	50.4	1.006
TBV46	6	15.0	362.7	433.2	0.837	33.1	63.5	0.521
TBV47	18	15.0	238.9	433.2	0.551	75.6	74.9	1.009
TBV48	12	9.3	554.5	829.5	0.668	113.0	107.4	1.052
TBV49	36	9.3	207.6	829.5	0.250	135.7	111.3	1.220
TBV8	6	35.3	104.8	120.5	0.870	8.5	27.7	0.306
TBV20	12	35.3	86.8	120.5	0.720	16.7	33.4	0.502
TBV13	18	35.3	75.5	120.5	0.627	23.1	34.4	0.671
TBV16	36	35.3	48	120.5	0.398	30.9	35.0	0.883
TBV5	6	23.8	202.5	243.7	0.831	16.4	40.0	0.408
TBV19	12	23.8	161.3	243.7	0.662	31.2	48.2	0.647
TBV12	18	23.8	138.2	243.7	0.567	42.2	49.6	0.852
TBV11	36	23.8	79.2	243.7	0.325	50.9	50.4	1.012
TBV9	6	15.0	407.7	496.6	0.821	32.9	60.9	0.540
TBV21	12	15.0	322.5	496.6	0.649	62.3	72.7	0.857
TBV14	18	15.0	247.2	496.6	0.498	75.6	74.8	1.011
TBV17	36	15.0	124.6	496.6	0.251	80.1	75.9	1.056
TBV10	6	9.3	786.8	979.9	0.803	63.5	90.7	0.700
TBV22	12	9.3	601.8	979.9	0.614	116.3	107.0	1.086
TBV15	18	9.3	415.2	979.9	0.424	126.9	109.8	1.156
TBV18	36	9.3	202.1	979.9	0.206	130.0	111.3	1.168
TBV34	6	35.3	130.5	148.9	0.876	9.1	26.1	0.351
TBV35	12	35.3	101.5	148.9	0.682	18.5	33.2	0.558
TBV35A	18	35.3	85.07	148.9	0.571	25.1	34.3	0.731
TBV30	6	23.8	231.9	265.8	0.872	16.3	37.8	0.430
TBV31	12	23.8	185.9	265.8	0.699	33.9	47.9	0.709
TBV32	18	23.8	151.1	265.8	0.568	44.6	49.5	0.901
TBV33	36	23.8	77.96	265.8	0.293	49.3	50.4	0.979

Table 6.15 The values used to produce the interaction diagrams for the diamond bird
beak T joints

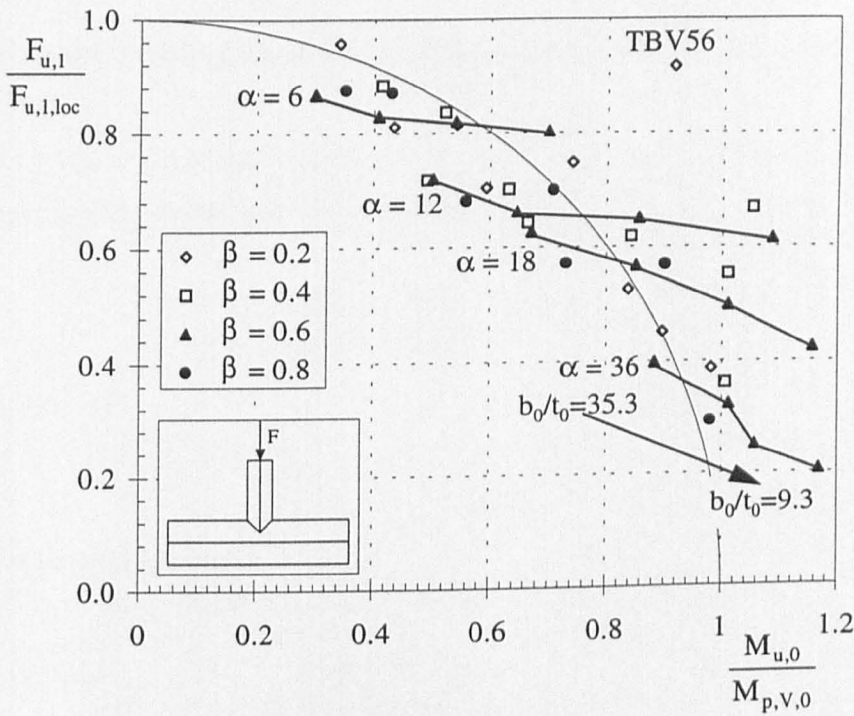


Figure 6.37 Interaction curve for the diamond bird beak T joint

Examining Figure 6.37 it can be seen that:

- the failure of joints with short chord lengths, i.e. low α , occurs when $F_{u,1}/F_{u,1,loc} \rightarrow 1$ and the moment in the chord does not contribute significantly towards the failure.
- failure occurs for long chord lengths, i.e. high α , when $F_{u,1}/F_{u,1,loc} \rightarrow 0$ and $M_{u,0}/M_{p,v,0} \approx 1$ when the dominant mode of failure is caused by chord bending.
- the values for the moment acting in the chord exceed the estimated reduced plastic moment capacity of the chord $M_{p,v,0}$. However, it was shown in Figure 6.16 that the moment observed in the longer and stockier joints exceeded the moment capacity of the chord section, so that this is not unexpected.
- as the slenderness of the chord decreases, so the results move down and to the right. The movement to the right is attributed to the presence of plastic hinges in the chord wall at the corners of the chord member, increasing the strength of the joint as a function of t_0^2 instead of t_0 (i.e. a plastic hinge forming in the chord under the brace member). The result of the increased strength of the joint is that a larger moment $M_{u,0}$ acts in the chord due to the action of $F_{u,1}$ and hence to ratio $M_{u,0}/M_{p,v,0}$ increases. This can be clearly seen when $\alpha = 6$ and when $\alpha = 12, 18$ & 36 although

the reduction in the $F_{u,1}$ due to the chord bending effect becomes progressively more evident.

Examining this data a lower bound (i.e. safe) solution that may be used to predict the joint capacity with the variation of chord length is given by

$$\frac{F_{u,1}}{F_{u,1,loc}} + \frac{M_{u0}}{M_{p,V,0}} = 1.2 \quad \text{Eqn 6.20}$$

with the limits of

$$\frac{F_{u,1}}{F_{u,1,loc}} \quad \text{and} \quad \frac{M_{u0}}{M_{p,V,0}} \leq 1$$

and is shown in Figure 6.38

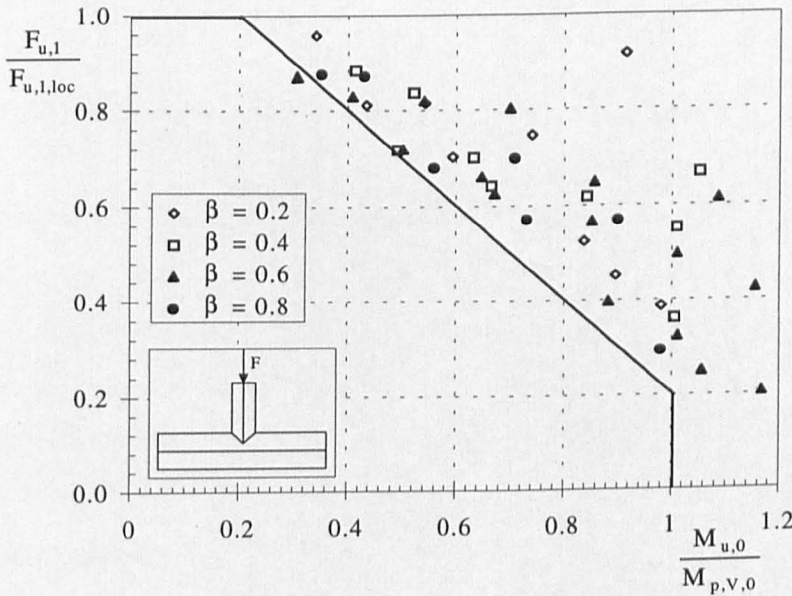


Figure 6.38 Interaction diagram for the diamond bird beak T joint showing the fit of the design prediction

6.13 Comparisons between the predicted joint capacity and the observed joint capacity

The diamond bird beak T joint capacities with the effects of chord bending obtained by finite element analysis are compared to the different methods of predicting the joint capacity considered in this Chapter are shown in Figure 6.39. The accuracy of the different predictions when compared to the finite element analyses are discussed in the following sections.

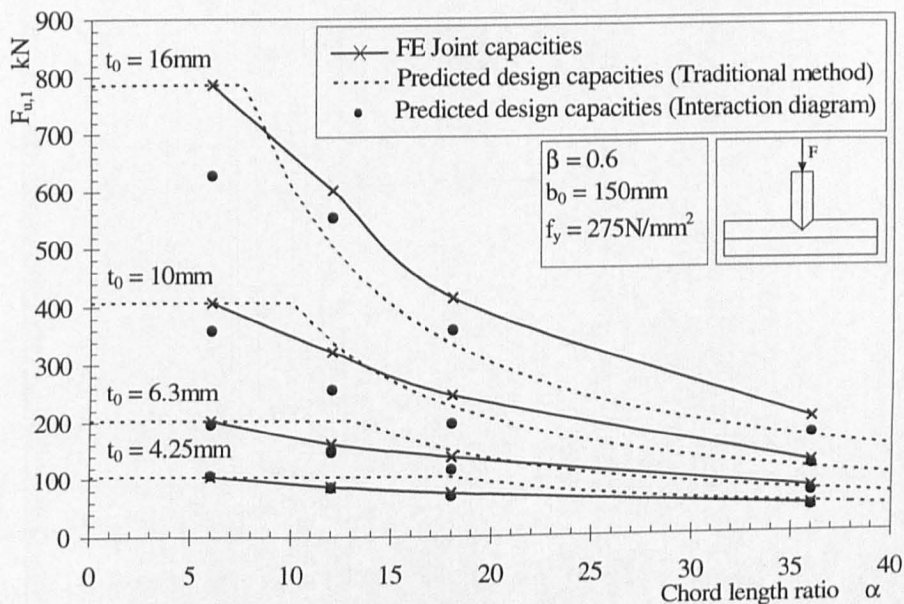


Figure 6.39 A comparison of the different design methods to the finite element joint capacities for diamond bird beak T joints with varying chord lengths

6.13.1 The traditional design method

The design methods used at present may overestimate or underestimate the results considerably, as discussed in detail in Section 6.4.4. The method is simple to understand and the calculations easily performed. However, the behaviour of the predicted joint design with chord length has little in common with the results obtained by finite element analysis.

6.13.2 Predicted design capacity from the interaction diagrams

The design capacity using the interaction design methods is compared with the joint capacities from the finite element analyses and is shown in Figure 6.39. Examining this figure it can be seen that the interaction design method gives a better representation of the variation of joint capacity with chord length and that the joint capacities of the slender chord sections are predicted with a reasonable accuracy, although the stockier sections are seriously underestimated.

Attempts have been made to rectify this discrepancy by modifying the design prediction in the form of

$$\frac{F_{u,1}}{F_{u,1,loc}} + \frac{M_{u0}}{M_{p,v,0}} = 1.2 f\left(\frac{b_0}{t_0}\right) \quad \text{Eqn 6.21}$$

where $f\left(\frac{b_0}{t_0}\right)$ is some function of the chord slenderness. However, no satisfactory solution has been found to date due to the large variation in the results with chord wall slenderness and the chord width ratio β .

6.13.3 Conclusions

The traditional design approach can be simply calculated by the designer with minimal reference to design codes and other data sources. The interaction approach is more complex and requires the local joint strength $F_{u,1,loc}$ and the moment capacity of the chord reduced for the effects of shear to be pre-calculated before the joint capacity can be determined. The fact that design equations are used twice in the calculation, to determine the local joint strength $F_{u,1,loc}$ and then the joint capacity $F_{u,1}$ will introduce an extra source of error into the calculation. There could be a possible improvement in the accuracy if the local joint capacity is calculated (by finite element analysis) for all the possible combinations of parameters. However, this would require a large database of knowledge to be consulted. The interaction design approach may be more suited for use in a computer based system where data could be referenced and the calculations performed in the background without the user being aware of the details of the calculation.

The interaction approach does give a better reflection of the variation in the joint capacity with chord length, although until a relationship incorporating the effects of the chord wall slenderness is found the accuracy of the method is not good.

6.14 RHS T joints

To provide a comparison for the diamond bird beak T joints, similar RHS T joints are examined in this section. The general arrangement of the RHS T joint can be seen in Figure 6.2 and an example of the finite element mesh in Figure 6.3. The material properties remain the same as before, that Young's Modulus $E = 207 \text{ kN/mm}^2$ and a yield stress $f_y = 275 \text{ N/mm}^2$.

The end of the chord is supported in the same manner as the diamond bird beak T joints, in that all the nodes at the end of the chord are restrained vertically to provide a reaction to the load applied to the brace. This is not likely to affect the joint strength of the traditional RHS T joint as the failure mechanism is independent of the length of

the chord, but is applied in this manner to keep to the principle of applying the minimum restraint at the end of the chord and to keep the joints as similar as possible.

The indentation is measured in a similar manner to the diamond bird beak T joints, between a point on the brace approximately $b_1/2$ from the connection on the centre line of the joint to the corner of the chord on the bottom face, shown in Figure 6.40. The plastic moment capacity of the chord has been determined by using Eqn 6.4.

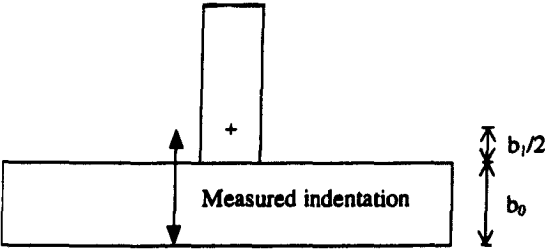


Figure 6.40 The method of measuring the indentation of the traditional RHS T joint

6.14.1 The results of the finite element analyses for the RHS T joints with the effects of chord bending

The method of loading to obtain the results with the effects of chord bending is shown in Figure 6.2 and the results of these finite element analyses are given in Table 6.16 for the RHS T joints.

6.14.2 Discussion of the results of the finite element analyses for the variation in joint capacity with chord length RHS T joints with the effects of chord bending

When traditional RHS X joints were studied in Chapter 4 it was established that the joint capacity was unaffected by the length of the chord, provided that there was sufficient chord length for the yield line pattern to form in the connecting face of the chord. The same yield line pattern can be expected to form in the traditional RHS T joint so that the local joint capacity can be expected to remain constant with changing chord length and any change in the joint capacity with chord length can be attributed to the chord bending effects.

An example of the effect of the variation in joint capacity with chord length can be seen in Figure 6.41 where four similar RHS T joints with $\beta = 0.6$ and different chord wall slendernesses and chord length are compared. The joint capacity can be seen to decrease with chord length and with increasing chord slenderness. The apparent

discontinuity of the curve where $b_0/t_0 = 9.3$ and $\alpha = 6$ may be due to a shear failure of the chord walls becoming more predominant in the failure mechanism.

Model	L_0 mm	α $2L_0/b_0$	b_0 mm	t_0 mm	b_0/t_0	β b_1/b_0	b_1 mm	t_1 mm	$F_{u,1}$ kN
RHST44	1800	24	150	6.3	23.8	0.2	30	3.0	38.4
RHST40	2700	36	150	6.3	23.8	0.2	30	3.0	34.6
RHST41	2700	36	150	10	15.0	0.2	30	3.0	82.1
RHST45	1800	24	150	16	9.3	0.2	30	3.0	199.7
RHST42	2700	36	150	16	9.3	0.2	30	3.0	160.0
RHST28	1350	18	150	4.25	35.3	0.4	60	5.0	27.0
RHST25	2250	30	150	4.25	35.3	0.4	60	5.0	25.4
RHST35	3600	48	150	4.25	35.3	0.4	60	5.0	23.2
RHST31	900	12	150	6.3	23.8	0.4	60	5.0	58.6
RHST27	1800	24	150	6.3	23.8	0.4	60	5.0	55.3
RHST20	2700	36	150	6.3	23.8	0.4	60	5.0	50.0
RHST29	1350	18	150	10	15.0	0.4	60	5.0	135.2
RHST24	2250	30	150	10	15.0	0.4	60	5.0	115.0
RHST34	3600	48	150	10	15.0	0.4	60	5.0	82.3
RHST30	900	12	150	16	9.3	0.4	60	5.0	338.6
RHST32	1350	18	150	16	9.3	0.4	60	5.0	299.0
RHST26	1800	24	150	16	9.3	0.4	60	5.0	248.1
RHST22	2700	36	150	16	9.3	0.4	60	5.0	178.6
RHST17	900	12	150	4.25	35.3	0.6	90	6.3	42.6
RHST16	1800	24	150	4.25	35.3	0.6	90	6.3	39.0
RHST15	2700	36	150	4.25	35.3	0.6	90	6.3	34.4
RHST61	3600	48	150	4.25	35.3	0.6	90	6.3	30.2
RHST4	450	6	150	6.3	23.8	0.6	90	6.3	92.3
RHST3	900	12	150	6.3	23.8	0.6	90	6.3	89.3
RHST2	1350	18	150	6.3	23.8	0.6	90	6.3	84.8
RHST5	1800	24	150	6.3	23.8	0.6	90	6.3	78.6
RHST6	2250	30	150	6.3	23.8	0.6	90	6.3	72.0
RHST1	2700	36	150	6.3	23.8	0.6	90	6.3	64.6
RHST7	3600	48	150	6.3	23.8	0.6	90	6.3	53.9
RHST10	900	12	150	10	15.0	0.6	90	6.3	207.9
RHST60	1350	18	150	10	15.0	0.6	90	6.3	186.5
RHST9	1800	24	150	10	15.0	0.6	90	6.3	159.7
RHST8	2700	36	150	10	15.0	0.6	90	6.3	118.5
RHST13	450	6	150	16	9.3	0.6	90	6.3	507.5
RHST19	900	12	150	16	9.3	0.6	90	6.3	449.2
RHST12	1350	18	150	16	9.3	0.6	90	6.3	348.0
RHST11	2250	30	150	16	9.3	0.6	90	6.3	220.2
RHST14	3600	48	150	16	9.3	0.6	90	6.3	137.1

Table 6.16 The variation of the joint capacity $F_{u,1}$ with chord length α for traditional RHS T joints with the effects of chord bending

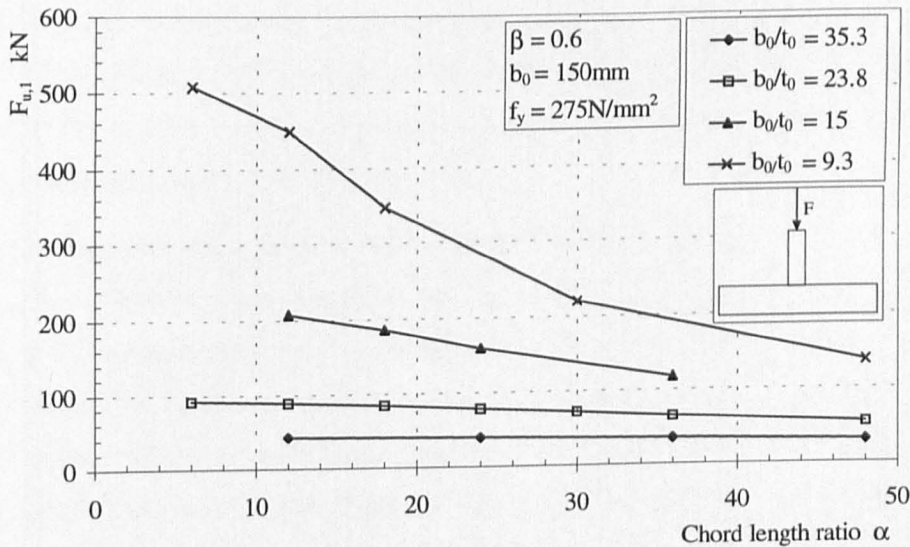


Figure 6.41 The variation of joint capacity with chord length for the traditional RHS T joint with the effects of chord bending

The variation in the normalised moment acting in the chord with the chord length can be seen in Figure 6.42. The joints where $b_0/t_0 = 9.3$ and $\alpha \geq 30$ can be seen to be failing by overall chord bending whilst the others fail by a combination of chord bending and local joint failure (with the possibility of a shear failure of the chord wall for the joint where $b_0/t_0 = 9.3$ and $\alpha = 6$).

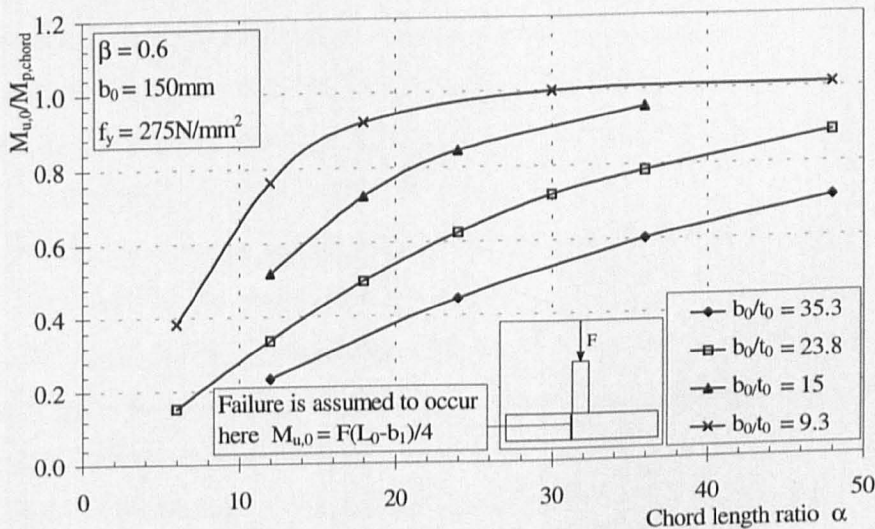


Figure 6.42 The variation of the normalised moment with chord length and chord wall thickness for traditional RHST joints with the effects of chord bending

It is interesting to compare this Figure with the corresponding diagram for the diamond bird beak T joints shown in Figure 6.16. In Figure 6.42 the limiting value for

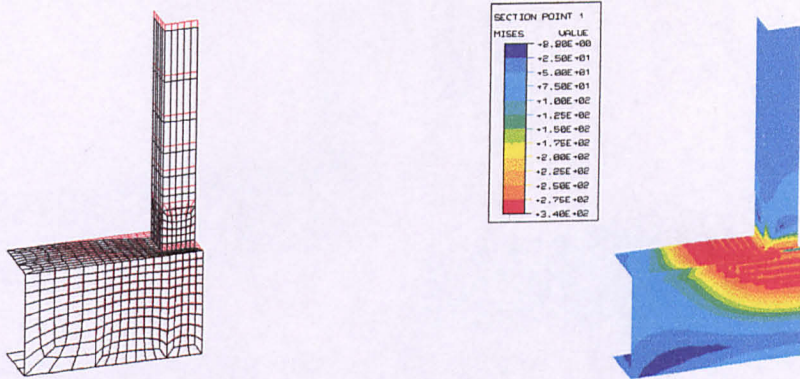
the normalised moment acting in the chord is 1, whereas in Figure 6.16 the limiting value is 1.16. Clearly the orientation of the chord in the traditional RHS T joint does not affect the moment capacity of the chord in the manner which has been observed in the diamond bird beak T joint.

6.14.2.1 Displaced shape and von Mises contoured stress plots

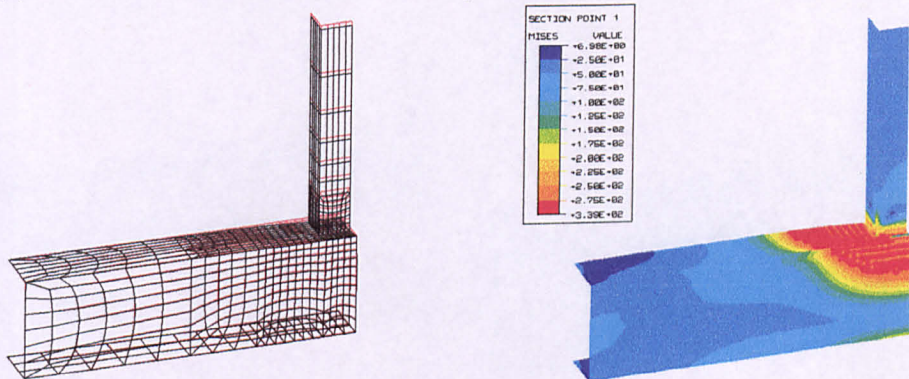
The displaced shape diagrams and the contoured stress plots are shown in Figure 6.43, for the outside level at the joint capacity for the traditional RHS T joints. The transition between a local joint failure in the shorter chord length joints to the failure of the chord by a plastic hinge forming in the vicinity of the brace for the longer chord length joints can be seen clearly in this figure. Examining the contoured stress plots carefully it can be seen that when $\alpha = 6$ or 12 there is little evidence of any increase of stress in the material on the lower part of the chord. The shape and size of the yield material in the top part of the chord is virtually identical between the two joints and it is concluded that failure is predominately of a local nature.

When $\alpha = 18$ there is evidence of the increase in stress on the lower part of the chord as the plastic hinge begins to form. The shape of the yielded material in the top part of the side wall of the chord shows a distinct change from the shorter chord length joints. The contoured stress plot when $\alpha = 24$ is very similar to that of the joint where $\alpha = 18$ however, there is a distinct increase in the size of the area of the material in the top face where the stress has increased, but the material has not yielded. It is concluded that these two joints represent a transitional region between the local failure and the overall chord bending failure.

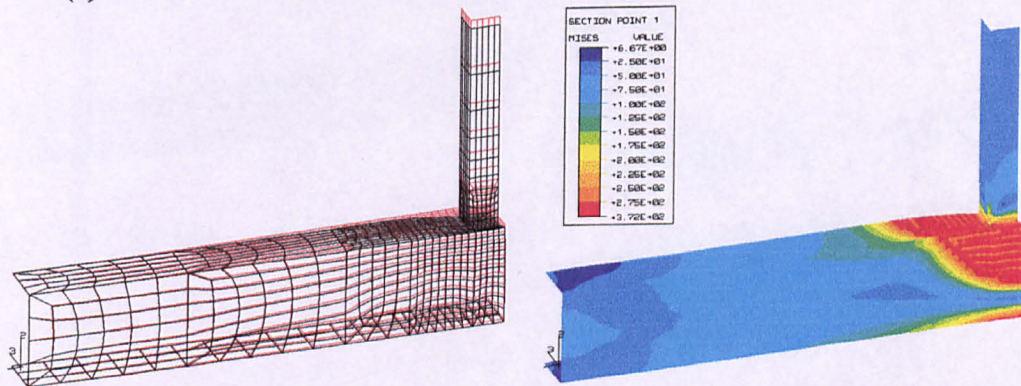
The displaced shape diagram when $\alpha = 30$ shows that there is a distinct bending of the chord, none of the displaced shape diagrams of the shorter chord length joints (i.e. $\alpha < 30$) have shown any significant bending of the chord. The area of yielded material in the lower part of the brace has increased in size significantly as has the area of material in the top face of the chord where there is an increase in the stress, but the material has not yielded. It is concluded that the failure is dominated by the formation of the plastic hinge in the chord under the brace.



(a) RHST4 $\alpha = 6$ $L_0 = 450\text{mm}$ $\beta = 0.6$ $b_0/t_0 = 23.8$ Load = 92.6kN

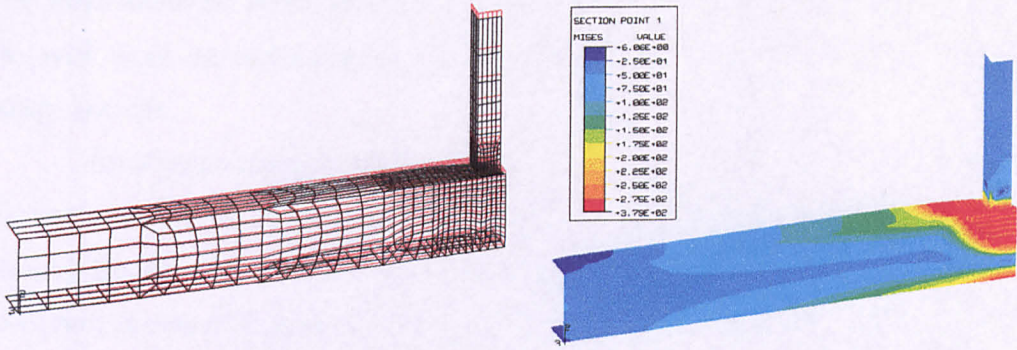


(b) RHST3 $\alpha = 12$ $L_0 = 900\text{mm}$ $\beta = 0.6$ $b_0/t_0 = 23.8$ Load = 89.3kN

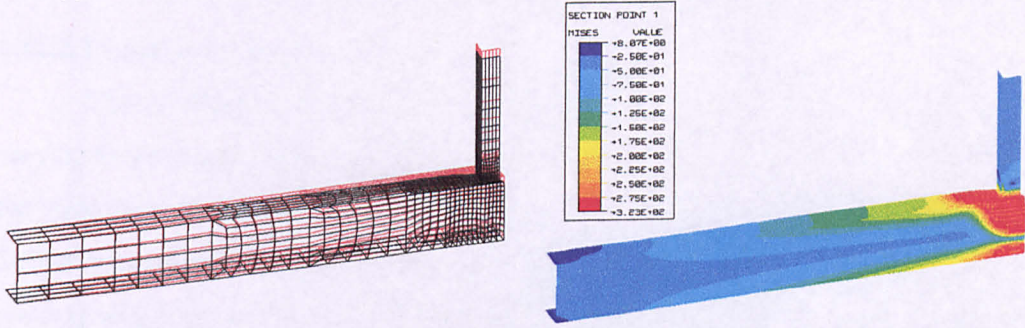


(c) RHST2 $\alpha = 18$ $L_0 = 1350\text{mm}$ $\beta = 0.6$ $b_0/t_0 = 23.8$ Load = 84.8 kN

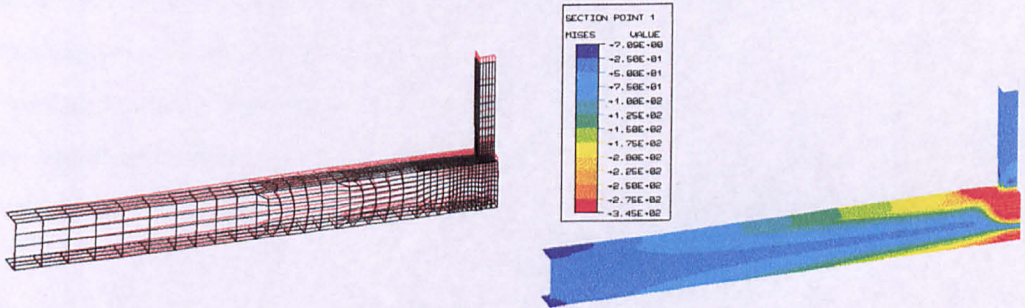
Figure 6.43 Displaced shape diagrams and von Mises contoured stress plots of the outside level for the traditional RHST joints at the joint capacity $F_{u,1}$. Joints loaded with the effects of chord bending



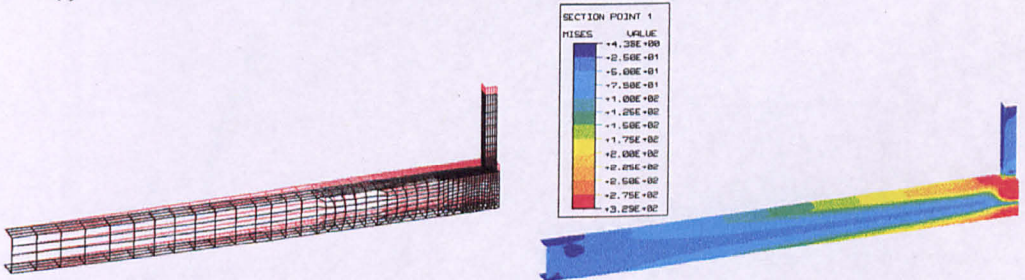
(d) RHST5 $\alpha = 24$ $L_0 = 1800\text{mm}$ $\beta = 0.6$ $b_0/t_0 = 23.8$ Load = 78.6kN



(e) RHST6 $\alpha = 30$ $L_0 = 2250\text{mm}$ $\beta = 0.6$ $b_0/t_0 = 23.8$ Load = 72.0kN



(f) RHST1 $\alpha = 36$ $L_0 = 2700\text{mm}$ $\beta = 0.6$ $b_0/t_0 = 23.8$ Load = 64.6kN



(g) RHST7 $\alpha = 48$ $L_0 = 3600\text{mm}$ $\beta = 0.6$ $b_0/t_0 = 23.8$ Load = 53.9kN

Figure 6.43 (cont.) Displaced shape diagrams and von Mises contoured stress plots of the outside level for the traditional RHS T joints at the joint capacity $F_{u,1}$. Joints loaded with the effects of chord bending

The joints where $\alpha = 36$ or 48 are very similar to that when $\alpha = 30$, but there is progressively more bending in the chord shown in the displaced shape diagrams and the

the areas where the stress shows an increase but has not yielded. The area of yielded material in all the joints (where $\alpha = 30, 36$ or 48) is remarkably consistent both in shape and size.

An attempt has been made in this section to distinguish the dominant mode of failure operating in any particular joint. Examination of Figure 6.42 shows that for those joints where $t_0 = 6.3\text{mm}$, even when $\alpha = 48$ the maximum moment operating in the chord is only 88% of the plastic capacity of the chord section, so it cannot be said that the failure is completely that of chord bending failure even for this very long joint.

6.14.2.2 Load indentation curves

The load/indentation curves are shown in Figure 6.44 for similar joints of varying chord length. When $\alpha = 6$ the failure is due predominately to the formation of the yield lines in the connecting face of the chord. No maximum load is attained, as further increases in load cause more rotation at the yield lines and additional in-plane yielding within the mechanism. However, when the long chord length joint e.g. $\alpha = 48$ is considered, a maximum value is attained as the failure is predominately that of chord bending as the moment acting in the chord approaches the moment capacity of the chord and a further increase in load cannot be supported. The intermediate curves show the transition between the local failure of the joint (i.e. yield line failure) through to an overall chord bending failure (i.e. moment capacity of the section is reached).

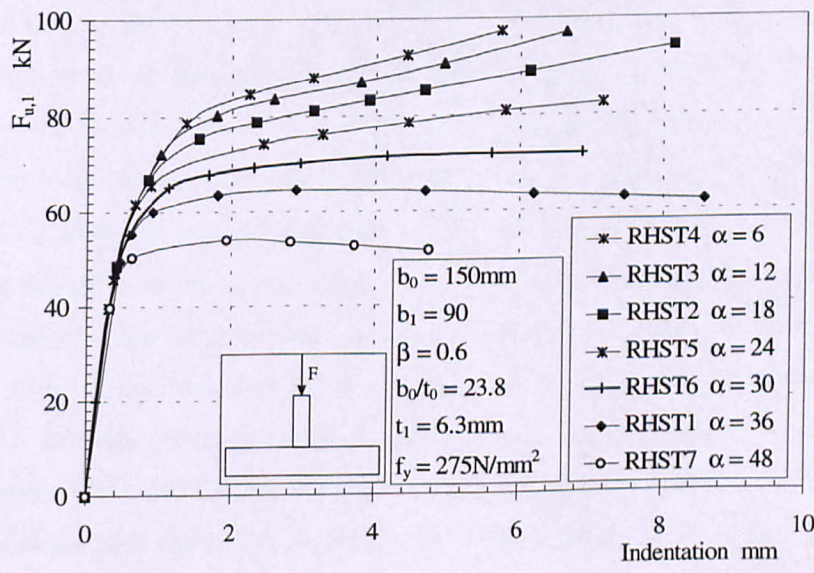


Figure 6.44 Example of the load/indentation curves for the traditional RHS T joints with varying chord length

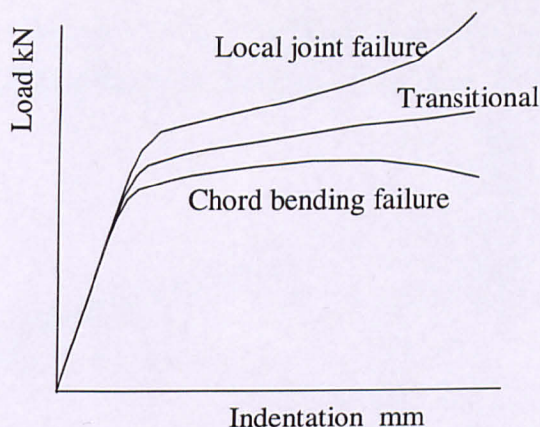


Figure 6.45 The three different forms of curves seen in Figure 6.44

Whilst the classification of the failure mechanism of the joints with different chord lengths used in the previous section is subjective, in that there are no clear boundaries between the different forms of failure, it is observed that the load/indentation curves shown in Figure 6.44 exhibit three distinct forms as shown in Figure 6.45. The first representing a local joint failure, where the rate of change of the slope is -ve but becomes +ve in the range of the observed data. The second representing the transitional region, where the rate of change of the slope of the graph is always -ve. (What happens beyond the range of data given in Figure 6.44 is not known) and the third and last, where a chord bending failure is observed and a maximum joint capacity is achieved. The classification of the failure mechanism with chord length observed by examination of the load/indentation curves agrees with that made from the contoured stress plot examined in the previous section.

The load/indentation curves for 4 similar joints with the same chord length ratio $\alpha = 12$ ($L_0 = 900\text{mm}$) but with different chord slenderness are shown in Figure 6.46 where the results have been normalised by the moment capacity of the chord wall. Examination of these curves shows that they are not coincident which would be expected if the failure was due to the formation of a yield line pattern. Instead, the normalised strength decreases with increasing chord wall thickness showing that another mechanism must be operating. Examining the moment acting in the chord it is found that at the joint capacity when $b_0/t_0 = 35.3$ the moment is 25% of the capacity of the chord however, when $b_0/t_0 = 9.3$ the moment is 76% of the capacity of the chord.

Showing that even though the same chord length is considered, stockier sections are failing by chord bending rather than a yield line failure mechanism.

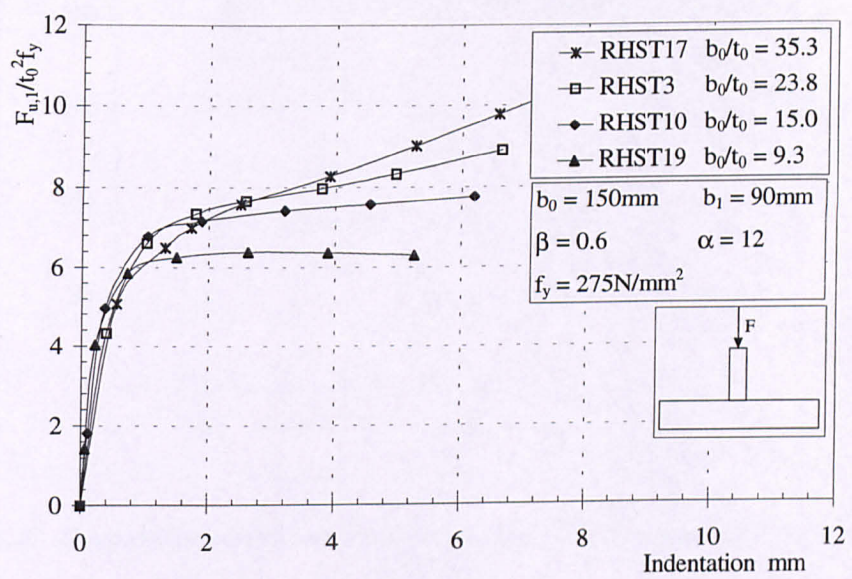


Figure 6.46 Example of the load/indentation curves for the traditional RHS T joints with varying chord slenderness

This should be expected as the joint capacity is a function of t_0^2 for the yield line failure and a function of t_0 when the failure is due to the formation of a plastic hinge in the chord. The fact that the curve for $b_0/t_0 = 9.3$ attains a maximum load confirms the chord bending failure is likely to be dominant in the failure mechanism. The intermediate curves show the transition as the chord bending becomes progressively more dominant in the failure mechanism as the curves have a lower normalised strength and exhibit less work hardening as the slenderness decreases.

6.14.2.3 Comparisons between the traditional RHS T joints and the diamond bird beak T joints

If Figure 6.41 is compared to Figure 6.14, where similar diamond bird beak T joints are studied, the curves show remarkable similarity. The most notable difference being the joint capacity at which the joints fail for the same size chord; the diamond bird beak T joints being significantly stronger (up to 100%) than traditional RHS T joint for shorter chord lengths. For the longer joints where the failure is due to chord bending then the joint capacities are more comparable.

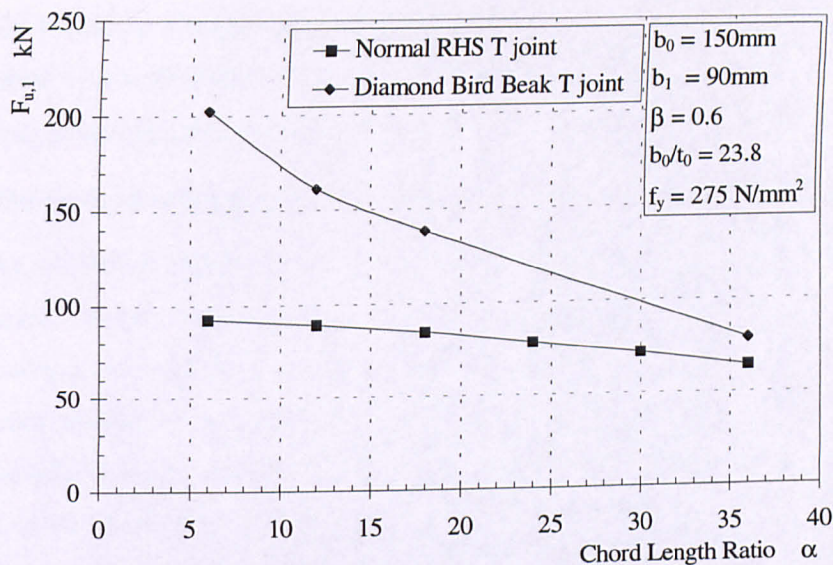


Figure 6.47 Comparison between identical bird beak and traditional RHS T joints, assuming butt welds

Figure 6.47 shows the comparative joint strengths of the traditional RHS and diamond bird beak T joint for identical joints (i.e. the same chord and brace members) over a range of chord lengths. The joint capacity for the diamond bird beak joint when $\alpha = 6$ can be seen to be inflated due to the support given to the joint by the boundary conditions at the end of the chord whilst the traditional RHS T joints derive no extra strength from the support conditions at the end of the chord. Additionally, if the traditional RHS T joint is constructed using a fillet weld (not modelled in these joints) then there will be an appreciable increase in the strength of the traditional RHS joints. As a result of this it is not completely correct to say that the bird beak joints are 100% stronger than the traditional RHS T joints when $\alpha = 6$.

At the beginning of this Chapter it was shown that the moment capacity of the chord in the traditional RHS joint configuration is slightly greater (6%) than that for the diamond bird beak configuration. Therefore the fact that the diamond bird beak joint is stronger than the traditional RHS joint when $\alpha = 36$ may seem surprising, although it would appear that the curves may converge outside the range of this figure. Comparing the moment acting in the chord of the two joints it can be seen with reference to Figure 6.16 and Figure 6.42 that in the diamond bird beak joint the moment is 100% of the moment capacity compared to only 80% for the traditional RHS joint. It could be expected that if the chord length were further increased, the

RHS joint would be stronger than the diamond bird beak joint however, the fact that the diamond bird beak joints can achieve a higher moment capacity than calculations predict may enable the bird beak joint to retain its strength advantage.

6.14.3 The method of loading used to remove the effects of chord bending

As the failure mechanism of a traditional RHS T joint is independent of the chord length, shorter chord lengths can be used to find a constant value of $F_{u,l,loc}$. It would therefore be expected that there should be no problem in applying the moment in the same manner as van der Vegte (1995) for CHS T joints and Yu (1995) for traditional RHS T joints shown in Figure 6.48a. However, as applying the moment as a series of incremental moments has been shown to be a better method to remove the effects of chord bending, the moment is applied in this manner and is shown in Figure 6.48b.

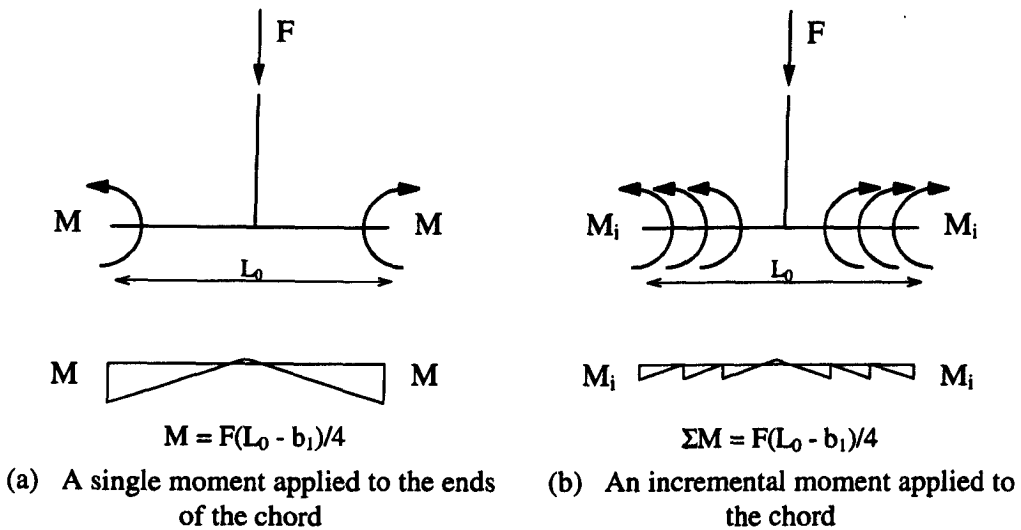


Figure 6.48 The methods of removing the effects of chord bending

6.14.3.1 The results of the finite element analyses for the RHS T joints without the effects of chord bending

The results of the joints analysed without the effects of chord bending are given in Table 6.17.

Model	L_0 mm	α $2L_0/b_0$	b_0 mm	t_0 mm	b_0/t_0	β b_1/b_0	b_1 mm	t_1	$F_{u,1,loc}$ kN
RHST40M	2700	36	150	6.3	23.8	0.2	30	3.0	40.3
RHST41M	2700	36	150	10	15.0	0.2	30	5.0	96.3
RHST42M	2700	36	150	16	9.3	0.2	30	12	220.4
RHST23M	2700	36	150	4.25	35.3	0.4	60	5.0	28.4
RHST20M	2700	36	150	6.3	23.8	0.4	60	5.0	60.1
RHST21M	2700	36	150	10	15.0	0.4	60	5.0	147.3
RHST22M	2700	36	150	16	9.3	0.4	60	6.3	355.3
RHST15M	2700	36	150	4.25	35.3	0.6	90	6.3	44.8
RHST1M	2700	36	150	6.3	23.8	0.6	90	6.3	94.1
RHST8M	2700	36	150	10	15.0	0.6	90	6.3	219.6
RHST18M	2700	36	150	16	9.3	0.6	90	6.3	507.5

Table 6.17 The local joint capacity $F_{u,1,loc}$ for traditional RHS T joints without the effects of chord bending

6.14.4 Discussion of the results of the finite element analyses for the RHS T joints without the effects of chord bending

It would have been thought that as the effects of chord bending have been eliminated, that the yield line prediction given in the CIDECT design guide for rectangular hollow sections Packer et al (1992) would predict with reasonable accuracy the local joint strength $F_{u,1,loc}$.

$$F_{u,1,loc} = \frac{t_0^2 f_{y,0}}{(1-\beta)} (2\beta + 4\sqrt{(1-\beta)}) \quad \text{Eqn 6. 22}$$

(for a T joint where $\theta = 90^\circ$).

However, this is not the case as can be seen in Figure 6.49 where the local joint capacities reported in Table 6.17 have been normalised by the plastic moment capacity of the chord wall $m_p (= f_y t_0^2/4)$ and plotted against the chord width ratio. The dotted line represents the predicted capacity of the joint as given by the yield line prediction. The yield line gives an upper bound solution and the failure mechanism is dominated by a different form of failure at low chord width ratios, most likely a punching shear failure of the top face of the chord.

Further examination of Figure 6.49 shows that even though the joint capacity has been normalised by the plastic moment capacity of the chord wall m_p , the non-

dimensional strength increases with chord wall slenderness. This effect can be eliminated by “normalising” the curves to a function of $t_0^{1.85}$, showing that the failure mode is not completely that of a yield line failure.

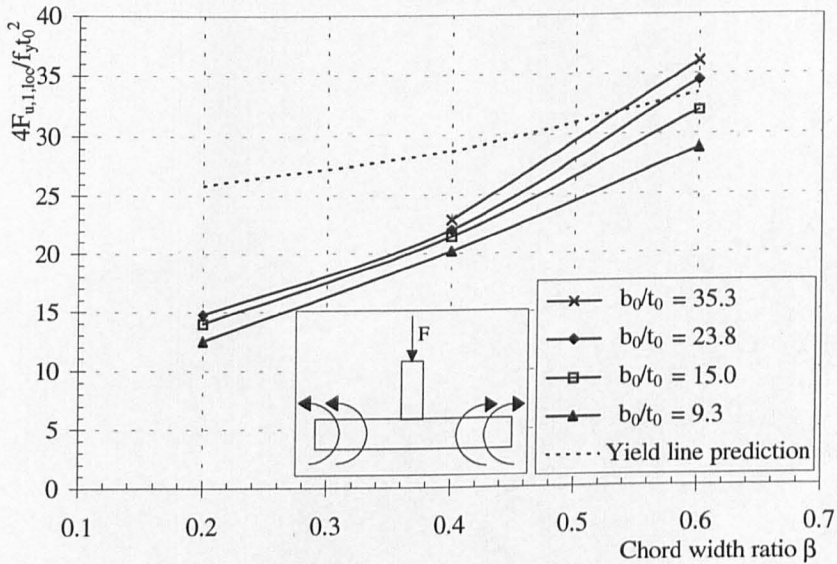


Figure 6.49 Local joint capacities normalised by the plastic moment capacity of the chord wall, $\alpha = 36$

Figure 6.49 shows that a good estimate can be made of the local joint capacity $F_{u,1,loc}$ when $\beta = 0.6$ and a reasonable estimation when $\beta = 0.4$. (It is thought likely that a reasonable estimation of the local joint capacity could be made for $\beta = 0.8$ as punching shear will not affect the failure load at this chord width, although no joints with this chord width ratio were examined.)

6.14.4.1 Displaced shape diagrams and von Mises contoured stress plots for the RHS T joints without the effects of chord bending

The displaced shape diagrams and von Mises contoured stress plots for RHS T joints loaded without the effects of chord bending for the outside level and at the joint capacity are shown in Figure 6.50. The deformations in the displaced shape diagrams have been magnified by a factor of 3 to show more clearly where the deformation is occurring. The joints chosen are identical except in chord length to confirm that the effects of chord bending have been removed.

The effects of chord bending can be seen to be removed by examining the displaced shape diagrams that reveal no deformation of the chord. Figure 6.51 shows the deformation shown in Figure 6.50c, zoomed in to the chord in the vicinity of the

brace, where it can be clearly seen that the failure is that of a local joint failure observed in the short chord length joints shown Figure 6.43a or b.

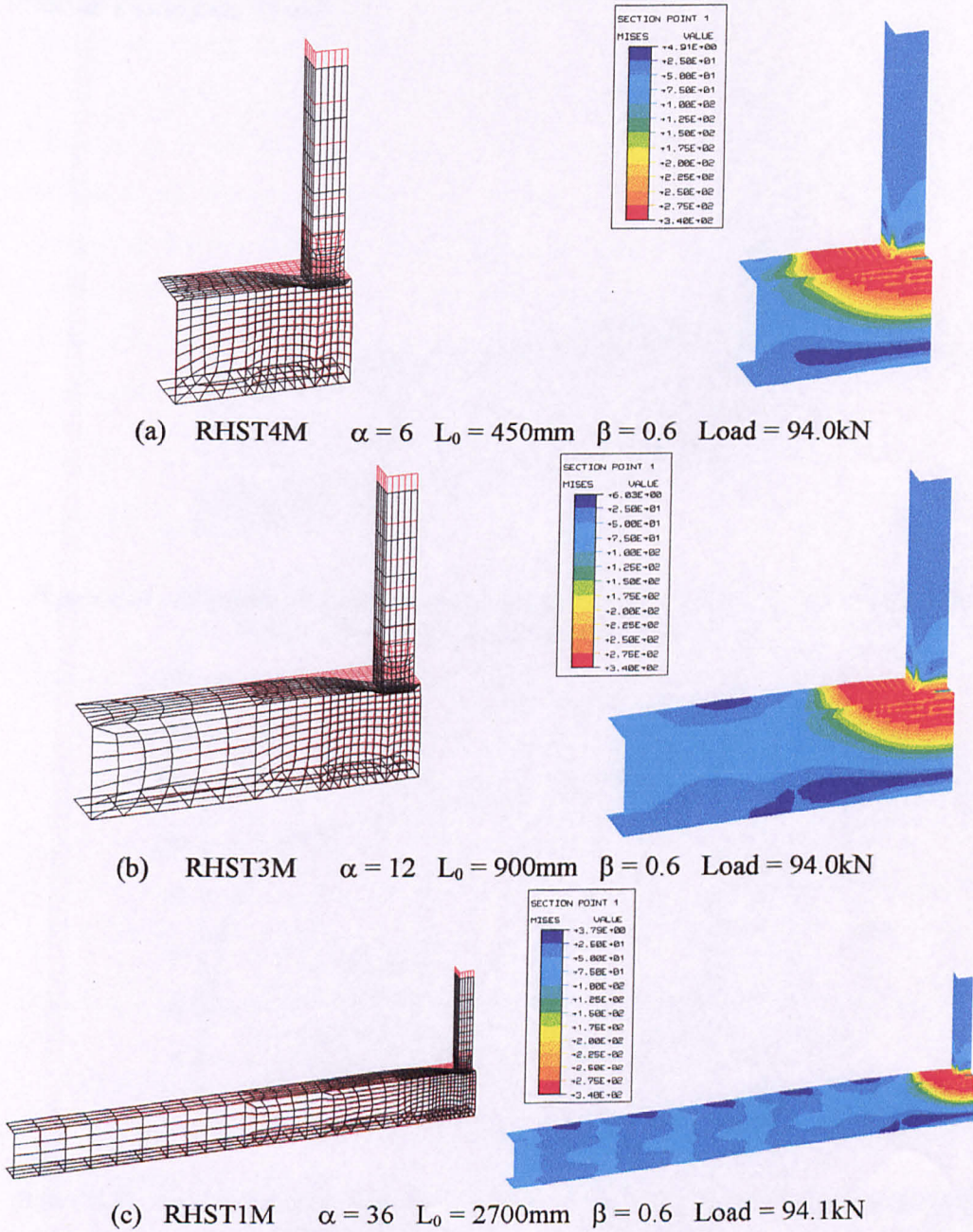


Figure 6.50 Displaced shape diagrams and von Mises contoured stress plots of the outside level for the traditional RHS T joints at the joint capacity $F_{u,l,loc}$. Joints loaded without the effects of chord bending

Examination of the von Mises contoured stress plots reveals that the mode of the failure is identical in all three joints in that the stress distribution is identical in all three figures. It is interesting to compare the stress distribution observed in Figure 6.50

to that observed in Figure 6.43a & b. The stress distribution pattern is virtually identical, confirming again that the dominant mode of failure in RHST3 and RHST4 is that of a local joint failure

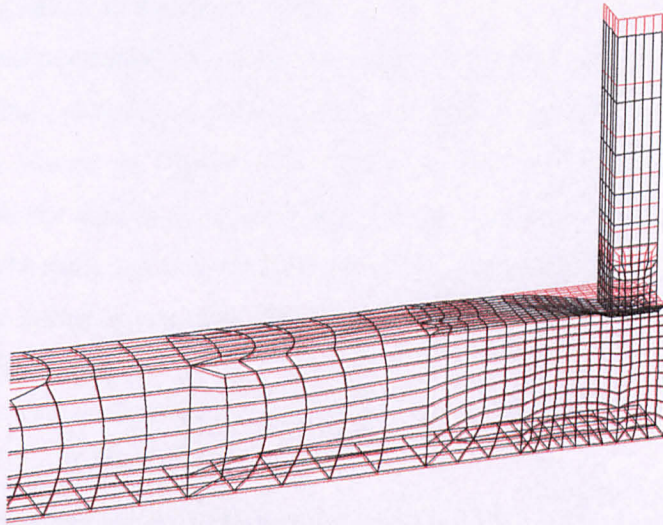


Figure 6.51 Displaced shape diagram of joint RHST1 zoomed in on the deformation in the vicinity of the brace. (displacements magnified by 3)

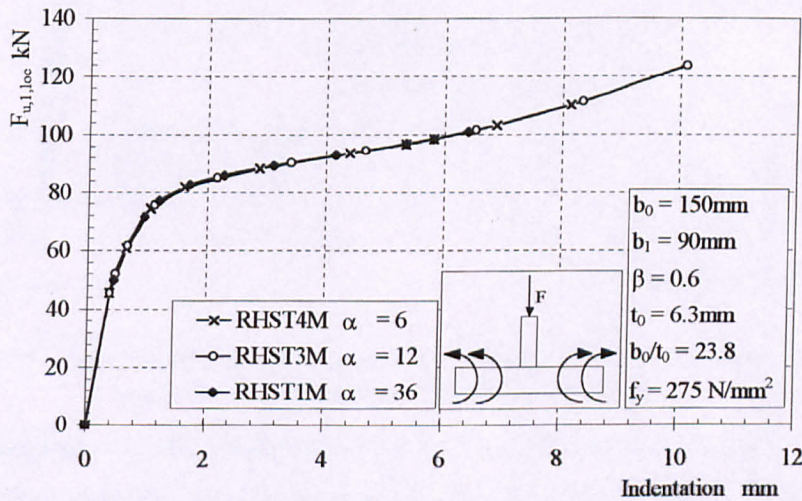


Figure 6.52 Load indentation curve for similar traditional RHS T joints with varying chord length without the effects of chord bending

6.14.4.2 Load indentation curves

The load/indentation curves shown in Figure 6.52 for three similar traditional RHS T joints without the effects of chord bending show that the local joint strength $F_{u,l,loc}$ is independent of chord length as the three curves are coincident with each other. If these load/indentation curves are compared with that for joint RHST4, where $\alpha = 6$

and the effects of chord bending have not been excluded as shown in Figure 6.44, it can be seen that they are again nearly identical to each other. This shows that when $\alpha = 6$ the joint capacity $F_{u,1}$ is equal to the local joint strength $F_{u,1,loc}$ and effects of chord bending are negligible at this chord length.

The load/indentation curves for the traditional RHS T joints (for similar joints with varying chord slenderness values) where the effects of chord bending have been eliminated are shown in Figure 6.53. There is a wide variation in the curves considering that the effects of chord bending have been removed and all the joints should fail by the same yield line pattern. It is likely that an additional mechanism is operating in the failure mechanism due to the increase in the membrane effect for the more slender chord walls.

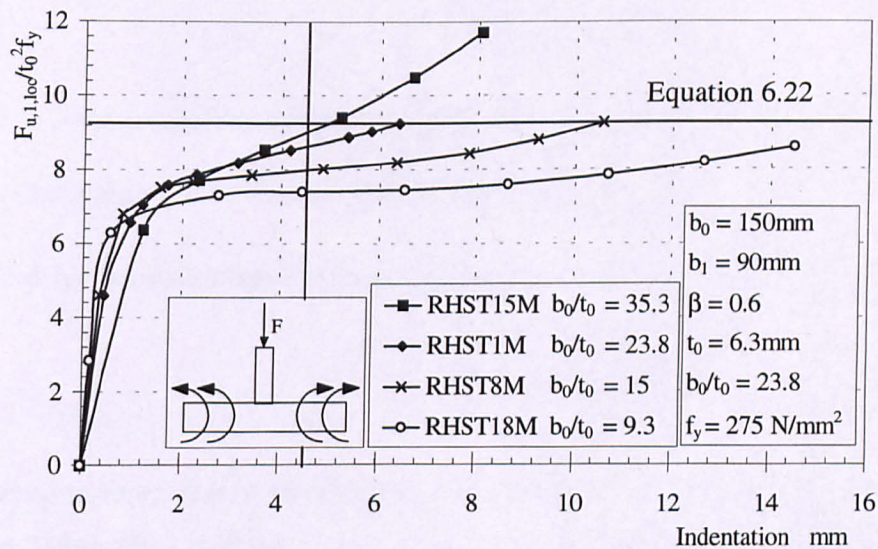


Figure 6.53 Examples of load/indentation curves for RHS T joints without the effects of chord bending for different values of slenderness

Examination of the results published by Yu (1995) show a similar increase in the normalised strength with increasing chord slenderness although the range of difference between her results is smaller than those reported here.

6.14.5 Calculation of the reduced moment capacity of the traditional RHS chord

Due to the different orientation of the chord, the calculation for the reduced plastic moment capacity of the chord changes. This is brought about by the different relationships between the shear and the bending moment and the fact that the flanges

the RHS section offer no resistance to the shear force applied perpendicular to the flange and all the shear is resisted by the webs of the section.

Wardenier (1982) gives the following for the relationship between the bending moment and the shear acting on a section.

For a solid rectangular section

$$1 = \left(\frac{M}{M_p} \right)^2 + \left(\frac{V}{V_p} \right)^2 \quad \text{Eqn 6.23}$$

For a RHS section

$$\frac{M}{M_p} = 1 - \left[1 - \sqrt{1 - \left(\frac{V}{V_p} \right)^2} \right] \frac{A_v}{2A - A_v} \quad \text{Eqn 6.24}$$

Where A is the area of the section and A_v the area of the section resisting the shear. If

the section is square, then $A \approx 2A_v$ and therefore $\frac{A_v}{2A - A_v} = \frac{1}{3}$

Therefore for Square rectangular hollow section Eqn 6.24 can be written as

$$5 = 9 \left(\frac{M}{M_p} \right)^2 + \left(\frac{V}{V_p} \right)^2 - 4 \sqrt{1 - \left(\frac{V}{V_p} \right)^2} \quad \text{Eqn 6.25}$$

This complex expression cannot easily be solved in the manner used previously and by van der Vegte when studying CHS T joints. However, a good representation of Eqn 6.25 can be approximated by the expression

$$1 = \left(\frac{M}{M_p} \right)^2 + \frac{1}{2} \left(\frac{V}{V_p} \right)^2 \quad \text{Eqn 6.26}$$

which is of the same form used before and can be solved relatively simply.

It can be seen from Eqn 6.26 that the function for the moment is the dominant term and the effect of shear is not particularly significant. Eurocode 3 Clause 5.5 (1992) states that when considering the moment resistance of a section, the effects of shear can be neglected if the shear load is less than 50% of the shear capacity. Yu (1995) develops this approach and uses the following relationships for the moment capacity of the chord reduced for the effects of shear $M_{p,v,0}$.

For Class 1 and 2 sections (where full plasticity moment capacity is developed) and $V < 0.5V_p$

$$M_{p,v,0} = M_p \quad \text{Eqn 6.27}$$

and for Class 1 and 2 sections and $V \geq 0.5V_p$

$$M_{p,v,0} = \frac{b_0 t_0^2 f_y \frac{(2\gamma-1)}{\sqrt{3}} (-C_1 + \sqrt{C_1^2 + 8}) \left(\frac{\alpha}{2} - \beta\right)}{4} \quad \text{Eqn 6.28}$$

where

$$2\gamma = \frac{b_0}{t_0} \quad \text{and} \quad C_1 = \frac{\left(\frac{\alpha}{2} - \beta\right)}{\sqrt{3} \left(1 - \frac{1}{2\gamma}\right)} - 2$$

For Class 3 sections (where only the elastic moment capacity is developed) and $V < 0.5V_p$

$$M_{e,v,0} = M_e = \frac{b_0^3 f_y \left(1 - \left(1 - \frac{1}{\gamma}\right)^4\right)}{6} \quad \text{Eqn 6.29}$$

For Class 3 sections and $V \geq 0.5V_p$

$$M_{e,v,0} = \frac{\frac{2\gamma-1}{\sqrt{3}} (-C_4 + \sqrt{C_4^2 - 4(1-C_5)}) b_0 \left(\frac{\alpha}{2} - \beta\right)}{4} \quad \text{Eqn 6.30}$$

where

$$C_4 = \frac{\sqrt{3} \left(\frac{\alpha}{2} - \beta\right)}{2 \left(1 - \frac{1}{2\gamma}\right)^2} - 2 \quad \text{and} \quad C_5 = \frac{\gamma \left(1 - \left(1 - \frac{1}{\gamma}\right)^4\right)}{\left(1 - \frac{1}{2\gamma}\right)^3}$$

Yu's approach whilst complying with Eurocode 3 and covering all possible options is thought to be overly complex. None of the sections considered in this work are classified as Class 3, although the majority of the joints come in the category of $V < 0.5V_p$ where the effects of shear do not have to be considered and $M_p = M_{p,v,0}$.

In order that shear is considered for all curves to avoid any discontinuities in the curve and to maintain a similar approach to that used previously in this work (and also by van der Vegte (1995)) Eqn 6.26 is used for the basis of the relationship of the bending moment and the shear.

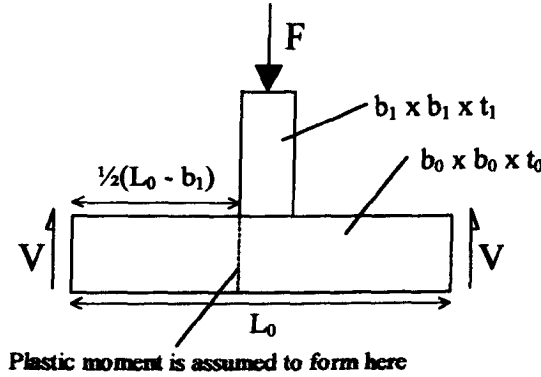


Figure 6.54 The loading of the traditional RHS T joint with the effects of chord bending

When the brace is axially loaded by a force F , the shear V and the moment M in the chord in the cross section at the edge of the brace section is given by

$$V = \frac{1}{2} F \quad \text{Eqn 6.31}$$

$$M = \frac{1}{4} F(L_0 - b_1) \quad \text{Eqn 6.32}$$

and V_p and M_p , the plastic capacities for the shear and moment in the chord respectively, are given by

$$V_p = \frac{2 b_0 t_0 f_y}{\sqrt{3}} \quad \text{Eqn 6.33}$$

$$M_p = \frac{1}{2} (3b_0^2 - 6b_0 t_0 + 4t_0^2) t_0 f_y \quad \text{Eqn 6.34}$$

Substituting Eqns 6.31 to 6.34 into Eqn 6.26 and solving for $F_{p,v,0}$, the assumed force in the brace when the chord fails by a combination of shear and bending, the value F , now called $F_{p,v,0}$ is found to be

$$F_{p,v,0} = \frac{4 b_0 t_0 f_y}{\sqrt{\frac{3}{2} + \left(\frac{\alpha - 2\beta}{3 - \frac{3}{\gamma} + \frac{1}{\gamma^2}} \right)^2}} \quad \text{Eqn 6.35}$$

The value of $M_{p,v,0}$ the moment capacity of the chord with shear present, can be found by substituting the value of $F_{p,v,0}$ into Eqn 6.32

$$M_{p,v,0} = \frac{b_0 t_0 f_y (L_0 - b_1)}{\sqrt{\frac{3}{2} + \left(\frac{\alpha - 2\beta}{3 - \frac{3}{\gamma} + \frac{1}{\gamma^2}} \right)^2}} \quad \text{Eqn 6.36}$$

6.14.6 Interaction diagrams for the traditional RHS T joints

The interaction diagram for the traditional RHS T joints shown in Figure 6.55 is plotted using the information calculated and given in Table 6.18. The values for $F_{u,1}$ and $F_{u,1,loc}$ have been determined by finite element analysis and are given originally in Table 6.16 and Table 6.17 respectively. The value for $M_{u,0}$ has been calculated by Eqn 6.32 and $M_{p,v,0}$ by Eqn 6.36.

Examining the interaction diagram shown in Figure 6.55, where the points are plotted for the joints analysed when the parameters of chord width ratio, chord length and slenderness were varied, the curves can be seen to be clearly banded according to the chord wall slenderness. This is caused by the fact that curves with different chord width ratios, but the same chord slenderness values, are virtually coincident with each other. Increasing the chord length of the joint causes the point to move in clockwise direction along the curve, i.e. short chord lengths where $F_{u,1}/F_{u,1,loc} \rightarrow 1$ and long chord lengths where $M_{u,0}/M_{p,v,0} \rightarrow 1$.

Model	α	$\frac{b_0}{t_0}$	$F_{u,1}$ kN	$F_{u,1,loc}$ kN	$\frac{F_{u,1}}{F_{u,1,loc}}$	$M_{u,0}$ kNm	$M_{p,v,0}$ kNm	$\frac{M_{u,0}}{M_{p,v,0}}$
RHST61	48	35.3	30.2	44.8	0.674	26.5	37.2	0.713
RHST15	36	35.3	34.4	44.8	0.769	22.4	37.1	0.606
RHST16	24	35.3	39.0	44.8	0.871	16.7	36.8	0.453
RHST17	12	35.3	42.6	44.8	0.953	8.6	35.5	0.243
RHST7	48	23.8	53.9	94.0	0.574	47.3	53.6	0.884
RHST1	36	23.8	64.6	94.0	0.687	42.2	53.4	0.789
RHST6	30	23.8	72.0	94.0	0.766	38.9	53.3	0.729
RHST5	24	23.8	78.6	94.0	0.836	33.6	53.1	0.633
RHST2	18	23.8	84.8	94.0	0.902	26.7	52.6	0.507
RHST3	12	23.8	89.3	94.0	0.950	18.1	51.3	0.353
RHST4	6	23.8	92.3	94.0	0.982	8.3	43.9	0.189
RHST8	36	15.0	118.5	219.6	0.539	77.3	80.6	0.958
RHST9	24	15.0	159.7	219.6	0.727	68.3	80.2	0.851
RHST60	18	15.0	186.5	219.6	0.849	58.7	79.6	0.738
RHST10	12	15.0	207.9	219.6	0.947	42.1	77.6	0.542
RHST13	6	9.3	507.5	507.5	1.000	45.7	101.5	0.450
RHST19	12	9.3	449.2	507.5	0.885	91.0	114.9	0.792
RHST12	18	9.3	348.0	507.5	0.686	109.6	117.3	0.935
RHST11	30	9.3	220.2	507.5	0.434	118.9	118.5	1.004
RHST14	48	9.3	137.1	507.5	0.270	120.3	118.8	1.012
RHST35	48	35.3	23.2	28.4	0.815	20.5	37.2	0.552
RHST25	30	35.3	25.4	28.4	0.892	13.9	37.0	0.375
RHST28	18	35.3	27.0	28.4	0.950	8.7	36.5	0.239
RHST20	36	23.8	50.0	60.1	0.831	33.0	53.5	0.617
RHST27	24	23.8	55.3	60.1	0.919	24.0	53.1	0.453
RHST31	12	23.8	58.6	60.1	0.974	12.3	51.4	0.239
RHST34	48	15.0	82.3	147.3	0.559	72.8	80.8	0.901
RHST24	30	15.0	115.0	147.3	0.781	63.0	80.5	0.782
RHST29	18	15.0	135.2	147.3	0.918	43.6	79.6	0.548
RHST22	36	9.3	178.6	355.3	0.503	117.9	118.7	0.993
RHST26	24	9.3	248.1	355.3	0.698	107.9	118.1	0.914
RHST32	18	9.3	299.0	355.3	0.842	96.4	117.4	0.822
RHST30	12	9.3	338.6	355.3	0.953	71.1	115.2	0.617
RHST40	36	23.8	34.6	40.3	0.859	23.1	53.5	0.432
RHST44	24	23.8	38.4	40.3	0.953	17.0	53.2	0.319
RHST41	36	15.0	82.1	96.3	0.853	54.8	80.7	0.680
RHST42	36	9.3	160.0	220.4	0.726	106.8	118.7	0.900
RHST45	24	9.3	199.7	220.4	0.906	88.4	118.2	0.748

Table 6.18 The values used to produce the interaction diagram for the traditional RHS T joints

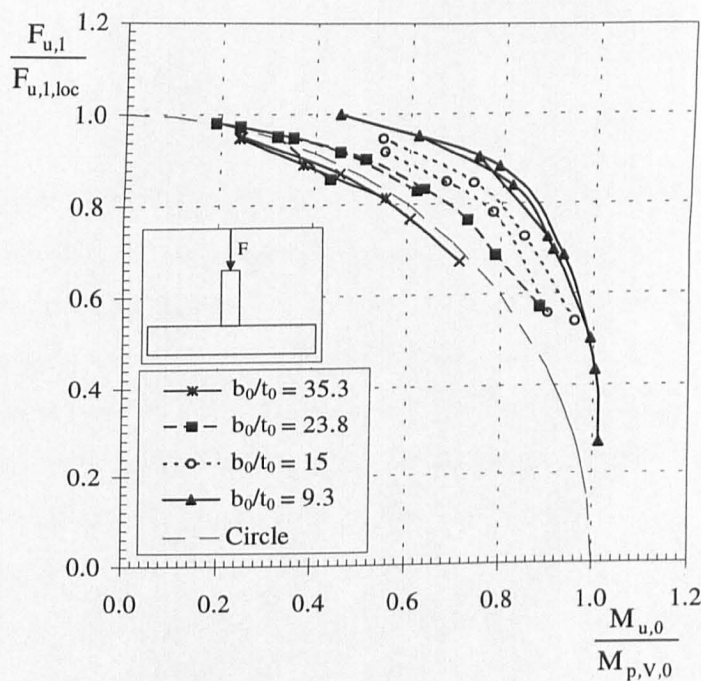


Figure 6.55 Interaction diagram for the traditional RHS T joint ($0.2 \leq \beta \leq 0.6$)

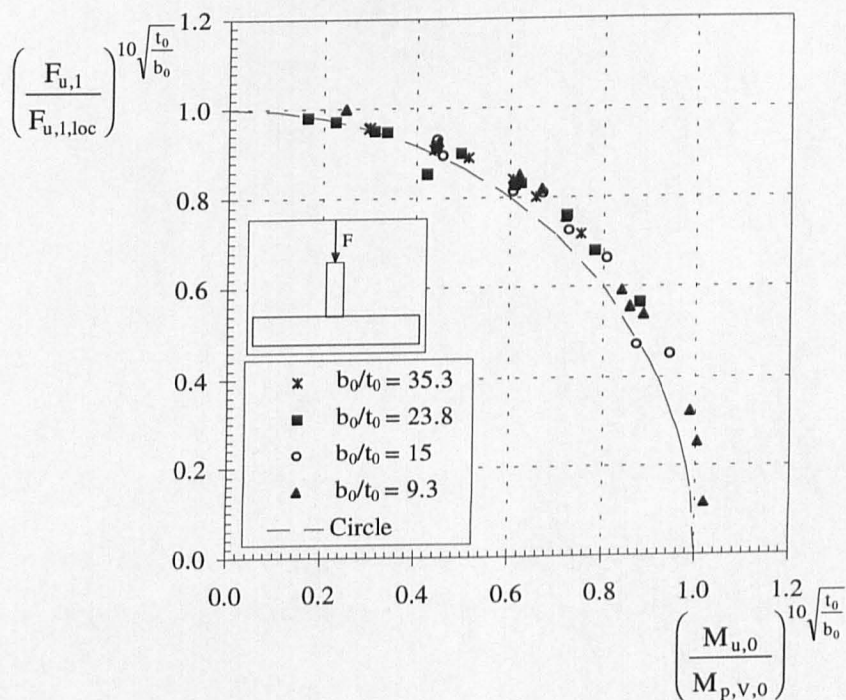


Figure 6.56 Modified interaction diagram for the traditional RHS T joint ($0.2 \leq \beta \leq 0.6$)

Analysing this data it has been possible to produce design guidance in the form of

$$\left(\frac{F_{u,l}}{F_{u,l,loc}} \right)^{10 \sqrt{\frac{t_0}{b_0}}} + \left(\frac{M_{u,0}}{M_{p,V,0}} \right)^{10 \sqrt{\frac{t_0}{b_0}}} \leq 1 \quad \text{Eqn 6.37}$$

for the traditional RHS T joint. The results shown in Figure 6.55 are modified by this relationship and shown in Figure 6.56 where the banding caused by the chord slenderness has been eliminated and a circular curve defined.

Comparing these results to the work done by Yu (1995) reveals that similar banding was noted, but in Yu's work the cause of the banding is the chord width ratio instead of the chord wall slenderness. The relationship between the force on the brace and the moment acting on the chord reported by Yu is

$$\frac{F_{u,l}^3}{F_{u,l,loc}^3} + \frac{M_{u,0}}{M_{p,V,0}} \frac{1}{1-\beta^2} \leq 1 \quad \text{Eqn 6.38}$$

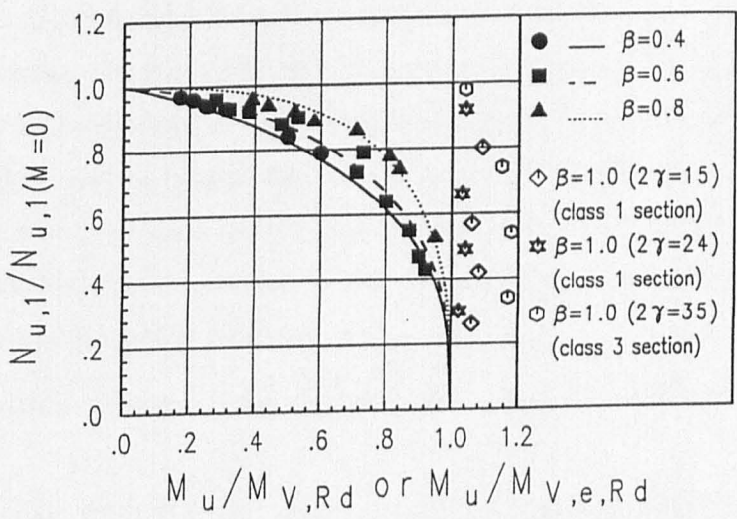


Figure 6.57 Interaction diagram produce by Yu (1995) for RHS T joints

How the designer is expected to solve this equation easily is not explained, Eqn 6.37 is arranged to have the same powers for each term and can be solved explicitly in the form of

$$F_{u,1} = \frac{1}{\left[\left(\frac{1}{F_{u,1,loc}} \right)^{10 \sqrt{\frac{t_0}{b_0}}} + \left(\frac{(L_0 - b_1)}{4M_{p,v,0}} \right)^{10 \sqrt{\frac{t_0}{b_0}}} \right]^{\frac{1}{10 \sqrt{\frac{t_0}{b_0}}}}} \quad \text{Eqn 6.39}$$

This is not so in Eqn 6.38 and an iterative technique will have to be employed.

Examining the results reported by Yu it is noted that the chord width ratios examined were $\beta = 0.4, 0.6, 0.8$ and 1.0 with chord wall slenderness values of 35, 24 and 15. All the points plotted in the interaction diagram for $\beta = 1.0$ are on the right hand side of the figure where $\frac{M_{u,0}}{M_{p,v,0}} \geq 1$ and are independent of the value $\frac{F_{u,1}}{F_{u,1,loc}}$.

The results of joints where $\beta = 0.8$ and 1.0 have been discounted in this work, because the failure will be dominated by a plastic hinge forming in the chord under the brace and the local joint strength is irrelevant, a fact which is confirmed by Yu's results. The points plotted for $\beta = 0.4$ and 0.6 appear to be virtually coincident with each other (which is in agreement with this work), with the most notable banding occurring when $\beta = 0.8$. This should be expected as a transition between the form of failure observed when $\beta = 0.4$ and 0.6 and the failure observed when $\beta = 1.0$. Therefore the reason for the difference between Yu's work and this work is attributed to the different range of parameters chosen for the joints analysed, in that the larger chord width ratios chosen by Yu have influenced the pattern observed.

6.14.7 A comparison between finite element values and the different design techniques

The traditional RHS T joint capacities with the effects of chord bending obtained by finite element analysis are compared to the different methods of predicting the joint capacity considered in this section and are shown in Figure 6.58.

The traditional design method, based on the yield line method, can be seen to predict the joint capacity of the short chord length joints (where $\alpha = 6$) with reasonable accuracy (with the exception of the joint where $\beta = 0.6$, $b_0/t_0 = 23.8$ and $t_0 = 16\text{mm}$). The joint capacity for the long chord length joints, when the moment capacity of the section is achieved is also predicted with reasonable accuracy. However, the joint capacities predicted for the transitional joints where the failure is a combination of the

local joint and chord bending failure are overestimated (i.e. unsafe) by up to 30%, the joint capacities observed from the finite element analyses.

The joint capacities predicted by the interaction curve, however, give a better estimation of the joint capacity and the variation of the joint capacity when the chord length is changed. The results presented here are better than those of the diamond bird beak joint because it was possible to normalise the joint capacities with chord wall slenderness and obtain a small band width of results. The interaction design curve gives similarly good predictions for the chord width ratios β of 0.2 and 0.4, but these are not presented to avoid repetition.

It is appreciated that the results shown in Figure 6.58 for the predicted design capacities using the interaction curves are being compared with the results that produced the interaction design curve and a good comparison could be expected, so that this work is not truly validated until the interaction curve is compared with independent results.

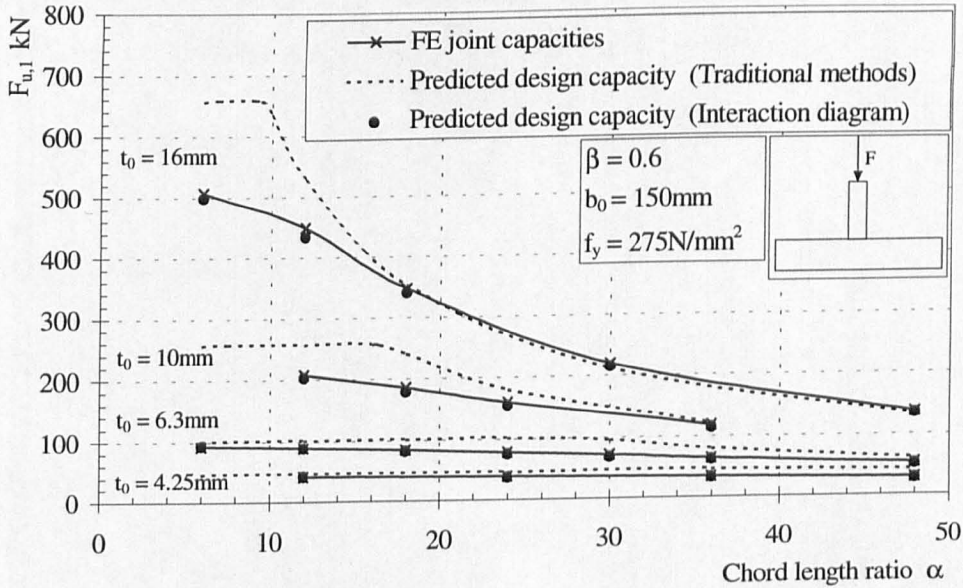


Figure 6.58 A comparison of the different design methods to the finite element joint capacities for diamond bird beak T joints with varying chord lengths

6.15 Comparison of the Interaction diagrams

The interaction diagrams for traditional RHS, CHS and diamond bird beak T joints are shown in Figures 6.58, 6.59 and 6.60 respectively. The Interaction diagram for the CHS T joints has been produced from the information published by van der

Vegte (1994). The chord width ratios have been added into this diagram to distinguish trends between the different results. Examining this figure it is immediately apparent that all the points for $\beta = 1.0$ $M_{u,0}/M_{p,V,0} > 1$, with the exception of one point where the slenderness is 50.8. This is in accordance with the work published by Yu (1995). However, more careful examination of this figure shows two tendencies which are contradictory to the results published by Yu. The first is that the results for $\beta = 0.2$ are on the right hand side of the figure and $F_{u,1}/F_{u,1,loc} \rightarrow 1$ and as the chord width ratio increases so the results move in a clockwise direction along the circle. The second is that as the chord wall slenderness decreases so the results show a small decrease in $F_{u,1}/F_{u,1,loc}$ and a large increase in $M_{u,0}/M_{p,V,0}$ moving the plotted points down and to the right.

An arc of a circle with its centre at the origin and a radius of 1 is shown on all the interaction diagrams as a reference that may be used to compare between the different diagrams. A circle is drawn as there can be seen to be a loose connection between the relationship of the shear and the bending moment in the chord

$$1 = \left(\frac{V}{V_p} \right)^2 + \left(\frac{M}{M_p} \right)^2 \quad \text{Eqn 6.40}$$

and a circle drawn on the Figures

$$1 = \left(\frac{F_{u,1}}{F_{u,1,loc}} \right)^2 + \left(\frac{M_{u,0}}{M_{p,V,0}} \right)^2 \quad \text{Eqn 6.41}$$

in that

$$\frac{F_{u,1}}{F_{u,1,loc}} \cong \frac{V}{V_p} \quad \text{Eqn 6.42}$$

Comparing these interaction diagrams it can be observed that:

- there is a clear banding of the points according to the chord wall slenderness. In the traditional RHS interaction diagram the plotted results form an arc centred about the origin according to the chord wall slenderness, whereas for the CHS and the diamond bird beak joints, the results plotted may be represented by straight lines, (disregarding the CHS points where $\beta = 1.0$).

Figure 6.59

Interaction diagram for the
RHS T joints

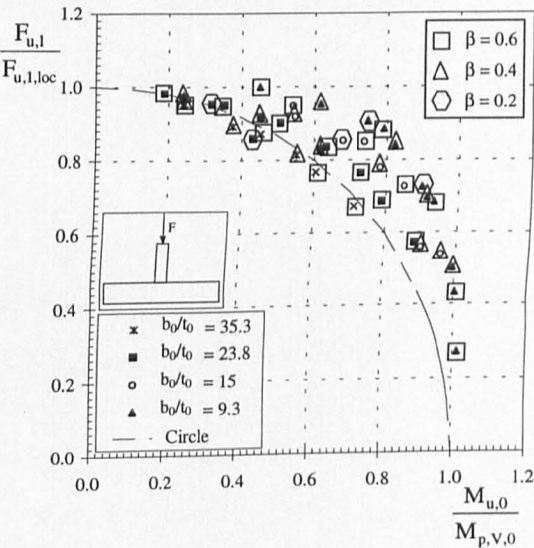


Figure 6.60

Interaction diagram for
the CHS T joints van der
Vegte (1995)

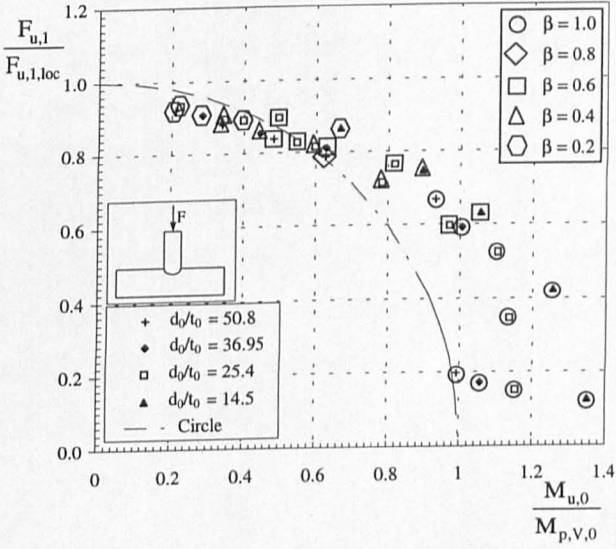
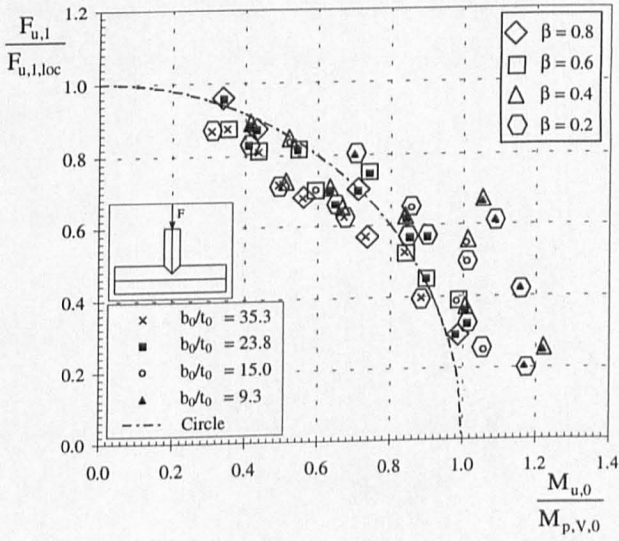


Figure 6.61

Interaction diagram for the
diamond bird beak T joints



- there are several points in the diamond bird beak and CHS interaction diagrams where the value $M_{u,0}/M_{p,v,0} > 1$. In the CHS diagram most of these points have a chord width ratio of $\beta = 1.0$ and it should be expected that the chord will fail by a plastic hinge forming near the brace (or possibly failure of the side walls of the chord) and the term for the joint failure $F_{u,1,loc}$ becomes meaningless. This can be seen by joining points of equal chord wall slenderness values when $\beta = 1.0$, which results in four nearly vertical lines. The fact that some of the points exceed $M_{u,0}/M_{p,v,0} = 1$ by a large amount indicates the increase in the moment capacity of the chord caused by the restraint offered by the brace.

For the diamond bird beak interaction diagram, chord width ratios of $\beta = 0.8$ & 1.0 were not considered due to similar problems that have been observed in the CHS diagram. However, several of the points have a value for $M_{u,0}/M_{p,v,0} > 1$, mainly for the low slenderness joints. The chord length ratio of the results plotted in this area vary from $\alpha = 12$ to 36 and the chord width ratio $\beta = 0.4$ & 0.6 . (This is shown in Figure 6.37). This should be expected as the moment operating in the chord exceeded the moment capacity of the chord, as it was observed in Figure 6.16 that the diamond bird beak T joints (loaded with the effects of chord bending) failed when the moment in the chord was 116% of the plastic moment capacity when $\beta = 0.6$ and $b_0/t_0 = 9.3$.

6.16 Summary

The diamond bird beak T joints were studied in some detail and it was found that the mean joint capacity of the short chord length T joint ($\alpha = 6$) with the effects of chord bending could be safely found by

$$F_{u,1} = 4 f_y t_0^2 \sqrt{\alpha^{0.5} \frac{b_0}{t_0}}$$

for the range of parameters $0.2 \leq \beta \leq 0.6$, $9.4 \leq b_0/t_0 \leq 35.3$, $b_0 = 150\text{mm}$ and $f_y = 275 \text{ N/mm}^2$

When the effects of chord bending were eliminated, the local joint strength used in the design of T joints using the interaction curve, could be estimated by

$$F_{u,1,loc} = 5.7 f_y t_0^2 \sqrt{\beta \frac{b_0}{t_0}}$$

for the range of parameters $0.2 \leq \beta \leq 0.6$, $9.4 \leq b_0/t_0 \leq 35.3$, $b_0 = 150\text{mm}$ and $f_y = 275 \text{ N/mm}^2$

A safe lower bound solution to predict the mean joint capacity of a diamond bird beak T joint using the interaction curve is given by

$$\frac{F_{u,1}}{F_{u,1,loc}} + \frac{M_{u,0}}{M_{p,v,0}} = 1.2$$

and that

$$\frac{F_{u,1}}{F_{u,1,loc}} \text{ and } \frac{M_{u,0}}{M_{p,v,0}} \leq 1$$

for the range of parameters $0.2 \leq \beta \leq 0.6$, $9.4 \leq b_0/t_0 \leq 35.3$, $b_0 = 150\text{mm}$ and $f_y = 275 \text{ N/mm}^2$

The interaction curve for the traditional RHS T joint was studied and it was concluded that a safe lower solution estimate of the design capacity could be given by

$$\left(\frac{F_{u,1}}{F_{u,1,loc}} \right)^{10 \sqrt{\frac{t_0}{b_0}}} + \left(\frac{M_{u,0}}{M_{p,v,0}} \right)^{10 \sqrt{\frac{t_0}{b_0}}} \leq 1$$

for the range of parameters $0.2 \leq \beta \leq 0.6$, $9.4 \leq b_0/t_0 \leq 35.3$, $b_0 = 150\text{mm}$ and $f_y = 275 \text{ N/mm}^2$

6.17 Conclusions

This Chapter has examined diamond bird beak and traditional RHS T joints of varying chord lengths, with the weld modelled as a butt weld in both cases. It has been shown that the diamond bird beak butt welded T joint is stronger in all the cases considered than the butt welded T traditional RHS T joint despite the fact that the moment capacity of the chord is slightly reduced in the diamond bird beak configuration.

The variation of the joint capacity with the chord length was examined for both forms of joints and compared to the traditional design method of considering the variation in chord length. The traditional method of joint design did not represent the variation in joint capacity with chord length very satisfactorily. Short chord length joints where the failure was principally that of a local joint failure and long chord length joints where the failure was principally that of chord bending were accurately

predicted. However, the joint capacity of any joint in the intermediate range where failure was attributed to a combination of local joint and overall chord bending failure was severely overestimated.

An alternative method of predicting the joint capacity, using an interaction relationship between the load on the brace and the bending moment in the chord was then examined. In both cases this method gave a better prediction of the behaviour of the joint capacity with increasing chord length. The large scatter in the results of the diamond bird beak T joints led to a lower bound estimate of the design capacity which underestimated the strength of the joints with a stocky chord wall however, this was a safe solution compared with the overestimate predicted by the traditional design methods. The interaction curve for the traditional RHS T joint could be normalised to account for the variation in the results with chord wall slenderness and the predicted strength could be estimated with reasonable accuracy. Although much further work should be done in this area, it is felt that the interaction curve is a definite improvement to the traditional method of predicting the joint capacity of a T joint.

When it is required to achieve consistent and reliable estimates of the local joint capacity by removing the effects of chord bending from a T joint, the method of applying the moment to the chord as a series of small increments is shown to be a more reliable method than that used by Yu (1995) and van der Vegte (1995). In the cases of the bird beak and CHS T joints there was a small variation in the joint capacity with chord length for the shorter chord lengths until the asymptotic strength was achieved.

7.

Member Orientation in Overlapped K joints

7.1 Introduction

In this Chapter a study of the effect of the brace angle θ , on the failure mode and joint capacity is carried out for both the traditional RHS and bird beak K joint configurations under different load and boundary conditions. The traditional overlapped RHS K joint configuration is studied to resolve the question posed by Crockett (1994) of whether an angle function is required in the design guidance given by CIDECT for overlapped K joints. Similar bird beak K joints are then studied to compare the strength and behaviour of the traditional RHS K joints with bird beak K joints to ascertain if the advantages demonstrated by bird beak configuration previously apply to K joints.

The models used to represent the traditional RHS K joints are the same models that Crockett (1994) used in his investigations on the boundary conditions effects, therefore the models have different material properties from those used previously in this thesis. The same material properties are transferred to the bird beak models so that comparisons can be made with the traditional RHS K joints. Full details of these material properties are given when describing the models.

7.2 The requirement for an angle function.

The inclination of the braces has long been recognised as having an important effect on the joint capacity for T joints, K and N gap joints, with the minimum capacity observed when the branch is positioned at 90^0 to the chord. This implies that the normal component of the branch force is critical in determining the joint capacity and when the branch is inclined the joint resistance, represented by the force in the inclined brace should be increased by

$$f(\theta) = \frac{1}{\sin \theta} \quad \text{Eqn 7.1}$$

This can be seen to occur when the failure mode is due to complete shearing of the chord for RHS K gap joints, shown in Figure 7.1. However, in other cases there is an additional effect of the larger footprint of the connection which further enhances the value of $f(\theta)$. Examples of this can be seen in RHS K gap joints where the mode of failure is due to punching shear failure or yield line deformation of the connection face of the chord member, shown in Figure 7.2 and Figure 7.3 respectively.

Clearly then, there is a case for considering the inclusion of an angle function in a design formula for K gap joints. However, the question posed is whether a case can be justified for overlapped K joints.

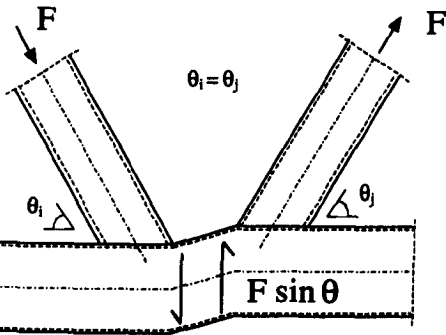


Figure 7.1 Overall shear failure of the chord

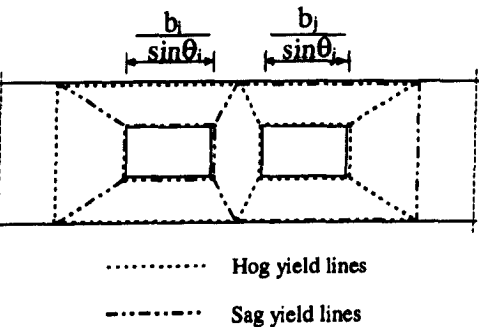
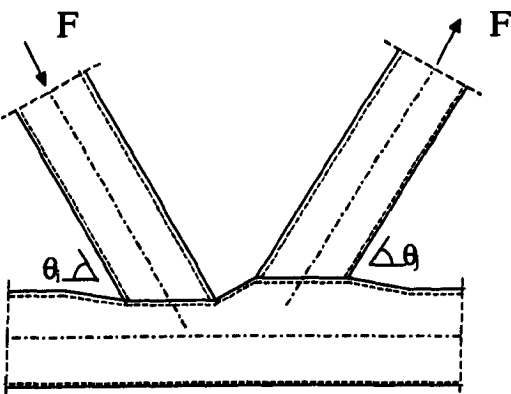


Figure 7.3 Flexural failure of the chord face

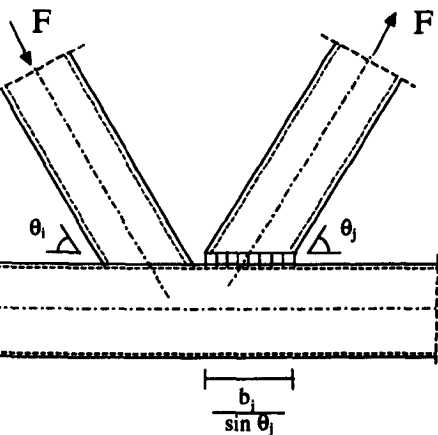


Figure 7.2 Punching shear failure of the chord face

The International Institute of Welding/CIDECT/Eurocode 3 design recommendations for RHS partially overlapped K joints, all use the effective width concept. This approach recognises that the strength of a transverse welded plate

connected to an RHS chord wall does not fully reach the full yield strength of the connection. The value of this contribution depends on the RHS wall slenderness ($2\gamma = b_0/t_0$) providing the reaction for the plate. A generalised expression for the effective width of

$$\frac{b_{eff}}{b_i} = \frac{C}{b_0/t_0} \cdot \frac{f_{y0}t_0}{f_{yi}t_i} \cdot f(\beta) \cdot \frac{1}{\sin\theta} \cdot f(n) \quad Eqn 7.2$$

where $C = \text{constant}$

was considered appropriate. However, the angle function could not be justified by test results and the effective width expression of

$$\frac{b_{eff}}{b_i} = \frac{C}{b_0/t_0} \cdot \frac{f_{y0}t_0}{f_{yi}t_i} \quad Eqn 7.3$$

was adopted.

The design recommendations given in Appendix K of Eurocode 3 and the CIDECT design guidelines, are based on the IIW recommendations for checking brace failure of a partially overlapped K joint in square RHS and are

$25\% \leq \lambda < 50\%$

$$N_{i,Rd} = f_{yi} t_i \left[b_{eff} + b_{e,ov} + \frac{\lambda_{ov}}{50} (2h_i - 4t_i) \right] \left[\frac{1.1}{\gamma_{MJ}} \right] \quad Eqn 7.4$$

$50\% \leq \lambda < 70\%$

$$N_{i,Rd} = f_{yi} t_i \left[b_{eff} + b_{e,ov} + 2h_i - 4t_i \right] \left[\frac{1.1}{\gamma_{MJ}} \right] \quad Eqn 7.5$$

$\lambda \geq 70\%$

$$N_{i,Rd} = f_{yi} t_i \left[b_i + b_{e,ov} + 2h_i - 4t_i \right] \left[\frac{1.1}{\gamma_{MJ}} \right] \quad Eqn 7.6$$

where

$$b_{\text{eff}} = \frac{10}{b_0/t_0} \frac{f_{y0}t_0}{f_{yi}t_i} b_i \quad \text{and} \quad b_{\text{e,ov}} = \frac{10}{b_j/t_j} \frac{f_{yj}t_j}{f_{yi}t_i} b_i \quad \text{but} \quad b_{\text{e,ov}} \text{ or } b_{\text{eff}} \leq b_i$$

(Note: no reference to any angle function)

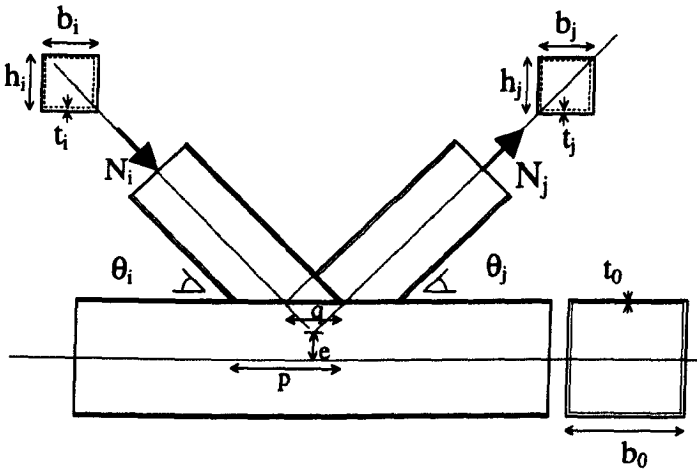


Figure 7.4 Representation of the terms used in Eqns 7.4 - 7.6

where

$$\lambda_{\text{ov}} = \frac{q}{p} \times 100 \quad \text{Eqn 7.7}$$

$$e = -\frac{1}{2} \left(h_0 - \frac{\left(1 - \lambda_{\text{ov}}/100 \right) h_i}{\cos \theta} \right) \quad \text{Eqn 7.8}$$

when the braces are at equal angles i.e. $\theta_i = \theta_j$

Considering the variation of the design value of the joint resistance, $N_{i,Rd}$, to the overlap λ , described by Eqn 7.4 - 7.6, the designed joint resistance increases linearly when the overlap increases from 25% to 50%. This represents the increasing efficiency of an overlapped joint as the applied load passes more directly through the overlapped portion of the joint so that the failure no longer occurs in the chord. The step functions given by Eqns 7.4 to 7.6 represent a crude simplification of the continuously increasing strength of the connection with increasing overlap.

7.3 Finite element model details for the traditional RHS K joints

The mesh of 970 elements is generated by the ABAQUS input deck. There is no verification of the traditional RHS overlapped K joints models used in Crockett’s thesis, but further mesh refinement, concentrating the elements in the areas of the joint produced only a 3% decrease in the joint capacity. Although this does not validate the model it at least shows that the model is performing adequately. Therefore in order that comparisons can be made with previous analyses the original mesh was used throughout this study:

- as the joint only has one plane of symmetry, half of the joint is modelled.
- eight noded thick shell elements (ABAQUS S8R) are used for the brace and chord members.
- fifteen noded solid elements are used for the fillet welds (weld case “e”, shown in Chapter 2). The hidden weld (i.e. the part of the continuous brace concealed by the overlapping brace) was connected to the chord by common nodes.
- the non-linear material properties used to represent the brace and the chord members plus the weld material are given in Table 7.1 and shown in Figure 7.5. (These properties are changed to the true stress/strain properties using Eqns 3.30 and 3.31.)

Stress N/mm ²	Strain
0	0.00
420	0.0020
420	0.0100
510	0.0405
540	0.1005
540	0.1500

Table 7.1 The Engineering Material Properties

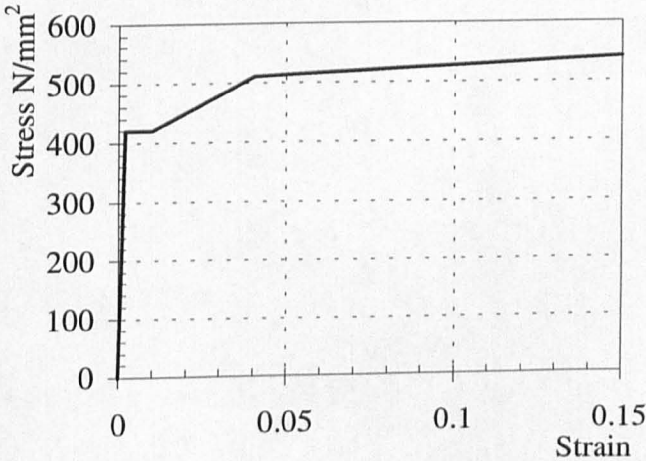


Figure 7.5 The Engineering Material Properties

- the non-linear geometry option was used to update the mesh at the beginning of every increment for the deformations which have already taken place.

- the chord dimensions were 150x150x6.3mm and the brace 90x90x6.3mm, giving a width ratio $\beta = 0.6$, slenderness ratio $b_0/t_0 = 23.8$ and $t_1/t_0 = 1$.
- in order to provide consistency between all the different joints of varying θ , the overlapped was kept consistent at 56%, the eccentricity varying between $0.25b_0$ and $0.35b_0$.
- the chord length was maintained as the footprint of the overlapped joint plus 800mm. The length of the brace was maintained at 400mm as shown in Figure 7.7.
- weld throat thickness was maintained at 6.3mm.
- the construction of the mesh was not altered when altering the angle θ , the key nodes were simply moved to their new positions.
- the eccentricity and overlap for the various models with different values of θ is given in Figure 7.7.

Inclination of the brace θ^0	30	40	50	60
Overlap	56%	56%	56%	56%
Eccentricity e/h_0	-0.356	-0.337	-0.306	-0.251
Eccentricity mm	53.4	50.55	45.9	37.65

Table 7.2 The eccentricities of the various models

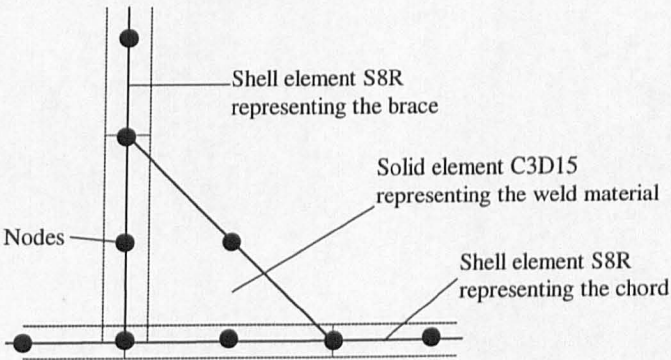


Figure 7.6 The arrangement of the elements representing the weld detail

Figure 7.7 and Figure 7.8 show the general arrangement and the finite element idealisation of the K joint under consideration.

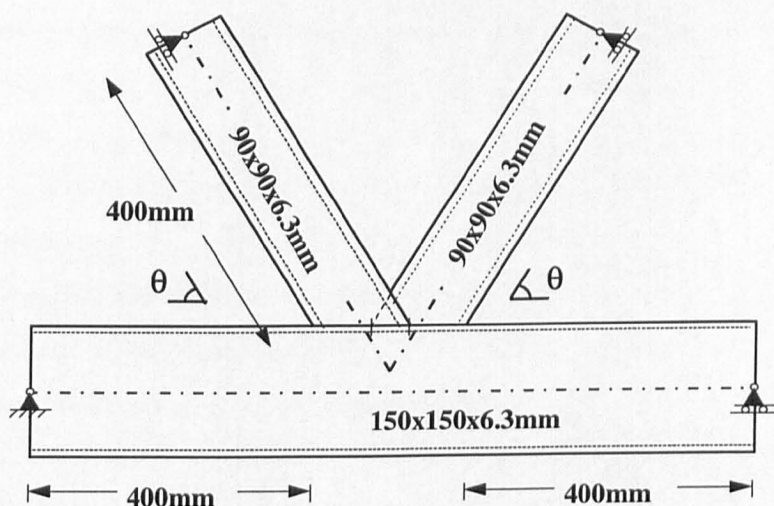


Figure 7.7 Partially overlapped K joint

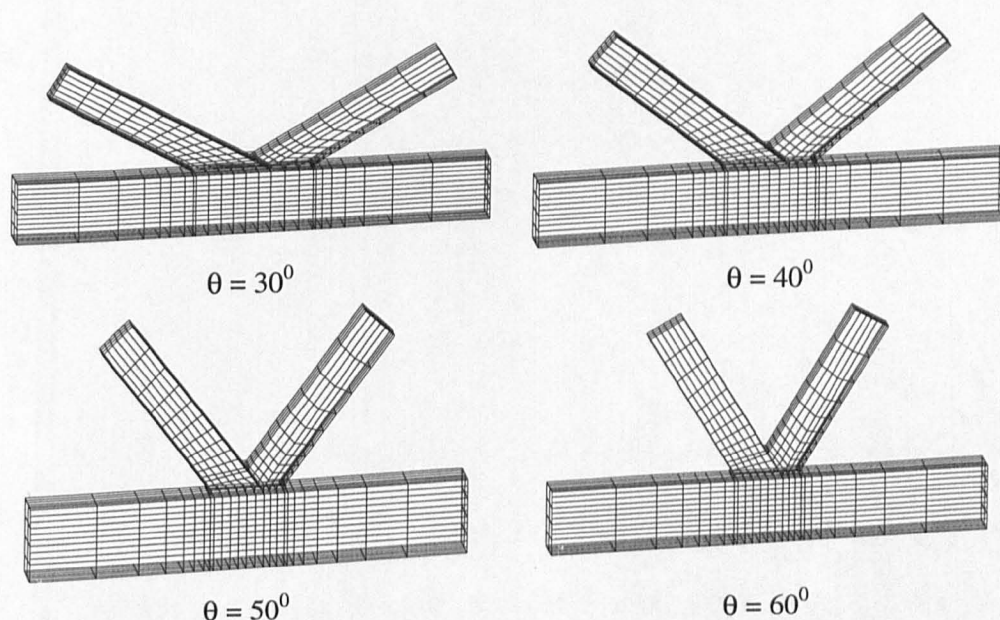


Figure 7.8 Finite element idealisation of the four traditional RHS K joints

7.3.1 The advantages of using a very high yield stress value

Crockett (1994) uses a very high yield strength for his models which originally dates back to some tests carried out in 1992 at the University of Nottingham (Davies 1992) as part of the European Coal and Steel Community (ECSC) sponsored project into the behaviour of three dimensional T joints. These test results provided a large data base of results on which Crockett based much of his work on the effects of modelling the weld and corner radii.

Steel producers are manufacturing increasingly high grades of steel that can be economically used in stronger, lighter structures. However, there are other considerations when using higher grades of steel, other than the higher strength of the material. Increasing the yield stress of the material has a significant effect on the buckling behaviour of simple struts, in that as the yield stress of the material is increased and all other parameters remain constant, increasingly stocky sections will fail by buckling. This is shown in Figure 7.9 where λ is the slenderness value, σ_y the yield stress of the material and σ_c the critical buckling stress.

The advantage of using a higher yield stress value in the finite element models, as this will automatically incorporate a greater tendency to local buckling, which will give safe results for materials with lower yield stress values.

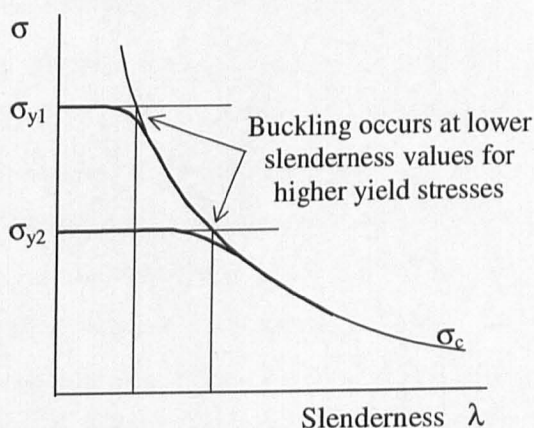


Figure 7.9 The effect of the yield stress on the buckling behaviour of a simple strut

7.4 The different boundary and the loading conditions.

Crockett (1994), in his thesis, showed that the boundary conditions and the sense of loading chosen when testing isolated joints can have a significant effect on the observed joint capacity. The boundary conditions chosen here are considered to represent the boundary conditions experienced in a truss structure as far as practicable. The ends of the branches are pinned rollers to allow axial movement but no major rotation of the member. The chord is supported by a fixed pin and a pinned roller which allows the axial and shear forces in the chord to be resisted, whilst allowing rotations at each end and axial movement at the roller. The four different load cases considered are shown in Figure 7.10. Equal loads are applied to the brace members to provide a balanced joint.

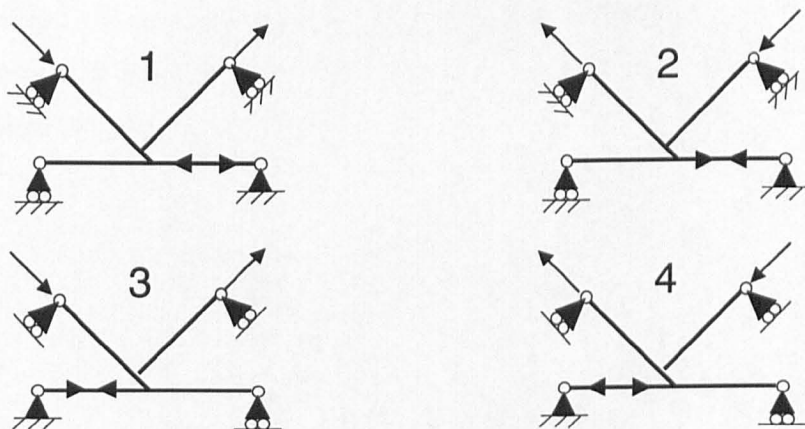


Figure 7.10 The four combinations of load and boundary conditions considered

7.4.1 Defining the joint capacity for the K joints

Previously in this work the joint capacity has been defined as the maximum load attained or the load, at an indentation of $3\%b_0$, of one of the brace members into the chord. Observing the indentation of a K joint is a lot more complex where the direction of the displacement (or a component of it) of the datum points has to be considered so that the movement of the datum points have a common vector. It then becomes very difficult to achieve consistent results where the angle of the branch member changes. It was considered that there was no advantage to be gained in using the indentation to define failure and in all the K joints studied in this work, failure has been defined as the maximum load attained or the load attained when the deflection at the end of either brace exceeded $3\%b_0$.

7.5 The results of the analyses for the traditional RHS K joints

The results of all the analyses for the traditional RHS K joints and all the load cases are given in Table 7.3 and shown graphically in Figure 7.11 where the results have been normalised by the squash load of the brace ($A_i f_{yi}$).

Failure can occur due to the over stressing of the chord due to combined axial load and bending exceeding the elastic capacity of the chord determined by the simple equation shown in Eqn 7.9, referred to as an L7 failure.

$$f_y = \frac{F_{u,0}}{A_0} + \frac{M_0}{Z_0} \quad \text{Eqn 7.9}$$

This expression for the force applied to the brace members producing first yield in the chord under the combined action of the axial force and moment acting in the chord can be rearranged to give

$$\frac{F_1}{A_1 f_{y1}} = \frac{A_0 / A_1}{2 \left(1 + \frac{A_0}{Z_0} (C e) k \right) \cos \theta} \quad \text{Eqn 7.10}$$

where

$$e = -\frac{1}{2} h_0 \left(1 - \frac{h_1 \left(1 - \frac{o_v}{100} \right)}{h_0 \cos \theta} \right) \quad \text{Eqn 7.11}$$

and

C is a factor which allows for the distribution of the joint moment amongst the members

k a reduction factor for the moment appropriate for the position of the critical chord section.

Figure 7.11 shows two curves representing the L7 chord failure according to Eqn 7.10, the lower where failure is assumed to occur at the centre line of the joint and the upper curve where the failure is assumed to occur adjacent to the heel of the brace. All the points above these lines represent cases where the elastic capacity of the chord has been theoretically exceeded for the chosen location.

7.6 Discussion of the results for the traditional RHS K-joints

It can be seen from Figure 7.11 that there is a wide variation in the joint capacities between the different load cases as θ varies. This section will examine the models where $\theta = 30^\circ$ and 60° separately and with reference to the contoured von Mises stress plots, the displaced shape diagrams and moment load interaction diagrams explain the failure mechanism.

In the contoured von Mises stress plots, drawn at maximum load for the outside surface, the red areas indicate regions of high stress where the material has yielded (i.e. $\sigma \geq 420 \text{ N/mm}^2$) and the blue areas indicate regions of low stress. All the displaced shape diagrams, also drawn at the maximum load, have had the displacements magnified by a factor of 3 so that small deformations can readily be identified.

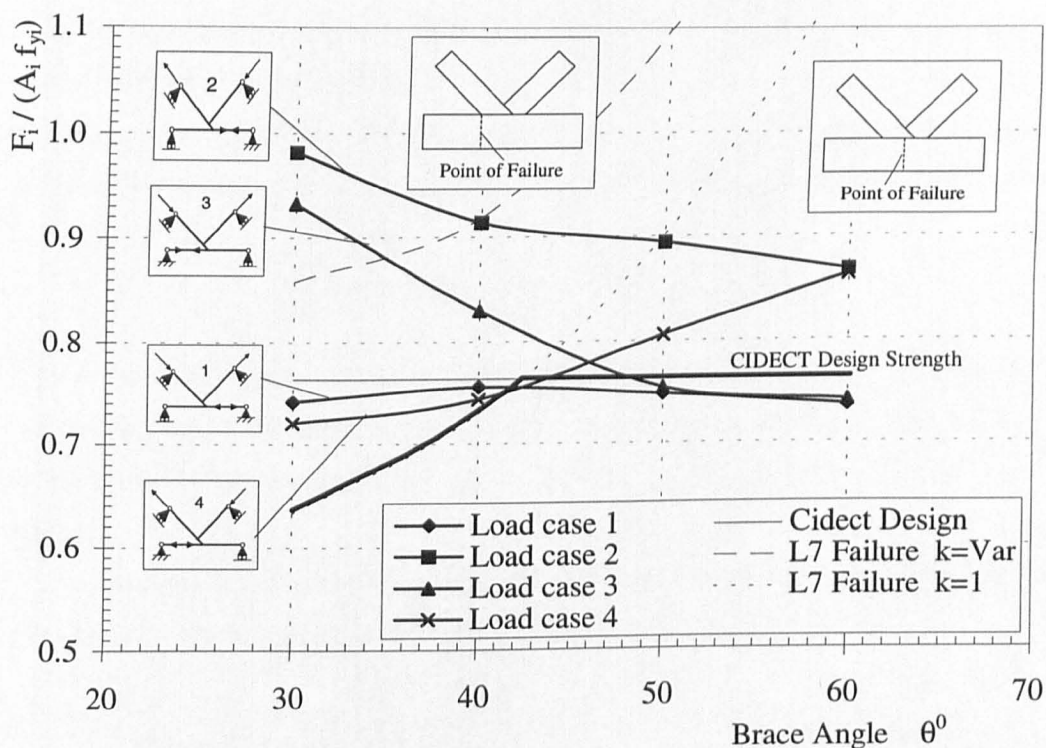


Figure 7.11 A summary of the results for the traditional RHS K joints

Angle	30 ⁰	40 ⁰	50 ⁰	60 ⁰
Load Case				
1	657.2 kN	670.0 kN	663.2 kN	652.7 kN
2	869.9 kN	809.6 kN	792.0 kN	767.9 kN
3	826.2 kN	734.9 kN	667.9 kN	657.1 kN
4	637.3 kN	657.7 kN	713.7 kN	763.7 kN

Table 7.3 A summary of the results for the traditional RHS K joints (overlap = 56%)

The moment/force interaction diagrams shown later in Figure 7.16 and Figure 7.18 relate the member (primary and secondary) moment to the axial force in that member at the points shown in Figure 7.12. It is appreciated that calculating the displacement of the centre lines of the member, by using the movement of a node originally on the centre line is not a completely accurate way of calculating the secondary moments acting in that member as movement of the centreline of the member may not be the same as that of the node chosen. However, useful indications about the failure mechanism are obtained by this method. The curves for the variation of the elastic and plastic moment capacity with load are plotted on the moment load

diagrams as a guide to determining the failure method. The variation of the normalised plastic moment capacity with load is virtually identical for both the chord and the brace and there is no significant difference between the two. There is a small difference between the two curves for the normalised elastic moment/load capacity in that

$$\frac{Z_1 f_y}{M_{p,1}} = 0.8295 \quad \text{and} \quad \frac{Z_0 f_y}{M_{p,0}} = 0.8527$$

This means that the curves diverge slightly at low loads. However, as the moment/load curves cross the elastic moment/load capacity curve at a relatively high load, the two curves for the brace and chord elastic moment/load capacity can be treated as a single curve.

For these reasons and to simplify the drawings only one curve (for the brace) will be shown for each of the elastic or plastic moment/load capacity.

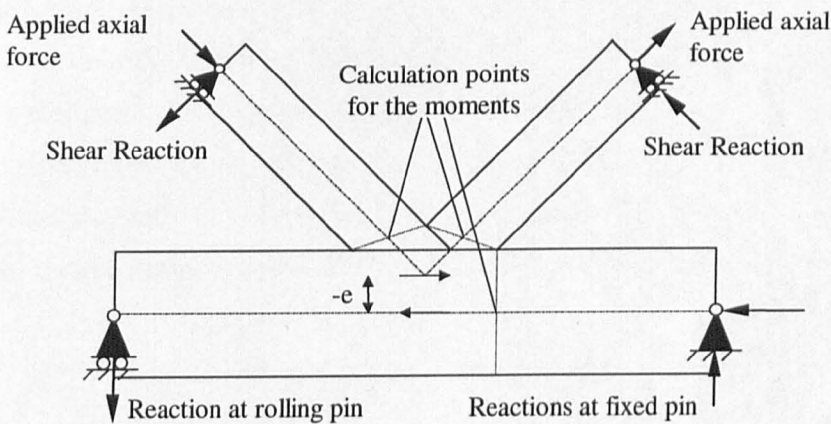


Figure 7.12 The calculation points of the moment/load interaction diagrams

7.6.1 The direction of the shear reactions at the brace members

The directions of the expected shear reactions at the rollers at the end of the brace members, for load case 1 shown in Figure 7.10, would be those shown in Figure 7.13a. However, the reactions experienced are those shown in Figure 7.13b.

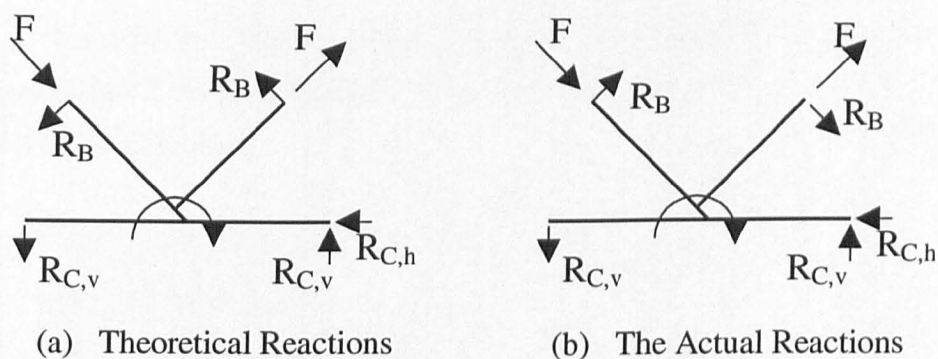


Figure 7.13 The theoretical reactions and the actual reactions experienced

This can be seen in the moment/load diagrams where the sense of the moment in the chord and the brace are always opposite to each other.

This is explained by examining the deformed shape diagrams for all the traditional RHS K joints shown in this Chapter. The top face of the chord, i.e. the connected face, offers very little resistance to the axial load applied to the brace members in that the compression member is punched into the chord face and the tension member is pulled out. Figure 7.14 shows the rotation at the joint caused by these displacements and as the ends of the brace members are constrained to move in an axial direction only, with no significant rotation of the member, the reactions at the rollers are reversed in order to comply with the boundary conditions.

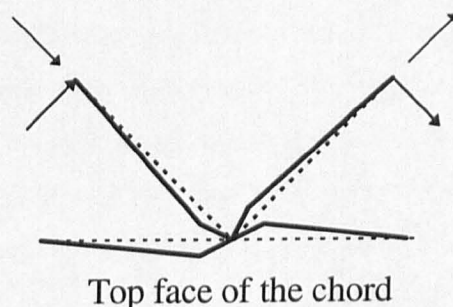


Figure 7.14 The action of the braces on the top face of the chord

Evidence of the deformation of the top face of the chord as described in this section can be seen in all the displaced shape diagrams for the traditional RHS K joint shown in this Chapter.

The axial contoured stress diagrams shown in Figure 7.15 show the sense of the moment acting in the brace members and therefore the shear reaction at the roller at the end of the brace member.

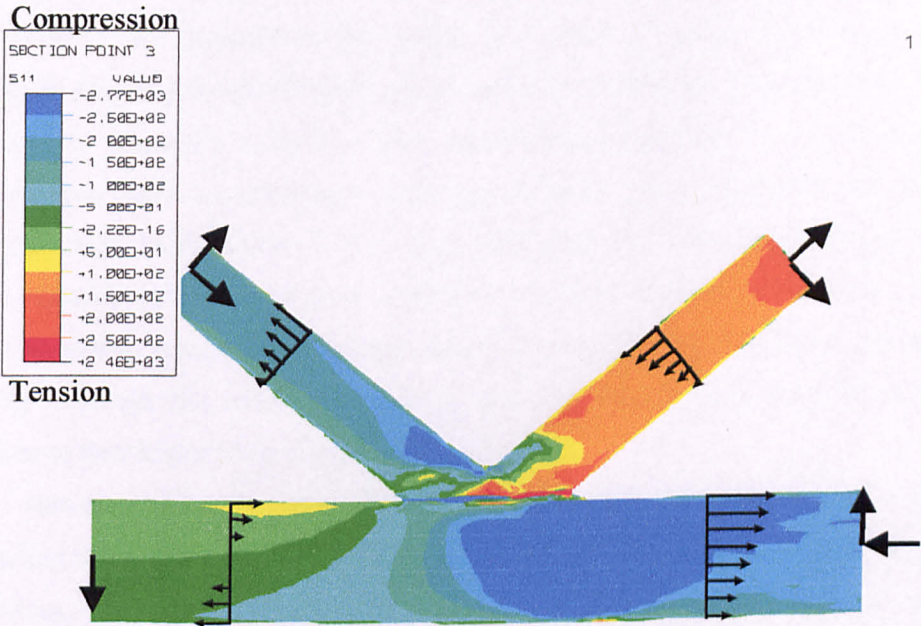


Figure 7.15 Illustration of the reactions/sense of the moments discussed

7.6.2 Traditional RHS overlapped K Joints where $\theta = 30^\circ$

Examining Figure 7.11 it can be seen that there are two probable modes of failure at $\theta = 30^\circ$, depending on whether the chord is in tension (load cases 2 & 3) or compression (load cases 1 & 4). The von Mises stress contoured plots and displaced shape diagrams shown in Figure 7.17 confirm that similar modes of failure must exist between these groups as there are distinct similarities in the diagrams for each pair of load cases.

Considering load cases 1 & 4, the displaced shape diagrams show the deformation of the top face of the chord in the areas indicated. The axial load and the bending moment both produce compression in the connecting face of the chord in this region, which leads to joint failure. This is confirmed by the moment/load interaction diagrams shown in Figure 7.16 where the chord is seen to fail before the braces, although at maximum joint capacity the braces are very close to failure.

Considering load cases 2 & 3, von Mises contoured stress plots and the displaced shape diagrams shown in Figure 7.17 indicate that there is wide spread

plastification and considerable deformation of the chord due to the rotation of the joint. Failure does not occur in the same manner as load cases 1 & 4 because the axial force and the moment acting on the chord both act in tension on the top face. Examination of the moment/load diagrams shown in Figure 7.16 reveals that there has been considerable strain hardening of the top face of the chord, which being in tension does not fail on reaching the plastic capacity. In load case 2 both the brace members attain their plastic capacities with the joint failure being attributed to failure of the discontinuous brace in compression shedding moment to the chord which then fails as well. However, in load case 3, the continuous brace (in compression) reaches the plastic capacity and begins to shed moment to the chord. Failure occurs as the chord attains its plastic capacity and the discontinuous brace (in tension) reaches the plastic capacity although the moment acting in both the braces operates in the reverse direction to that indicated by Figure 7.13b.

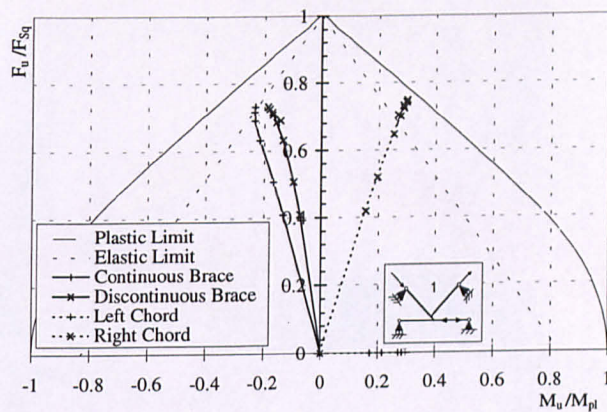
However, given the large deformations that have occurred at joint failure, concluding that the discontinuous brace (in tension) fails at the plastic capacity may be misleading, due to errors in determining the secondary moments. Similarly the errors in determining the secondary moment would explain why the compression member exceeds the plastic capacity in both cases which is unlikely to happen.

Table 7.4 gives a brief summary of the different failure mechanisms and the order in which they occur.

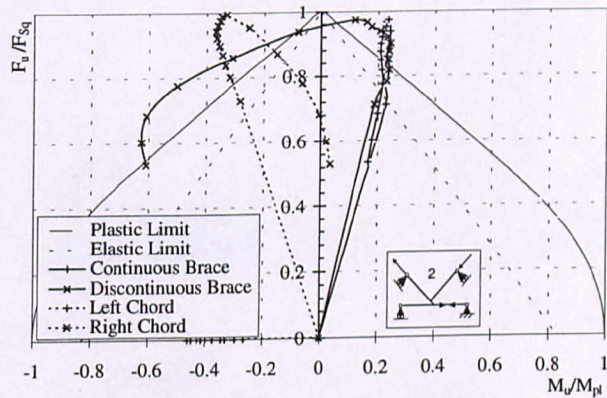
Load Case	Failure Mechanism	Failure Load
1	Plasticification of the top face of the chord in compression	0.731 $F_{Sq,1}$
2	Plasticification of the top face of the chord in tension Plasticification of the continuous brace in tension Plasticification of the discontinuous brace in compression	0.974 $F_{Sq,1}$
3	Plasticification of the top face of the chord in tension Plasticification of the continuous brace in compression Plasticification of the discontinuous brace in tension (possibly)	0.947 $F_{Sq,1}$
4	Plasticification of the top face of the chord in compression	0.710 $F_{Sq,1}$

Table 7.4 A summary of the failure mechanisms at $\theta = 30^\circ$

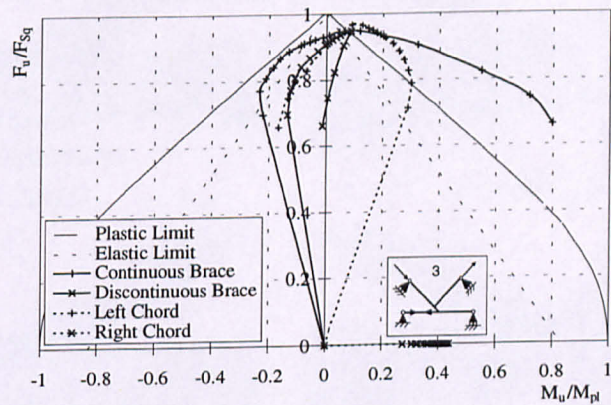
1



2



3



4

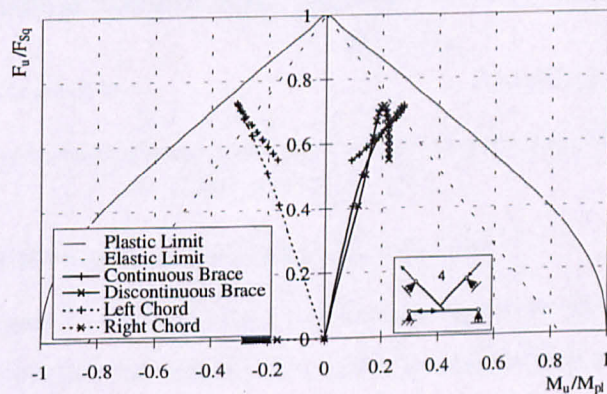


Figure 7.16 Chord and Brace moment/load interaction diagrams $\theta=30^\circ$

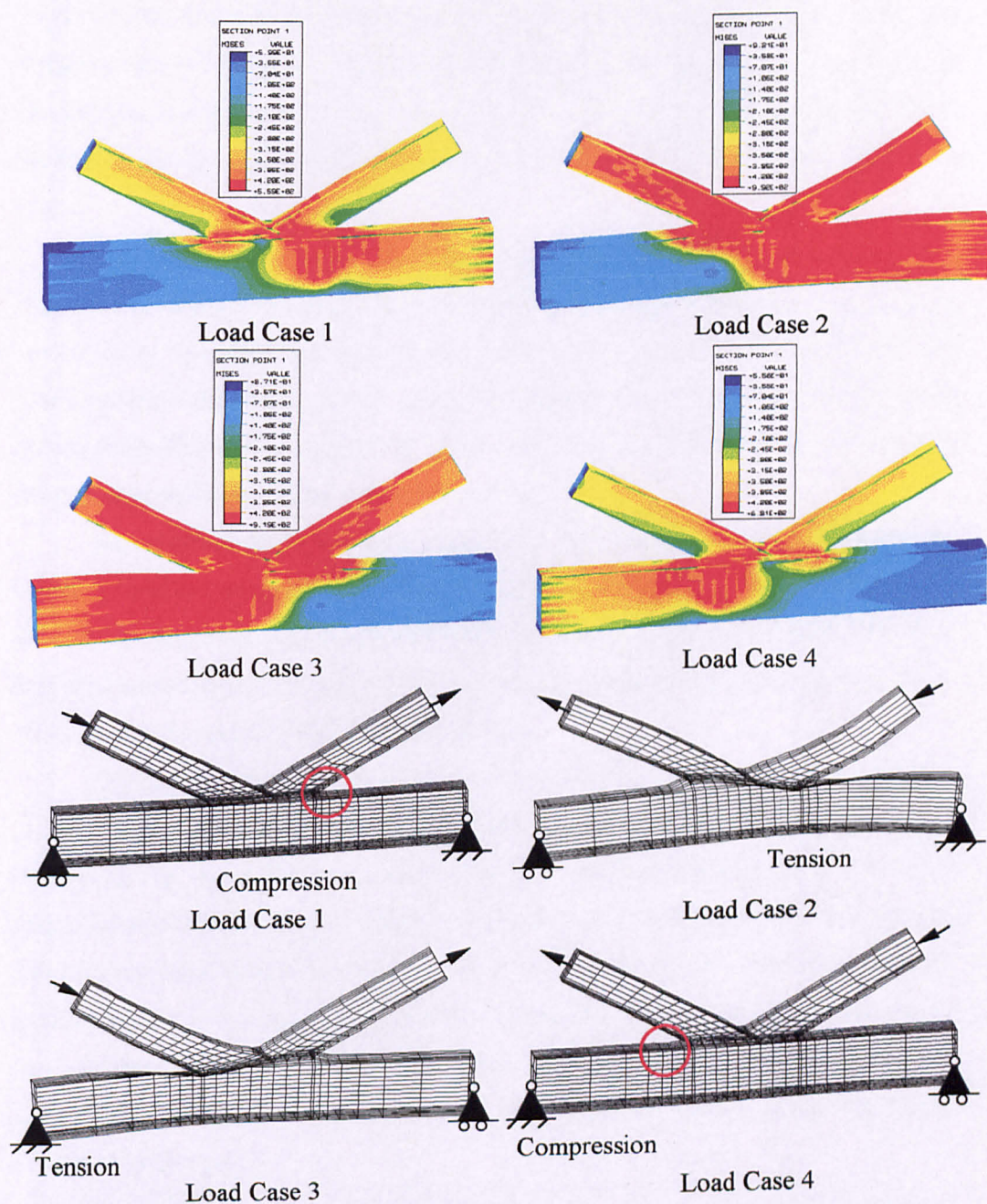


Figure 7.17 von Mises contoured stress plots and displaced shapes at the maximum load for the outside surface $\theta = 30^\circ$

7.6.3 Traditional RHS overlapped K Joints where $\theta = 60^\circ$

Examining Figure 7.11 it can be seen that there are again two probable modes of failure depending on whether the continuous brace is in tension (load cases 2 & 4) or compression (load cases 1 & 3). The sense of loading in the chord is not important as for each pair one is in tension and other is in compression. The failure loads given in

Table 7.3 are virtually identical for these groups and examining the displaced shape diagrams shown in Figure 7.19 indicates that each pair appear to have the same failure mechanism. The lack of stiffness of the top face of the chord in resisting the axial loads applied to the brace members can be seen in all the load cases, causing the joint to rotate.

Considering load cases 1 & 3, the moment/load interaction diagrams shown in Figure 7.18, indicate just how similar the failure mechanism must be as the diagrams are virtually identical. Examining these diagrams it appears that the chord and discontinuous brace play no part in the mechanism as they remain well within the elastic limit. The failure appears to occur only in the continuous brace, which is in compression when the plastic capacity is reached.

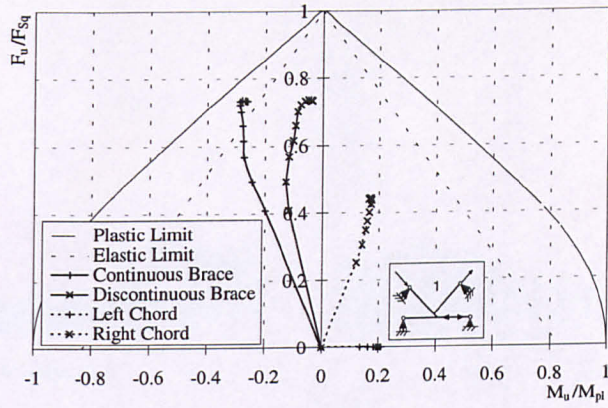
Examination of the von Mises contoured stress plots in Figure 7.19 shows that failure is confined to the top face of the chord and the lower part of the brace members as would be expected from the moment/load interaction diagrams. The displaced shape diagrams would appear to confirm that the failure occurs only in the continuous brace as this is the one member with any deformation.

Considering load cases 2 & 4, the moment/load diagrams show that joint failure occurs when both the braces have reached their plastic capacities. The chord remains well inside the elastic limit and does not contribute to the failure mechanism. The deformation of both the braces, shown in Figure 7.19, would appear to confirm that failure is confined to brace members. This would account for the increase in the joint capacity for these two load cases over the previous two load cases by the increase in the work done to cause this extra deformation. Evidence of the extra work required to cause failure can be seen in the increased area of plasticity shown in the von Mises contoured stress plots.

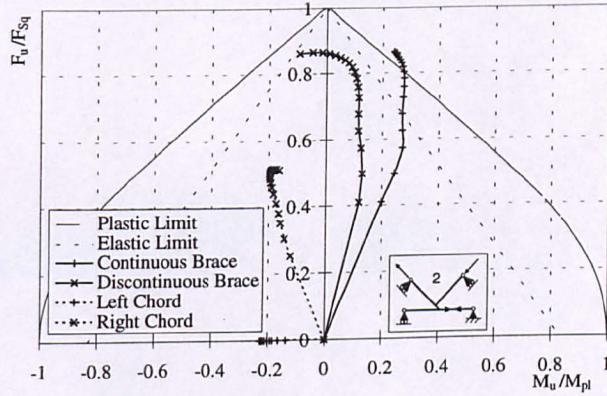
Load Case	Failure Mechanism	Failure Load
1	Plasticification of the continuous brace in compression	$0.737 F_{Sq,1}$
2	Plasticification of the continuous brace in tension Plasticification of the discontinuous brace in compression	$0.767 F_{Sq,1}$
3	Plasticification of the continuous brace in compression	$0.742 F_{Sq,1}$
4	Plasticification of the continuous brace in tension Plasticification of the discontinuous brace in compression	$0.762 F_{Sq,1}$

Table 7.5 A summary of the failure mechanisms at $\theta = 60^\circ$

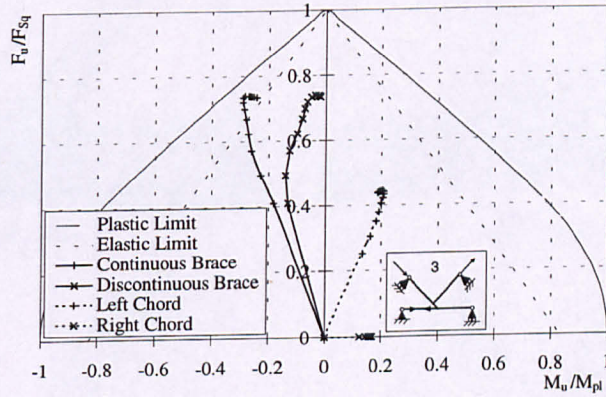
1



2



3



4

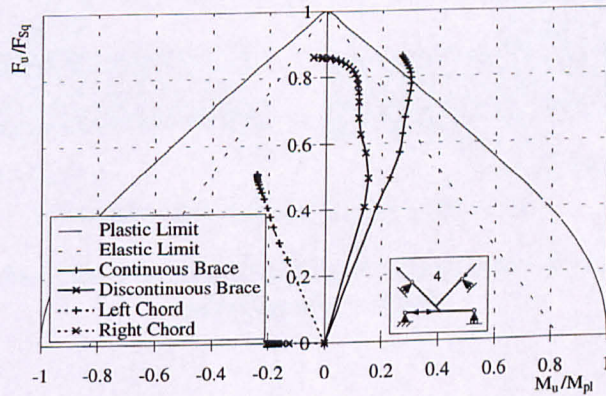
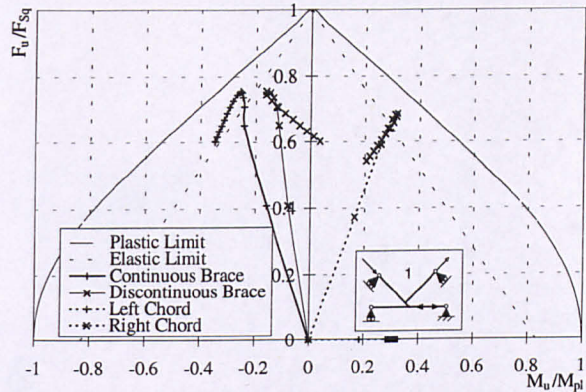


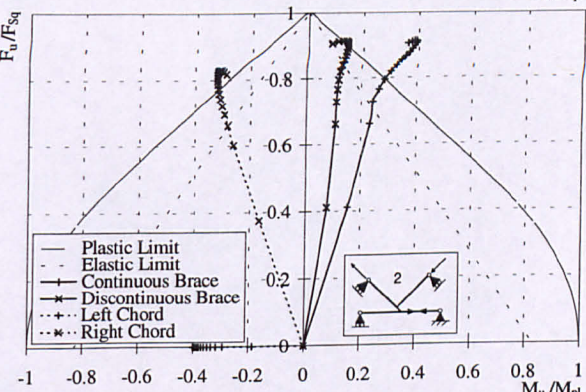
Figure 7.18 Chord and Brace moment/load interaction diagrams $\theta = 60^\circ$

7.6.4 Traditional overlapped RHS K joints $\theta = 40^\circ$ and 50°

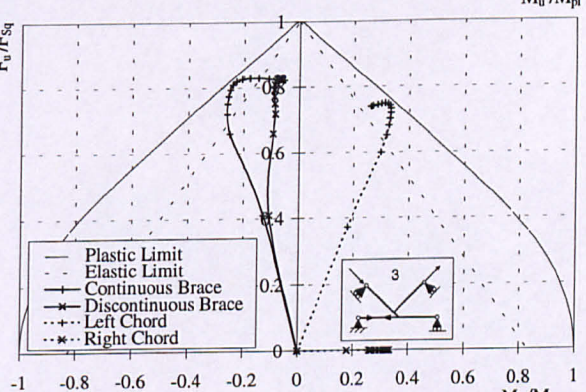
1



2



3



4

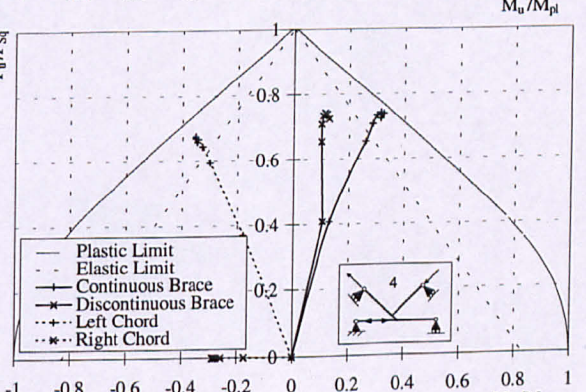
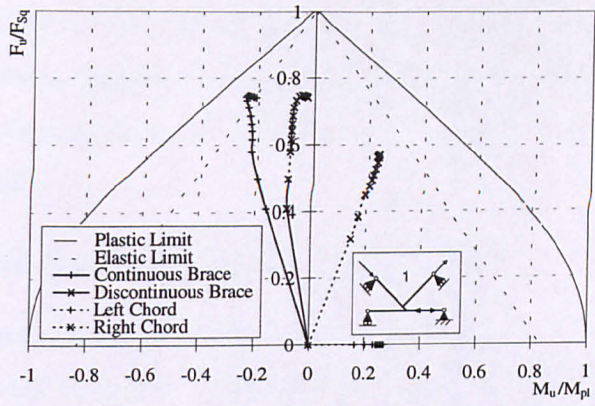
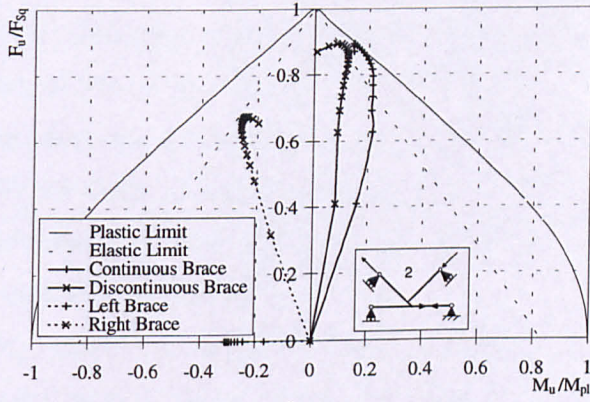


Figure 7.20 Chord and brace interaction diagrams $\theta = 40^\circ$

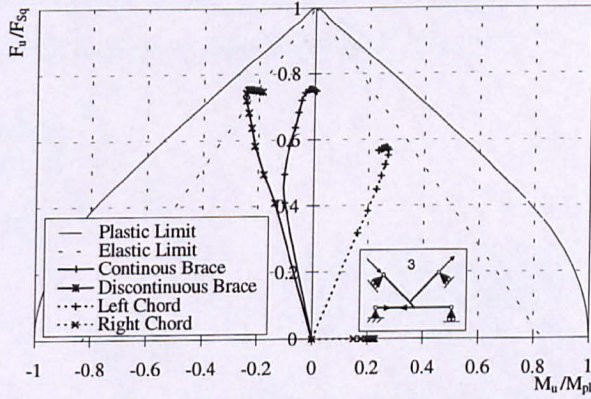
1



2



3



4

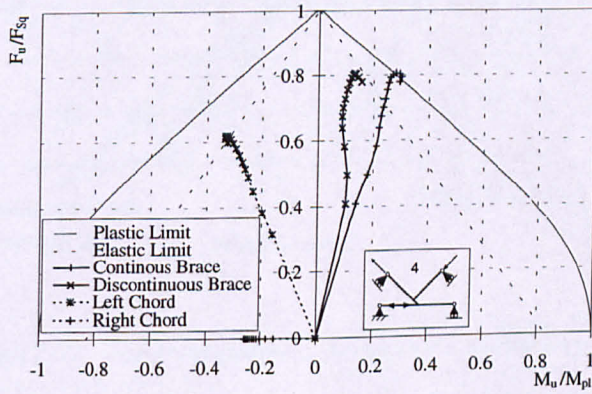


Figure 7.21 Chord and brace interaction diagrams $\theta = 50^\circ$

The joints with $\theta = 40^\circ$ or 50° are not discussed in detail. However, study of the moment/load interactions diagrams, shown in Figure 7.20 and Figure 7.21, reveals a transition between failure in the chord at $\theta \leq 40^\circ$ to a failure in the brace members for larger angles of $\theta \geq 50^\circ$.

7.7 The effect of disconnecting the hidden weld

Standard practice in the fabrication of K joints is to tack weld both members into position on the chord and then weld around the perimeter of the connection. This results in one face of the overlapped brace not being properly welded, referred to as the hidden weld. Crockett (1994) observed that if the hidden weld is considered to be unconnected then the joint capacity is reduced. As some joints analysed previously failed at values below the CIDECT design recommendations it was felt necessary to investigate exactly how much the joint capacity is reduced by this condition. Only the joints which may be critical have been analysed.

In the models, where the continuous brace is loaded in compression, the unconnected edge of the brace at the concealed intersection has been prevented from passing through the chord wall by use of an equation constraint.

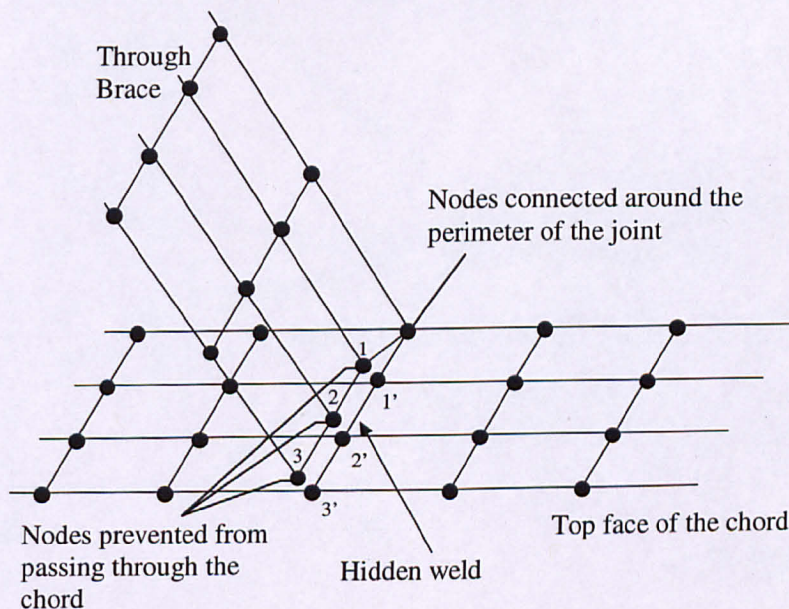


Figure 7.22 The arrangement of nodes at the hidden weld

The vertical displacements of the respective nodes in the chord and the brace walls being made equal, shown in Figure 7.22. This allows a vertical reaction to be passed

between brace and chord but no horizontal reactions, as would be the case if the unconnected face of the brace was allowed to slide over the chord wall. In the cases where the continuous member is in tension, then the nodes on the brace have no restraint on them and they are free to move away from the chord.

Angle Load Case	Hidden weld	30°	40°	50°	60°
1	Disconnected	636.7 kN	650.5 kN	657.0 kN	647.4 kN
	Connected	(657.2 kN)	(670.0 kN)	(663.2 kN)	(652.7 kN)
2	Disconnected				
	Welded	(869.9 kN)	(809.6 kN)	(792.0 kN)	(767.9 kN)
3	Disconnected			667.3 kN	653.3 kN
	Welded	(826.2 kN)	(734.9 kN)	(667.9 kN)	(657.1 kN)
4	Disconnected	630.7 kN	652.5 kN		
	Welded	(637.3 kN)	(657.7 kN)	(713.7 kN)	(763.7 kN)

Table 7.6 The results of the analyses when the hidden weld is released

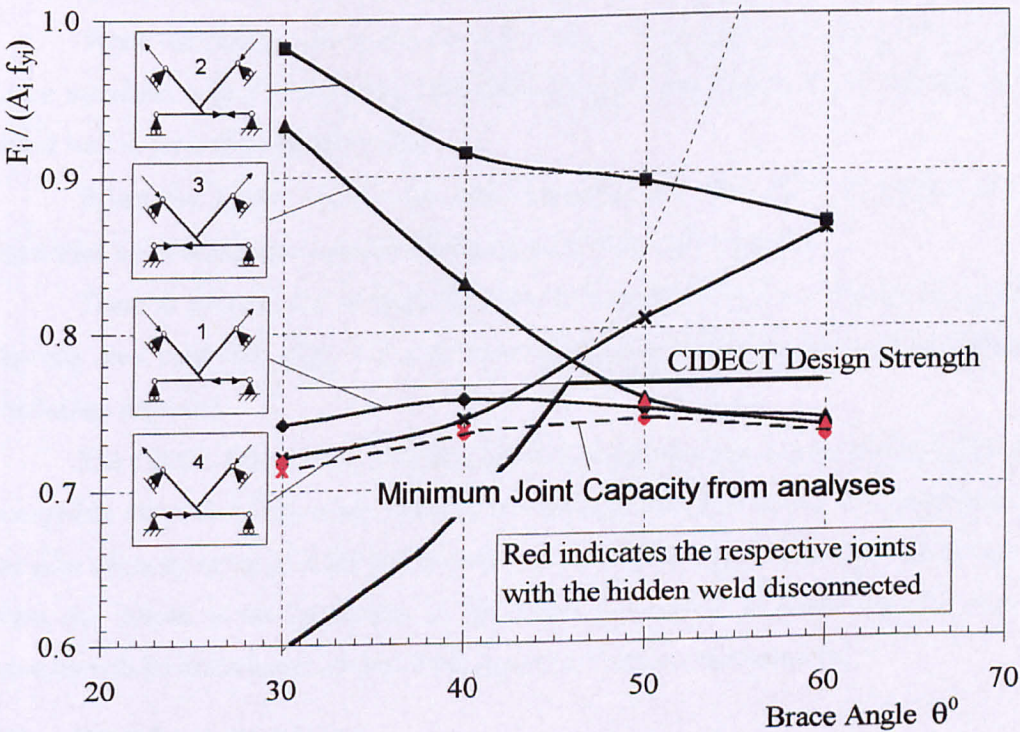


Figure 7.23 The effect of not welding the hidden joint upon joint capacity

The results of the analyses are given in Table 7.6 and shown in Figure 7.23. The main effect of releasing the hidden weld is to:

- reduce the overall strength marginally from that observed previously

- reduce the range between the different load cases in most of the load cases observed, for example load cases 1 & 4 at $\theta = 30^\circ$, where previously there was a significant difference in capacity.

The CIDECT design guide predicts a joint strength of 676 kN, when the failure is not attributed to a failure of the chord, whilst the minimum that can be expected from the joints analysed is only 647.4 kN a reduction of 4.2%. Clearly there is scope for further work in this area to verify whether a reduction in the CIDECT design guidance is necessary.

7.8 Conclusions about the failure of the traditional RHS K joints

Two different forms of failure were identified, the first when $\theta \leq 40^\circ$ and the failure occurred in the chord (when either there was a local failure of the top face of the chord in compression or the general plasticification of the chord in tension). The second when $\theta \geq 50^\circ$ and the failure is confined to the brace members.

When the failure was in the chord (i.e. $\theta \leq 40^\circ$) the sense of overlapping of the brace members was not important. The joint strength was dependent on whether the chord was in tension or compression.

When the failure was in the brace members (i.e. $\theta \geq 50^\circ$) the higher joint capacities were achieved when the continuous member was in tension.

There is no case for an angle function in a design formula, although the joint capacity does vary with angle it is predominately determined by the load and boundary conditions imposed.

The CIDECT/Eurocode 3 formula based on the effective width concept gives a reasonable estimate of the joint capacity. However, it has been shown to overestimate the joint capacity by up to 4.2% based on these results. The largest difference occurring when the failure is predominately in the chord, although it is likely that the joint capacity will be determined by the chord capacity in these circumstances.

7.9 Bird beak K-joints

In order that a comparison can be made between the traditional RHS and bird beak K joints, the analyses described in the first part of the Chapter for traditional RHS joints are repeated for the bird beak K joints. All the parameters are maintained as closely as possible to those for the original traditional RHS K joints.

All the traditional RHS K joints were defined by keeping the overlap constant at 56%, however, due to the geometry of bird beak joints the projected shape of the brace members on the chord is irregular as shown in Figure 7.24. Consequently the definition of the overlap has very little meaning in defining the geometry of the joint and the eccentricity.

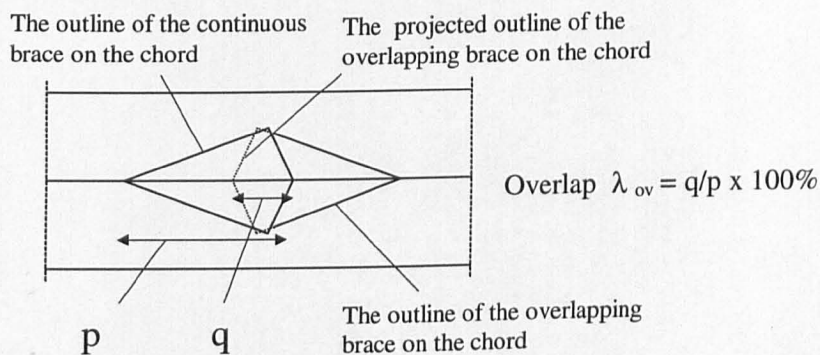


Figure 7.24 The projected shape of the braces on the chord of a bird beak K joint

In order that there could be a comparison between traditional RHS and bird beak K joints for a particular value of θ , the geometry of the bird beak joint was adjusted so that both joint types had the same eccentricity in absolute (millimetres) terms, shown in Table 7.2. The moment caused by the eccentricity will then be equal for the same applied force and have a similar effect on the chord of either joint type using identical sections. (It should be borne in mind that the elastic and plastic moment capacities are reduced when a RHS section is used in a diamond configuration whereas the depth of the section is increased by $\sqrt{2}$. Thus any attempt to base to the eccentricity on a ratio of the eccentricity and the depth of the section will lead to larger eccentricities in the diamond configuration and hence larger moments for the same applied force, although the moment capacity of the section is actually lower.)

This arrangement of the geometry has resulted in a bird beak K joint where three corners of the overlapping brace rest on the overlapped member. This is conceded as being a little unrealistic since it is probable that the joint would be designed so that the corners of the brace coincided with each other on the face of the chord producing a stronger joint that would also be simpler to produce.

7.10 Model details of the bird beak K joint

As with the traditional RHS K joints there is one plane of symmetry and therefore only half the joint is actually modelled. Examples of the finite element mesh for the three different models used in the analyses can be seen in Figure 7.25.

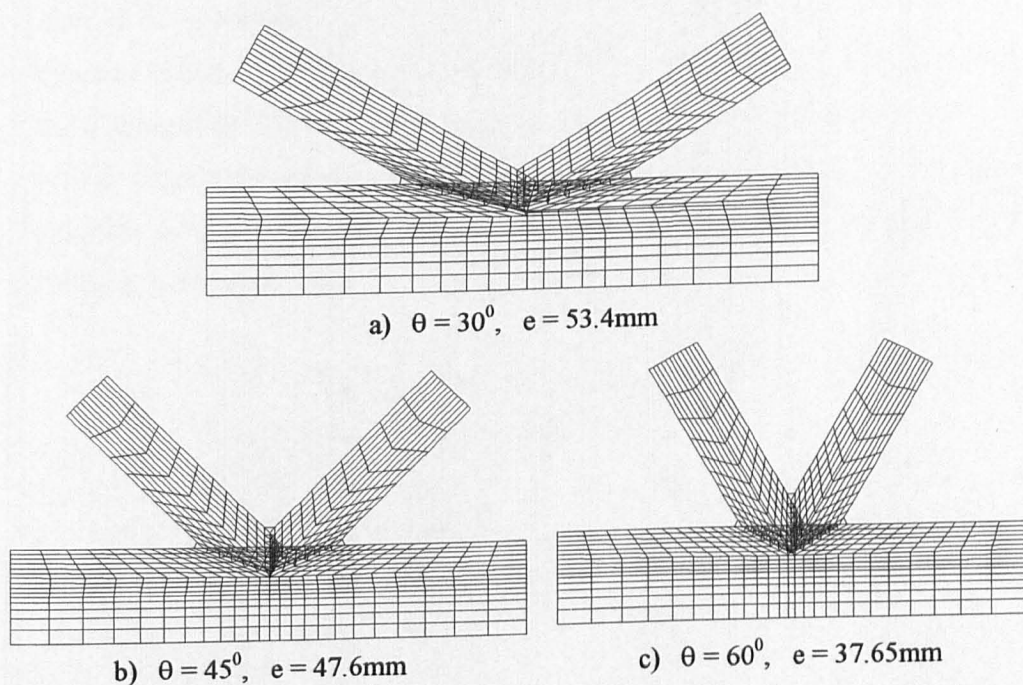


Figure 7.25 Finite element idealisation of the 3 bird beak K joints, $\beta = 0.6$

- the mesh of approximately 800 elements is generated by FEMVIEW (1989) using 8 node thick shell elements (ABAQUS S8R) for the chord and brace members. Fifteen noded solid elements (ABAQUS C3D15) have been used to represent the visible welds, whilst the hidden welds of the continuous brace were connected to the chord by common nodes. The arrangement of the weld detail is the same as that shown in Figure 7.6 for the traditional RHS joints.
- the same non-linear material properties as shown in Table 7.1 and Figure 7.5 are used in these bird beak models.
- chord dimensions 150x150x6.3mm and brace dimensions of 90x90x6.3mm give a width ratio $\beta=0.6$, chord wall slenderness ratio $2\gamma=23.8$ and the thickness ratio $\tau = t_1/t_0 = 1$
- chord length was maintained as the footprint of the overlapped joint plus 800mm, in the same manner as the traditional RHS joints shown in Figure 7.7

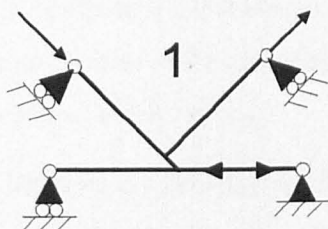
- weld throat thickness was maintained at 6.3mm
- length of the brace was maintained at 400mm, in the same manner as the traditional RHS joints shown in Figure 7.7
- the construction of the mesh for the joints with different values of θ , was kept the same so far as possible.
- the same boundary conditions and load cases were used as shown in Figure 7.10 for the traditional RHS joint. However, there were no end plates fitted to the chord or braces which may affect the joint capacity observed. Each node had individual restraints to support the shear and axial load according to the loading condition imposed, in the same manner used in previous Chapters

Model	θ	End Chord length mm	Brace Length mm	Weld modelled
BKJ3E-1	30°	400	400	No
BKJ3E-1-LC	30°	700	400	No
BKJ3E-1-LB	30°	400	700	No
BKJ3W-1	30°	400	400	Yes
BKJ6E-1	60°	400	400	No
BKJ6E-1-W	60°	400	400	Yes
BKJ6E-1-LC-W	60°	700	400	Yes
BKJ6E-1-LB-W	60°	400	700	Yes

Table 7.7 Parameters varied in the initial investigations

7.11 Initial investigation on the bird beak K joints

Previous studies of the bird beak joint configuration have shown how the chord length affects the joint capacity. In this investigation it was felt necessary to study the effects of changing the length of chord and braces in turn. Table 7.7 details the changes that were made to the models during the initial investigation whilst Figure 7.26 shows the effect on the brace deflection of the different models. The end chord length is defined as the shortest distance between the joint and the end of the chord, shown in Figure 7.7.



The load condition used during the initial investigations

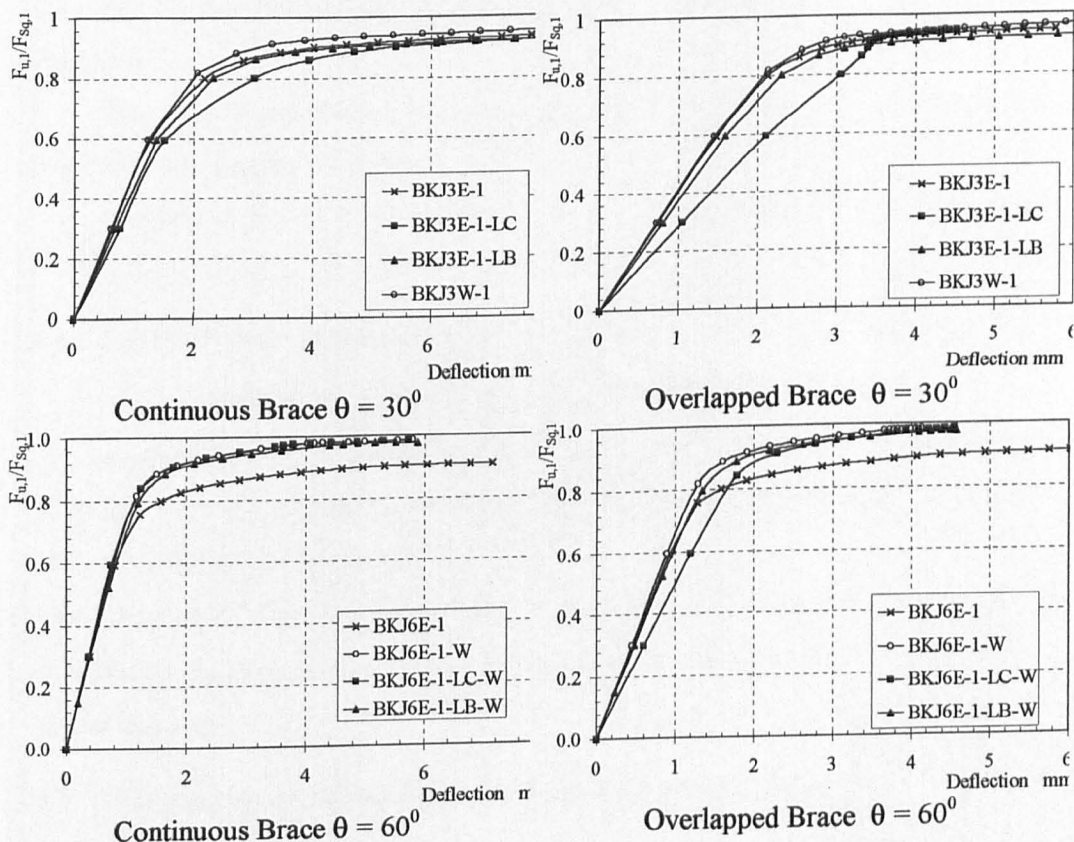


Figure 7.26 A comparison between different models of bird beak K joint

The moment/load interaction curves were also studied, but show no noticeable differences and are not presented.

7.11.1 Discussion of the initial investigation for $\theta = 30^\circ$

For the four joints analysed, using load case 1, the results show similar behaviour with some small differences.

Only one joint had a weld modelled BKJ3W-1 and was only slightly stronger (up to 5% $F_{sq,1}$) than the non-welded models.

A decrease in the stiffness of both of the braces when the chord was increased in length can be observed in the joint BKJ3E-1-LC, although it is particularly evident in the overlapped brace.

7.11.2 Discussion of the initial investigation for $\theta = 60^\circ$

For the four joints analysed the results show similar behaviour with some small differences.

Only one model did not have the weld modelled BKJ6E-1 and is noticeably weaker than the others (7% F_{sq1}).

A decrease in the stiffness of the overlapped brace can be observed in the joint with the longer chord length BKJ6E-1-LC-W.

7.11.3 Conclusions from the initial investigations.

As a result of the initial investigation it is concluded that:

- the length of the members does not significantly affect the joint capacity although it may affect the stiffness of the brace and that the member length can be the same as for the traditional RHS K joints.
- the inclusion of the weld does have a significant affect on the joint capacity particularly for larger angles of θ , therefore the weld is included in all the subsequent joints discussed.

7.12 The results of the analyses of the bird beak K joints

The results of all the analyses for the bird beak K joints is given in Table 7.8 and shown in Figure 7.27. The models analysed in this section have the properties outlined in section 7.10.

Angle Eccentricity Load Case		30° 53.4mm	45° 47.3mm	60° 37.6mm
1	3% b_0 (Max)	827.7 kN (864.0)	892.6 kN (811.6)	850.7 kN (-)
2	3% b_0 (Max)	839.1 kN (872.1)	851.7 kN (854.4)	867.0 kN (-)
3	3% b_0 (Max)	817.2 kN (-)	825.1 kN (830.7)	857.7 kN (-)
4	3% b_0 (Max)	807.2 kN (854.2)	(-) (857.2)	863.7 kN (-)

Table 7.8 A summary of the results for the bird beak K joints

Failure was defined as the load where the deflection on either brace exceeded 3% b_0 (or the maximum if obtained before the 3% b_0 deflection was exceeded). The results shown in Figure 7.27 have been normalised against the brace squash load ($A_i f_{yi}$).

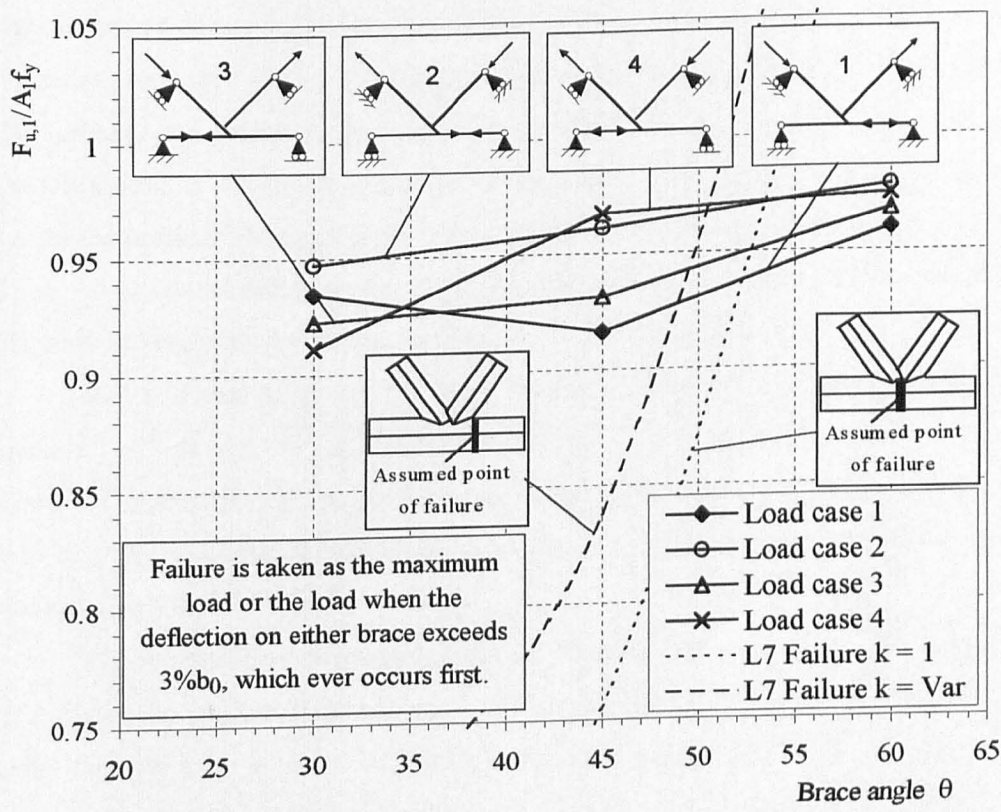


Figure 7.27 A summary of the results for the bird beak K joints

7.13 Discussion of the results for the bird beak K joints

Comparing Figure 7.27 with Figure 7.11 it is immediately apparent that the bird beak K joints are up to 20% of $F_{Sq,1}$ stronger than the respective traditional RHS K joints and that the range of the results of the bird beak joints is a lot smaller. Identifying different failure groups is difficult, although it appears that the joint is stronger when the continuous brace is loaded in tension with one exception which will be discussed later.

There are two general points that can be made from examination of all the displaced shape diagrams. Figure 7.30, Figure 7.32 and Figure 7.34 that show there is very little deformation of the faces of the joint members, which is common to most of the traditional RHS K joints. This is attributed to the increased stiffness of the corners

of the members (opposed to the flat faces of the traditional RHS joints) on which the joint is formed and accounts for the increase in joint capacity observed. The second point can be seen from further examination of the displaced shape diagrams which show that there is no lozenging of the chord, that has been a weakness in the T and X joints observed previously. With the balanced loading applied to the K joints in this Chapter, the vertical components of the applied load to the braces cancel each other out and therefore there is no “crushing action” on the chord. This has the advantage that the moment capacity of the chord is not reduced, due to the reduction of the cross sectional depth. Therefore the full capacity of the diamond configuration may be utilised resisting the moment caused by the eccentricity and the axial force in the chord.

In the stress plots, the red areas indicate regions of high stress where the material has yielded (i.e. $\sigma \leq 420 \text{ N/mm}^2$) and the blue areas indicate regions of low stress. All the displaced shape diagrams have the displacements magnified by a factor of 5 so that the very small deformations, common to all these bird beak K joints can be readily identified.

The moment/load interaction diagrams discussed in this section also have the ultimate plastic capacity plotted, based on the ultimate tensile stress of the material rather than the yield stress to indicate the maximum capacity of the section. The fact that some of the plotted lines exceed this value indicates that inaccuracies do occur in determining the secondary moment acting on the member. In the same manner as before only the elastic and plastic moment/load capacities of the brace are plotted, as these curves are virtually identical to those for the chord (discussed previously in Section 7.6)

7.13.1 The direction of the reactions on the brace members

In Section 7.6.1 the reactions on the braces for the traditional RHS joints was discussed. It was noted that the rotation of the joint, due to lack of stiffness of the top face of the chord, the reactions on the brace were in the opposite sense to those of the chord. Examination of the moment/load diagrams for the bird beak K joints shows that the reactions on the brace and the chord are always of the same sense, resisting the moment caused by the eccentricity, as in the example shown in Figure 7.28

show that there is no lozenging of the chord, that has been a weakness in the T and X joints observed previously. With the balanced loading applied to the K joints in this Chapter, the vertical components of the applied load to the braces cancel each other out and therefore there is no “crushing action” on the chord. This has the advantage that the moment capacity of the chord is not reduced, due to the reduction of the cross sectional depth. Therefore the full capacity of the diamond configuration may be utilised resisting the moment caused by the eccentricity and the axial force in the chord.

In the stress plots, the red areas indicate regions of high stress where the material has yielded (i.e. $\sigma \leq 420 \text{ N/mm}^2$) and the blue areas indicate regions of low stress. All the displaced shape diagrams have the displacements magnified by a factor of 5 so that the very small deformations, common to all these bird beak K joints can be readily identified.

The moment/load interaction diagrams discussed in this section also have the ultimate plastic capacity plotted, based on the ultimate tensile stress of the material rather than the yield stress to indicate the maximum capacity of the section. The fact that some of the plotted lines exceed this value indicates that inaccuracies do occur in determining the secondary moment acting on the member. In the same manner as before only the elastic and plastic moment/load capacities of the brace are plotted, as these curves are virtually identical to those for the chord (discussed previously in Section 7.6)

7.13.1 The direction of the reactions on the brace members

In Section 7.6.1 the reactions on the braces for the traditional RHS joints was discussed. It was noted that the rotation of the joint, due to lack of stiffness of the top face of the chord, the reactions on the brace were in the opposite sense to those of the chord. Examination of the moment/load diagrams for the bird beak K joints shows that the reactions on the brace and the chord are always of the same sense, resisting the moment caused by the eccentricity, as in the example shown in Figure 7.28

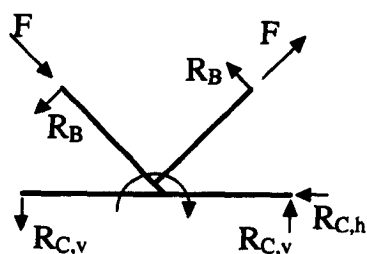


Figure 7.28 An example of the reactions for the bird beak K joint

Examination of the displaced shape diagrams reveals the reason for this, in that all the displacements are very small and the stiffness of the corners of the chord on which the joint is formed prevents the rotation of the joint. This rigidity allows the braces to resist the moment caused by the eccentricity.

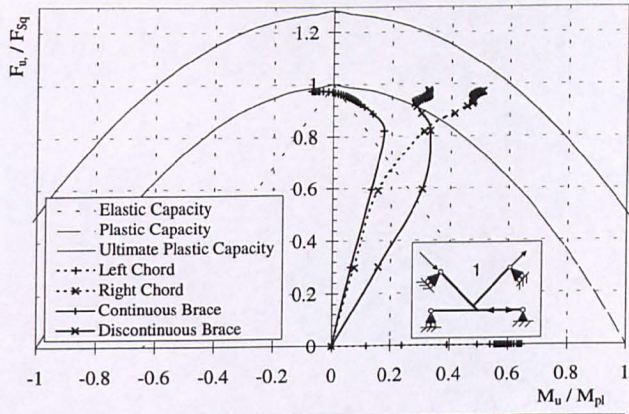
7.13.2 Bird beak K joints where $\theta = 30^\circ$

Determining and classifying the mode of failure is very difficult for this series of models as there is no distinct pattern. Examination of Figure 7.27 shows that there is no similarity with the traditional RHS K joints where the chord in tension (load cases 2 & 3) is a stronger arrangement than the chord in compression (load cases 1 & 4). All the points representing the joint capacities for $\theta = 30^\circ$ are above the line representing L7 failure at the centre of the chord, indicating that chord failure should be the predominate mechanism.

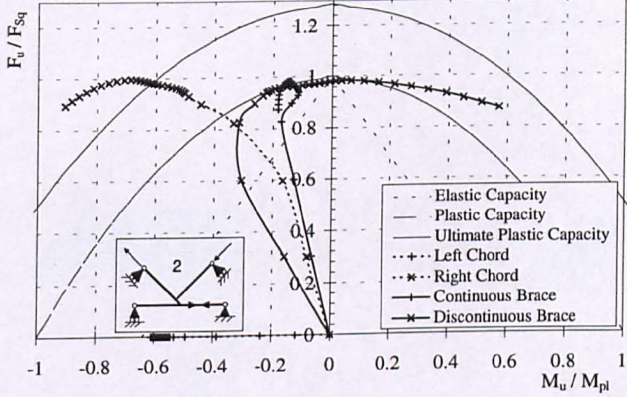
The contoured stress plots in Figure 7.30 show very little with regards to the form of the failure, except that there is large scale plasticification to the loaded members, which is in agreement with the moment/load curves shown in Figure 7.29. Examination of these moment/load diagrams shows that:

- in all cases the discontinuous brace attracts more moment than the continuous brace.
- in all cases the method of failure appears to be the plasticification of the chord, followed by the plasticification of the discontinuous brace and then the plasticification of the continuous brace.
- in load cases 1 & 2 the chord attracts less moment than load cases 3 & 4.
- there are similarities between the moment/load plots of the braces in load cases 1 & 3 and load cases 2 & 4 in the way the brace moments change sense and the chord behaviour, although this is not reflected in the joint capacities.

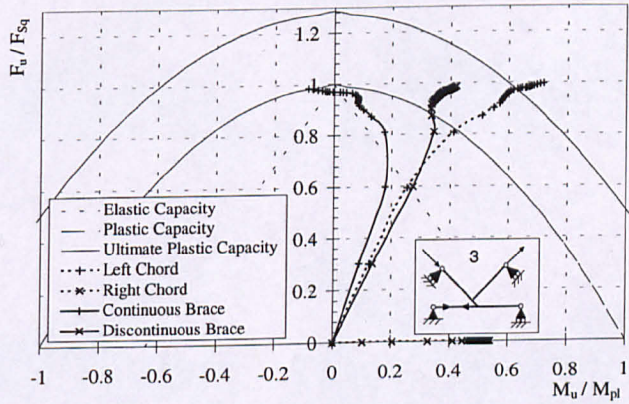
Load case
1



Load case
2



Load case
3



Load case
4

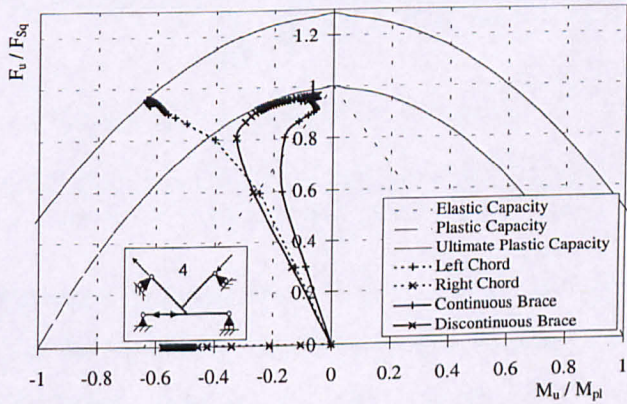


Figure 7.29 Moment load interaction diagrams for the bird beak joint $\theta = 30^\circ$

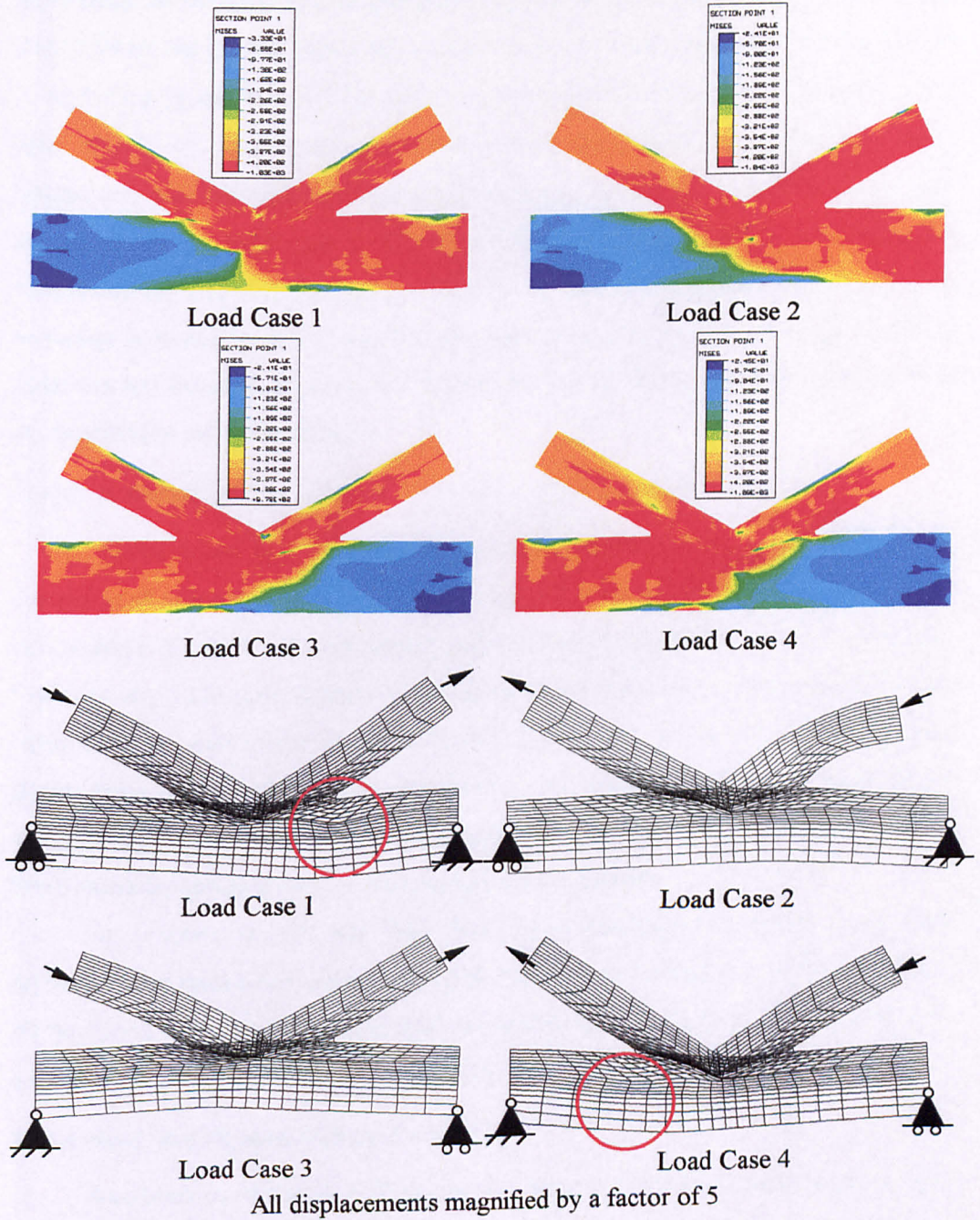


Figure 7.30 Bird beak K joints von Mises and displaced shape diagrams at maximum load for the outside surface, for $\theta = 30^\circ$

In the displaced shape diagrams shown in Figure 7.30, for load cases 1 & 4 where the loaded part of the chord is in compression, there appears to be evidence of the plasticification of the chord, circled in red on the diagrams. This is very similar to the L7 failure observed in the traditional RHS joints, with the stiffness of the corners

preventing deformation until a large part of the chord has been plastified. In load cases 2 & 3 where the loaded part of the chord is in tension, the compression brace appears to be failing by bending. Whilst this is not so distinct for load case 3, it was the only joint at $\theta = 30^\circ$ not to reach a maximum value. Had the computation been carried further it is possible that the bending of the compression brace would be of the same magnitude as for load case 2. Given the narrow range of results and conflicting indicators, the differentiation of the load cases has proved impossible. However, in summary it would be fair to say that the high level of plasticity exhibited in all the members has caused a general joint failure and several different mechanisms seem to be operating to cause the failure.

7.13.3 A comparison of the bird beak to the traditional RHS K joints

Chord failure is common to both joint configurations when $\theta = 30^\circ$ however, for the load cases 1 & 4 for the traditional RHS joints, the weakness due to the deformation of the chord wall caused joint failure at a relatively low joint capacity. There is very little plastification of the material at joint failure, which occurs in the chord in the vicinity of the deformation. For load cases 2 & 3 for the traditional RHS joints, there is considerable joint deformation and widespread plasticification of the material when failure occurs. The joint capacities observed occur when the chord and brace members are approaching their squash load capacities.

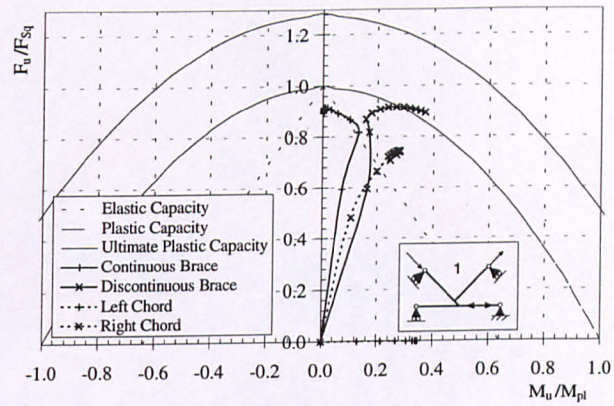
In contrast to this the bird beak joint configuration shows very little deformation at failure and widespread plasticification of the material. Failure occurs in all the joints when the chord and brace members are approaching their squash load capacities, at similar levels to the load cases 2 & 3 of the traditional RHS joints.

7.13.4 Bird beak K joints where $\theta = 45^\circ$

Examination of Figure 7.27 shows that there is a relatively wide range of joint capacities at $\theta = 45^\circ$. The joints where the continuous brace is loaded in tension, (load cases 2 & 4), having the larger capacity. All the points representing the joint capacities at $\theta = 45^\circ$ lie very close to the curve for the L7 failure at the centre of the chord. It is therefore expected that failure will be a combination of mechanisms involving both the brace and the chord members.

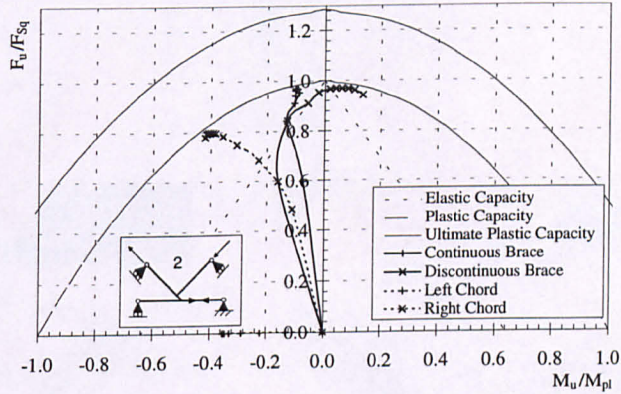
Load case

1



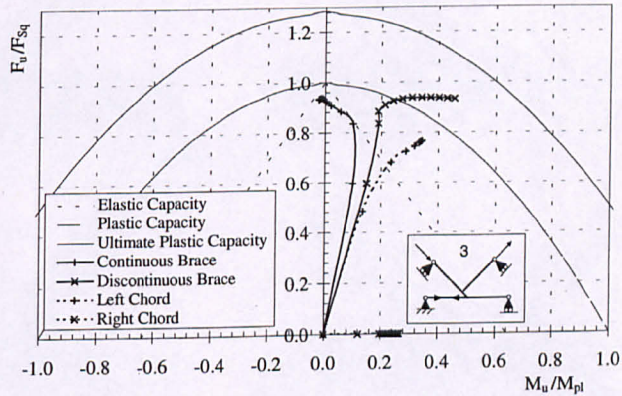
Load case

2



Load case

3



Load case

4

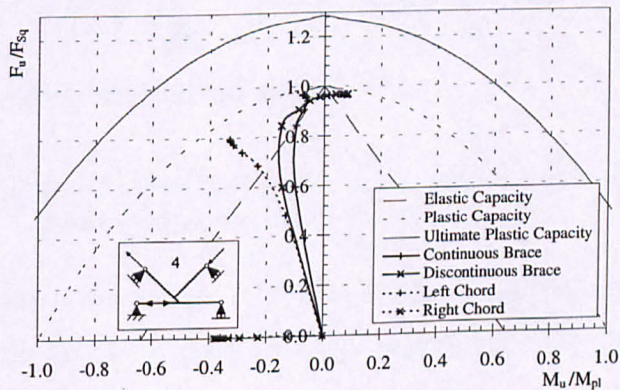


Figure 7.31 Moment load interaction diagrams for the bird beak joint $\theta = 45^\circ$

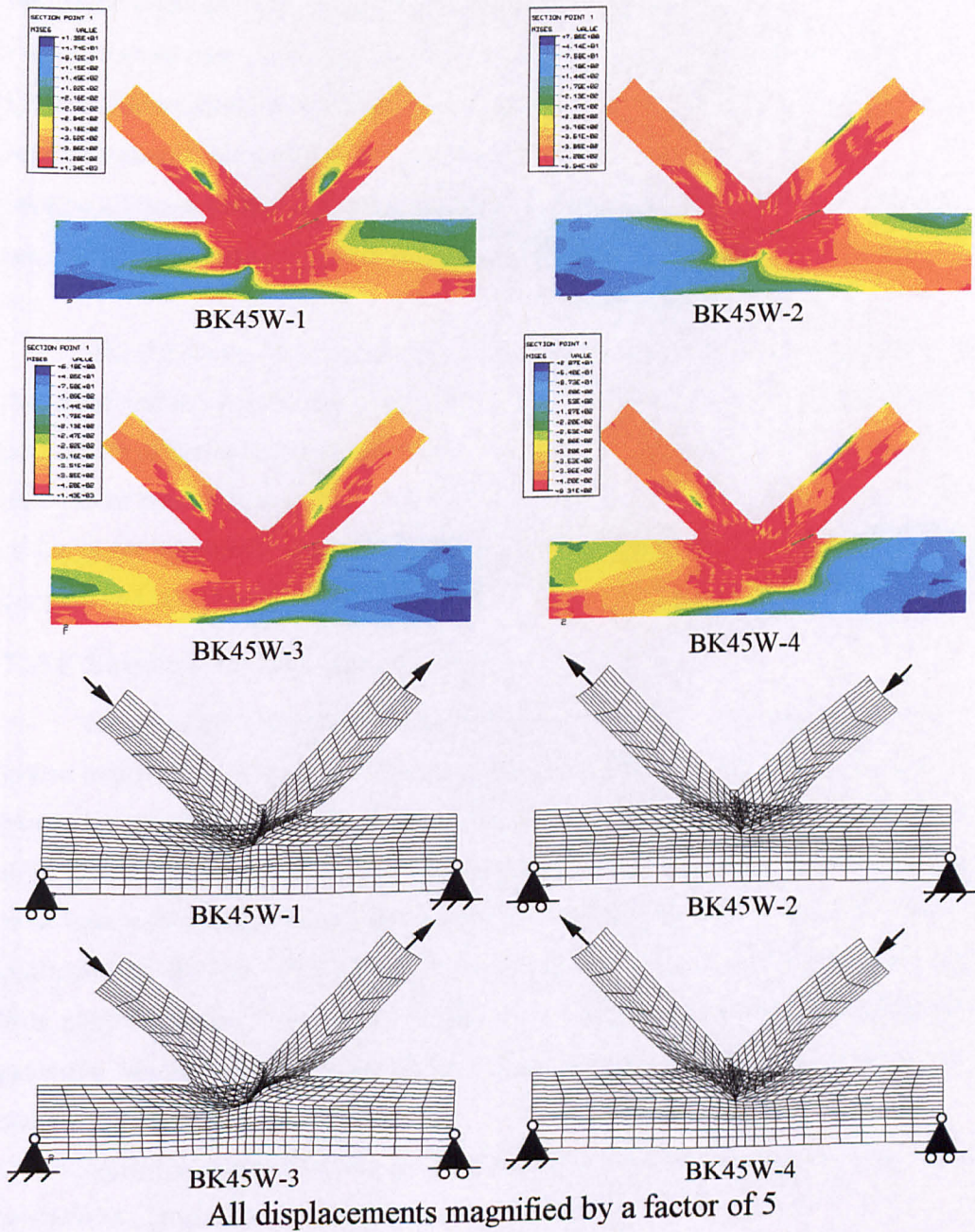


Figure 7.32 Bird beak K joints von Mises and displaced shape diagrams at maximum load for the outside surface, for $\theta = 45^\circ$

The reason for the decrease in the strength of load case 1 is not understood however, modelling error is ruled out as all the joints have been copied from this one with the load and boundary conditions changed.

The moment/load interaction diagrams shown in Figure 7.31 show similar trends to those discussed in the previous section. However, the chord does not reach

the plastic capacity, with exception of load case 2. The elastic capacity of the chord is exceeded in all cases as all the points shown in Figure 7.27 for $\theta = 45^\circ$ are above the L7 failure line indicating an elastic chord failure. Load cases 2 & 4 show that at failure both the braces have reached the plastic capacity, whilst load cases 1 & 3 the continuous brace loaded in compression has failed to reach the plastic capacity and this may be the reason that load cases 1 & 3 have a lower joint capacity than load cases 2 & 4.

The displaced shape diagrams shown in Figure 7.32 show both deformation of the chord and the braces. The deformation of the chord is from the punching in and pulling out of the respective brace members. The brace members in the vicinity of the chord have been deformed, spread out in compression and narrowed in tension which is due to the movement of the other brace. There is a small amount of bending in the compression brace in load cases 2 & 4.

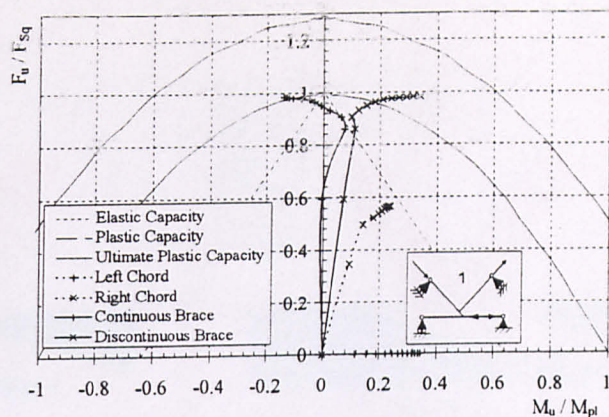
7.13.5 Bird beak K joints where $\theta = 60^\circ$

Examination of Figure 7.27 shows that the joints where the continuous brace is loaded in tension are somewhat stronger (load cases 2 & 4) although the capacity of the joints is very similar. The moment/load interaction diagrams shown in Figure 7.33 show that the failure is confined to the brace members and is principally due to the axial load in the brace, the secondary moment only being significant at failure. This is confirmed by the von Mises contoured stress plots in Figure 7.34 which show very little plasticification of the chord except in the vicinity of the brace members and extensive plasticification of the brace members with significantly more in the compression brace.

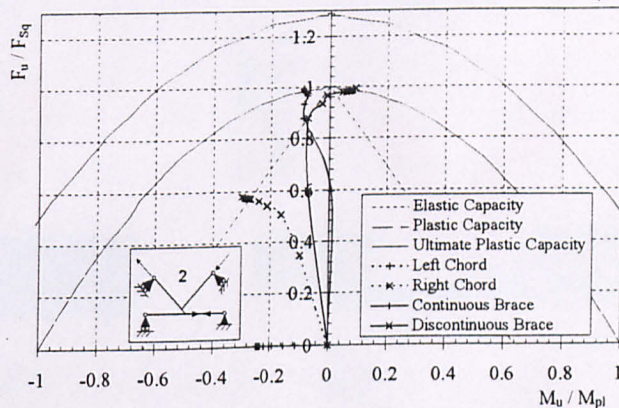
Again the similarities for the moment/load diagrams noted in Section 7.13.1 can be seen in the moment/load diagrams for $\theta = 60^\circ$.

The displaced shape diagrams shown in Figure 7.34 show similar behaviour to those models where $\theta = 45^\circ$ in the deformation of the braces at the base of the members and in that there is bending in the compression brace.

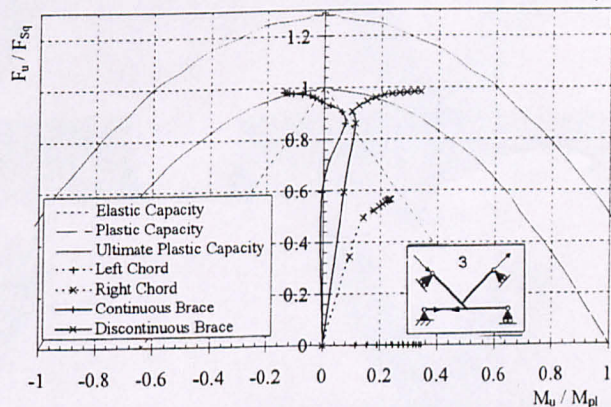
Load case
1



Load case
2



Load case
3



Load case
4

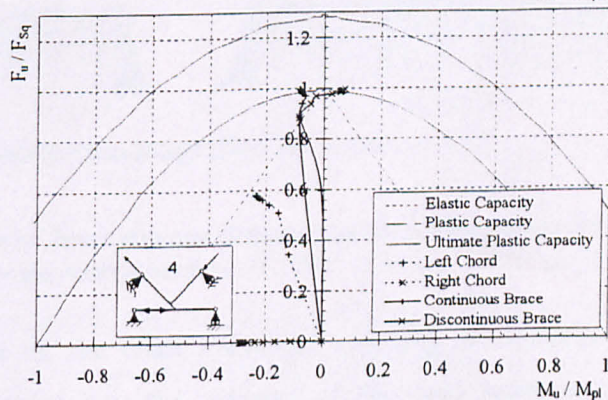


Figure 7.33 Moment load interaction diagrams for the bird beak K joint, $\theta = 60^\circ$

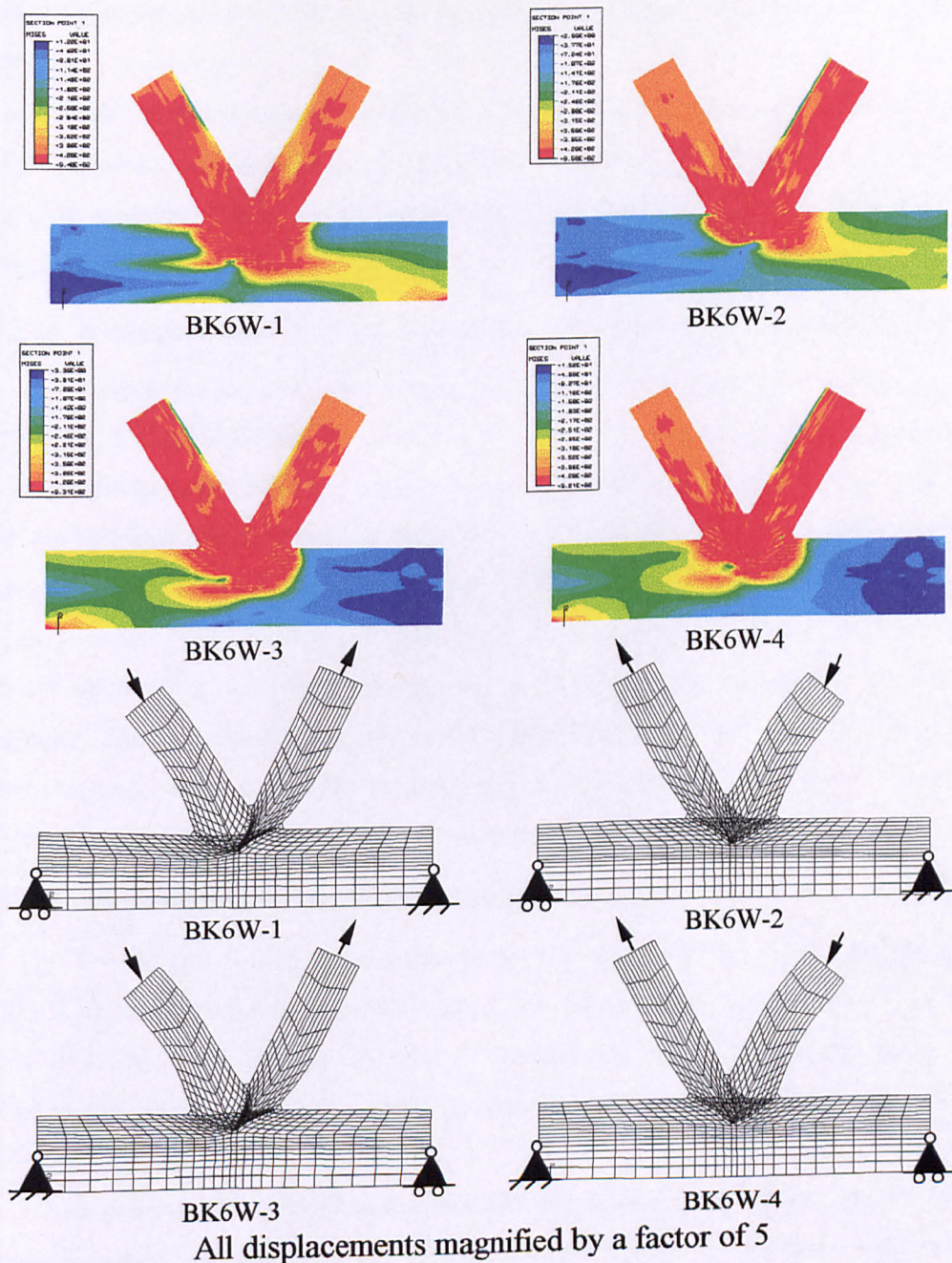


Figure 7.34 von Mises contoured stress plot and displaced shapes at the maximum load for the outside surface, $\theta = 60^\circ$

The distortion at the base of the brace members, spreading in compression and narrowing in tension, explains why the presence of the weld increases the joint capacity of joints where $\theta = 60^\circ$ noted earlier in the initial investigations. Clearly the

presence of the extra material due to the weld acts to restrain the deformation in this area.

All the joints where $\theta = 60^\circ$ failed to reach a maximum joint capacity in the time allowed for the computer analysis. Given more time a maximum may have been reached however, due to the widespread plasticification a lot of CPU time would be required for little benefit.

7.13.6 A comparison of the bird beak to the traditional RHS K joints for $\theta = 60^\circ$

Failure occurs only in the brace members for both joint configurations. However, the deformation that occurs in the brace members for the traditional RHS joint causes a weakness, which leads to a joint failure at a capacity below that observed for the bird beak joints. In the traditional RHS joints the plasticification of the material occurs in the vicinity of the joint, where the deformation occurs. Whereas in the bird beak joint the plasticification of most of the brace members reflects that the joint failure occurs at a load where the brace members are approaching their squash load capacity. The only deformation observed in the bird beak joints, which is very small and does not cause a significant weakness, is the widening/narrowing of the X-sectional shape of the member due to the action of the other brace.

7.13.7 Conclusions about the failure of the bird beak joint

The increase in the joint capacity of the bird beak K joints over the traditional RHS K joints is derived from the stiffness of the corners of the member on which the joint is formed. The lack of stiffness of the faces of the RHS members is not a disadvantage and if the effective width concept is applied to the bird beak joint, the effective width may be said to be 100%.

In general the mode of failure was the plasticification of one or both of the brace members, although when $\theta = 30^\circ$ the plasticification of the chord may have contribute towards the failure mechanism.

All the joints of varying values of θ seem to have similar failure modes, as all the moment/load interaction diagrams show similar trends, the only variation being the decrease in the significance of the chord in the failure mechanism as the angle θ increases.

The definition of overlap which is widely used in the design of traditional RHS joints is meaningless for bird beak joints. Bird beak joint would be best described by the eccentricity (either relative or absolute) of the brace members.

The lozenging of the chord, which has been seen to be a weakness of other bird beak joint configurations, is not present as there is no cross loading of the chord in the K joints studied in this Chapter. This has enabled the bird beak K joint to develop the advantages of the diamond configuration of the chord and to be substantially stronger than similar traditional RHS K joints.

7.13.8 Design information

Examination of Figure 7.27 shows that the plastic collapse of the chord will be the limiting factor for the joints where $\theta \leq 45^\circ$ when the axial force in the chord and the moment due to the eccentricity are calculated by

$$1 \geq \frac{2F_1 \cos \theta}{A_0 f_{y,0}} + \frac{1}{2} \frac{2eF_1 \cos \theta}{Z_0 f_{y,0}} \quad \text{Eqn 7.12}$$

where

A_0 is the area of the chord

F_1 is the axial load applied the brace

$f_{y,0}$ if yield stress of the chord

e is the eccentricity of the joint

Z_0 is the elastic modulus of the chord

θ is the angle between the brace and the chord members

For the joints where the plastic collapse of the chord is not critical, limiting the axial force in the brace to

$$F_1 = 0.9 A_1 f_{y,1} \quad \text{Eqn 7.13}$$

will give a conservative estimate of the joint capacity, for the parameters of $b_0/t_0 = 23.8$, $\beta = 0.6$, when the joint is arranged so that the corners of the brace members intersect on the chord and angle between the chord and the brace is $30 < \theta < 60$.

7.14 The principal differences between the traditional RHS K joints and the bird beak K joints

The principal difference between the traditional and the bird beak overlapped K joints studied in this Chapter, is the manner in which failure occurs. The dominating factor of the failure mechanism in the traditional RHS K joints was the rotation of the joint due to the lack of stiffness of the top face of the chord in resisting the axial loads applied to the brace members. The tension member was pulled out and the compression member was pushed into the top face of the chord causing the joint to rotate. For low angles of θ ($\theta < 45^\circ$) and in load cases 1 & 4, this caused a weakness in the top face of the chord, which being loaded in compression failed at relatively low joint capacity. For load cases 2 & 3, the chord was loaded in tension, and the weakness caused by rotation of the joint in the top face of the chord did not produce failure. The rotation of the joint continued until the joint was badly deformed and failure occurred due to the widespread plasticification of the joint. For larger angles of θ (i.e. $\theta > 45^\circ$), the rotation of the joint caused a weakness in the brace members which led to joint failure. For load cases 1 & 3 the rotation caused a weakness in the compression brace, which led to joint failure. In load cases 2 & 4 the rotation caused a weakness in both the brace members leading to a joint failure at slightly higher joint capacity than load cases 1 & 3.

In the bird beak joints, the stiffness of the corner of the chord on which the joint is formed prevented this rotation, and permitted the brace members to resist the moment caused by the eccentricity. The individual failure mechanisms are difficult to determine however, generally failure occurred due to the plasticification of the members at joint capacities much higher than those observed for the traditional RHS K joints. For the joints where $\theta = 30^\circ$, plasticification occurs in the brace members and the part of the chord carrying the axial load which leads to joint failure. For the joints where $\theta = 60^\circ$, the failure of the joint occurs due to the plasticification to the brace members only. The axial load in the brace members at joint failure generally was greater than 90% of the squash load of the brace member.

The sense of the reactions at the rollers on the brace are different with the two joint configurations, due to the rotation of the chord connecting wall in the traditional RHS joint. In the traditional RHS joints the reactions on the brace members act in the

same sense as the moment caused by the eccentricity of the joint whereas in the bird beak joint configuration the reactions on the brace members act to oppose the moment caused by the eccentricity of the joint.

The joint capacities observed for the bird beak joint are generally higher and more consistent for the different load cases than for the traditional RHS joints for all angles of θ .

7.15 Conclusions on traditional and bird beak K joints

At the beginning of this Chapter a question was posed as to whether there is any justification for an angle function in the CIDEKT/Eurocode 3 design formula for the traditional RHS overlapped K joint. This Chapter has shown conclusively that the joint capacity varied considerably with the brace angle θ and load/boundary conditions. By taking the lower bound of these results there is no need to introduce an angle function in the design formula. For the models analysed, the CIDEKT/Eurocode 3 design formula estimated with reasonable accuracy (with up to a 4.2% overestimate) the lowest joint capacity produced by the different load and boundary conditions for a given brace angle.

Failure usually occurred when one of faces of the brace or chord, (depending on the brace angle θ ,) deformed reducing that member's moment capacity, particularly if that member was loaded in compression. It was also shown that the joint rotated under load, the brace members did not contribute to resisting the moment caused by the eccentricity.

The overlapped bird beak K joints, where the joint is formed on the corner of the RHS section utilised the stiffness of the corners to great effect. There was very little deformation and no rotation of the joint as it was loaded. The brace members contributed to resisting the moment caused by the eccentricity until the maximum joint capacity was achieved. The combination of these two effects allowed the overlapped bird beak K joints to achieve much higher joint capacities (up to 30% higher) than similar traditional overlapped K joints, (i.e. with the same RHS sections, brace angle and eccentricity). Failure occurred when either the brace or chord member approached their plastic capacity for combined moment and axial load.

8.

Bird Beak K joints with a Purlin Load

8.1 Introduction

If bird beak K-joints are to be used in a truss framework it is inevitable that purlin loads will occur either at the joint or between the joints in some cases, as the load is transferred to the truss, shown in Figure 8.1. In this Chapter a study is made of the effects of applying these purlin loads to bird beak K joints. The nature of this Chapter is more of a preliminary investigation rather than a comprehensive study of the effects of purlin loads as there are a large number of parameters that can be varied in the boundary and load conditions alone.

The model chosen to analyse the effects of the purlin loads is the bird beak model for $\theta = 45^\circ$ examined in the previous Chapter. This model was chosen because it was potentially the most critical of all the models analysed in Chapter 7, although it is recognised that any of the other joints may have a failure mode which could be more critical when a purlin load is applied.

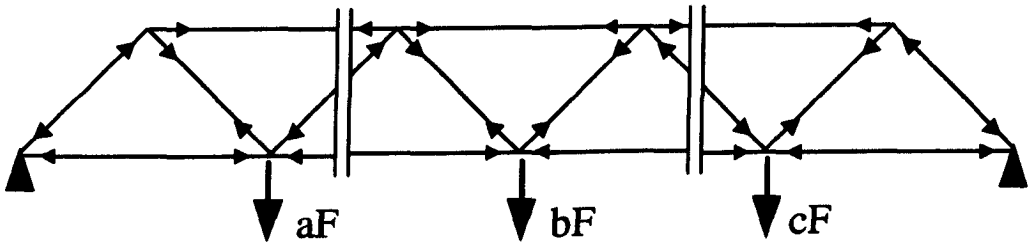


Figure 8.1 An example of a truss loaded with many purlin loads

8.1.1 The axial load in the chord members

From the example truss shown in Figure 8.1 it can be seen that axial loads in the chord members are inevitable when purlin loads are applied to the truss arrangement. In this Chapter the effects of the purlin load itself on the joint capacity is studied followed by the reduction in the joint capacity when axial loads are considered in the chord.

For overlapped K joints, Eurocode 3 and CIDECT recommendations do not make an allowance for the axial load in the chord reducing the joint capacity, i.e. k_n or $f(n) = 1$, as the load in the brace members is considered to be transferred directly between the brace members through the overlapping part of the joint. In the case of through loading of the chord (a K joint with a purlin load applied to the opposite side of the chord), CIDECT (Packer et al 1992) recommends that if the cross loading is significant, then the joint should be checked as an X joint with equivalent members sizes. In which case the axial loading of the chord is taken into account for this particular load case. No similar reference can be found in EC3.

The validity of this method of assessing the joint capacity of an overlapped bird beak K joint with a purlin load, with and without an axial load in the chord will be studied and appropriate design recommendations made.

8.2 Method of loading used

The effects of the purlin load will be analysed for the four different boundary and load conditions used in Chapter 7, with tension or compression purlin loads applied to the K joint. The total loading on the joint is, however balanced, although unequal loads will have to be applied to the braces to achieve this.

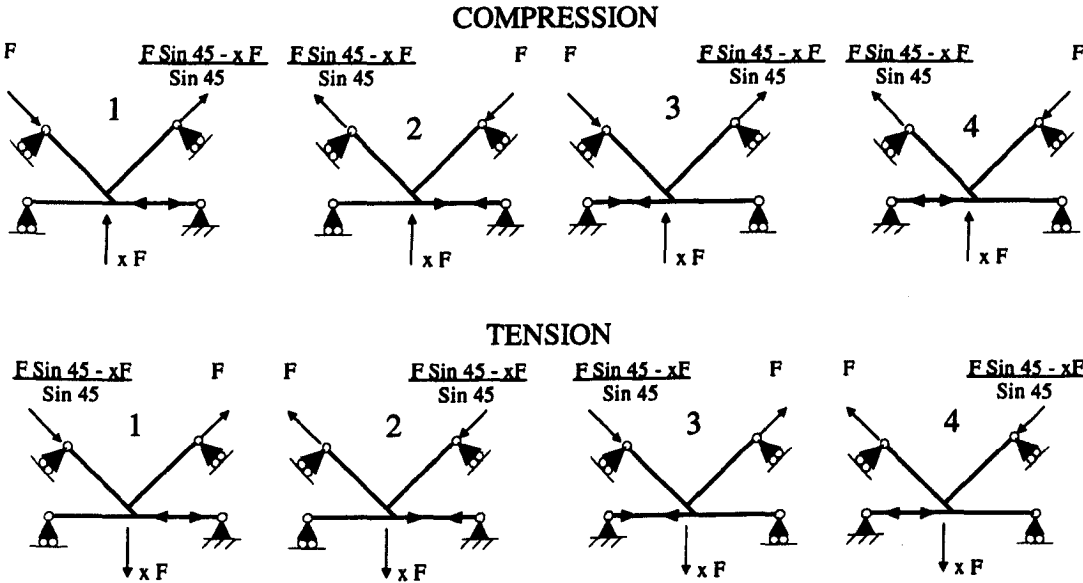


Figure 8.2 The eight combinations of load and boundary conditions considered
($\theta_1 = \theta_2 = 45^\circ$)

The load applied to the purlin is a fixed proportion (x) of the load applied to the braces in the manner shown in Figure 8.2 (Compression is considered +ve and Tension -ve). The failure load of the joint will be considered as the value of F , when the deflection of either brace is 3% b_0 . During the investigation the size of the proportion of the load applied to the purlin will be varied ($-0.4 < x < 0.4$) to examine the effects on the joint capacity and failure mechanism. It is appreciated that a purlin load of 0.4 of the squash load of the brace is very high, and a truss design is unlikely to have such high purlin loads, although possible at a support in a continuous girder.

8.3 Initial investigations

Loading the K joint with a purlin load is similar to the X joints studied earlier, in that the chord is subjected to a load that will cause lozenging. An initial investigation was carried out to investigate the effect of the length of the chord and the restraint offered by the member carrying the purlin load on the joint capacity.

8.3.1 The method of supporting the purlin load

The restraint offered by the member supporting the purlin load is likely to affect the joint capacity as it will effect the lozenging of the chord. Under certain circumstances it could even be the limiting factor on the strength of the joint considered. In this initial investigation three different forms of supporting the purlin load were considered as shown in Figure 8.3.

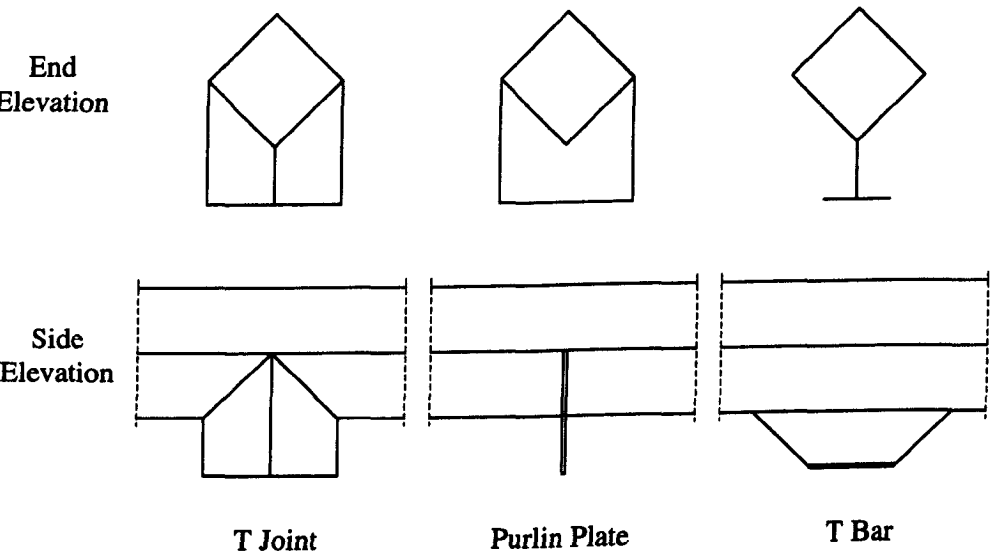


Figure 8.3 Three different forms of supporting the purlin load

8.3.1.1 The T joint

The T joint arrangement offers the chord the maximum restraint against lozenging and distributes the purlin load over a wide area of the chord making local failure of the chord wall less likely. The stiffness of a short RHS member also removes the possibility of buckling or tripping of the member (when due to the deformation of the chord, the action and reaction forces on the member become out of line causing a moment that leads to premature failure).

Despite these advantages, this method was discounted without any models being tested for the following reasons:

- the difficulty in attaching the member carrying the purlin load.
- the extra expense of fabricating the joint was thought to be unjustifiable.
- the advantages of this method are only apparent when very high purlin loads are considered, which would be in excess of the normal loads carried by a truss arrangement with several loading points. One possible exception to this is a truss where a single load is applied at the mid point; however, this is a special case which will be discussed later.

8.3.1.2 The purlin plate

This is a very simple arrangement where a plate is cut to fit the chord profile and welded into position. The member carrying the purlin loads can easily be fastened to the plate by welding or bolting.

The restraint offered by the plate in preventing the lozenging of the chord is likely to affect the joint capacity. Local failure of the chord wall is likely when large purlin loads are applied and there is a possibility of the plate tripping when a compressive load is applied to the joint.

8.3.1.3 The T bar

In this arrangement a length of T bar is welded to the lower corner of the chord to support the purlin loads. The ends of the bar have been tapered to avoid stress concentrations, which may cause local failure. The member carrying the purlin loads may be bolted to the T bar although the number of bolts that can be used is restricted. No restraint is offered to the chord in this method and therefore the thickness of the plate will not affect the strength of the joint. There is a possibility of the T bar tripping when a compressive load is applied to the joint.

8.3.2 Applying a compressive purlin load

To avoid the possibility of the purlin plate and the T bar tripping, a restraint was applied to the purlin plate/T bar to ensure that it remained vertical in the finite element model. This restraint is justified by the presence of the purlin or side rail in a truss structure that would act to restrain this tripping behaviour. The purlin or side rail itself is prevented from moving bodily in a lateral direction by the presence of tie rods fitted at intervals along the member in a similar manner to that shown in Figure 8.4.

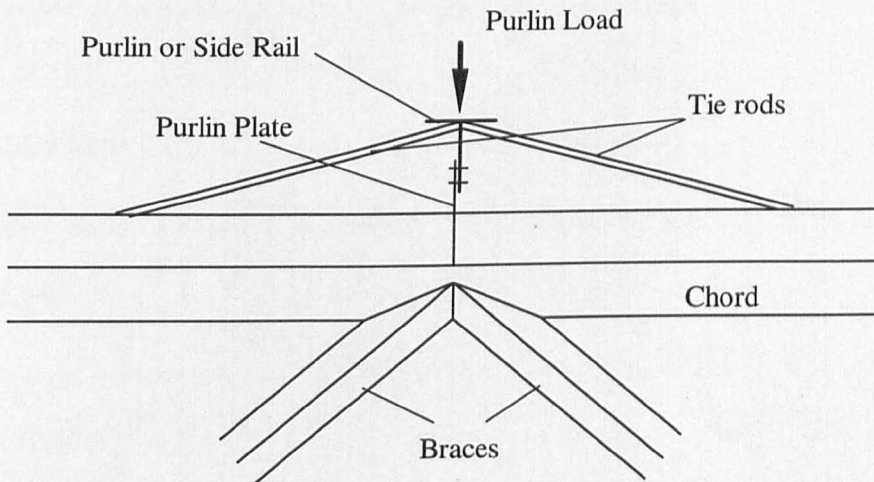


Figure 8.4 The restraint offered by the member carrying the purlin load

8.3.3 The results of the initial investigation

The results of ten different models are presented in Tables 8.1, 8.2 & 8.3 to investigate the effect of the different methods of carrying the purlin load. Table 8.1 and Table 8.2 shows the results when the purlin is load by $0.1559F$ and $0.3118F$ in tension respectively. The increase in thickness of the purlin plate does not significantly affect the joint capacity, although the joint capacity is significantly reduced when the T bar is considered. This reduction in joint capacity is attributed to the deformation caused by the T bar on the chord.

Examination of the joint capacities shown Table 8.3, when the joints are loaded in compression by a purlin force $0.4F$, show similar trends as when the joints are loaded in tension. Increasing the thickness of the purlin plate causes a small increase the joint capacity whilst loading the joint through the T bar arrangement significantly reduces a joint capacity.

Examination of the von Mises contoured stress plots for the K joints with a purlin, show considerable yielding of the corners of the chord suggesting the formation of yield lines in the same manner as the T and X joints studied previously. Two different chord lengths are examined to discover what effect chord length has on the joint capacity. Table 8.3 shows that there is only a marginal difference between the joint capacities when different chord lengths are considered and that further variation of the chord length were not considered necessary as the increase in chord length where a difference may be found would be unrealistic in a truss structure.

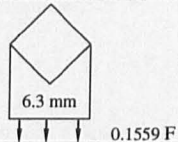
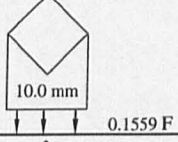
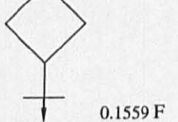
Model	Tension	$F_{u,1} / F_{Sq,1}$	Load kN
2BK45P63		0.9657	855.5
2BK45P10		0.9705	859.8
2BK45T		0.9388	831.7

Table 8.1 Purlin loaded in tension by 0.1559P (Load case 1)

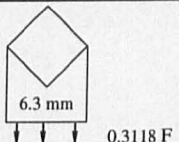
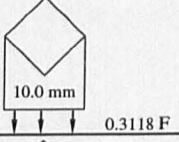
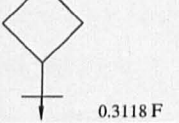
Model	Tension	$F_{u,1} / F_{Sq,1}$	Load kN
4BK45P63		0.7720	683.9
4BK45P10		0.7829	693.6
4BK45T		0.6877	609.2

Table 8.2 Purlin loaded in tension by 0.3118P (Load case 1)

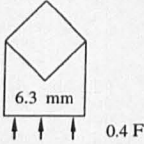
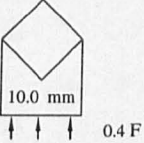
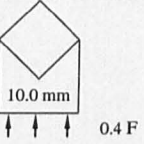
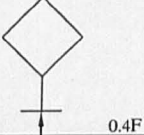
Model	Compression	$F_{u,1} / F_{Sq,1}$	Load kN
4BK45P63C Chord length 1076 mm		0.7528	666.9 kN
4BK45PC Chord length 1076 mm		0.7960	705.2 kN
4BK45PLC Chord length 1876 mm		0.7973	706.3 kN
4BK45T		0.6377	564.9 kN

Table 8.3 Purlin loaded in compression by 0.4 P (Load case 1)

8.3.4 Conclusions of the initial investigation when loading the chord with a purlin load

In deciding which arrangement should be used to apply the purlin load to the chord, the following points were considered:

- the fabrication costs of the T joint arrangement is unlikely to outweigh the benefits of the extra strength, therefore this arrangement is unlikely to be used in a practical situation.
- the arrangement where the T bar is welded to the bottom of the chord has proved to be the weakest method of supporting the purlin load in all analyses carried out in the initial investigation.
- the purlin plate, which is almost as simple as the T bar to fit, is appreciably stronger and is considered to be the more practical arrangement of transferring the purlin load to the chord. Of the two thicknesses of purlin plate analysed, the thicker 10mm plate, is slightly stronger in compression than the 6.3mm plate. The costs of fabricating and fitting the thicker plate is minimal and therefore it is considered that it would be cost effective to use the thicker plate.

All the models analysed in the remainder of this Chapter, all use a purlin plate 10mm thick, unless otherwise stated.

8.3.5 Determining the failure capacity of purlin loaded K joints

The failure capacity of the joint is defined as the point when the deflection of either brace exceeds 3% b_0 and the actual joint capacity is the value F , defined in Figure 8.2. From the load/deflection curves shown this provides a conservative estimation of the joint capacity. Although a line representing 3% b_0 is shown on the load/deflection curves, the actual value is calculated by linear interpolation rather than relying on the “curve smoothing operation” performed in Excel 5a (Microsoft 1993).

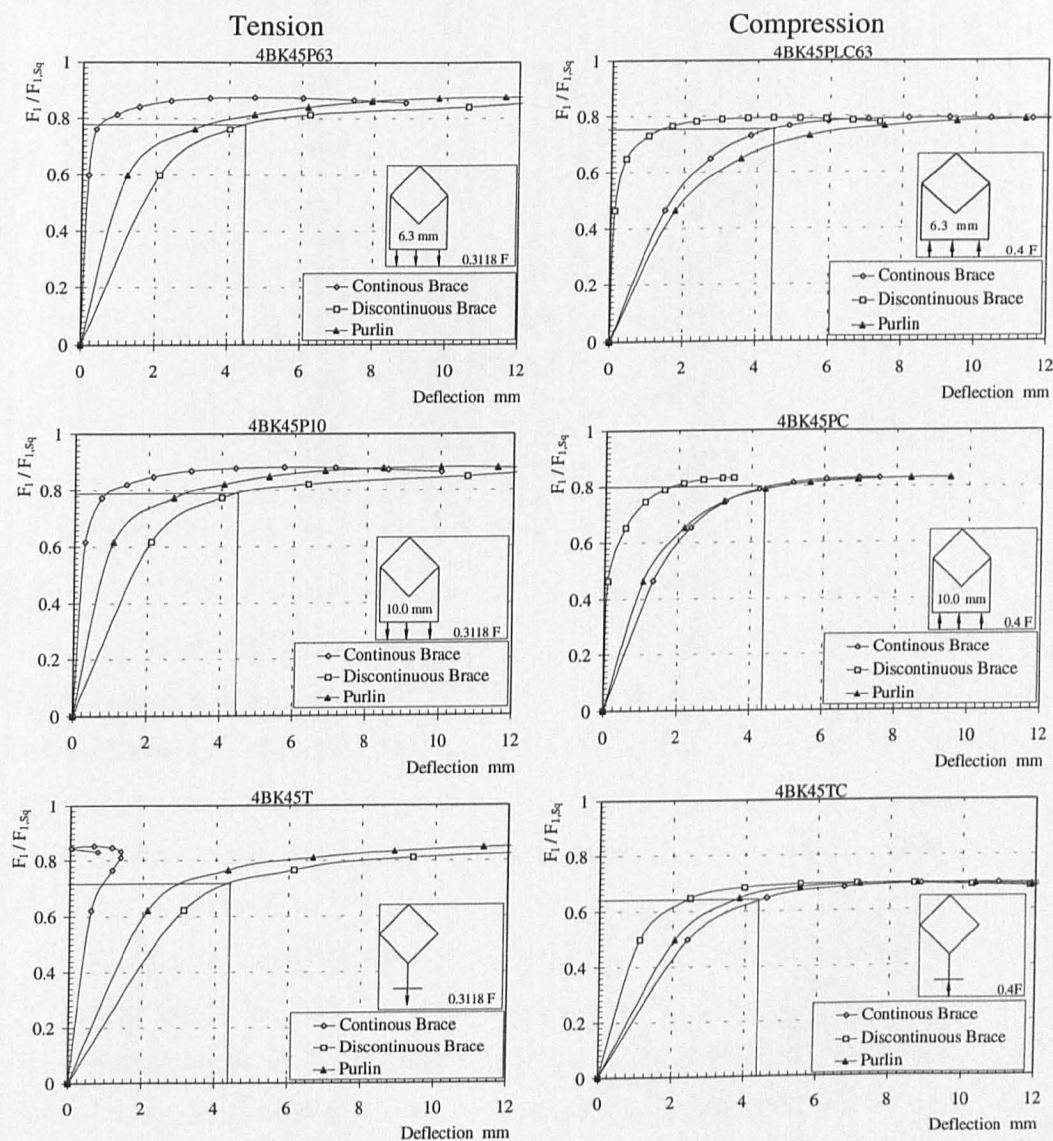


Figure 8.5 Examples of the load/deflection curves for purlin loaded K joints (Load case 1)

The deflection measured is the displacement observed at the ends of the member being considered.

8.4 The results of the analyses of the purlin loaded K joints

The results of the analyses for the bird beak joints where $\theta = 45^\circ$ for all of the load cases 1 & 4 with purlin loads varying from 0.4 tension to 0.4 compression are given in Table 8.4 and are shown graphically in Figure 8.6. Details of the method and size of the loading applied to each joint are given in Figure 8.2.

Load Case	1		2		3		4	
Purlin load	$F_{1,sq}$	kN	$F_{1,sq}$	kN	$F_{1,sq}$	kN	$F_{1,sq}$	kN
-0.4 F	4BK45PLT-1		4BK45PLT-2		4BK45PLT-3		4BK45PLT-4	
	0.8123	719.6	0.9267	821.0	0.8940	792.0	0.8493	752.4
-0.2 F	2BK45PLT-1		2BK45PLT-2		2BK45PLT-3		2BK45PLT-4	
	0.9463	838.3	0.9762	864.8	0.9594	849.9	1.0014	887.1
0.0 F*	BK45W-1		BK45W-2		BK45W-3		BK45W-4	
	0.8947	792.6	0.9614	851.7	0.9314	825.1	0.9676	857.2
0.2 F	2BK45PLC-1		2BK45PLC-2		2BK45PLC-3		2BK45PLC-4	
	0.9705	859.7	0.9490	840.7	0.9807	868.8	0.9427	835.2
0.3 F	3BK45PLC-1		3BK45PLC-2		3BK45PLC-3		3BK45PLC-4	
	0.9257	820.1	0.8728	773.2	0.9158	811.3	0.8917	789.9
0.4 F	4BK45PLC-1		4BK45PLC-2		4BK45PLC-3		4BK45PLC-4	
	0.7973	706.4	0.7556	669.4	0.7807	691.7	0.7676	680.0

* Purlin Plate not fitted on this series of models

Table 8.4 The results of the analyses for the purlin loaded K joints

Examination of Figure 8.6 reveals some interesting features. When the purlin is loaded in tension, load cases 2 & 4 are stronger than load cases 1 & 3. This tendency is reversed, however, when the purlin is loaded in compression, load cases 1 & 3 have a higher joint capacity than load cases 2 & 4. There also appears to be a decrease in strength when a purlin load is zero, this effect being most distinct for load cases 1 & 3, which appears illogical.

These trends can be explained by considering the method of loading and the definition of the failure load. The decrease in the joint capacity when there is no purlin load was considered first. It is possible that the purlin plate, which is not physically present for the joints with a zero purlin load, strengthens the joint, which causes the increase in the joint capacity. However taking load case 1 as an example, an analysis was run where the purlin plate was physically present, but no purlin load was applied. The joint capacity increased from 792.6 kN (0.8947 brace squash load $F_{1,sq}$) to 803.9

kN (0.9075 brace squash load $F_{1,sq}$) which although this indicates a small increase in strength does not account for the differences shown in Figure 8.6

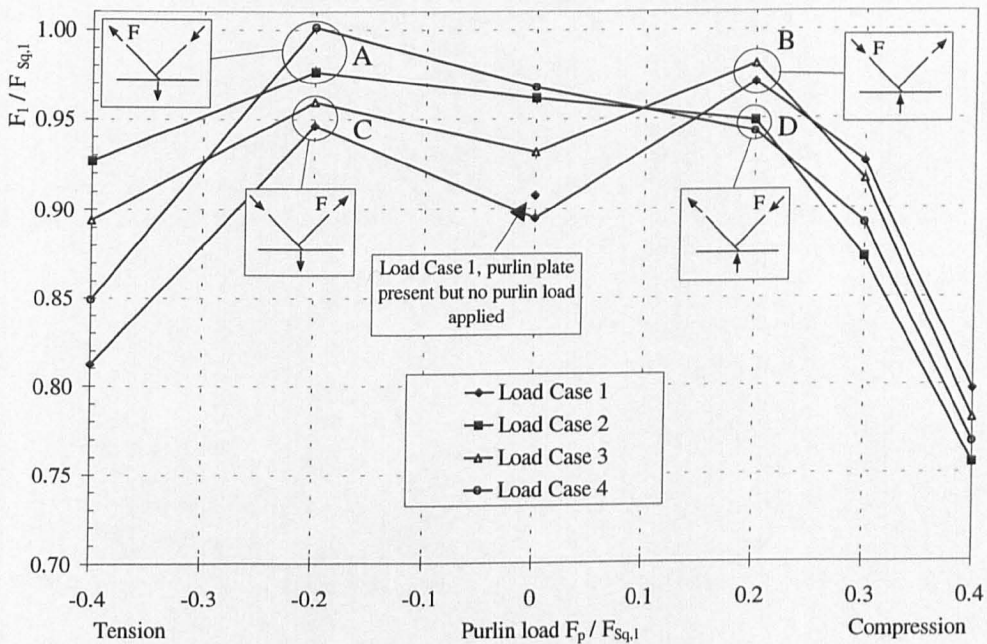


Figure 8.6 The results of the analyses for the purlin loaded K joints

Secondly, if the method of loading for the joints with a purlin load is considered, it is noted that the loading in one brace is much higher than the other and the axial force in the chord is reduced

$$\text{Axial force in the chord, no purlin load} = 2 F \cos \theta$$

$$\text{Axial force in the chord, with a purlin load} = F \cos \theta \left(\frac{\sin \theta - x}{\sin \theta} + 1 \right)$$

However, the larger axial force in the brace defines the joint capacity, even though the axial force in the other members is reduced. The effect of this is to allow a larger axial load to be achieved in the brace with the higher loading ratio, which explains why an increase in the joint capacity appears to be achieved when a purlin load is applied.

This can also be seen in the moment load diagrams, shown in Figure 8.7 and Figure 8.9 where the purlin is loaded by 0.2F in tension and compression respectively, where the brace with the higher loading ratio exceeds the plastic capacity before the chord. Compared to the moment load diagram shown in Figure 8.8, where there is no purlin applied to the chord, the chord is clearly seen to reach the plastic capacity before either of the brace members.

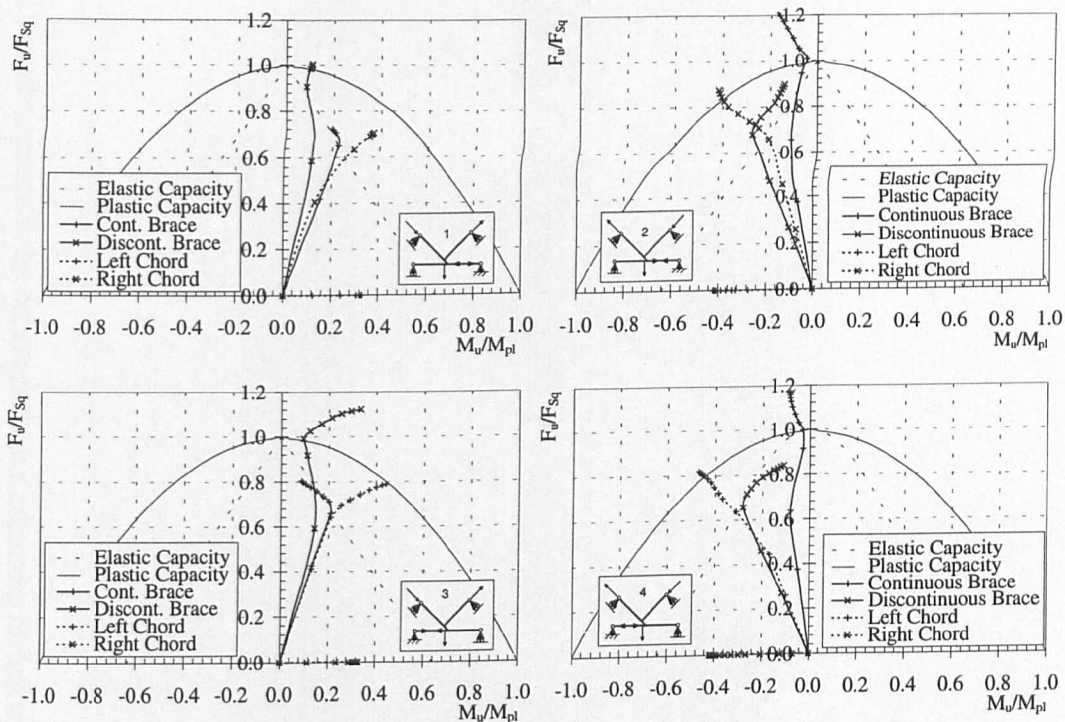


Figure 8.7 Moment/load interaction diagrams for the purlin bird beak joint $\theta = 45^\circ$ $x=0.2$ Tension

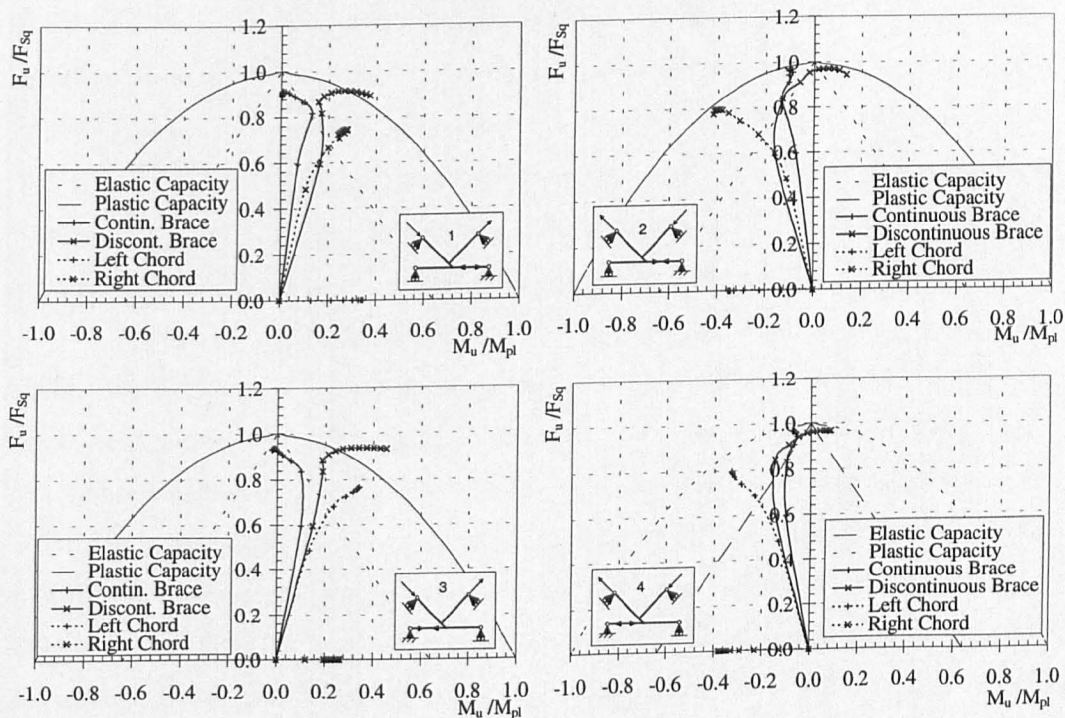


Figure 8.8 Moment load interaction diagrams for the bird beak joint $\theta = 45^\circ$ no purlin plate

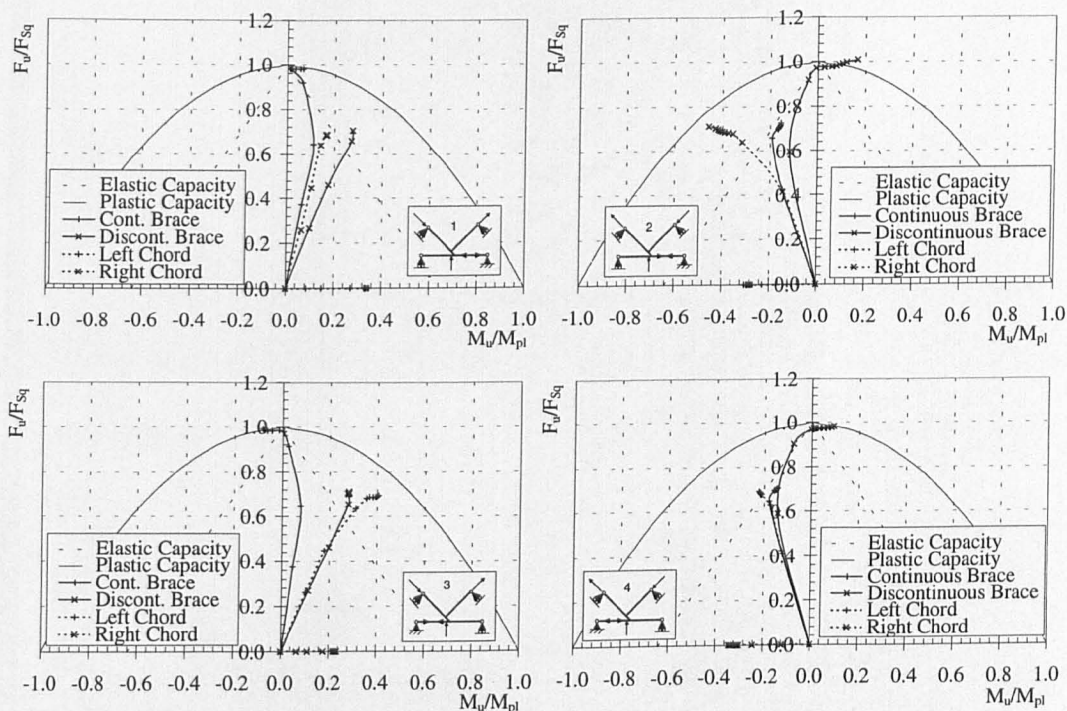
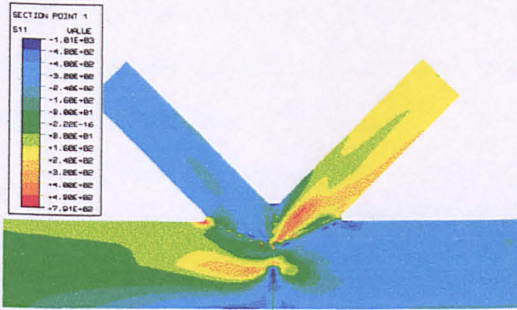


Figure 8.9 Moment/load interaction diagrams for the purlin bird beak joint $\theta = 45^\circ$ $x=0.2$
Compression

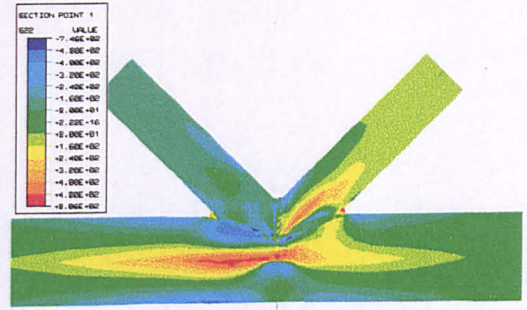
There are two possible explanations as to why the load cases 2 & 4 have a higher joint capacity when the purlin plate is loaded in tension than load cases 1 & 3. (This tendency is reversed when the purlin plate is loaded in compression.) Either there is a “hydrostatic effect” on the stresses present in the chord, i.e. when chord has both compression stresses axially and transversely, the observed stress in the chord may raise above the yield stress or it is again due to the nature of the loading on the joint.

Considering the “hydrostatic stress” effect on the chord, it is true that the highest joint capacities are observed when both the chord and the purlin plate are loaded in the same sense, tension or compression. However, Figure 8.7 and Figure 8.9, which show the moment load interaction curves for K joints loaded with a purlin load, indicate that the failure occurs primarily in the brace loaded with the full force F . In some of the analyses the chord does not even reach the plastic capacity, therefore this form of failure is unlikely to affect the joint capacity. Examination of some sample stress plots shown in Figure 8.10 show that yielding is confined to the vicinity of the purlin plate and the brace. This is best shown in the von Mises stress plot where the material that has yielded is shown in red (stress is greater than 420 N/mm^2).

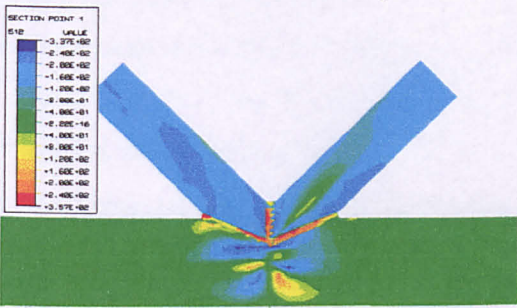
Joints loaded in Compression $\theta = 45^\circ$



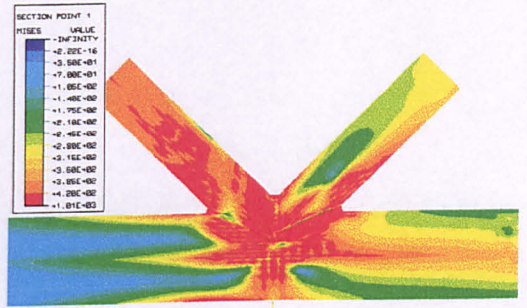
2BK45PLC-1 Axial Stress plot



2BK45PLC-1 Transverse Stress plot

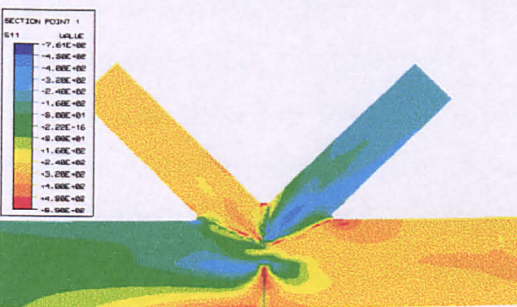


2BK45PLC-1 Shear Stress plot

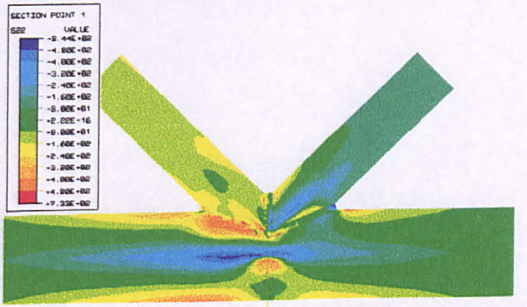


2BK45PLC-1 von Mises Stress plot

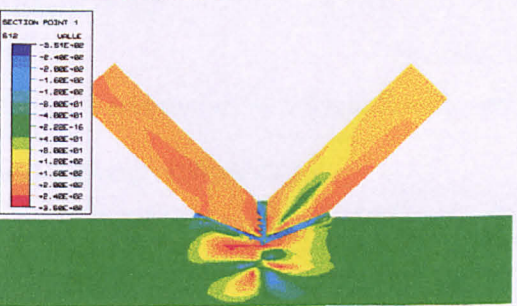
Joint loaded in Tension $\theta = 45^\circ$



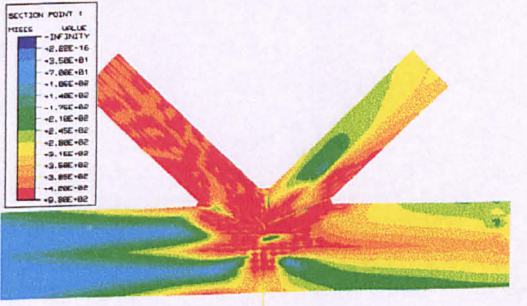
2BK45PLT-2 Axial stress plot



2BK45PLT-2 Transverse stress plot



2BK45PLT-2 Shear stress plot



2BK45PLT-2 von Mises stress plot

Figure 8.10 Examples of the contoured stress plots when a purlin load is applied to the chord

The axial and transverse stress plots show very little material in the chord where the stress has risen above the yield stress as would be expected if this “hydrostatic stress” effect was taking place. It is therefore unlikely that any form of “hydrostatic stress” effect is taking place

It was noted in Chapter 7 that the highest joint capacities were achieved when the through brace was loaded in tension. With reference to Figure 8.2 and Figure 8.6 where the 8 results of the K joints with a purlin load of 0.2 (tension & compression) are divided into four groups (A to D) according to the loading condition. Examining Figure 8.6 it can be seen that:

- the results when the purlin plate are loaded in tension (and the larger axial force is tensile) A & C, are significantly higher as a group, than when the purlin plate is loaded in compression (and the large axial force is compressive) B & D.
- the higher joint capacities are achieved when the larger axial force is applied to the continuous brace, tensile or compressive A & B, than when the larger force is applied to the discontinuous brace C & D.

Although it may be stating the obvious, it is therefore concluded that:

- a brace member is stronger when loaded in tension than compression
- the continuous brace is stronger than the discontinuous brace.

It may be further concluded that for the K joints and all the load cases considered that the dominant effect is the extra strength of the continuous brace on the joint capacity and the effect of the member being loaded in tension is less significant. This can be seen by comparing the differences of the mean values of groups A & C (change member loaded by largest axial force) and A & B (change direction of loading) in that

$$(A \sim C) > (A \sim B)$$

The same relationship also holds for CD and BD.

8.4.1 Design information

In Chapter 7 it was concluded that the plastic collapse of the chord was critical in most of the joints when no purlin load was applied to the chord. When a purlin load is applied, the axial load in the chord is reduced and the plastic collapse of the chord is less likely to be critical. Examination of Figure 8.6 shows that for the a purlin load

in the range of $-0.25 < F_p < 0.25$ of the brace squash load $F_{1,sq}$, the joint strength can still be calculated by

$$F_{u,1} = 0.9 A_1 f_{y,1} \quad \text{Eqn 8.1}$$

and in the unlikely case that the purlin load is higher, $-0.4 < F_p < -0.25$ or $0.25 < F_p < 0.4$ then the joint strength may be defined by

$$F_{u,1} = 0.75 A_1 f_{y,1} \quad \text{Eqn 8.2}$$

The axial load and bending moment in the chord should still be checked in all cases to ensure that the elastic capacity of the chord is not exceeded.

8.5 A special case where only one purlin load is applies to a truss

8.5.1 Introduction

In Section 8.3.1, when the methods of supporting the purlin load were discussed, an arrangement called the T joint, shown in Figure 8.3, was discounted as too costly and complicated, as the majority of purlin loads are fairly low in comparison to the chord capacity. However, if the purlin load is only applied at the centre of the truss arrangement, as shown in Figure 8.11, then the extra cost of providing a T joint arrangement to support the purlin load could be justified as the purlin load would be significantly larger and only requires one support per truss.

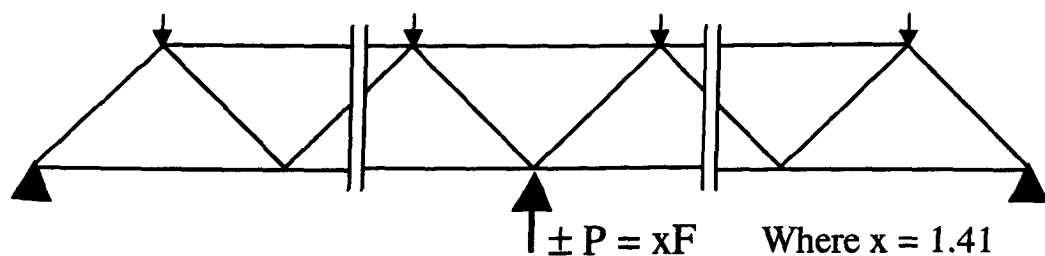


Figure 8.11 Example of a truss arrangement where the purlin load may be very high

The difference in the loading method of this particular type of joint was felt to be worth investigating as the cross loading of the chord is significant and this is the form of loading which CIDECT considers should be designed as a X joint, where the effects of the axial load and bending moment acting in the chord should be considered. Constructing the arrangement to carry the purlin load in the form of a T

joint then has the added advantage that any approximation made by assuming the joint is a X joint is more likely to valid.

This section will examine the variation of joint capacity of a diamond bird beak K joint with an axial chord load, where the cross loading of the chord is significant to establish that designing the K joint as a X joint is valid and that the decrease in the joint capacity as the chord load increases is accurately predicted.

8.5.2 Method of loading a diamond bird beak K joint where there is an axial chord load and the cross loading of the chord is significant

The four methods of loading the models analysed are shown in Figure 8.12, where the value F defines the joint capacity. The chord is axially loaded with no restraint on the brace members allowing them to move freely according to the deformation of the chord. When the chord load is attained, the roller restraints and load are applied to the brace members.

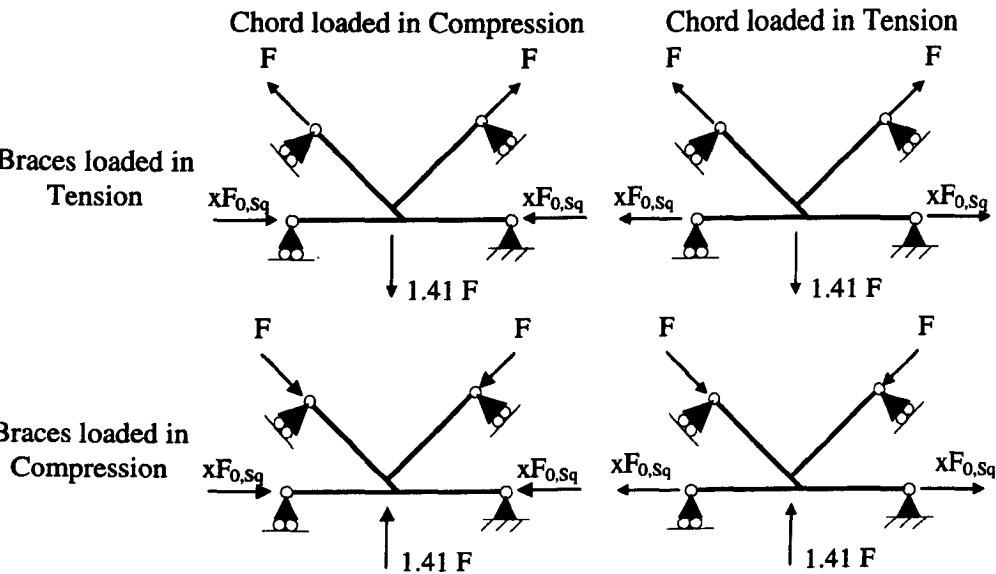


Figure 8.12 Four different methods of loading diamond bird beak K joint with a substantial cross loading of the chord and an axial chord load

8.5.3 The results of the analyses for diamond bird beak K joints where there is an axial chord load and the cross loading of the chord is significant

The results of the analyses for diamond bird beak K joints where there is an axial chord load and the cross loading of the chord is significant are given in Table 8.5 and shown graphically in Figure 8.13.

Model	Method of loading the chord	Method of loading the brace members	Joint Capacity	
			$F_{t,sq}$	kN
14BK45T	0	Ten.	0.5227	463.1
14BK45C	0	Comp.	0.3468	307.2
2C-14BK45C	0.2 Comp	Comp.	0.3443	305.0
4C-14BK45C	0.4 Comp	Comp.	0.3378	299.3
6C-14BK45C	0.6 Comp	Comp.	0.3204	283.8
8C-14BK45C	0.8 Comp	Comp.	0.2847	254.3
8C-14BK45T	0.8 Comp	Ten.	0.2847	288.2
8T-14BK45C	0.8 Ten	Comp.	0.3253	252.2
8T-14BK45T	0.8 Ten	Ten.	0.5376	476.3
9C-14BK45C	0.9 Comp	Comp.	0.228.6	228.6

Table 8.5 The joint capacities of the K joints where there is an axial chord load and the cross loading of the chord is significant

The expected decrease in the joint capacity due to the axial force in the chord is represented in this figure by two functions given in the CIDECT design recommendations. (Eurocode 3 Annex K uses the same formula, although the signs are changed to allow for the fact that in Eurocode 3 compression is +ve.) The first for CHS joints (Wardenier 1991)

$$f(n')=1+0.3n'-0.3n'^2$$

Eqn 8.3

where $f(n') = 1$ when $n' \geq 0$ (tension)
and the second for RHS joints (Packer et al 1992)

$$f(n) = 1.3 + \frac{0.4}{\beta} n$$

Eqn 8.4

where $f(n) \leq 1$

Eqn 8.3 is considered as it was used by Ishida et al (1993) to describe the decrease in the joint capacity of a gap bird beak K joint with an axial loading on the chord.

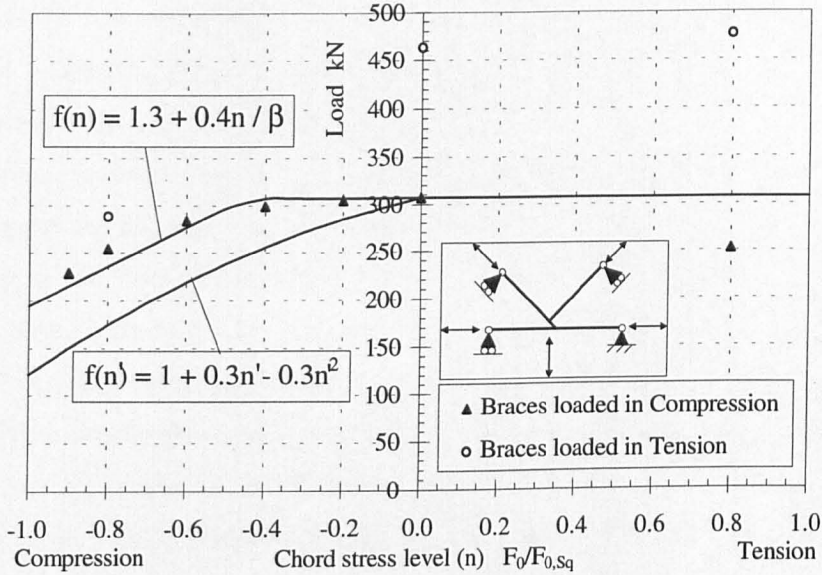


Figure 8.13 The variation in joint capacity of the K joints where there is an axial chord load and the cross loading of the chord is significant

8.5.4 The discussion of the results for diamond bird beak K joints where there is an axial chord load and the cross loading of the chord is significant

The capacity of joint 14BK45C (=307.2kN) has been used to define the strength of the joint when there is no axial load applied to the chord so that an accurate base level can be established to compare the decrease in the joint capacity as the axial load is applied.

Examining the results shown in Figure 8.13 it can be seen that the lowest joint capacities are obtained when the braces are loaded compression, regardless of whether the chord is loaded in tension or compression. This shows an anomaly in that the functions for the decrease in joint capacity when an axial load is applied to the chord predict that there should be no decrease in the joint capacity if the chord is loaded in tension. Regrettably when this research was carried out, loading the chord in tension was not thought to be critical and only a few joints were tested under these conditions. On consideration this should be expected as an overlapped K joint is not affected by the sense of the chord load in the same manner as a gap K joint in that in the gap joint

the load from the brace members has to be transferred through the chord and is therefore sensitive to the sense in which the chord is loaded. In the overlapped joint the

load from the brace members is transferred directly between the brace members and the sense of loading in the chord is not important and that the joint capacity is only going to be affected by the stress level present in the chord.

When the braces are loaded in tension higher joint capacities are achieved and therefore are not critical. It is, however, interesting to note that the joint capacities now display the type of behaviour that would be expected by examination of the function given in Eqns 8.3 & 8.4, i.e. the lowest capacity is achieved when the chord is loaded in compression and the highest when the chord is loaded in tension.

When the chord is loaded in compression for the overlapped bird beak K joint, the function $f(n)$ given in the RHS design guide (Packer et al 1992) predicts the decrease in the joint capacity with reasonable accuracy, whilst the function for $f(n)$ given in the CHS design (Wardenier et al 1991) overestimates the decrease in the joint capacity significantly.

It was stated in the beginning of this section that this form of joint and loading condition would in fact be designed as X joint with equivalent member sizes. Using Eqn 4.7, (shown here as Eqn 8.5) for the joint capacity of a diamond bird beak X joint (where the chord length is such that the asymptotic strength has been achieved) the expected joint capacity can be calculated.

$$F_{u,1} = \frac{2.6}{1-0.6\beta} f_y t_0^2 \left(\frac{b_0}{t_0} \right)^{0.4} \quad \text{Eqn 8.5}$$

Considering two chord width ratios of $\beta = 0.6$ and 0.8 (representing the chord width ratio of the braces and an average of the chord width ratio of the T joint holding the purlin load and the braces) the joint capacities of the equivalent X joint are 240.6 and 296.2 kN. It is likely that a designer would chose the lower value and indeed using this value a safe joint capacity (i.e. underestimated) would be achieved in all the loading conditions examined. If the average value for the chord width ratio is chosen, in this case a representative value is obtained for the joint capacity when no load is applied to the chord and safe estimate is made when a compressive load is applied to

the chord, (although there is no margin for error). The joint capacity would however, be overestimated should a tensile load be applied to the chord.

8.5.5 Conclusions

From this short examination of the behaviour of an overlapped bird beak K joint where there is a significant cross loading and an axial load applied to the chord has revealed that:

- the lowest joint capacities are obtained when the brace members are loaded in compression, regardless of whether the chord is loaded in tension and compression.
- when the chord is loaded in compression, the function $f(n)$ given by the CIDECT RHS design guide gives an accurate representation of the variation of the joint strength with axial load.
- when the brace members are loaded in tension, the joint capacities vary in a similar manner to that predicted by the functions in the design guides, but these joint capacities are not critical
- contrary to the advice given in the design guides, that there is a decrease in the joint capacity when the chord is loaded in tension and the braces in compression

8.6 Summary

A preliminary study has been made in this Chapter of the behaviour of overlapped bird beak K joints where $\theta = 45^\circ$ and purlin load was applied to the chord. During the course of the study different methods of securing the purlin load to the chord were investigated and the effect that they had on the joint capacity. The arrangement referred to as the T bar provided no support against deformation to the chord and the lower joint capacities were observed for this arrangement. The purlin plate, whilst being relatively easy to fit did provide a measure of support against the deformation of the chord and consequently a higher joint capacity was observed.

Examining the joint capacities when a purlin load was applied to the chord showed that there were significant differences in the strength of the joint when the load and boundary conditions and the sense of loading on the purlin plate were changed. These differences were attributed to the facts that the continuous brace is stronger than the discontinuous brace and that the brace member is stronger in tension than in compression. The strength of the joint could be determined by

$$F_{u,1} = 0.9 A_1 f_{y,1}$$

where the load on the purlin plate F_p was in the range of $-0.25 < F_p < 0.25$ of the brace squash load $F_{1,sq}$. When a higher purlin load was applied to the chord such that F_p was in the range of $-0.4 < F_p < -0.25$ or $0.25 < F_p < 0.4$ then the joint strength could be determined by

$$F_{u,1} = 0.75 A_1 f_{y,1}$$

When an axial load was applied to the chord in these joints then the joint capacity was determined by the plastic failure of the chord.

A special case was then examined where there was a significant cross loading of the chord in the presence of an axial load in the chord and CIDECT recommends that overlapped K joints are designed as X joints with an equivalent sized members. This was found to provide a safe solution when the chord width ratio was assumed to that of the braces however, when an average chord width ratio between the braces and the T joint carrying the chord load was considered a better estimate of the joint capacity in this case was found although it was not a safe estimate in all loading cases.

The decrease in the predicted joint capacity as the chord load increased was compared against two functions published by CIDECT to predict the decrease in the joint capacity. The function for $f(n)$ published in the RHS design guide (Packer et al 1992) gave a better representation of the variation of the joint capacity as the chord was loaded, but an anomaly where the braces loaded in compression and the chord loaded in tension was shown to exist.

9.

Conclusions and Recommendations for Further Work

9.1 Introduction

The principal aim of the work presented in this thesis was to increase the understanding of behaviour of the bird beak joints and to expand the parameter range of joints that have been studied. This has been achieved by examining a selection of bird beak X, T and overlapped K joints and by making comparisons to similar traditional RHS and CHS joints. The study of the behaviour of bird beak joints using finite element methods has revealed many interesting features and characteristics of bird beak joints. Controlled parameter variation and changing boundary conditions have uncovered forms of behaviour that would have been difficult and expensive to determine from laboratory experimental work. While it has not been possible to formulate a yield line failure clearly, the database of finite element results and the analysis carried out for the X joints will provide a foundation for such an approach to be tackled in the future.

The main conclusions are summarised in this Chapter, giving joint strength equations where appropriate.

9.2 Diamond and square bird beak X joints

The strength of bird beak X joints was found to vary significantly with chord length, boundary conditions at the end of the chord, chord width ratio β and chord wall slenderness b_0/t_0 etc. all which have been investigated. When the ends of the chord are completely free of any boundary conditions, the effect of chord length can be divided into three categories:

- short chord length joints ($\alpha \leq 10$) where the joint capacity increased rapidly with length
- medium length joints ($10 \leq \alpha \leq 40$) where the capacity still increases with chord length, although at a significantly reduced rate to that observed in the short chord length joints

- long chord length joints ($a \geq 40$) where there was no variation in the joint capacity with chord length and this is referred to as the asymptotic joint capacity

When the ends of the chord are held encastré the same categories can be used to define the transition points, although the joint capacity now decreases with increasing chord length.

The parametric study has shown the importance of the chord width ratio β and the chord wall slenderness ratio b_0/t_0 in the evaluation of joint strength, the asymptotic mean joint capacity of the diamond bird beak X joint can be predicted by

$$F_{u,1} = \frac{2.6}{1-0.6\beta} 275 \left(\frac{f_y}{275} \right)^{0.8} t_0^2 \left(\frac{b_0}{t_0} \right)^{0.4}$$

for the range of parameters of $0.2 \leq \beta \leq 0.9$, $9.4 \leq b_0/t_0 \leq 35.3$ and for the range of yield stress of $275 \leq f_y \leq 400$ N/mm².

A full parametric study of the asymptotic square bird beak joint strength was not carried out. However, by comparing the results of the joints (studied in the investigation of the variation of joint capacity with chord length, where $\beta = 0.6$ and $b_0/t_0 = 23.8$), it is considered that the square bird beak X joint capacity is approximately 10% lower than that for the diamond bird beak X joints.

In some circumstances, where there is a relatively slender brace wall (in comparison the chord wall slenderness) and low chord width ratio, the deformation of the chord caused the brace member to fail in shear, as the brace does not have the capacity to resist the deformation of the chord. Therefore the shear capacity of the brace may be a limiting factor on the strength of the joint and in all cases the joint capacity should not exceed

$$F_{u,1} = 4 b_1 t_1 \frac{f_y}{\sqrt{3}}$$

9.2.1 Theoretical analysis of the X joints

Limited localised yielding was observed along the corners of the chord section in the bird beak joints similar to that found when yield lines are assumed in a failure mechanism. However the failure mechanism is a great deal more complex and is thought to also include:

- in-plane yielding of the chord wall in the vicinity of the brace members

- twisting of the chord faces, although this has little effect on the value of the collapse load
- in-plane bending of the chord faces

It has not been possible to derive an independent theoretical model where the collapse load could be simply estimated from the joint parameters.

9.3 Diamond bird beak T joints

Diamond bird beak T joints where $\theta = 90^\circ$ were examined and compared to similar traditional RHS T joints. Joints with varying chord length ratio α were used to examine whether the mode of failure was a local joint failure or an overall chord bending failure or a combination of both. The method used to predict the joint capacity in a design procedure was then examined to determine the accuracy of calculating the strength of the joint. The traditional method of joint design was then compared to a new innovative interaction method which uses both the force acting on the brace and the moment acting in the chord to determine the strength of the joint. Generally the interaction method was found to be an improvement giving a better indication of the strength of the joint as the chord length was varied.

9.3.1 T joints loaded with the effects of chord bending

The manner in which the shorter chord length diamond bird beak T joints failed was found to be very similar to that of the diamond bird beak X joints in that yield lines can be assumed to form at the corners of the chord section and that there was considerable in-plane yielding in the vicinity of the brace. As the chord length increased so the failure became more progressively that of an overall chord bending failure associated with the maximum moment in the chord under the brace. The diamond bird beak T joints demonstrated an interesting phenomenon whereby the moment acting in the chord can exceed its plastic moment capacity at the assumed point of failure. This was particularly noticeable for the stockier sections studied.

Although the plastic moment capacity of a square RHS section bending about its diagonal is less than that when bending about an axis perpendicular to any face, the diamond bird beak T joints were shown to be stronger than similar traditional RHS T joints for all the chord lengths considered. Using the analyses of joints where $\alpha = 6$, the strength of diamond bird beak T joints was empirically determined to be

$$F_{u,1} = 4 f_y t_0^2 \sqrt{\beta^{0.5} \frac{b_0}{t_0}}$$

for the range of parameters $0.2 < \beta < 0.6$, $9.4 < b_0/t_0 < 35.3$, $f_y = 275 \text{ N/mm}^2$.

9.3.2 T joints loaded without the effects of chord bending

To establish an interaction relationship between the branch axial load and chord bending moment it is necessary to establish the local joint capacity $F_{u,1,loc}$ in the absence of any chord bending moment. An improved method of removing the effects of chord bending was developed where the moment was applied to the chord in a series of incremental steps along the chord length. In the case of CHS T joints this was shown to produce a better representation of the local joint capacity where the failure was localised to the area around the brace and consistent results could be achieved with different chord lengths without altering the material properties of any part of the chord. The von Mises contoured stress plots for the diamond bird beak T joints showed that at failure the effected part of the chord was much less localised than the CHS T joints, but that the area of yielded material was relatively constant as the chord length was increased.

When the effects of chord bending were removed from the diamond bird beak T joints, the joint capacity varied with chord length in a similar manner to the diamond bird beak X joints with similar boundary conditions at the end of the chord.

The strength of the diamond bird beak T joint without the effects of chord bending can be determined by using

$$F_{u,1,loc} = 5.7 f_y t_0^2 \sqrt{\beta \frac{b_0}{t_0}}$$

for the range of parameters $0.2 < \beta < 0.6$, $9.4 < b_0/t_0 < 35.3$, $f_y = 275 \text{ N/mm}^2$.

9.3.3 Interaction diagrams

The plotted points in the interaction diagram produced for the diamond bird beak T joint displayed a wide spread in the results according to the slenderness of the chord and according to the chord width ratio. It was not possible to reduce the spread

in the results and a lower bound limit was used to predict the joint strength of the diamond bird beak T joint

$$\frac{F_{u,1}}{F_{u,1,loc}} + \frac{M_{u,0}}{M_{p,v,0}} = 1.2$$

with the limits

$$\frac{F_{u,1}}{F_{u,1,loc}} \quad \text{and} \quad \frac{M_{u,0}}{M_{p,v,0}} \leq 1$$

This produced a safe estimate of the joint capacity, although severely underestimating the strength of the stockier chord wall sections.

The plotted points in the interaction diagram produced for the traditional RHS T joint displayed a spread in the results according the chord slenderness, but in a regular manner and it was possible to reduce the spread and achieve a good estimate of all the joint capacities by using

$$\left(\frac{F_{u,1}}{F_{u,1,loc}} \right)^{10} \sqrt{\frac{t_0}{b_0}} + \left(\frac{M_{u,0}}{M_{p,v,0}} \right)^{10} \sqrt{\frac{t_0}{b_0}} \leq 1$$

This is in contrast with Yu 1995, where her results varied according to the chord width ratio β . This was found to be attributed to the different range of chord width ratios examined but otherwise the results were reasonably compatible.

9.4 Traditional RHS overlapped K Joints

Traditional RHS overlapped K joints were studied in detail to see whether an angle function should be included in the design formula published by CIDECT. Various load and boundary conditions were examined for different brace member inclinations ($30^\circ \leq \theta \leq 60^\circ$). Although the mode of failure and joint capacity varied with the different load and boundary conditions it was established that the branch angle did not have a significant influence on joint strength. The design formula published in the CIDECT design guide (Packer et al 1992) gave a good estimation of the joint capacity although it marginally overestimated the strength of the joints analysed.

The moment/load curves produced showed that the shear reactions at the end of the braces were in the opposite sense to that expected, in that the moment produced by the reaction acted in the same sense as the moment caused by the eccentricity of the

joint. This was attributed to the rotation of the joint as it was loaded and subsequently deformed.

9.5 Diamond bird beak K joints

Similar overlapped bird beak K joints were studied (with the same absolute eccentricity values) and were found to be substantially stronger than traditional RHS overlapped K joints. The failure of the joints generally being attributed to plasticification of the chord or the brace when the moment/load capacity was achieved. It was determined that for the joints analysed the joint capacity could be determined by

$$1 \geq \frac{2F_1 \cos \theta}{A_0 f_{y,0}} + \frac{1}{2} \frac{2eF_1 \cos \theta}{Z_0 f_{y,0}}$$

when the failure may occur in the chord and

$$F_{u,1} = 0.9 A_1 f_{y,1}$$

where the failure occurs in the brace for the parameter range of $30^\circ \leq \theta \leq 60^\circ$, $\beta = 0.6$, $b_0/t_0 = 23.8$, $t_0/t_1 = 1$.

Very little deformation occurred in the joints at failure due to the stiffness of the corners of the section on which the joint is formed. The reactions at the end of the braces, unlike the traditional RHS overlapped K joint, acted to oppose the moment caused by the eccentricity of the joint.

One of the reasons why the bird beak K joint is so much stronger is that there is no cross loading of the chord to cause lozenging of the chord section. In the presence of a purlin load to the chord it was found that the strength of the joint was not diminished until a relatively large purlin load of 25% of the brace squash load was applied. When very large purlin loads were applied to the chord of between ± 0.25 and ± 0.4 of the brace squash load then the joint strength was reduced to

$$F_{u,1} = 0.75 A_1 f_{y,1}$$

A special case when the cross loading of the chord was very high and the CIDECT RHS design recommendations (Packer et al 1992) states that overlapped K joints should be designed as X joints with similar member sizes was considered. In this particular case the axial load (and bending moment) acting in the chord should then be taken into account and the joint strength reduced accordingly. The function published

in the CIDECT RHS design recommendations gave an accurate representation of the variation in the joint capacity as the load in the chord was varied although it failed to predict a decrease in the joint capacity when the braces were loaded in compression and the chord in tension.

9.6 General advantages and disadvantages of bird beak joints

The main advantage of the bird beak joints is that the joint is formed using the corners of the sections and therefore can utilise the stiffness of corners in transferring the load from one member to the other.

The advantages of the bird beak X and T joint are considered to be:

- a smoother transfer of the brace axial force into the chord due to the alignment of the members in the diamond configuration
- the brace, providing it is strong enough, acts to restrain any lozenge deformation in the chord in the immediate vicinity of the joint
- a greater weld length than that for the traditional RHS joint

The strength advantage of the bird beak K joints where there is no cross loading of the chord, utilises the stiffness of the corners to great effect and demonstrates that there can be large increase in the efficiency of a truss using bird beak joints.

During the course of the work reported in this thesis some disadvantages have emerged such as:

- the lower moment capacity of the diamond section configuration
- the lack of stiffness of the diamond section when a cross loading is applied to the chord causing lozenge or crushing of the section
- the variation of the joint capacity when there is a cross loading of the chord with chord length and the boundary conditions at the end of the chord.

Despite these disadvantages it is felt that the bird beak joint configurations offer a more efficient joint arrangement, the use of which will increase as problems in the fabrication are overcome by increasing automation in the manufacturing process.

9.7 Future investigation

Bird beak joints are a relatively new form of joint configuration which have yet to achieve wide spread popularity. Very little research has been carried out besides

the work done in Japan together with this investigation. It has not been possible to cover all the aspects of joint behaviour in this work and there is a wide scope for future investigations that could include some of the following:

- the parametric studies should be widened to include a greater range of variation, including β , b_0/t_0 , α , the joint angle θ and higher strength materials.
- to examine further the reason for the wide scatter of the results in the interaction diagrams for the bird beak joints, particularly when compared to other forms of joint. (Very recent thoughts are that this may be associated with the variation in the shear resistance with length for the RHS section in the diamond configuration and that this should be examined)
- to expand the work on K joints to allow for change in the parameters such as the eccentricity (which will in turn affect the gap or overlap of the joint), the chord width ratio β and chord wall slenderness b_0/t_0 .
- to investigate other forms of loading such as in-plane and out-of-plane bending using finite element methods to complement the work carried out in Japan, so that a greater depth of understanding of the failure can be achieved.

An excellent data base of results has been obtained from the finite element investigations carried out in this work which should allow a more rigorous theoretical determination of the joint strength to be developed in future.

References

ABAQUS (1996) ABAQUS versions 5.3, 5.4 & 5.5. Hibbitt Karlson & Sorreson (HKS) Inc. 35 Angel Street, Providence, Rhode Island 02906, USA.

API (1993). American Petroleum Institute. Recommended practice for the planning, design and constructing fixed offshore platforms - Load and resistance factored design, RP2A-LRFD, Parts 1 & 2. 1st Edition July 1993. American Petroleum Institute, 1220 L street, Northwest Washington, DC20005. (also ISO Draft International Standard ISO/DIS 13819-1 & ISO/DIS 13819-2)

AWS D1.1-92 (1992). American Welding Society, Structural Welding Code.

Bauer D., G. Redwood (1988) Triangular truss joints using rectangular tubes. Journal of Structural Engineering. ASCE, Vol114, No. 2, Feb 1988, pp408-424

BS4848 (1991) BS4848 Hot rolled structural steel sections, Part 2 Hollow sections. British Standards Institution, 2 Park Street, London. (also known as ISO 657 Hot rolled sections: Part 14, Hot finished structural hollow sections, dimensional and sectional properties)

BS6363 (1983) BS6363 Cold formed hollow sections. British Standards Institution, 2 Park Street, London. (to be replaced by EN10219-2 soon)

British Steel (1994a). Hot finished SHS sizes and properties. British Steel, Corby, Northants.

British Steel (1994b). Cold formed hollow sections. British Steel Corby, Northants.

CIDECT (1986). CIDECT Monograph No. 6 The strength and behaviour of statically loaded welded connections in structural hollow sections. (Eds T.W. Giddings and J Wardenier) British Steel Corporation. Corby, Northants.

Clough R.W., (1960). The Finite Element Method in-plane stress analysis. Proceedings of 2nd ASCE Conference on Electronic Computation. Pittsburgh, PA.

Crockett P. (1994). Finite element analysis of welded tubular sections. Ph.D. Thesis. Nottingham University, UK. July 1994.

Davies G., M.G. Coutie and M Bettison (1993). The behaviour of three dimensional rectangular hollow section T joints under axial branch loads. Tubular Structures V. (Eds MG Coutie and G Davies) E & FN Spon, London.

Dutta D., & K. Hoffmann (1996). CIDECT research and development in the use of hollow steel sections and their impact on Eurocodes and other international standards. Tubular Structures VII. (Eds J. Farkas and K. Jarmai) A.A. Balkema, Rotterdam, Netherlands.

Eurocode 3 (1992). Design of steel structures, Part 1.1: General rules and rules for buildings. April 1992. British Standards Institution, 2 Park Street, London. (ENV 1993-1-1)

Eurocode 3 (1994). Annex K: Hollow section lattice girder sections. British Standards Institution, 2 Park Street, London. (ENV 1993-1-1/A1:1994)

FEMVIEW (1989) FEMGEN/FEMVIEW - The finite element pre and post processor - User manual. FEMVIEW Ltd.

Fundament, A., (1995). The strength and stiffness of double tee joints. The department of Civil Engineering Nottingham University, UK.

Grunberg, M., (1994). The strength and stiffness of X joints. Department of Civil Engineering, Nottingham University, UK.

IIW (1989) International Institute of Welding. Design recommendations for hollow section joints - predominately statically loaded. 2nd Edition 1989. IIW Doc XV-701-89.

Ishida, K., T. Ono and M. Iwata (1993). Ultimate strength formula for joints of a new truss system using Rectangular Hollow Sections. Tubular Structures 5. (Davies and Coutie Ed.), E & FN Spon, London. pp 511-518

Jamm, W. (1951)*. Gestaltfestigkeit geschweizter Rohrverbindungen und Rohrkonstruktionen bei statischer Belastung, Schweißen und Schneiden, Sonderheft.
*Not read by the author, but included for completeness

Korol R.M., Mizra F.A. (1982) Finite element analysis of RHS T joints. ASCE, Sept 1982, pp2081-2098.

Lu, L.H., G. D. Winkel, Y. Yu and J. Wardenier (1994) Deformation limit for the ultimate strength of hollow section joints. Tubular Structures VI (Holgate and Wong Ed) Balkema, Rotterdam. pp 341-347. (Also IIW Doc XV-E-94-215)

Marshall P.W. (1992) Design of welded tubular connections - Basis and use of AWS code provisions. Elsevier Science Publishers BV Amsterdam, The Netherlands

Microsoft (1993) Excel 5a manuals. Microsoft Corporation.

NAFEMS (1986) A Finite Element Primer. Dept. Trade and Industry, HMSO, Glasgow.

Ono, T., M. Iwata and K Ishida (1991). An experimental study on joints of a new truss system using Rectangular Hollow Sections. Tubular structures 4th International

Symposium. (J. Wardenier and D Dutta Ed.), Delft University press, Netherlands. pp 344-353

Ono, T., M. Iwata and K Ishida (1993) Local failure of joints of a new truss system using rectangular hollow sections subject to in-plane bending moment. *Tubular Structures V*. (Davies and Coutie Ed.), E & FN Spon, London. pp 503-510

Ono, T., M. Iwata and K Ishida (1994) Local failure of joints of a new truss system using rectangular hollow sections subject to out-of-plane bending moment. *Tubular Structures VI*. (Grundy, Holgate & Wong Ed.). A.A. Balkema, Rotterdam, Netherlands. pp 441-448

Packer, J., J. Wardenier, Y Kurobane, D Dutta and N Yeomans (1992). CIDECT Design guide for rectangular hollow sections (RHS) joints under predominantly static loading. TyV Rheinland GmbH, KØln.

Steller, A. (1996) Planar Lattice girders in rectangular hollow sections. Department of Civil Engineering, Nottingham University, UK.

Togo, T. (1967)* Experimental study on mechanical behaviour of tubular joints. Ph.D. Thesis, Osaka University, Osaka, Japan. (in Japanese) *Not read by the author, but included for completeness

Turner M.J., R.W. Clough, H.C. Martin and L.C. Topp (1956). Stiffness and deflection analysis of complex structures. *Journal Aeronautical Science* Volume 23, No 9. pp 805-823, 854.

Turner, M.J., E.H. Dill, H.C. Martin, R.J. Melosh (1960). Large deflections of structures subjected to Heating and external loads. *Journal of Aero. Sci.* No. 27 pp 97-96.

UEG (1985) Design of tubular joints for offshore structures. UEG Offshore research (a part of CIRIA). Page Bros Ltd., Norwich, Norfolk

Vegte, G.J. van der, 1995. The static strength of uni-planar and multi-planar tubular T- and X-joints. Ph.D. thesis, Delft university press. Netherlands.

Vegte, G.J. van der & J. Wardenier (1994a). The static behaviour of uni-planar Tubular steel T-joints excluding the effect of chord bending. The 4th International Offshore and Polar Engineering Conference. (Yukio Ueda et al Ed). ISOPE, Golden, Colorado.

Vegte, G.J. van der & J. Wardenier (1994b). An interaction approach based on brace and chord loading for uni-planar tubular T-joints. Tubular Structures VI. (P. Grundy, et al Ed), A.A. Balkema, Rotterdam.

Wardenier J., Y. Kurobane, J.A. Packer, D. Dutta, N. Yeomans. (1991). CIDECT Design guide for Circular Hollow Sections (CHS) joints under predominately static loading. Verlag TyV Rheinland, K hn.

Wardenier, J. (1982). Hollow Section Joints. Delft University Press, Netherlands.

Yu, Y., J Wardenier (1995). Influence of the chord bending on the ultimate capacity of RHS T-joints. The 5th International Offshore and Polar Engineering Conference. ISOPE, Golden, Colorado.

Yu, Y., J Wardenier (1996). Influence of chord bending moments on the ultimate load capacity of X joints in rectangular hollow sections. Tubular Structures VII. (Eds J. Farkas and K. Jarmai) A.A. Balkema, Rotterdam, Netherlands.

Yura J.A., N. Zettlemoyer, I.F. Edwards (1980). Ultimate capacity Equations for Tubular joints. Proceeding Offshore Technology Conference, Paper OTC 3690, Houston, Texas, U.S.A.

Zienkiewicz and Cheung (1965) Finite elements in the solution of field problems. Engineer, Vol. 220, pp 507-510.